Single Vial Monitoring of Pharmaceutical Freeze Drying Processes using Through Vial Impedance Spectroscopy

Bhaskar Pandya

Leicester School of Pharmacy, De Montfort University

Leicester, United Kingdom

Circulation

First Supervisor: Professor Geoff Smith

Second Supervisor: Dr Irina Ermolina

January 2020

PhD Thesis

In partial fulfilment of the requirements for the degree of

Doctor of Philosophy

Submitted to

De Montfort University

Declaration

I, Bhaskar Pandya, confirm that the content presented within this thesis is my own work. I confirm that information derived from other sources has been referenced appropriately.

Part of this work has been presented at various conferences (Section 12)

Pandya B, Matejtschuk P, Jeeraruangrattana Y, Smith G, Ermolina I. (2019) Multiplexing Through Vial Impedance Spectroscopy (TVIS) with Comparative Pressure Measurement for the Determination of the Primary Drying Endpoint of Immunoglobulin (IgG). Poster presentation at: **ISL-FD's 9th International Symposium on Lyophilization of Pharmaceuticals**, 2019 Sept 2-6; Ghent, Belgium

Pandya B, Smith G, Polygalov E, Ermolina I. (2018) Application of Through Vial Impedance Spectroscopy for Lyophilization Process Development. Poster presentation at: **Freeze Drying of Pharmaceuticals and Biologicals**, 2018 Sept 18-21; Garmisch Partenkirchen, Germany

Pandya B, Smith G, Polyglov E, Ermolina I. (2017) New impedance based methodologies to determine the vial heat transfer coefficient and the endpoint of primary drying. Poster and Podium presentation at: **UK-PharmSci**; 2017 Sept 5-7; Hatfield, UK.

Jeeraruangrattana Y, **Pandya B**, Smith G, Ermolina I. (2016) The Application of Through Vial Impedance Spectroscopy (TVIS) for Optimization Freeze-Drying Process. Poster presentation at: **EPSRC EHDA Network: International PharmTech**, 2016 Nov 4; Leicester, UK

Pandya B, Smith G, Ermolina I. (2016) Freeze Drying Monitoring Using LyoDEA® Process Control. Poster Presentation at: **QbD Symposium**, 2016 Mar 16; Leicester, UK

Contents

List of Figures

List of Tables

List of Abbreviations

A_v: Vial outer cross-sectional area projected onto the shelf

BDS: Broadband Dielectric Spectroscopy

C: Capacitor

C_s: Solution capacitance

C''_{PEAK}: Peak imaginary amplitude

$C'(0.2MHz)$: Real part capacitance measured at a characteristic frequency of 0.2 MHz

$C'(100\ kHz)$: Real part capacitance measured at a characteristic frequency of 100 kHz

C_{eu}: Eutectic concentration

$C_g{}'$: Maximal freeze concentration

C_G: Glass wall capacitance

C_i: Interfacial capacitance

C_∞: Instantaneous Capacitance

Co: Cole Cole

CPE: Constant Phase Element

CQA: Critical Quality Attribute

CPP: Critical Process Parameter

dm/dt: Mass transfer rate

dq/dt: Heat transfer rate

DSC: Differential Scanning Calorimetry

ε_0: Permittivity of free space

ε_g: Relative permittivity of the glass vial or dielectric constant of the glass vial

F_{PEAK}: Peak frequency of the dielectric loss peak

FDA: Food and Drug Administration

FDM: Freeze Dry Microscopy

γ: Admittance

Hz: Hertz

H_s: Enthalpy of sublimation

I: Current

kHz: kilo Hertz

K_v: Overall vial heat transfer coefficient to the product

K_c: Heat transfer coefficient from the shelf to the product via the points of contact (direct conduction)

K_g: Heat transfer coefficient to the product via conduction of gas molecules (e.g. water vapour) within the vial bottom concavity

K_r: Heat transfer coefficient to the product via heat radiation

LFD: Low Frequency Dispersion

MW: Maxwell Wagner

MHz: Mega Hertz

MTM: Manometric Temperature Measurement

mBar: Milli Bar

ω: Angular frequency

P_i: Vapour pressure of ice at the sublimation interface

P_c: Vapour pressure of ice at the condenser surface

P_{ch}: Partial pressure of water vapour in the drying chamber

P_{ch}^{set}: Programmed chamber pressure

PAT: Process Analytical Technology

PRT: Pressure Rise Test

QbD: Quality by Design

φ: Phase angle

R_p: Resistance to the vapour flow through the dry layer or dry layer resistance

R_s: Resistance to vapour flow from the stopper inserted into the vial neck

R_c: Resistance to vapour flow in the duct connecting the condenser and the drying chamber

RTD: Resistance Temperature Detector

R: Resistor

R_s: Solution resistance

τ: Time constant

T_{eu}: Eutectic melting point

T_g: Glass transition temperature

T_g': Glass transition temperature of the maximally freeze-concentrated solute

T_c: Collapse temperature

T_n: Ice nucleation temperature

T_f: Equilibrium freezing point

T_i: Product temperature at the sublimation interface

T_s: Shelf temperature

T_b: Product temperature at the vial bottom-centre

$T(F_{PEAK})$: Product temperature predicted from F_{PEAK} in the region bounded by the electrodes

TPP: Target Product Profile

TC: Thermocouple

TEMPRIS: Temperature Remote Interrogation System

TDLAS: Tunable Diode Laser Absorption Spectroscopy

V: Voltage

$|Z|$: Impedance Magnitude

Z: Impedance

Acknowledgements

The PhD program was sponsored under a fully funded High Flyers Research Scholarship Scheme, introduced by De Montfort University to encourage their alumni to pursue doctoral studies. Having secured a BSc (Hons) degree in Pharmaceutical and Cosmetic Science from DMU in 2013 and a Masters by Research (MRes) degree in Pharmaceutics from the University College London School of Pharmacy, I was one of the fortunate ones to have cleared the interview and secured a three-year high flyers scholarship at DMU in 2015 to work on a project under the supervision of my primary supervisor, Professor Geoff Smith, and my second supervisor, Dr Irina Ermolina. I would like to express my deepest gratitude to De Montfort University for offering me a PhD scholarship and both my supervisors for their contribution to this work.

I would like to extend my special gratitude to Geoff, who saw a glimmer of potential in me and gave me an opportunity to work with him in the field of freeze drying and impedance spectroscopy. He also taught me how to present complex experimental data in various forms (e.g. posters, presentations, journal-style writing). My trips with Geoff and my colleagues to several UK and international conferences over the course of the doctoral program have been really enjoyable and stimulating. Were it not for Geoff's extensive professional network, it wouldn't have been possible for me to meet the experts from the global freeze-drying community. I would like to especially thank Irina for being so approachable and immensely helpful during the final stages of this thesis. I would also like to thank all the technicians at De Montfort University for providing me with their expertise and support.

Professor Afzal Mohammed (external examiner) from Aston University, Birmingham, and Dr Dan Fei (Internal Examiner) from De Montfort University, are greatly appreciated for reviewing this thesis. Their valuable comments have helped me improve the quality of this work.

I would like to thank my colleagues Yowwares, Anand and Zakia for their kindness, friendship, support and all the good times which I will always cherish. I would also like to thank my other colleagues, Joe, Longinus, Pathum and Vaithi for all the stimulating conversations we have had.

I would like to especially thank my best friend Bhumika for her continuous faith in me. In the end, I am grateful to my parents for being the pillars of strength and inspiration in my life and for their continuous support, without whom I would not have aspired to pursue doctoral studies.

Abstract

Currently, there is no single process analytical technology (PAT) in the market that can provide non-invasively, product and process related information which is representative of the entire batch at key stages of the freeze drying process: (i) the ice nucleation onset and the ice solidification endpoint, and the resulting ice crystal structure at the end of the freezing stage; and (ii) the true batch endpoint of ice sublimation to ensure all the ice is removed before switching to the secondary drying stage.

Through Vial Impedance Spectroscopy (TVIS) employs a pair of electrodes that measure the electrical impedance of the glass vial and its contents. TVIS has been used as a PAT tool for the non-invasive monitoring of the critical events during the freeze drying process. While it has already been established previously that the TVIS parameters, F_{PEAK} (sensitive to product temperature) and $C'(0.2MHz)$ (largely sensitive to phase change) can be employed together to determine the ice nucleation onset and the ice solidification endpoint respectively, and C''_{PEAK} can be used for drying rate determination (largely sensitive to ice cylinder height), the present work involves the use of F_{PEAK} and $C'(0.2MHz)$ to demonstrate a direct dependency of ice nucleation temperature (or the freezing method) on the ice growth time, and subsequently the stability of the ice crystal microstructure determined using C''_{PEAK}. Further, the present study establishes a high sensitivity of another TVIS parameter, $C'(100\ kHz)$, towards the changes in the shape of the ice sublimation interface and subsequently the removal of the last vestiges of ice from a single vial during primary drying. This feature has been exploited for the prediction of the primary drying endpoint at any vial location by employing a mathematical methodology, which has been extended to a simple sugar solution, wherein visual imaging cannot be used to detect ice disappearance.

Finally, TVIS was multiplexed with batch measurement sensors (comparative pressure measurement and pressure rise test) for a comparison between the batch endpoint and the TVIS endpoints predicted at the shelf edge and the core. It has been demonstrated none of the PAT tools can determine the true endpoint of the batch (though the TVIS method is a significant improvement over one that relies on the thermocouple response). In conclusion, the study highlights a significant potential of TVIS for delivering additional product and process related information when it is multiplexed with batch measurement tools non-invasively, such as the thermal history of the sample before primary drying and the primary drying endpoints at various locations on the shelf.

1 Introduction

The global health market has witnessed a significant increase in the number of biopharmaceuticals or biologics (e.g. monoclonal antibodies, therapeutic proteins, enzymes, vaccines) in the recent years. In fact, around 40 % of the 6000 or more injectable products which are in clinical development are comprised of biologics (Walsh 2018), with around 155 active biopharmaceutical entities approved in the United States and/or the European Union between January 2014 and July 2018. With several major biologics nearing their patent expiries by 2022 (Lawrence and Lahteenmaki 2014), biosimilars are expected to gain prominence in the global biologic landscape. This is evident from the fact that around 30 % of the 188 biosimilars are currently in phase 3 clinical trials (FirstWord 2018). The primary reason for such predominance of biopharmaceuticals is the high prevalence of diseases indications that include, but are not limited to, cancer, inflammation-related disorders, diabetes, respiratory conditions, hemophilia, migraine and HIV (Walsh 2018).

One major challenge in biopharmaceutical drug development is to maintain the long-term stability of these products. A large proportion of biopharmaceuticals are unstable in aqueous solutions, which makes it difficult for a commercially viable shelf life. This is due to the fact that the solvent phase, usually water, exposes the drug to several degradation pathways (Reubsaet, et al. 1998). It is no surprise therefore that lyophilisation or freeze-drying has become a frontrunner in the manufacture of dry biopharmaceuticals, which is supported by the fact that in 1998, lyophilised products constituted 11.9 % of all new injectable or infusible drugs; and by 2015, their number had increased to more than 50 % (Shanley 2017).

1.1 Freeze-drying

Freeze drying is a well-established desiccation process, during which the solvent, typically water, is removed from the frozen material by sublimation at a reduced pressure, followed by a process of desorption at an elevated temperature, which removes the unfrozen water (Franks 2007). Thus, a complete freeze-drying cycle comprises three important stages: (i) a freezing stage, to form ice and

crystallise out any solutes; (ii) a sublimation (primary drying) stage, whereby ice is removed by a direct transformation of the frozen solution to its gaseous counterpart without crossing the liquid-vapour phase boundary, and (iii) a desorption (secondary drying) stage, during which most of the unfrozen water is removed by evaporative drying. The target residual moisture content of the freeze-dried cake is typically less than 1 % for a small molecule (Pikal, M. J. and Shah 1997; Tang, X. L. and Pikal 2004) and from 1 to 3 % for a biologic drug (given the requirement for some water to stabilise the native structure of the biological drug molecule) (Breen, E. D., et al. 2001; May 2004; Pikal, M. J., et al. 1991; Sarciaux and Hageman 1997). The target product is highly porous, with a very large surface area, which dissolves quickly when reconstituted with water (Velardi, S. A., et al. 2009). Further, as discussed earlier, the various pathways for degradation remain dormant owing to the presence of little or no water. An extended stability of the formulation containing the active pharmaceutical ingredient is thus achieved (though the requirement for cold chain storage at −8 to −2 °C may nevertheless remain).

1.2 Process Principle and Steps

The drug solution can be initially prepared in either water, organic or mineral solvent (e.g. diethyl amine, carbon dioxide) or in a cosolvent (e.g. tert-butanol with water) (Rey, L. and May 2004a). Given that water is the most common solvent used for formulating solutions for freeze-drying, non-aqueous solutions are outside the scope of this discussion. As mentioned earlier, freeze-drying comprises (i) freezing, (ii) primary drying and (iii) secondary drying. The principle of freeze-drying can be understood from the way water behaves when it is subjected to various temperatures and pressures as demonstrated in the schematic in Figure 1(a), where the three physical states of water (liquid, solid and gaseous vapour) are defined by the values of pressure (y-axis) and temperature (x-axis), and the phase boundaries, namely the fusion curve (liquid-solid phase boundary), the vapourisation curve (liquid-gas boundary) and the sublimation curve (solid-gas boundary).

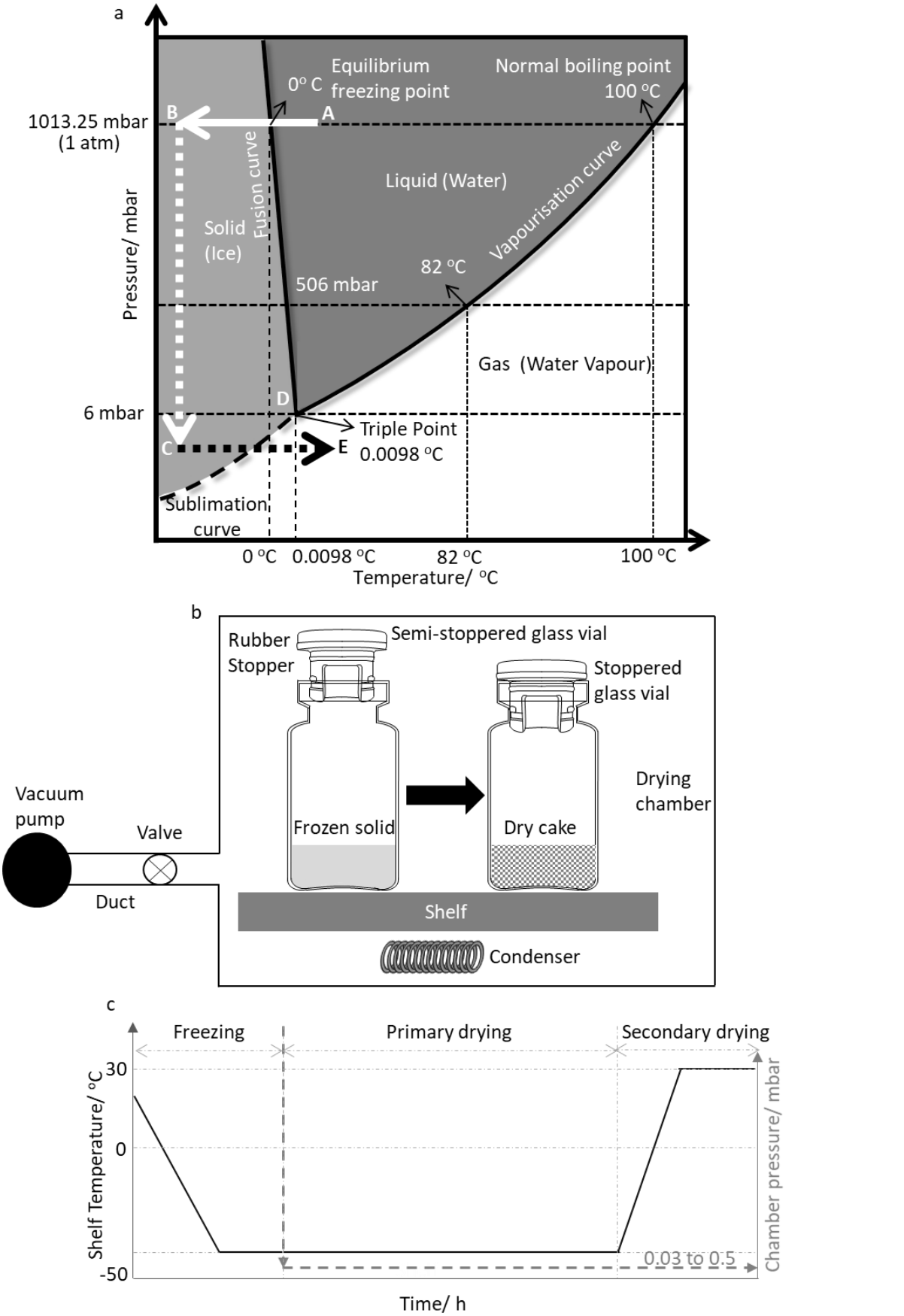

Figure 1(a) A schematic of the phase diagram of water; (b) a schematic of a freeze-drying system; (c) an example of the time-lines of the controllable process parameters, shelf temperature and the chamber pressure; adapted from Franks (2007).

As illustrated in Figure 1(a), at atmospheric pressure (1 atm or 1013.25 mbar), let us consider that the temperature of the liquid (e.g. water) is at some value higher than the equilibrium freezing point, i.e. 0 °C (point A). If the water is heated, the saturated vapour pressure increases and at some point (the normal boiling point of 100 °C) it equals the external atmospheric pressure, thereby forming bubbles of saturated vapour within the liquid. In other words, the molecules of water have sufficient energy to escape from the bulk liquid and form bubbles, which burst at the liquid surface causing the phenomenon known as boiling. When the pressure is reduced to a lower value (e.g. 506 mbar), the boiling point reduces to 82 °C because the saturated vapour pressure exceeds the external pressure (506 mbar) at a lower temperature.

In the context of freeze-drying, when water is frozen from ambient temperature (point A) to a value (point B) well below the equilibrium freezing point (0 °C) then water crosses the liquid-solid boundary and freezes at atmospheric pressure. But only when the pressure is reduced below 6 mbar (point C) and the temperature is increased beyond the triple point of water (0.0098 °C) (point D) will the water cross the sublimation curve to enter the vapour phase (point E), i.e. ice transforms into vapour directly at a reduced pressure. Note that the triple point is a temperature at which all the three states of water exist in equilibrium with each other.

A schematic of the essential components of a freeze-drying system (Franks 2007) is shown in Figure 1(b) which comprises a vacuum-tight chamber, fitted with temperature-controlled shelves, and a condenser maintained at a temperature well below that of the shelf (e.g. -60 °C), which traps the water vapour on its surface via condensation. The condenser is either located within the drying chamber (under the shelves) or in a separate compartment connected to the drying chamber via a duct with a valve that regulates gas flow. The solution to be freeze-dried is invariably contained in hundreds to thousands of semi-stoppered glass vials (only one is shown in the schematic) depending on the scale, which rest on stainless steel shelves. There is a heat exchanger system (not shown) that circulates a heat exchanging fluid through the shelves such that it continuously maintains the shelf temperature

at the desired set-point. The chamber can be evacuated with a vacuum pump via a valve regulates the flow of air in and out of the chamber. An example of the time-profiles of the shelf temperature and the chamber pressure is shown in Figure 1(c), where the three major stages of freeze-drying are depicted. The different steps that the product goes through can be mapped onto the phase diagram of water as in Figure 1(a), wherein: (i) the solid white arrow illustrates a decrease in the shelf temperature from ambient to a sub-zero temperature at atmospheric pressure, (ii) the dotted white arrow illustrates a decrease in the chamber pressure at the sub-zero temperature, and (iii) the dotted black arrow illustrates an increase in the shelf temperature for primary drying and a subsequent secondary step at the reduced pressure. During the primary and the secondary drying phases, the water vapour liberated from the product is transferred to a cold condenser. At the end of the secondary drying, the stoppers are pushed down the vial neck (Figure 1b) and subsequently sealed to prevent moisture ingress.

1.2.1 Freezing

The freezing stage is often defined as the process of crystallisation of supercooled water (Petzold and Aguilera 2009). The freezing stage involves the lowering of the product temperature to below the melting point of ice and the eutectic/glass transition temperature of any solute(s) that undergoes eutectic freezing or glass transition. The amount of ice and the structure of the ice crystals that form during freezing have a significant bearing on the overall efficiency of the freeze drying process. In effect the ice crystal morphology determines the pore size, pore shape and the tortuosity of the dries matrix that form during the sublimation of ice in the primary drying stage (Searles, et al. 2001a; Searles 2004). The freezing process is propagated through ice nucleation followed by the growth of the ice crystals. The resulting ice morphology depends on the degree of supercooling and the rate of ice crystal growth (or freezing rate). The main feature of the freezing stage is the phenomenon of supercooling, as it dictates the number, the morphology and the size distribution of ice crystals (Searles, et al. 2001b).

Degree of Supercooling and Ice Nucleation Temperature

It is important to recognise that water never freezes at the equilibrium freezing point (0 °C) (Rey, Louis 2010) and in fact, continues to supercool several degrees below 0 °C, typically over a broad temperature range from -10 to -20 °C, which is dictated by the amount of particulate matter in a research and development non Good Manufacturing Practice environment of the solution being frozen (Pikal, Michael J. 1990; Searles 2004). In fact, pure water can supercool to as low as -40 °C (Moore and Molinero 2011) thus it is not surprising to find that in clean GMP production environments, the degree of supercooling may be as low as -30 °C or more (Konstantinidis, et al. 2011). The temperature at which the ice nuclei first form is known as the ice nucleation temperature and the difference between the equilibrium freezing point and the ice nucleation temperature is termed the "degree of supercooling" (Searles, et al. 2001). The ice nucleation temperature is impacted by the properties of the formulation (e.g. presence of soluble solutes causing depression of the freezing point) (Roos, et al. 2018), the process conditions (e.g. cooling rate which determines ice growth time), the type of container (i.e. surface) and the presence of particulate matter (i.e. additional surfaces) (Pikal 1990; Pikal, Michael J., et al. 2002; Rambhatla, Shailaja, Ramot, Bhugra and Pikal 2004a).

Nucleation and Ice Crystal Growth

Liquid water transforms into ice through a series of intermediate events: primary nucleation, secondary nucleation and ice crystal growth, which eventually leads to solidification. Primary nucleation is a stochastic or a spontaneous event, which is dependent on the changes in the density and molecular rearrangements in the bulk solvent. These originate from fluctuations in the extent of Brownian motion, and lead to formation of metastable clusters of water molecules formed via hydrogen bonding that break up rapidly owing to the sufficient free energy which they possess at higher temperatures. The lifetime of stable clusters thus increases with a decrease in temperature (Franks 2007). As the solution temperature decreases, the formation of thermodynamically stable aggregates of a critical radius is achieved and nucleation occurs. In a pure filtered solvent with no impurities, the critical size is achieved at very low temperatures and ice nucleation is dependent on

self-association of water molecules alone (process called homogeneous nucleation). However, in the case of a solution with impurities, nucleation can occur at higher temperatures. Nucleation then begins by adsorption of the crystallising species onto the surface of the solid particles, thereby forming a stable aggregate larger than the critical size at higher temperatures than it would be if nucleation were to occur in the absence of impurities (a process known as heterogeneous nucleation) (Franks 2007).

Primary nucleation is immediately followed by secondary nucleation, during which ice crystallisation occurs over the surrounding liquid volume with a velocity in the order of mm/s (Searles, et al. 2001). Crystallisation is an exothermic process, hence the heat released in the process is absorbed by the sample, due to which the temperature rises to nearly 0 °C (Searles, et al. 2001; Searles 2004). As the product temperature continues to decrease, the ice crystals formed during nucleation grow in size. Subsequent to crystallisation, solidification occurs as the heat of crystallisation is removed by the driving force between the product temperature and the shelf (Searles, et al. 2001; Searles 2004). Furthermore, solidification can occur via either (i) global supercooling or (ii) local supercooling. During global supercooling, a similar level of supercooling is achieved in the entire liquid volume. Solidification then progresses through the already nucleated volume (Searles, et al. 2001) and the heat of crystallisation is removed relatively slowly through the already solidified layer and the vial bottom to the shelf. This type of solidification is a consequence of slow shelf freezing. In contrast, local supercooling occurs when only a small fraction of the sample volume is supercooled until the point of secondary nucleation, which is generally attributed to quench freezing (e.g. liquid nitrogen immersion). In this situation, the ice solidification front is in close proximity to the ice nucleation front in terms of space and time even as the front moves into the non-nucleated sample volume (Searles, et al. 2001).

Once the ice has formed, most of the water phase is separated as ice crystals while the remaining water forms a concentrated solution with the solute (a phenomenon called freeze concentration or cryo-concentration). The frozen matrix is reminiscent of a honey comb structure, wherein the cells resemble the ice crystals and the solutes concentrate in the interstitial spaces

between the ice crystals (known as freeze-concentration or cryo-concentration) (Franks 2007) . A further decrease in the temperature leads to eutectic crystallisation and/or glass transition of the solutes. As a result, the matrix supports its structure after ice sublimation.

Eutectic Crystallisation and Glass Transition

The freezing behaviour of solutes can be illustrated using a supplemented phase diagram for a binary mixture of water and solutes, as depicted in Figure 2. Let us consider that the liquid solution is at point A. As the temperature decreases, the solution supercools, and undergoes nucleation and ice crystallisation. As the temperature decreases further, the solution follows the equilibrium freezing curve and more ice becomes crystallised, which leads to an increase in the concentration of the solutes. On further decrease in temperature, the solution becomes more and more viscous until the concentration reaches a critical level. In the case of the crystallising excipients (e.g. glycine, mannitol) the solution undergoes eutectic freezing at the eutectic concentration C_{eu} and the solutes crystallise: the freeze-concentrate is then comprised of a saturated eutectic mixture of solute molecules and small ice crystals in the interstitial regions between pure ice crystals at the corresponding eutectic temperature, T_{eu}. In reality, it is not surprising to find that the crystallization is delayed owing to the presence of other components (Franks 2007). This results in (i) supersaturation of the solute, and (ii) creation of a non-equilibrium state that can potentially inhibit complete crystallization (which can ultimately lead to the formation of a metastable glass) (Jennings, Thomas A. 1999). Crystallisable solutes (e.g. mannitol) can also exist as polymorphs (i.e. numerous crystalline forms).

In the amorphous systems (e.g. sucrose, lactose, trehalose) or multicomponent systems (both crystalline and amorphous phases are present) the interstitial spaces between ice crystals can contain a substantial amount of unfrozen water (as much as 20 %): it is not possible to remove the unfrozen water during ice sublimation unlike in a pure crystalline system, where all the water is frozen and can be removed during ice sublimation (Kasper and Friess 2011). As a consequence, the unfrozen amorphous water must be removed via diffusion or desorption during the secondary drying stage. As

depicted in Figure 2, the solution containing amorphous solutes follows the equilibrium freezing curve until the solute concentration reaches $C_g{}'$ (known as the maximal freeze concentration). The corresponding temperature, known as the glass transition temperature of the maximally freeze-concentrated solute ($T_g{}'$) is a point on the glass transition curve, below which the system remains in a rigid glassy state and above it is a rubbery-like viscous liquid. The temperature value of the aforementioned phase transitions ($T_g{}'$ and T_{eu}) are frequently determined experimentally, using differential scanning calorimetry (DSC) (Ward, K. R. and Matejtschuk 2004).

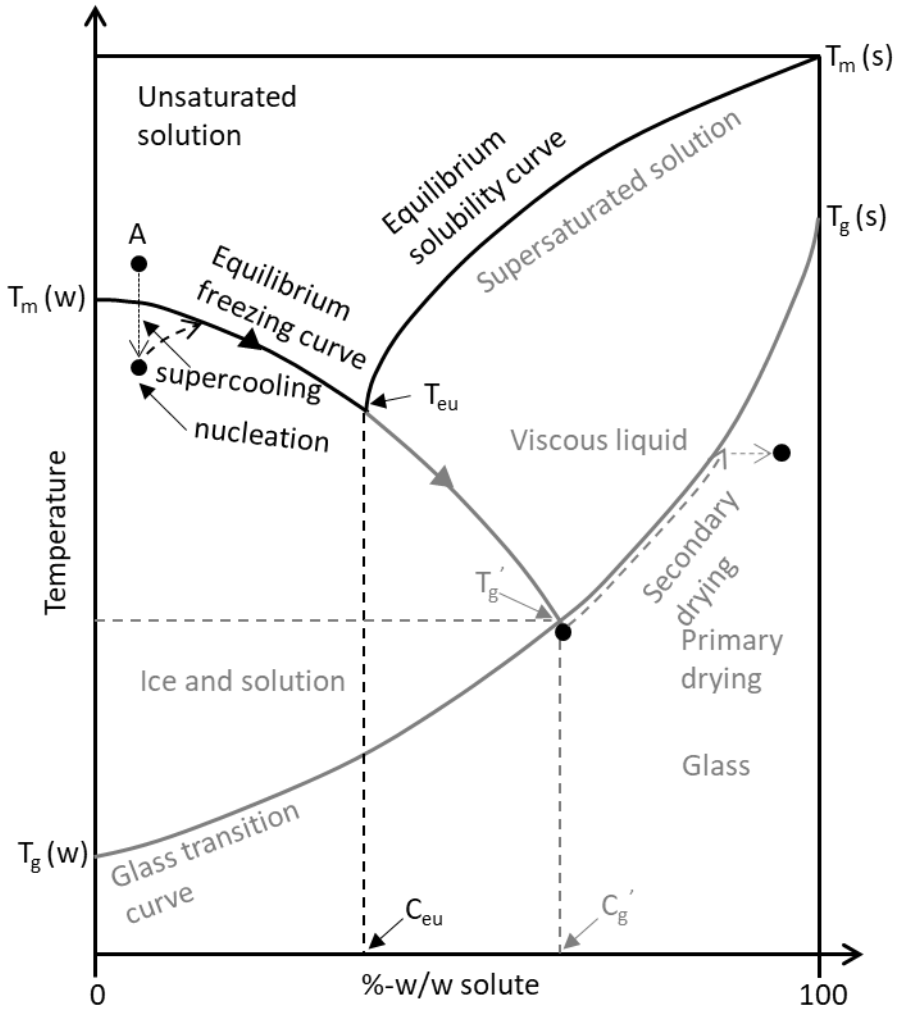

Figure 2: Supplemented phase diagram of a binary mixture of water (w) and solute (s). The crystallisation of solute and vitrification of solute are represented by black and grey lines, respectively. T_m and T_g are the melting temperature and the glass transition temperature, respectively. Supercooling of liquid water begins at point A, which follows ice nucleation and ice crystallisation (and ultimately solidification). Crystallisation of solute occurs when the eutectic concentration C_e is reached at the eutectic temperature T_{eu}. During vitrification, eutectic freezing is inhibited, and the solute reaches $C_g{}'$ at a glass transition temperature of the maximally freeze-concentrated solute, $T_g{}'$. Adapted from Kasper and Friess (2011); Liu (2006).

Manipulation of the Freezing Stage

The heterogeneous and stochastic nucleation of ice is a challenging issue in freeze-drying process control because it results in intra and inter-batch heterogeneity in the drying times (Constantino and Pikal 2004; Searles, et al. 2001). Moreover, the low temperatures and low pressures used throughout the freeze-drying cycle result in a time consuming and energy intensive process. It follows that a number of approaches have been developed to shorten the longest and most energy intensive part of the process, namely the primary drying stage. The majority of these approaches involve tailoring the freezing stage to the requirements of the product and are based on (1) controlling the **cooling rate** pre-nucleation; (2) **annealing** after allowing the ice nucleation to occur stochastically (Searles, et al. 2001); or (3) using other technological alternatives for **controlling the ice nucleation temperature** (Geidobler, R. and Winter 2013; Kasper and Friess 2011).

It must be recognised that a higher ice nucleation temperature (or low degree of supercooling) allows for an extended time for the formation of a small number of large ice crystals, which in turn results in a larger specific surface area of the dry layer and lower dry layer resistance (Konstantinidis, et al. 2011) thereby improving the primary drying efficiency (Searles, et al. 2001). One study reported that with every 1 °C increase in the ice nucleation temperature, the primary drying time was shortened by 4 % (Searles, et al. 2001). In general, it can be stated that a high nucleation temperature (low degree of supercooling) which yields a larger ice crystal size distribution, can result in a more effective freeze-drying process. The ice nucleation temperature is therefore, one of the critical process parameters in the design space for the lyophilisation cycle development (Arsiccio, Andrea and Pisano 2018).

Cooling rate

It is worth noting here the difference between cooling rate and freezing rate. The rate at which the vial is cooled is referred to as the cooling rate; whereas freezing rate applies to the rate of ice crystal growth post-nucleation (Rey, L. and May 2004b). In fact, the freezing rate is dependent on cooling rate, since cooling rate determines the degree of supercooling, which in turn determines the initial number and size of ice crystals formed during crystallisation and therefore the freezing rate, which ultimately determines the final ice crystal size and morphology (Searles, et al. 2001). Figure 3 shows the impact of cooling rate on the degree of supercooling and the subsequent outcomes. A low degree of supercooling implies smaller amount of heat of ice crystallisation is absorbed by the supercooled solution, which leads to an instantaneous freezing of a small amount of water, thereby resulting in a smaller number of ice crystals. During crystal growth, these crystals grow larger in size and dendritic in shape owing to an enhanced diffusion to the ice front at higher nucleation temperatures (Kasper and Friess 2011).

In addition, a higher ice nucleation temperature results in a slow ice crystal growth rate (G) as expressed in Equation 1: (Petzold and Aguilera 2009):

$$G = \beta(T_f - T_n)^n \qquad \text{Equation 1}$$

where the T_n and T_f are the ice nucleation temperature and the equilibrium freezing temperature respectively, and β and n are experimental constants. The difference between the two temperatures is termed the degree of supercooling. It follows that a high degree of supercooling (lower ice nucleation temperature) relates to a faster ice growth rate, or shorter ice solidification time, which in turn results in smaller ice crystals and vice versa.

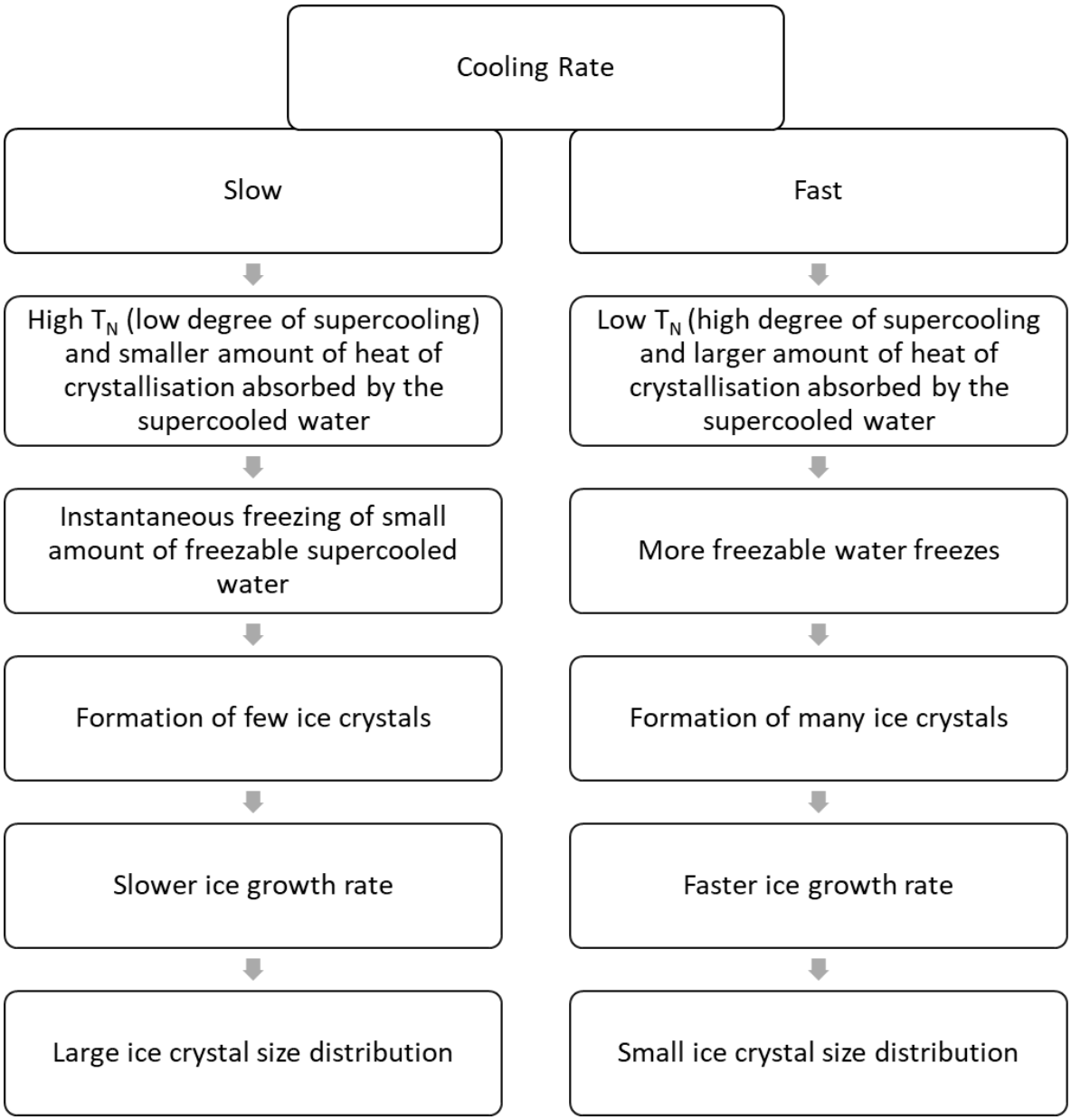

Figure 3: Impact of cooling rate on the degree of supercooling

The two noteworthy methods for modifying the cooling rate are: (1) Shelf ramp freezing; and (2) Quench freezing. **Shelf ramp freezing** is the most common method of freeze-drying, wherein vials are placed in a hexagonal array on temperature controlled stainless steel shelves. The shelf ramp method facilitates global supercooling but leads to a variation in ice nucleation temperatures from vial to vial. Shelf ramp cooling rates are largely constrained by the temperatures of the coolant (e.g. silicone oil-based coolants) which flows through the shelves and the thermal mass of the dryer and the batch of product, and provide rates in the order of 0.1 to 5 °C/min (Randolph and Searles 2002) to temperatures ranging from -55 to -60 °C (Ganguly, A., et al. 2018; Meissner, et al. 2011). Another method, **precooled shelf freezing**, can be considered as an alternative to the conventional shelf freezing method, wherein vials are placed on the shelves after cooling the shelves to a predefined temperature (e.g. -40 °C, -45 °C) (Hottot, Aurélie, et al. 2007; Searles, et al. 2001; Tang and Pikal 2004). This method can facilitate ice nucleation to occur at higher nucleation temperatures thereby enabling a slower freezing rate post nucleation. One experimental study reported that the median nucleation temperature for samples frozen on a shelf pre-cooled between -40 and -44 °C was increased by 3.5 °C as opposed to the samples frozen using the shelf ramp freezing method (Searles, et al. 2001). However, it was also demonstrated that a significant variability in ice nucleation temperatures was observed when the samples were placed on a shelf at -44 °C, indicating the limitation of the pre-cooled shelf ramp freezing method in achieving consistent nucleation across the batch. Further, Hottot and co-workers studied the effect of loading temperatures on the mean ice crystal size and reported that loading temperatures did not significantly impact the ice crystal size (Hottot, et al. 2007). Therefore, the choice of the shelf temperature set-point must be carefully assessed if this method is to be used.

Quench freezing is a rapid freezing method, whereby sample containers are frequently immersed in liquid nitrogen until ice completely solidifies. Other common media include dry ice, liquid propane, dry-ice ethanol or acetone. For example, with liquid nitrogen immersion, temperatures as low as -190 °C, providing cooling rates of 80 to 900 °C/min are possible (Bhatnagar, et al. 2007). Quench freezing promotes low degree of supercooling and a fast ice crystal growth rate (therefore small ice

crystals) (MacKenzie, et al. 1977). Although the method has been known to induce less supercooling compared to slower cooling methods (Heller, et al. 1999; Randolph and Searles 2002) it induces local supercooling only in a small fraction of the liquid volume and causes freezing via directional solidification (Dawson and Hockley 1992). Notwithstanding the beneficial effect of quench freezing in one study, wherein it was shown to prevent phase separation (Heller, et al. 1999) the method invariably results in heterogeneous ice crystal morphologies and cannot be applied at the manufacturing scale (Kasper and Friess 2011).

From the above discussion, it can be concluded that the shelf ramp freezing method is limited by the cooling rate of the shelf temperature and both the pre-cooled shelf and the quench freezing methods don't have practical solution to achieving ice nucleation at high temperatures. In the absence of any advanced technique, an intermediate annealing stage is frequently included before starting primary drying.

Annealing

Annealing is an intermediate process step between the initial freezing stage and the primary drying stage, whereby the frozen product is re-heated to a sub-freezing temperature above T_g' (e.g. 10-20 °C) but below T_{eu}, and then maintained at the elevated temperature for several hours, and subsequently re-cooled to a final temperature before initiating primary drying (Searles, et al. 2001; Searles 2004; Tang and Pikal 2004). The primary purpose of annealing is to achieve a large, uniform inter-vial ice crystal size distribution and promote further crystallisation of ice (through de-vitrification and re-crystallisation) within the frozen matrix, thereby improving the consistency of drying behaviours from vial to vial and decreasing overall cycle time (Searles 2004). In effect, annealing removes the dependency of the ice crystal size and morphology on the ice nucleation temperature. The second purpose of annealing is to facilitate crystallisation of the active ingredient and other crystallisable excipients (e.g. glycine, mannitol) (Rey 2010).

The consequences of annealing have been summarised in Figure 4. When the product temperature is raised above T_g', the molecular mobility of the bulk is increased (Searles 2004). Increased molecular mobility leads to melting of the small ice crystals, which enables them to attain a state of lower free energy (Searles, et al. 2001). According to the Kelvin equation, smaller ice crystals melt preferentially because of their high vapour pressure, which is associated with a higher free energy compared to larger ice crystals, which induce a lower vapour pressure, hence associated with a state of lower free energy (Searles 2004). Further, an increased temperature facilitates diffusion of the melted ice crystals into the surviving ice crystals (Kasper and Friess 2011). In addition, a re-warming up to a temperature above T_g' leads to diffusion of the unfrozen water out of the amorphous phase and its conversion to the predominant ice form (a process known de-vitrification), thereby increasing freeze-concentration (Searles 2004). As the surviving ice crystals are annealed for a defined period at the elevated temperature, the mean ice crystal size increases with annealing hold time (Randolph and Searles 2002; Searles 2004). As a consequence, the inter-vial heterogeneity associated with ice crystal size distribution decreases with time. In other words, the longer the annealing hold time, the more time given to the vials with the smaller ice crystals to catch up to those with larger ice crystals (Randolph and Searles 2002; Searles, et al. 2001; Searles 2004). Consequently, during re-cooling, the smaller ice crystals do not re-form on re-cooling because the larger ice crystals serve as additional nucleation sites for further crystallisation (Searles, et al. 2001).

Furthermore, annealing above T_g' facilitates re-liquification and crystallisation of the metastable glassy forms of crystalline excipients (Lu and Pikal 2004). In this case, the rationale for annealing is that a metastable form the crystalline bulking agent is likely to depress T_g'. Moreover, the metastable materials are likely to re-crystallise on storage, thereby impacting reconstitution times (Hawe and Friess 2006; Lueckel, et al. 1998). This potential instability issue can also lead to vial breakage especially at high fill depths. This may be avoided by operating the primary drying stage at low shelf temperatures (e.g. -25 °C for mannitol) (Pyne, et al. 2002).

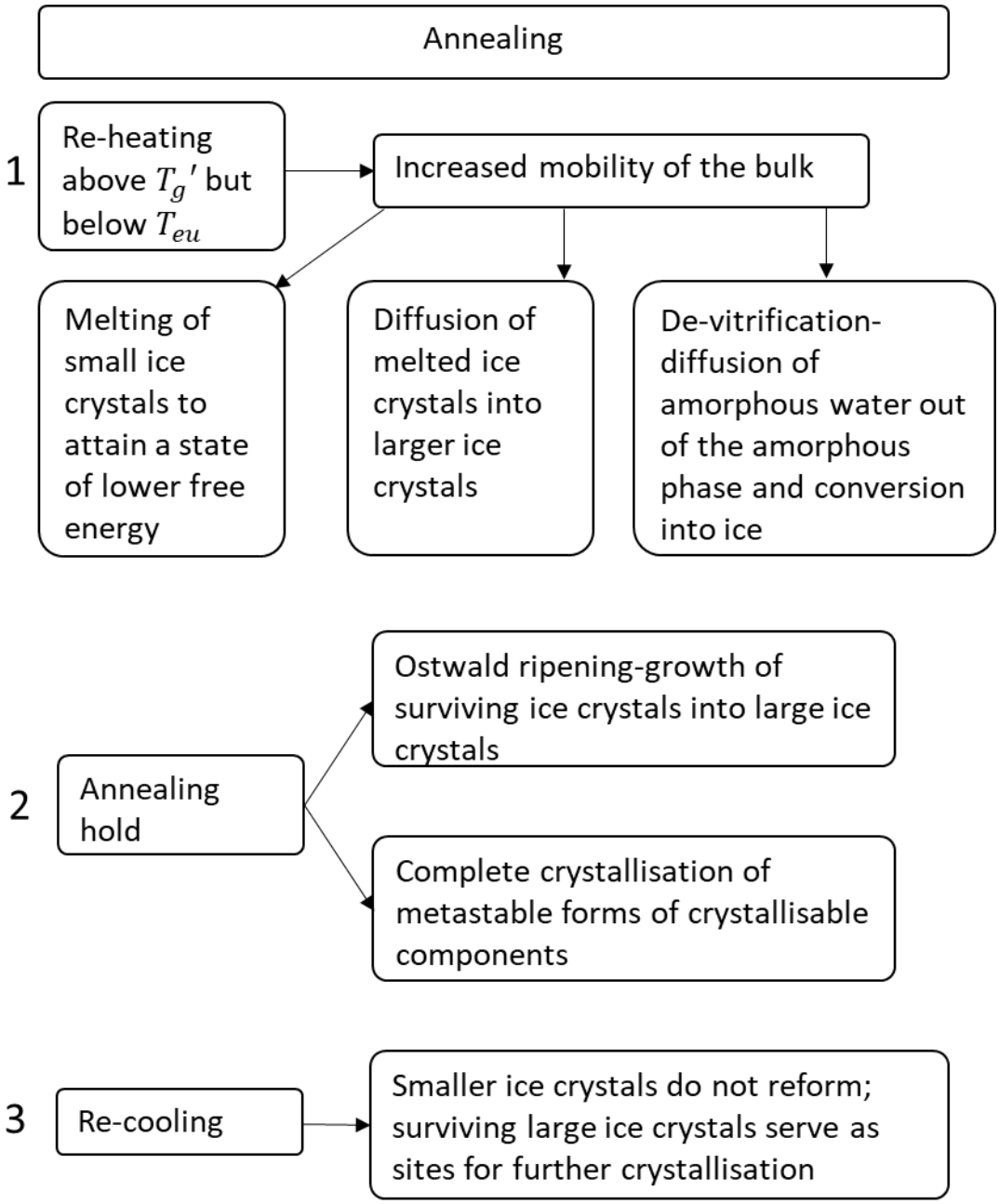

Figure 4: Consequences of annealing

In regard to the impact of annealing on the primary drying performance for formulations contained in glass vials, some of the earlier studies have reported a 3-fold decrease in the primary drying time for matrices with a homogeneous ice crystal morphology compared to the non-annealed samples (Searles, et al. 2001; Searles, et al. 2001). Further, a 10 % and 15 % reduction in primary drying time was reported at -10 °C for 4 h and at -2.5 °C for 4 h, respectively. In another experimental study involving annealing of 10 % w/w Maltodextrin at -10 °C, a 23 % decrease in the primary drying time was reported when the annealing hold time was increased from 1 to 3 h. It was also shown that a further increase in the hold time by 2 h resulted in only a 3 % decrease in the primary drying time (Smith, et al. 2014b) indicating that a very long hold time might not be necessary, which could otherwise prolong the overall cycle time. In spite of the above findings, the impact of annealing on the primary drying efficiency is perceived to be controversial. For example, it was reported that annealing of mannitol-trehalose sodium chloride formulation resulted in an increase in both the dry layer resistance and primary drying time which was ascribed to the crystallisation of solutes during annealing (Lu and Pikal 2004). Further, a 20 % increase in the primary drying time was reported for a protein formulation with a high fill depth annealed at -15 °C for 2 h, which was attributed to the formation of a crust at the top of the dried matrix (Esfandiary, et al. 2016). In addition, there is some evidence that annealing does not significantly impact the primary drying time for a formulation with a high solids content. This is usually due to the fact that a dried matrix with a high solids content will be less porous, thereby increasing the resistance to vapour flow resulting in a decrease in the sublimation rate (Franks 2007). Furthermore, given that annealed matrices have lower specific surface area, it can lead to increased resistance to desorption and hence proportionally elongated secondary drying times, as reported elsewhere (Mousavi, et al. 2005; Pikal 1990). In concluding the above discussion, it should be recognised that the annealing may not always lead to an efficient lyo-cycle and hence its inclusion should be evaluated on a case-by-case basis.

Controlled Nucleation

With the controlled nucleation techniques, it is possible to induce ice nucleation simultaneously in all the vials at relatively high temperatures (e.g. -5 °C) resulting in larger ice crystals, which has obvious advantages over a freezing protocol which allows ice nucleation to occur stochastically: reduced protein aggregation, faster primary drying rate, better visual appearance, more uniform residual water content, faster reconstitution times, and few chances of vial breakage (Awotwe−Otoo, et al. 2014; Awotwe-Otoo, et al. 2013; Bursac, et al. 2009; Geidobler and Winter 2013; Geidobler, Raimund, et al. 2012; Konstantinidis, et al. 2011; Patel, Sajal M., et al. 2009). There are several methods for controlling ice nucleation, which have been reviewed in the scientific literature (Assegehegn, et al. 2019; Geidobler and Winter 2013; Kasper and Friess 2011). Only the techniques of major commercial importance have been discussed here: (i) the high-pressure shift or depressurisation technique (Gasteyer, et al. 2007; Konstantinidis, et al. 2011); (ii) the ice fog technique (Rambhatla, Shailaja, Ramot, Bhugra and Pikal 2004b) .

High-Pressure Shift or Depressurisation Freezing

High-pressure shift freezing involves a quick evacuation of the drying chamber following a re-pressurisation of the chamber to a high pressure (e.g. 2 bar), thereby simultaneously inducing ice nucleation at the solution surface in all the vials simultaneously. The primary mechanism of nucleation is not well understood but the authors speculate it to be a combination of factors: (1) evaporative cooling on de-pressurisation); (2) the release of dissolved gases, forming cold bubbles inducing nucleation); and (3) surface cooling due to a disturbance to the solution surface owing to rapid pressure change (Gasteyer, et al. 2007).

The high-pressure shift/depressurisation technique is available from Praxair, Inc (ControLyo^{TM}) at the industrial scale. Although most commercial scale dryers are capable of withstanding high pressures there are no supporting experimental studies published so far. Further, the technique has been shown to be successful in both laboratory (1 m^2 shelf area) and small industrial scale (5 m^2 shelf

area) freeze dryers, wherein ice nucleation temperature was controlled within 1 °C of their equilibrium freezing point (Bursac, et al. 2009). In the same study, by applying the depressurisation technique, the authors reported a 27 % decrease in primary drying time for 5 %w/w sucrose, improved dried product uniformity, and a reduction in absolute standard deviation in residual moisture content from 4.6 % to 2.1 % compared to shelf-ramp freezing. In another study, a 40 % reduction in primary drying time for 5 %w/w mannitol solution was reported when the depressurisation technique was applied (Konstantinidis, et al. 2011). More recently, Awotw-Otoo et al. have used the method to obtain a primary drying time reduction of up to 21 % for formulations containing a monoclonal antibody (Awotwe−Otoo, et al. 2014; Awotwe-Otoo, et al. 2013). In conclusion, the depressurisation technique can be effective at inducing ice nucleation over a wide range of sample sizes simultaneously as it relies on the manipulation of the pressure inside the drying chamber to which all samples are exposed to the same degree (Assegehegn, et al. 2019).

Ice Fog Technique

On application of the ice fog technique, first introduced by Pikal and co-workers (Rambhatla, et al. 2004) the water vapour present in the drying chamber gets converted into fine ice crystals when a cold stream of Nitrogen gas is passed into the chamber. The ice crystals are then transferred to the supercooled solution thereby inducing nucleation at the surface. The main disadvantage of this method was that it could take as long as 30 min to induce ice nucleation in all the vials. Therefore, the same authors modified the method by lowering the temperature of Nitrogen gas from -40 to -50 °C and achieved ice nucleation in all the vials within 5 min. Subsequently Patel et al. (2009) achieved ice nucleation within 1 min by evacuating the chamber in the range 66.7 to 64 mbar before introducing cold nitrogen (the method is known as reduced pressure ice fog technique). More recently, it was shown that controlled ice nucleation can be achieved without the need for Nitrogen gas (Geidobler, et al. 2012). Here, a depressurisation of the chamber to ∼3.7 mbar and an immediate re-pressurisation to atmospheric pressure induces ice nucleation instantly. The important driving forces for ice

nucleation are thought to be the evolution of water vapour from the vials on application of the vacuum and conversion of the water vapour into ice crystals on coming in contact with the cold condenser, which is separated from the chamber by a valve in the duct. On re-pressurisation via the cold condenser, these ice crystals are blown back to the solution surface, inducing ice nucleation. An advantage of this method is that it does not require any hardware modifications provided the chamber pressure can be controlled precisely.

At the industrial scale, the ice fog technique is available from Linde Gases in collaboration with IMA Life North America (trade name VERISEQ® nucleation technology) (Azzarella, et al. 2016; Chakravarty, et al. 2012) and from Millrock Technology, Inc. (trade name FreezeBooster® Controlled Nucleation Technology). There is some evidence of the success of the ice fog technique at the industrial scale in a range of commercial freeze dryers (Azzarella, et al. 2016; Chakravarty, et al. 2012); however more studies are needed to assess the full potential of this technique.

1.2.2 Primary Drying

Primary drying or the ice sublimation phase involves: (i) the lowering of the chamber pressure, typically ranging from 50 to 200 mTorr (or 0.066 to 0.266 mbar); and (ii) supplying of heat by raising the shelf temperature (usually between -40 and -20 °C) which together drive the transfer of ice out of the product via sublimation and its crystallisation onto the condenser, which is maintained at low temperature (e.g. -50 °C or lower) (Jennings 1999; Tang and Pikal 2004). Typically, primary drying is very time consuming and energy intensive, as it can take up to several days as opposed to freezing (∼few hours) and secondary drying (∼hours) (Franks 1998; Tang and Pikal 2004). During primary drying, the ice crystals sublimate into water vapor, leaving behind a porous matrix of amorphous phase (with the unfrozen water) and/or crystalline excipients. The sublimation of ice starts from the top layer of the frozen product and proceeds towards the bottom. The subdivision of the ice front from the dry layer is known as the ice-vapour interface or sublimation interface (Franks 2007; Pikal 1990).

It is well known to every freeze drying exponent that the sublimation rate and therefore primary drying time, are dependent the equipment (e.g. heat transfer, pressure regulation), the container (e.g. vial geometry, thermal conductivity/ heat transfer coefficient) and the formulation (fill height, dry layer resistance to vapour flow). Extensive research into optimising the primary drying stage has necessitated the monitoring of the critical parameters impacting mass transfer (i.e. sublimation rate), ice interface temperature, resistance to the vapour flow through the dried matrix and chamber pressure.

It is worth mentioning at this point that there are two essential factors impacting ice sublimation: (1) difference between the vapour pressure of ice at the sublimation interface (P_i) and the vapour pressure at the condenser surface (P_c); (ii) the difference between P_i and the partial pressure of water vapour in the drying chamber (P_{ch}). Out of two factors, the first is the real driving for ice sublimation (Rey and May 2004). Given that the ice vapour pressure increases exponentially with temperature as demonstrated in Figure 5, then it is the temperature difference between the sublimation interface and the condenser surface that drives the sublimation process. In other words, the colder the condenser, the greater is the driving force for sublimation at the same shelf temperature and chamber pressure setpoints (Rey and May 2004).

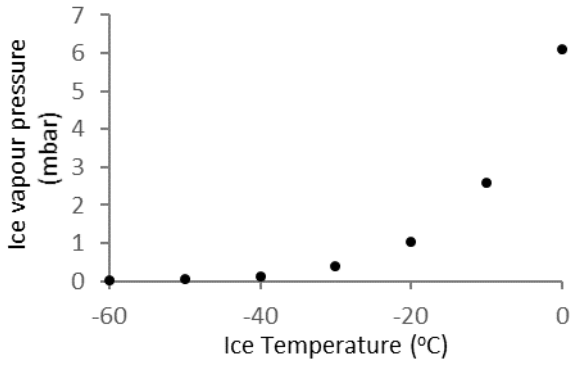

Figure 5: Vapour pressure of ice at the different temperatures (Oetjen 1999).

On the other hand, chamber pressure affects the sublimation rate, but it is not necessarily the real driving force. However, in practice, the chamber pressure is still maintained below the saturated vapour pressure of ice at that operating ice temperature. As a general rule, the optimal chamber pressure (P_{ch}^{set}) can be determined using Equation 2 (Tang and Pikal 2004) at the known target product temperature in order to achieve an optimal sublimate rate:

$$P_{ch}^{set} = 0.29 \,.\, 10^{(0.019.T_i)} \qquad \text{Equation 2}$$

T_i (or the temperature at the sublimation interface) is arguably the most critical parameter during the primary drying stage. As shown above, it not only determines the value of P_{ch}^{set}, but its maximum allowable value during primary drying is impacted by the collapse temperature (T_c) or the glass transition temperature ($T_g{}'$) of the freeze-concentrate and the eutectic melting temperature (T_{eu}) for crystalline excipients. As a general rule, it is recommended that T_i should be 3-5 °C below $T_g{}'$ (Jennings 1999). Operating primary drying above the maximum allowable temperature can lead to what is referred to as **melt-back**, defined as the melting of the eutectic mixture of ice crystals with the crystalline excipients; or **collapse**, which refers to viscous flow of the maximally freeze-concentrated amorphous system (Franks 2007).

Coupled Heat and Mass Transfer During Primary Drying

Were it not for the fact that product temperature cannot be directly controlled, primary drying would not be considered to be the riskiest step in a freeze drying process . In freeze drying only three process variables can be controlled: the shelf temperature (T_s), chamber pressure (P_{ch}^{set}) and time (t) (Pikal 1990). During ice sublimation, the flow of water vapour faces different resistances (Pikal, M. J., et al. 1984) such as: (i) R_p or resistance of the product dry layer that forms as the ice sublimation interfaces advances down the vial; (ii) R_s or resistance from the stopper inserted into the vial neck; (iii) R_c or the resistance experienced by the vapour flow in the pathway between the chamber and the condenser in freeze dryers where the chamber is connected to the condenser via a duct. Out of the three sources of resistance, R_p is the most significant (Pikal 1990) especially in the case of formulations

with high solids content and high fill depth (Pikal, et al. 1984; Searles 2004). Furthermore, the value of R_p is impacted by the ice crystal structure which develops during the freezing stage (Searles 2004). The rate of mass transfer (dm/dt) can be expressed as (Pikal, et al. 1984):

$$\frac{dm}{dt} = \frac{P_i - P_{ch}}{R_p + R_s} \qquad \text{Equation 3}$$

Note that in Equation 3, the term R_c should be added to the other resistances in the denominator when factoring in the resistance to the vapour flow in the duct connecting the chamber and the condenser. Furthermore, the term P_{ch} can be replaced with P_c when expressing the equation in terms the pressure differential between the sublimation front and the condenser.

Mass transfer is also linked to heat transfer. For ice sublimation to proceed, a continuous supply of energy is needed, and this energy is equal to the heat of sublimation of ice (ΔH_s ≈2.97 J/kg) (Rey and May 2004). During primary drying, the rate of heat input to the product $\left(\frac{dq}{dt}\right)^{out}$ depends on dm/dt and ΔH_s (Pikal, et al. 1984), as expressed in Equation 4:

$$\left(\frac{dq}{dt}\right)^{out} = \frac{dm}{dt}.\Delta H_s \qquad \text{Equation 4}$$

The rate of heat input to the product also depends on other factors, namely the vial geometry, vial location and the process parameters of shelf temperature and chamber pressure (Franks 2007; Pikal, et al. 1984; Rambhatla, Shailaja and Pikal 2003; Scutella, Passot, et al. 2017) as demonstrated in Equation 5:

$$\left(\frac{dq}{dt}\right)^{in} = A_v.K_v.(T_s - T_b) \qquad \text{Equation 5}$$

where, A_v is the outer cross-sectional area of the vial projected onto the shelf, T_b is the product temperature at the bottom centre of the vial, K_v is the vial heat transfer coefficient between the shelf and the product. The equation assumes that all the heat required to sublimate the ice is provided by the shelf (a condition that applies to core vials).

Furthermore, as long as a steady state period exists, Equation 4 and Equation 5 can be re-expressed as follows:

$$\frac{dm}{dt}.\Delta H_s = A_v.K_v.(T_s - T_b) \qquad \text{Equation 6}$$

Equation 6 represents the coupled heat and mass transfer during the steady state period of the primary drying stage. A steady state period is characterised by (i) a constant difference between T_s and T_b; and (ii) a planar geometry of the ice sublimation interface with respect to the vial bottom. In other words, the ice sublimation interface reduces in height in a horizontal plane parallel to the vial base (Pikal, et al. 1984).

Heat Transfer Mechanisms

It should be noted that a standard freeze drying vial is curved inwards from the bottom such that not all of the vial bottom touches the shelf surface. As a result, the heat transfer from the shelf to the vial bottom is dependent on (i) the area of contact between the vial bottom and the shelf; and (ii) the vial bottom concavity (Pikal, et al. 1984; Scutella, et al. 2017). The value of K_v can be described as sum of three heat transfer mechanisms as illustrated in Figure 6 and can be expressed as:

$$K_v = K_c + K_g + K_r \qquad \text{Equation 7}$$

where,

- K_c refers to direct conduction from the shelf to the glass at the points of contact, which is assumed to be proportional to the shelf temperature (Kuu, et al. 2006).
- K_g refers to conduction of gas molecules (e.g. water vapour) trapped within the vial bottom curvature, which increases with increase in pressure (Pikal, et al. 1984; Pisano, Fissore, et al. 2011; Scutella, et al. 2017) as described below:

$$K_g = \frac{C_2 P_{ch}^{set}}{1 + \frac{l}{\lambda_{amb}} C_2 P_{ch}^{set}} \qquad \text{Equation 8}$$

where P_{ch}^{set} is the chamber pressure, λ_{amb} is the molecular conductivity of the gas (e.g. water vapour) at ambient pressure, l is the average distance between the bottom curvature of the vial and the shelf, and the coefficient C_2 is equal to

$$C_2 = \Lambda_0 \frac{\alpha_c}{2 - \alpha_c} \left(\frac{273.15}{T_{gas}} \right)^{0.5} \quad \text{Equation 9}$$

where Λ_0 is the free molecular flow heat transfer coefficient of the gas at 0 °C, T_{gas} the temperature of the gas participating in heat conduction, determined as an average of the temperature at the sublimation interface and the shelf temperature, α_c the accommodation coefficient (Scutella, et al. 2017). Mass transfer is severely limited at pressures lower than 50 mTorr (Zhai, Suling, et al. 2005).

- K_r refers to radiative fluxes towards the product from the chamber walls, the bottom shelf, the top shelf and the dryer door, the relative contribution of each being dependent on the location of the vial on the shelf. For vials surrounded by their nearest neighbours (termed core vials), there are only two radiative fluxes that contribute to radiative heat flow to the product, namely the radiative flux from the bottom shelf and the radiative flux from the top shelf (Pisano, et al. 2011); each of them being proportional to the difference in the fourth powers of the absolute temperatures, and to the effective emissivity for heat exchange, and a view factor. The radiation heat transfer is then be described by (Pikal, et al. 1984):

$$K_r = 4\,(e_s - e_v)\,\kappa T^3 \quad \text{Equation 10}$$

where e_s emissivity of the shelf surface, e_v emissivity of the vial, T is average temperature, κ is Stefan-Boltzmann constant.

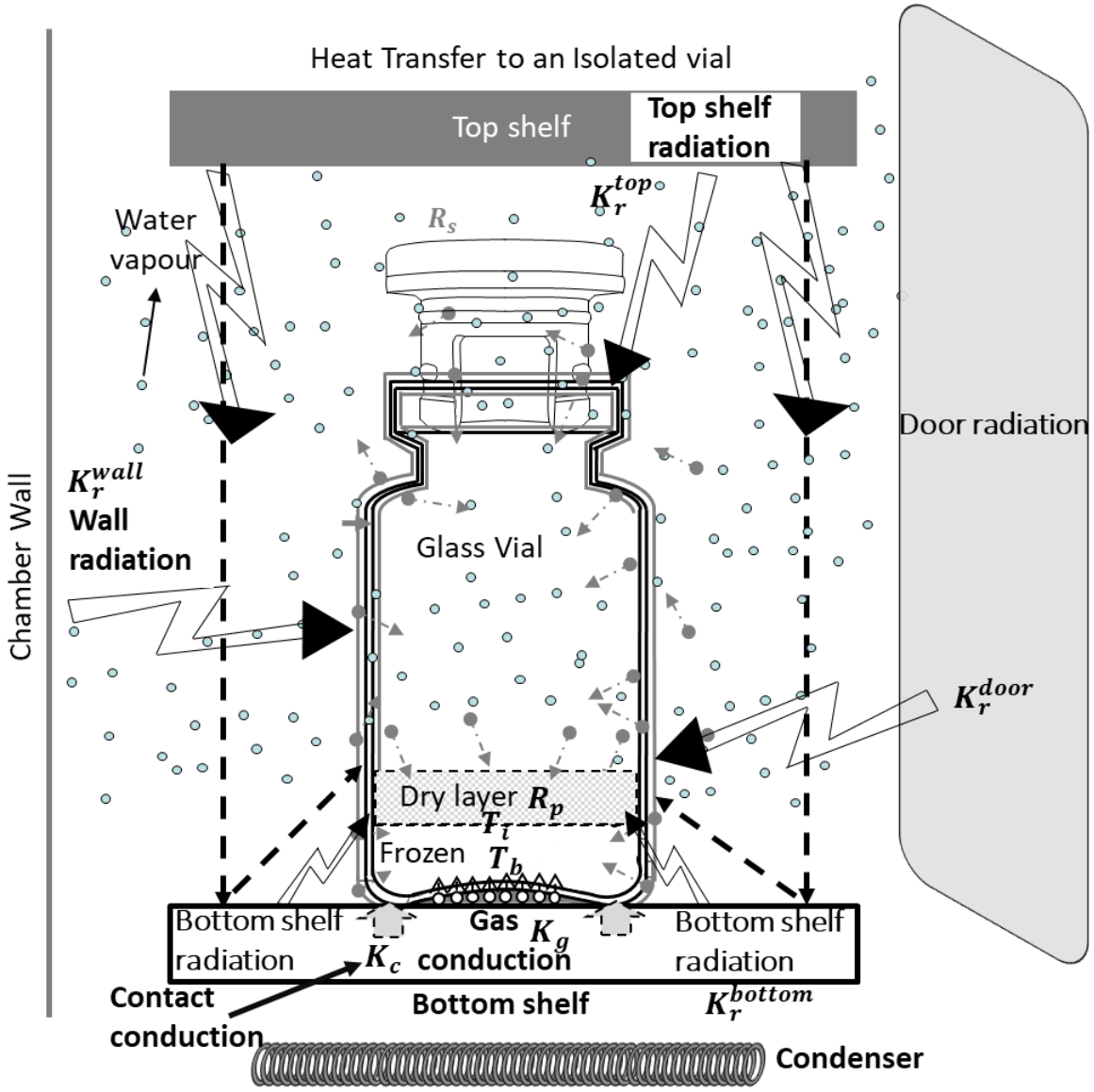

Figure 6: Mechanisms of Heat Transfer to an isolated vial. Adapted (Pikal, et al. 1984; Scutella, Plana-Fattori, et al. 2017)

Heterogeneity in Heat transfer and Mass Transfer

For a vial located at the front edge of the shelf (known as the edge vial) heat radiation from the door is the single most significant heat contribution especially in lab scale freeze dryers with a Plexiglass door (Pikal, et al. 1984; Rambhatla and Pikal 2003). In fact, the average edge vial at the front was reported to sublime 15 % faster than a typical internal vial (Pikal, et al. 1984). In another study it has been reported that a typical front edge vial runs up to 4 °C warmer than the core vials (known as the edge vial effect) (Tang, X. L., et al. 2006). In the same study, it was reported that a vial located at the side edge of the shelf ran 1 °C warmer than the vial in the middle. Further, it was reported that an edge vial at the front edge near the chamber door sublimed twice as fast as the one in the middle of the shelf (Rowe, et al. 1980). In addition, the K_v value for an edge vial can was reported to be twice as greater than the value for a core vial (Tchessalov 2017).

Furthermore, in many freeze-drying operations, the edge vials are surrounded by a guardrail which keeps the vials falling off the shelf. In one of such studies involving a vial placed on the side of the shelf in contact with a guardrail and another vial placed at some distance away from the guardrail, the role of gas conduction surrounding the vials was reported to be much more significant than radiation (Scutella, et al. 2017). The authors reported the contribution to the overall heat flow to the vial in contact with a guardrail constituted a 50 % from gas conduction, 36 % via heat transfer from the bottom shelf; 10 % radiation from the rail; and 5 % via radiation from the internal walls and the top shelf, respectively, at a chamber pressure of 4 Pa and shelf temperature of 0 °C.

It is also true that the variability in the vial geometry (contact area and vial bottom concavity) leads to a variability in the vial heat transfer coefficient, which in turn results in the variability in the product temperature (Scutella, et al. 2017). The authors ascribe this variability in vial geometry to production limits, which can change depending on the model of the container and the manufacturer. Moreover, as discussed previously, one should also account for the variability in the mass transfer resistance (R_p) which is strongly dependent on the ice crystal structure formed during freezing (besides

formulation properties). In one experimental study comprising sublimation experiments with either stochastic or controlled ice nucleation protocols, a product temperature variability of up to 4.4 °C during primary drying was reported, which was ascribed to the variability in R_p (Scutella, et al. 2018). From the above discussion, the variability in both K_v and R_p can be significant in terms of the impact on primary drying times across the batch. Thus, it is evident that the heterogeneity in the drying behaviour is a serious issue in freeze drying. It follows that a safety margin (in terms of product temperature) resulting from the impact of vial location and vial geometry must be carefully assessed depending on the operating conditions (Scutella, et al. 2017; Tang and Pikal 2004). Alternatively. the impact of radiation may be reduced by employing thermal shields. For example, placing empty vials in the outer row of a cluster of vials or by attaching an aluminium foil on the chamber door and by using less emissive stainless-steel chamber doors as opposed to Plexiglass doors (Ganguly, Arnab, et al. 2013; Kuu, et al. 2005; Rambhatla and Pikal 2003) .

1.2.3 Secondary Drying

When all of the ice has been removed during the primary drying stage, the sample still contains between 5 to 50 % unfrozen water (depending on formulation) associated with the solute fraction that did not freeze during the initial freezing stage (Franks 1998; Tang and Pikal 2004). The purpose of secondary drying is to promote desorption of this bound water by raising the temperature of the product (up to 25 °C or higher) under vacuum, aiming to achieve optimal stability by reducing the residual water content (usually to 1 % w/w) (Tang and Pikal 2004). In the amorphous phase, the unfrozen water is dissolved as a solution with solute molecules within the bulk, which must first diffuse out of the amorphous phase to appear at the surface of the porous solid before it can be desorbed (Pikal, M. J., et al. 1990). Given that water acts as a plasticiser in the formulation, the glass transition temperature (T_g) of the formulation is low at the beginning of secondary drying and increases as the water content decreases. Further, since diffusion is a relatively slow process, a rapid increase in temperature will lead to viscous flow of the amorphous phase leading to structural collapse (Franks 2007; Pikal, et al. 1990). Therefore, during the temperature ramp of the secondary drying stage, the

shelf temperature should be ramped up judiciously to keep the product temperature below T_g of the amorphous phase. A ramp rate of 0.1 to 0.2 °C/min is recommended for amorphous formulations to prevent the product temperature from exceeding T_g (Tang and Pikal 2004). Such low rates are not required for crystalline products as they do not potentially collapse during the secondary drying stage. Consequently, higher ramp rates (0.3 to 0.4 °C/min) can be used for crystalline products (Tang and Pikal 2004).

It has been demonstrated that at the beginning of the secondary drying phase, there is a rapid decrease in the residual moisture content followed by its value reaching a plateau (Pikal, et al. 1990). As discussed earlier, given that desorption occurs from the surface of the matrix, it implies that the drying rate is higher for matrices with a higher specific surface area (smaller pores) leading to shortening of secondary drying times. It follows that a lower solid content (less 10 %w/w) and a higher degree of supercooling during the freezing stage will improve the secondary drying efficiency (Pikal, et al. 1990). Besides, the specific surface area can also be increased by increasing the fill volume (Pikal, et al. 1990). Unlike in the primary drying stage, wherein the sublimation rate depends on cake thickness and chamber pressure, it has been reported that there is no significant effect on increasing the pressure at least up to 200 mTorr (Pikal, et al. 1990).

1.3 Pharmaceutical Quality of Freeze-Dried Products

The International Council for Harmonization (ICH) defines pharmaceutical quality as “the suitability of either a drug substance or a drug product for its intended use”, and further states ‘the quality cannot be tested into products; i.e. quality should be built in by design’ (ICH 2009). A safe and efficacious commercial drug product requires a sufficient level of quality, which can otherwise pose a medicinal risk, thereby causing a threat to the patient, either directly or indirectly. Besides, unacceptable quality poses a financial burden in several forms (e.g. batch rejections and recalls, damage to reputation, legal costs) (Blackburn, et al. 2011; Sangshetti, et al. 2017).

1.3.1 Quality by Design and Process Analytical Technology

The paradigm of the pharmaceutical quality assurance has been shifting from an “end product testing” approach to a more “building quality into the product” approach for drug development and manufacturing, more commonly known as Quality by Design (QbD) (ICH 2009). In brief, the QbD approach involves the following principles (Rathore 2009):

- Identification of target product profile (TPP) and critical quality attributes (CQA) that ensure product efficacy,
- Risk analysis and defining of a product design space by controlling the critical process parameters (CPPs) to deliver CQAs
- Development of a robust control strategy to ensure the reproducibility of the process

The remaining part of the discussion will focus on the preliminary stages of the QbD, particularly process understanding, which involves the use of process analytical technologies (PAT). It has been stated in the Guidance for Industry PAT: a framework for Innovative Pharmaceutical Development, Manufacturing and Quality Assurance issued by the US Food and Drug Administration (FDA) in September 2004, that suitable process analytical technologies (PATs) must be employed to in every pharmaceutical manufacturing process, with a goal of monitoring of the product to obtain the desired

product characteristics (FDA 2004). In the context of quality by design for freeze drying, the following sections describe the quality attributes of a freeze-dried product, the critical process parameters in lyophilization process control and the available systems for freeze-drying monitoring. Some of the techniques that are useful for off-line analysis of the freeze-dried product have also been included.

1.3.2 Critical Quality Attributes (CQA) of the Lyophilised Products

A critical quality attribute (CQA) is defined as 'a physical, chemical, biological or microbiological property or characteristic that should be within an appropriate limit, range, or distribution to ensure the desired product quality (ICH 2009)'. The quality of a lyophilized finished product develops during its entire processing from the liquid formulation, through different stages of freeze-drying to form a dry solid cake sealed in the desired container (Constantino and Pikal 2004). The general CQAs of a freeze-dried product are defined in Table 1.

Table 1: Critical quality attributes of the freeze-dried product (Breen, E., et al. 2001; Constantino and Pikal 2004; FDA 2014; Nail, Steven L. and Searles 2008; Patel, S. M., et al. 2017)

CQA	Requirements
Stability	Should be of sufficient level until the defined date of expiry
Sterility	Level of contaminants should below a predefined limit of detection
Moisture content	Monitoring of the residual amount of ice in the product is essential to identify the endpoints of (i) the primary drying stage, without prolonging the step unnecessarily; and (ii) the secondary drying stage to ensure the moisture content is within predefined levels
Visual Appearance	Elegant looking cake with a uniform cake appearance that does not shown any observable signs of collapse/meltback, cracking and shrinkage
Reconstitution time	Should completely dissolve within seconds to minutes, particularly for parenteral products

Stability of the freeze-dried product impacts therapeutic efficacy and safety (Carpenter, et al. 1997). Then, moisture content affects the storage stability of the product. Besides, other properties of the product (e.g. crystallinity, polymorphism, glass transition temperature) can influence stability (Patel, S. M., et al. 2013; Trappler 2013). As regards reconstitution time, it can serve as empirical indicator of the porosity of the dry cake. Reconstitution time is slower for collapsed products (Constantino and Pikal 2004).

1.3.3 Critical Process Parameters (CPP) of a Freeze Drying Process

A CPP is one whose "variability has an impact on a critical quality attribute and therefore should be monitored or controlled to ensure the process produces the desired quality" (ICH 2009). The CPPs for a typical freeze drying process are defined in Table 2.

Table 2: Critical Process Parameters (CPP) for freeze-drying process control (Franks 2007; Oetjen 1999; Rey and May 2004; Tang and Pikal 2004)

CPP	Description
Product Temperature	The product temperature above the critical temperatures, namely the glass transition temperature of the maximally freeze-concentrated solution (T_g') or the eutectic melting point for a crystalline product (T_{eu}) can induce product collapse/melt back, causing increased reconstitution times and deleterious impact on the stability of active ingredient.
Shelf Temperature	Should be maintained to ensure the product temperature does not exceed the maximum allowable temperature
Chamber Pressure	Should be lower than the saturated vapour pressure of ice at the operating product temperature of the sublimation front, as it impacts the sublimation rate. Typically, the set point should be above 50 mTorr and preferably below 200 mTorr.
Condenser Temperature and Pressure	Should be a value (e.g. -60 °C) which corresponds to a vapour pressure lower than the saturated vapour pressure of ice at the sublimation interface. The difference in the water vapour pressure between the ice sublimation front and the condenser surface provides the real driving force for ice sublimation.
Sublimation Flux	How aggressive the lyo-cycle can be? This depends on the condenser capacity and the duct connecting the drying chamber and the condenser. In addition, it is useful to determine the vial heat transfer coefficient from the shelf to the product (K_v) and the dry layer resistance to vapour flux (R_p). These parameters are used for the determination of the heat flux and the vapour flux.

1.4 Process Analytical Technologies for Freeze Drying Process Control

A process analytical technology has been defined as “a system for designing, analysing and controlling the manufacturing through timely measurement (during the process) of critical quality and performance attributes of raw and in-process materials and process with the goal of ensuring final product quality” (ICH 2009). Depending on the utility in the freeze-drying process, PATs have been classified as:

- Off-line: The sample is analysed away from the process stream after removing it from the process
- On-line: The sample is diverted from the process, analysed, and returned to the process stream.
- In-line: The sample is monitored invasively or non-invasively without removing it from the process

The choice of PAT is case dependent. However, the freeze-drying exponents have proposed some general features of an ideal technique (Fissore, et al. 2018; Nail, Steven, et al. 2017; Patel, S. M. and Pikal 2009):

- Applicable for scale up and compatible with existing apparatus
- Measurement representative of the batch, capturing the desired product attributes and process variables
- Good sensitivity and reproducibility
- Ability to withstand steam sterilisation

Furthermore, the recent research interest in real time (in-line) lyophilization monitoring has grown towards two groups of in-line PATs: (1) single vial techniques that do not interfere with the heat and mass transfer process; (2) batch sensors (physical or those based on mathematical modelling) that can monitor the whole batch and take into account, the heterogeneity in the product dynamics due to the relative contributions from the various mechanisms of heat transfer depending the vial location

(Fissore, et al. 2018; Nail, et al. 2017; Patel and Pikal 2009). In-line PATs in conjunction with the off-line technologies are frequently applied to control a freeze drying cycle. Some of the noteworthy technologies have been briefly described in the upcoming sections.

1.4.1 Off-line Techniques

The techniques that are most common used to study phase transitions are Differential Scanning Calorimetry (DSC), electrical impedance measurements (Angell 2002; Kilmartin, et al. 2000) and Freeze Dry Microscopy (FDM) (Ward, K. and Matejtschuk 2019). Some noteworthy techniques on characterising the ice crystal morphology/porosity of the dry layer have been mentioned. Further, a gravimetric method for determining sublimation rates offline has been described.

Differential Scanning Calorimetry (DSC)

DSC is the most widely used method of thermal analysis in the pharmaceutical industry. In principle, a sample is heated or cooled at a controlled linear rate (usually 5 to 10 °C/minute) in an inert atmosphere (usually Nitrogen gas). When the sample undergoes a range of thermal events including melting, crystallisation, glass transitions or decompositions reactions, the temperature and energy associated with these events can be assessed by the DSC apparatus. The information could be directly related to the solid-state structure and therefore, helps to differentiate polymorphs and measure glass transitions.

The main disadvantage of DSC is that given that DSC utilises small volumes for analysis, the estimates for the glass transition temperature (T_g') is non-representative of the actual solution for freeze-drying. This is attributed to the impact of heterogeneities in the freezing rates that invariably results in differing degrees of the amount of ice formed on freezing, and hence the freeze concentrate in the unfrozen fraction. Container geometry and product fill heights can both impact ice formation.

Electrical Resistance

Impedance measurements have been performed in the characterisation of the freezing behaviour for several decades (Rey, L. R. 1960). The majority of impedance measurements are performed at a fixed frequency (e.g. 1 kHz) using pair of pin electrodes placed in a cryostat measurement cell containing the solution. As the solution is heated through the glass transition temperature, the measured electrical impedance mirrors the mobility of delocalised charges (ions) in the frozen solution. However, this is a product invasive method, as the electrodes act as additional nucleation sites, thereby impacting the freezing behaviour, particular the ice nucleation temperature and consequently the ice crystal morphology (Ward and Matejtschuk 2019).

Freeze Dry Microscopy (FDM)

The use of FDM for a microscopic examination of the phase transitions experienced by a formulation has been studied. The FDM apparatus comprises a stage which is temperature controlled by Liquid Nitrogen and an electric heating source, coupled with a vacuum pump which maintains low pressures (e.g. 0.2 mbar) to simulate freeze-drying conditions. Typically, a droplet of the formulations is placed onto the sample holder, which is then frozen to a low temperature, the sample stage is evacuated and then the temperature is ramped up slowly. Photographic images of the product are captured throughout the process. At low temperature the drying front progress slowly (from the edges of the droplet towards the centre, leaving behind an identifiable dry layer. As the temperature of the sample approaches the collapse temperature, drying front leaves behind distinct zones of collapse. FDM can thus be used to define the the set points for the shelf temperature for a real freeze drying cycle (Meister and Gieseler 2009; Zhai, S., Taylor, Sanches and Slater 2003a). Similarly, this technique has been utilized for characterising formulations with crystalline excipients undergoing eutectic transitions (Ward and Matejtschuk 2019).

Techniques for the Determination of Product Morphology

Whether freezing is left to the fate of stochastic ice nucleation or it is controlled, the size of the ice crystals can be determined using two categories of techniques, namely the off-line techniques and the in-line techniques. Examples of offline techniques include: (i) scanning electron microscopy (SEM) or its combination with image analysis (Arsiccio, A., et al. 2018; Grassini, S., et al. 2016), and X-ray tomography to determine the pore size distribution in the freeze-dried product (Pisano, et al. 2017); (ii) Brunauer-Emmett- Teller (BET) for measuring surface area of the cake which is related to pore size (Rambhatla, et al. 2004). These will not be discussed in detail.

Gravimetric Determination of Sublimation Rates at Various Shelf Locations

The sublimation rates and the vial heat transfer coefficient (K_v) can be calculated off-line, for individual vials of the batch at various representative locations of the shelf to study the drying behaviour of the product for a given freeze dryer (Fissore, et al. 2015). That then allows one to compare the estimate determined from this method with other in-line measurement techniques (e.g. TDLAS) (Nail, et al. 2017). In principle, the gravimetric method involves loading the dryer with pre-weighed vials and weighing them again after the completion of 25-30% of ice sublimation at the given shelf temperature and chamber pressure (Figure 7). Here the assumption is that as long as ice doesn't sublimate by more than 25-30%, the shape of the sublimation interface is assumed to be flat, implying that relative heat contributions from the various heat sources don't change (Pikal, et al. 1984). With the knowledge of the product temperature from a temperature sensor (e.g. thermocouple) the sublimation rate and therefore the vial heat transfer coefficient at that pressure can be determined using the classic steady state heat and mass transfer relationship described by Pikal et al.(Pikal, et al. 1984), which is also given in Equation 6. The method is then repeated at the subsequent chamber pressures and other shelf temperature to finally complete the thermal mapping of the shelf. While this method provides a true picture of the hot and cold spots on the shelf, it requires one to interrupt the process, reweigh all the vials and place them back into the dryer to determine the drying rate and K_v

at the next chamber pressure. More practical approaches is taken by two in-line measurement tools; (i) an in-line Microbalance for single vial monitoring (Fissore, et al. 2018; Patel and Pikal 2009; Pikal, M. J., et al. 1983); (ii) Tuneable Laser Absorption Spectroscopy (TDLAS) (Gieseler, Kessler, et al. 2007); both of them have been discussed later.

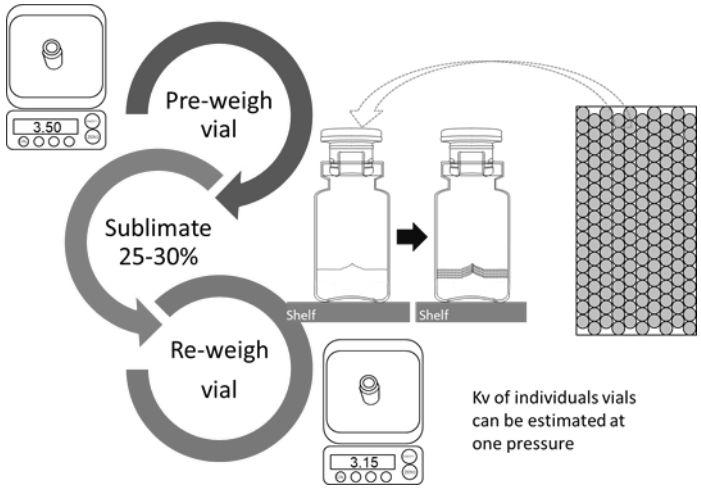

Figure 7: Off-line determination of the sublimation rates using a Gravimetric method.

Dielectric Spectroscopy

The term "dielectric" refers to a material with limited electrical conductivity. Dielectric spectroscopy measures the dielectric properties of a material as a function of frequency. Dielectric properties refer to the ability of a material to get polarised in an electromagnetic field. Dielectric spectroscopy can operate in the frequency range 10^{-6} to 10^{-12} (Barker and Antonijevic 2011; Kremer 2002; Pearson and Smith 1998). Depending on the applied frequency, a material can polarise via different mechanisms (Barker and Antonijevic 2011; Pearson and Smith 1998):

- ionic polarisation or surface conductance
- interfacial polarization or space charge
- dipolar reorientation of molecules
- atomic polarisation (stretching of atomic bonds)
- Electronic polarisation (distortion of electron orbitals with respect to atomic nuclei

Dielectric spectroscopy encompasses different methodologies for the determination of dielectric properties:

- Frequency-domain methods (ac-impedance analysis, IA)
- Time-domain methods (e.g. time domain reflectometry, TDR)
- Nonisothermal methods analysis (e.g. dielectric thermal analysis, DETA, and thermally stimulated currents, TSC).

A common fundamental principle behind all measurements of the dielectric properties is that the sample is subjected to a small voltage (electrical perturbation) and the resulted current is measured, known as the dielectric response. The ratio between the observed current and the applied voltage mirrors the physico-chemical properties of the sample. The physico-chemical properties refer to permittivity ε' and conductivity σ of the material, where ac conductivity results from dc conductivity and dielectric loss (Pearson and Smith 1998). By scanning the material over a frequency range, a dielectric spectrum can be obtained in the real part and in the imaginary part (Barker and Antonijevic 2011).

Various off-line studies have adopted the DETA approach for freeze-drying monitoring because the measurements can be performed in the freeze-drying temperature range of interest. More specifically, molecular mobility of water and excipients in freeze-dried products has been evaluated (Bhardwaj and Suryanarayanan 2011; Bhardwaj and Suryanarayanan 2012; Her and Nail 1994; Yoshioka, et al. 1999; Yoshioka and Aso 2005). The knowledge of the molecular mobility has allowed for the prediction of the stability of the freeze-dried protein formulations (Bhardwaj and Suryanarayanan 2012; Duddu, et al. 1997; Duddu and Dal Monte 1997; Pearson and Smith 1998). In addition, moisture content in the freeze-dried products has been determined using the same method (Ermolina, et al. 2007a; Ermolina, et al. 2007b; Ermolina and Smith 2010; Suherman, et al. 2002).

One frequency domain method, impedance analysis (IA) has been used in-line for the monitoring of the freeze-drying process. Two measurement tools that use the method are: (i) LyoRX

system; and (ii) Through Vial Impedance Spectroscopy (TVIS) which have been discussed the section on single vial techniques under the sub category “Spectroscopic Methods”.

1.4.2 In-Line PATs for Freeze Drying

The currently available PATs, intended for freeze drying, can be roughly divided into two categories: single vial and batch measurement techniques.

1.4.2.1 Single Vial Techniques

Microbalance (Gravimetric Method)

A microbalance uses a gravimetric method to determine the loss of ice mass during the primary drying stage (Fissore, et al. 2018; Patel and Pikal 2009; Pikal, et al. 1983). It comprises a balance with a holding arm that involves periodical lifting and weighing of the vial over a ~10 s period. The technique has been applied to measure sublimation rates and hence the primary drying endpoint. The technique has also been shown to measure the dry layer resistance (R_p) and rate of desorption during secondary drying. A modification of this system (LyoBalance by Martin Christ) can be installed in pilot scale freeze dryers that allows for the measurement of 15 vials simultaneously.

There are several disadvantages of this technique. First, the measurement involves repeated interruption to the conduction heat transfer from the shelf to the product over the duration of the measurement (Roth, et al. 2001). Second, the vial receives an additional heat contribution from radiation heat transfer when the vial is lifted from the hexagonal array (Fissore, et al. 2018; Patel and Pikal 2009). This was also observed for a syringe and higher sublimation rate was reported when it was placed outside the cluster of other syringes (Hottot, A., Andrieu, Vessot, et al. 2009). This atypical drying behaviour can be avoided by shielding the vial with an aluminium foil or placing other vials on the side as demonstrated in a couple of studies, which reported that a drying rate similar to that for the batch was obtained for the monitored vial when it was shielded from side radiation (Barresi, et al. 2009a; Carullo and Vallan 2012).

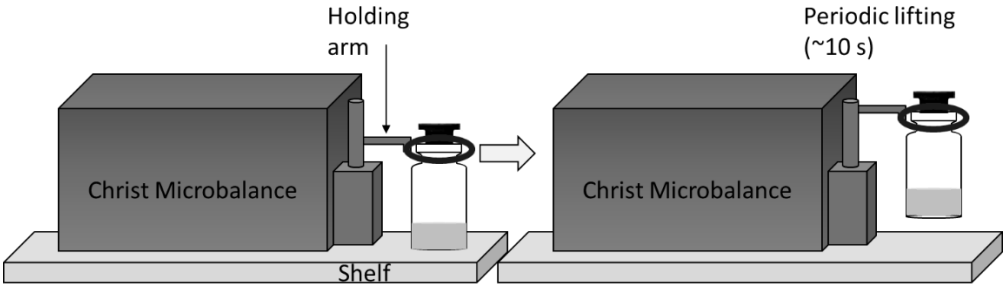

Figure 8: Schematic of Christ Microbalance with vial positioned in holding arm. Reproduced from Roth et al.(2001).

Product Temperature Measurement

Thermocouples (TC) are used for measuring the product temperature of a few individual vials during freeze drying (Cameron and Butler 1997). A TC is made up of different metal wires (e.g. Type-T: copper/constantan) individually connected to a plug at one end and fused together at the sensing end, forming a junction. When subjected to different temperatures, a TC produces a voltage that can be expressed in terms of temperature (Pollock 1991). A TC wire should be thin such that it allows easy insertion of the probe into the vial into a precise location and is un-perturbing to other vials in its path. In practice, the sensing tip is positioned in contact with the bottom-centre of the vial base (Figure 9a) because the ice mass in the bottom-centre is expected to be last to sublimate (Roy and Pikal 1989).

Although reliable information on product temperature is needed throughout the freeze drying process, the use of TC is particularly important during freezing and primary drying. It must be ensured the product freezes to the desired sub-zero temperature and is held for a sufficient period at the operating shelf temperature set-point (Nail, et al. 2017). During ice nucleation and crystal growth, a TC senses a sharp rise in the product temperature due to the release of heat of crystallization, which then decreases relatively slowly during the crystal growth phase as the TC continues to sense the evolution of heat until the point when the TC response equilibrates to value a few degrees from that of the shelf temperature (Franks 2007). On application of the vacuum during the primary drying stage, the product temperature decreases initially and attains a constant value for a brief period. At some point, the sensing tip gradually loses contact with the ice, which manifests as a step like increase in the

product temperature until it reaches a new steady state value close to that of the shelf temperature, which is the first indication that the ice sublimation is nearly complete (Roy and Pikal 1989). At this point, an additional soak period of 10 to 20 % of the primary drying time is usually added to ensure all the ice has been removed (Tang and Pikal 2004).

A **resistance temperature detector** (RTD) (Figure 9b) is based on the principle that as the temperature varies, the resistance of the material also varies proportionately (Cameron and Butler 1997). Like thermocouples, RTDs can also be applied for the determination of the primary drying endpoint. RTDs are known to be more accurate and precise than thermocouples; however, an RTD measures the average temperature across the sensing element (Nail, et al. 2017).

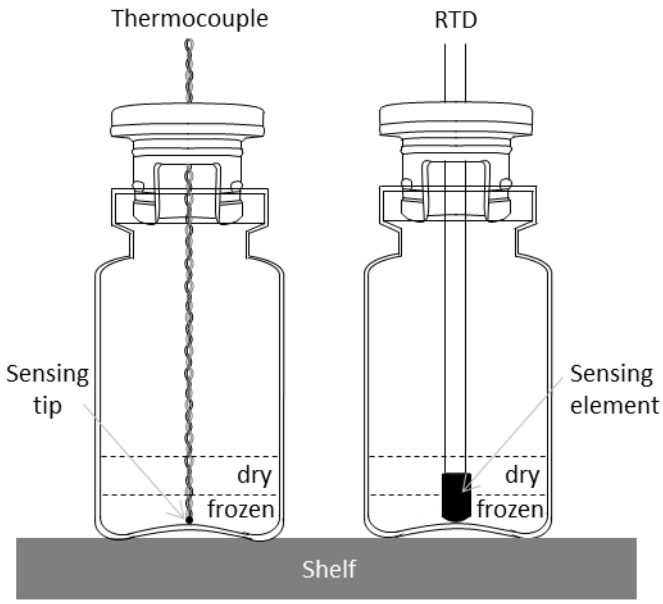

Figure 9: (a) a conventional thermocouple which is point measurement probe and (b) a resistance temperature detector (RTD) which records the average temperature sensed by the whole element. A hypothetical situation is shown where the sublimation front has passed down the top edge of the sensing element of the RTD. Therefore, the product temperature will be equal to the average of the temperature of the dry layer and the that of the frozen solid, which can be misleading when determining the endpoint.

The wireless **Temperature Remote Interrogation System** or TEMPRIS® can be applied for the determination of the primary drying endpoint. A schematic of the system is as shown in Figure 10. It comprises: (i) a transmitter, which is attached to the dryer door; (ii) an interrogation unit connected to a computer; and (iii) a wireless probe. The wireless probe comprises a Teflon tube which is inserted through the rubber stopper, and then connected to the antennae, which are attached to a 2 mm sensing element, which contacts the bottom-centre of the vial base (Schneid, Stefan and Gieseler 2008). The sensing element comprises a quartz crystal which vibrates at a frequency as a function of temperature. Like a thermocouple, the TEMPRIS® also records the product temperature throughout the freeze-drying process. In one experimental study involving TEMPRIS probes and the thermocouple sensors placed in the core and the edge vials, the core vial product temperature timelines from the TEMPRIS were shown to be in excellent agreement with those from the thermocouple sensors. Moreover, for the edge vials, the characteristic abrupt increase in the product temperature due to the loss of contact between the product and the thermocouple tip was not observed for those that had the TEMPRIS probes (Schneid and Gieseler 2008).

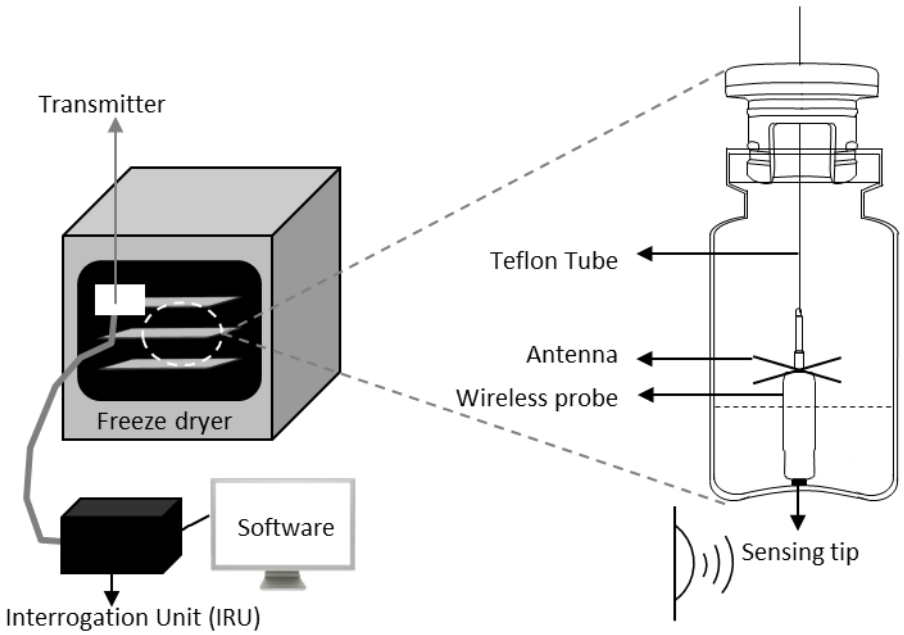

Figure 10: A schematic of the wireless Temperature Remote Interrogation System (TEMPRIS®, iQ Mobil Solutions,GmbH, Holtzkirchen, Germany). Reproduced (Schneid and Gieseler 2008)

The major advantage of TEMPRIS over TCs and RTDs is the wireless and passive battery-free measurement principle (Patel and Pikal 2009; Schneid and Gieseler 2008). One might expect further adoption of these wireless technologies now that robotic systems are available for loading the sensor into the vial as an integral part of the filling line, enabling compatibility with the automatic vial loading systems (Tempris 2020). A commercial wireless temperature system, WTMplus, introduced by Martin Christ has been retrofitted into their pilot and production scale freeze-dryers.

Impact of Probe Insertion into the Product

Different Drying Behaviour

It is evident from Figure 9 and Figure 10 that a significant part of the probe (including wiring) in all the 3 cases contacts the product, thereby making it an additional source of nucleation sites during freezing. In one instance, the product containing probes were reported to nucleate up to 5 °C higher than the product without a probe (Nail, et al. 2017; Roy and Pikal 1989). A higher ice nucleation temperature is equated with a larger ice crystal morphology, the larger ice crystals leave behind larger channels during sublimation, and therefore, a lower resistance to the flux of water vapour through these channels (Searles, et al. 2001). In general, a 10 % decrease in the drying time for a monitored vial has been reported (Nail, et al. 2017). Further, the sensing tip of thermocouples and RTDs provides an additional heat source to the product, consequently resulting in an increase in the product temperature in the monitored vial and hence a faster primary drying time.

Edge effects

The pseudo steady state value of the product temperature in the probed vials at the end of the primary drying is either approximately the same as that of the shelf temperature when the monitored vial is positioned in the core region of the batch; or it is a few degrees higher than the shelf temperature, when the monitored vial is located in the periphery of the shelf. This is attributed to the

fact that the edge vials receive an additional heat contribution via gas conduction and/or radiation (Pikal, et al. 1984; Rambhatla and Pikal 2003; Scutella, et al. 2017). The endpoint from an edge vial is, therefore, misleading and can result in a product collapse in the core vials if the one switches to secondary drying before all the ice has been removed. Hence, the temperature probes should be inserted in both the edge vials and the core vials. At least at the lab scale, it is possible to perturb different shelf locations thereby accounting for the heterogeneity (Bosca, Corbellini, et al. 2013; Thompson and Jr. Ling 2013). Given that the tip of the probe should be placed where ice is expected to remain longest (Roy and Pikal 1989) it is all the more important to have an accurate determination of the temperature in that region. For obvious reasons, the point when all the ice is removed from the dried bulk cannot be detected visually from the outside owing to the opacity of the product. In most freeze drying operations, monitoring the temperature with a thermocouple/RTD stands out as the most preferred method; however, ensuring that the thermocouple wire is kept straight so that the tip touches the bottom-centre of the vial base is a tedious process and requires a careful positioning of the probe. Even a small displacement from the critical position can affect the temperature reading (Fissore, et al. 2018). Therefore, Nail et al. have recommended the use of special devices for correct positioning of the probes, but all of them are patented (Douglas, et al. 1990; Douglas and Thompson 1995; Sutherland, et al. 1997). In addition, monitored vials at the Pilot or the production scale are positioned only at the edge. Positioning the probes in the core requires one to lean over the front part of the batch which is likely to compromise sterility (Nail, et al. 2017).

Uncertainties in the product temperature

The product temperature from a thermocouple is reliable only over the first few hours of sublimation and hence it is not possible to detect the point of 100 % ice sublimation in that vial. In fact, at some point before the end of the primary drying stage, the sensing element loses thermal contact with the product and hence starts to indicate the end of sublimation. However, it has been proven that at the point when product temperature rises sharply, there is still ice present at the bottom of the vial

which implies that the sensor starts to register the temperature of the dry layer (Bosca, Barresi, et al. 2013; Chen, et al. 2008).

Furthermore, the size of the sensing tip differs significantly between an RTD (length 7 mm) and a thermocouple (e.g diameter 0.2 mm) (Nail, et al. 2017). This is demonstrated in Figure 9. It follows that the contact area between the product and the sensing element is much larger in the case of an RTD. As the sublimation front advances down the top edge of the sensing element, the RTD will measure the average temperature of the partially dry layer and the frozen solid leading to erroneous detection of the endpoint. Recently, a new RTD based data logger (Ellab, Hilleroed, Denmark) has been launched whose sensing element is comparable to that of a thermocouple. This makes Ellab more reliable than a conventional RTD given that the temperature is more likely to be a "point" measurement as the size of the sensing element decreases (Nail, et al. 2017).

Sterility and Compatibility Issues

In addition to the aforementioned drawbacks, the insertion and manual handling of the probes can compromise sterility of the product. This also makes them incompatible with automated loading systems.

Because of the aforementioned limitations of product-invasive probes, the recent developments in single vial product temperature monitoring methods involve the measurement from the "outside", i.e. those methods that do not interfere with the dynamics of the product.

Probes External to the Vial (Non-Contact Measurement)

In regard to non-invasive individual vial monitoring of product temperature, **plasma sputtering** has been proposed, with the goal to embed thin film thermocouples or **sputtered thermocouple arrays** into the glass wall (Grassini, S., et al. 2013; Grassini, Sabrina, et al. 2014; Oddone, et al. 2015; Parvis, M., et al. 2012; Parvis, Marco, et al. 2014). However, these sensors are not compatible with the existing freeze-dryers and containers as they involve the use of modified vials. Alternatively, the use of **optical fibres with fibre Bragg gratings** (FBGs) embedded into the shelf has been proposed (Kasper, Wiggenhorn, et al. 2013). FBGs are based on the measurement of the refractive index which is dependent on temperature. On irradiation of the fibre, light is reflected and refracted in the FBGs and the refractive index can be expressed in terms of temperature (Kasper, et al. 2013). Although FBGs are much better than thermocouples and RTDs in terms of sensitivity, response time and resolution, thereby enabling detection of excipient crystallization, glass transition and endpoint, they require special shelves and/or a correct positioning of the vials to ascertain an accurate measurement (Kasper, et al. 2013).

Heat Flux Monitoring

It is possible to monitor the freezing stage (onset of ice nucleation) and the primary drying stage (primary drying endpoint) from a calorimetric determination of the vial heat transfer coefficient (K_V) (Chen, et al. 2008; Fissore, et al. 2018; Jennings, T. A. and Duan 1995). The method involves the use of arrays of paired thermocouples, which are either attached non-invasively to the vial bottom of an empty vial and the bottom of the vial containing the product (Jennings and Duan 1995); or to the top of the shelf and the vial bottom (Chen, et al. 2008). The former method is known as drying process monitoring (DPM) and the latter is called the heat flux transducer method. In general, heat flux sensors are useful in monitoring the product temperature during the freezing stage but require the value of K_V for monitoring the temperature during primary drying. In addition, the primary drying times have been reported to be shorter when compared to comparative pressure measurement of Pirani and

Capacitance Manometer pressure sensors (Vollrath, et al. 2017) (see section on “Pressure Monitoring”).

One issue of concern as regards heat flux monitoring is the fact that the sensors require careful positioning of the vial on the sensing module to maintain good thermal contact. Previously, Chen et al. attempted to improve the thermal contact by placing a flat copper disc between the vial bottom and the shelf, as depicted in Figure 11. However, whether performing a measurement in this manner yields reliable results, is a question of debate (Fissore, et al. 2018). In the attempt to improve the thermal contact, Vollrath et al.(2017) have evaluated an improved system which comprises an array of ~50-60 differential thermocouples connected in series (Ling 2015).

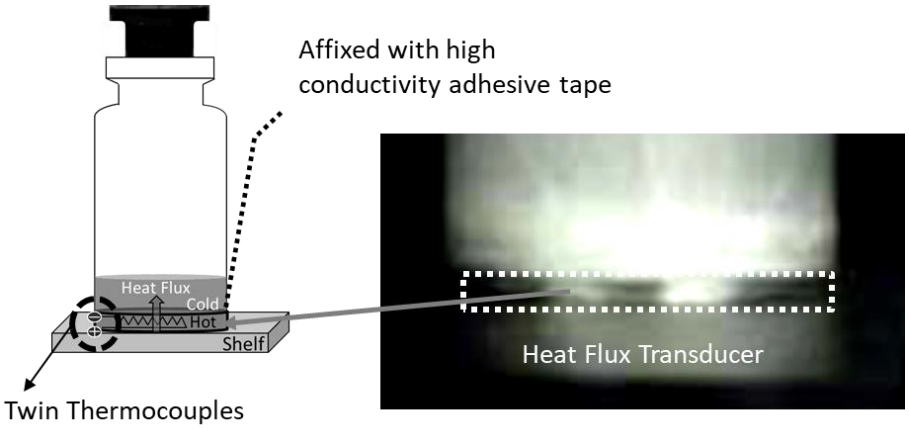

Figure 11: Schematic and photograph of a type of heat flux transducer system comprising a flat copper bottom under the vial bottom and the shelf. Adapted from Chen et al. (Chen, et al. 2008)

Soft Sensors

Freeze-drying monitoring using mathematical modelling has been known for several years. Some of the earliest models were quite complex, could not be applied in-line and did not account for heat conduction in the glass wall (Millman, et al. 1985; Pikal, M. J. 1985). In other models, many simplifications that did not account for a proper energy balance to describe the heat transfer in the glass vial were introduced (Hottot, Aurélie, et al. 2006; Zhai, et al. 2005). A soft sensor is a tool based on the fundamental energy and mass balance equations that can be used to estimate in-line any variable (e.g. T_i, K_v, R_p) when combined with a prior knowledge of the product temperature at the vial bottom determined using a thermocouple (Velardi, Salvatore A. and Barresi 2008) or a wireless sensor (TEMPRIS®) (Schneid and Gieseler 2008) or a non-contact temperature sensor (e.g. plasma sputtered thermocouples) (Grassini, et al. 2014; Parvis, et al. 2012). Soft sensors have also been proposed for the determination for predicting pore diameters based on the knowledge of R_p (Velardi and Barresi 2008). Further, Fissore et al. proposed a model for predicting optimum chamber pressure for a given shelf temperature, aiming to predict the minimum primary drying time. The same authors predicted a varying temperature scheme with the goal to estimate the maximum allowable product temperature and hence a shorter primary drying (Fissore, et al. 2008). In addition, at the production scale, it has been possible to use a low invasive temperature sensor to measure the product temperature and use a model for predicting the shelf temperature, which was reported to be agree well with the model, indicating the potential for soft sensors to be used in automated loading systems (Corbellini, et al. 2010).

Infrared (IR) Thermography

An application of the Infra-Red Camera has been proposed for the monitoring of the different stages of the freeze-drying process for a group of vials. The first use of thermal imaging was introduced by Emteborg et al., who placed their system outside the freeze dryer (on the top) for measuring the evolution of the product temperature in a batch of vials positioned on the top shelf, without any interference to the dynamics of the product (Emteborg, et al. 2014). However, the system measures the product temperature at the top of the product giving no information on the product temperature at the sublimation interface or at the vial bottom.

More recently, Fissore et al. have developed a novel IR camera imaging system placed inside the dryer for the non-invasive determination of the evolution of the temperature gradient and freezing front rate, which in turn, are used to predict the ice crystal size distribution (Colucci, et al. 2019). In the same study, rather than measuring the dry layer resistance of a lyophilised product, the study uses a mechanistic model developed by Velardi and co-workers (Velardi and Barresi 2008) for predicting the dry layer resistance at the end of the freezing process, thereby being able to predict the primary drying time and the product temperature. Furthermore, the same IR camera apparatus has also been used to determine the product temperature distribution in a group of vials at the bottom of the product during primary drying, the primary drying endpoint, and certain process parameters, namely the vial heat transfer coefficient and the dry layer resistance (Lietta, et al. 2019). As regards the product temperature, the results showed that value of the product temperature determined from IR thermography agreed with that measured by thermocouples with an uncertainty within ± 1 °C. Further, it was demonstrated that the product temperature from the IR camera and the ratio between the Pirani and the Capacitance manometer signals (these are batch measurement tools; see “Pressure Monitoring Sensors” in Section 1.4.2.2) reached their respective pseudo steady state values at the same time, suggesting good agreement for the determination of the end of sublimation. Similar agreements were observed in the case of the estimates for the dry layer resistance.

One potential drawback of the method that it possible to monitor only the front row vials. Nevertheless, because the IR camera shields the front vials from radiation, the estimates of the sublimation flux for the front row vials agreed well with those in the centre vials of the batch. Therefore, the authors expect that the sublimation dynamics in the front row vials should be representative of the batch.

Photographic Imaging for Visual Examination

It is possible to use photographic imaging for the visual monitoring of the ice sublimation front. The method involves capturing of photographs of the sublimation front during the primary drying stage at suitable time intervals. Previously, photographic imaging and other measurement techniques have been compared to study the sublimation kinetics at the microscale (Zhai, S., Taylor, Sanches and Slater 2003b) or at the laboratory scale (Chen, et al. 2008; Zhai, et al. 2005). One study involved the estimation of the height of the sublimation front for pure ice by visual observation, which was compared with a theoretical model; both estimates were reported to be in good agreement (Zhai, et al. 2005). In another study, estimates of sublimation rate determined from the photographic method and that determined from heat flux monitoring were compared (Chen, et al. 2008). In the same study, sublimation endpoints between the one estimated visually and the one determined from thermocouple response were compared. The photographs confirmed the presence of significant amount of ice mass at the point when there was a sharp rise in the product temperature, meaning the sensing tip had started to sense the dry region of the product while there was still present at the bottom of the vial. In this instance, the photographic method demonstrated the need for a correct positioning of the sensing element in contact with the bottom centre of the vial, when using a thermocouple for the determination of the endpoint.

The drawbacks of the photographic examination of the sublimation front include: (i) sublimation behaviour of pure ice is non-representative of the sublimation behaviour of a product (Patel and Pikal 2009); (ii) the ice sublimation front loses its planar geometry towards the end of

primary drying (Patel and Pikal 2009) which can lead to erroneous estimations in the height of the sublimation front; (iii) the method requires a direct line of site and is only applicable in dryers with a transparent door, and therefore its application is limited to laboratory scale.

Spectroscopic Methods

Impedance Spectroscopy

In addition to the off-line methods based on the time-domain dielectric spectroscopy methodology for the characterisation of the freeze-dried products (Barker and Antonijevic 2011; Pearson and Smith 1998) (described in Section 1.4.1) dielectric spectroscopy has also been applied for the in-line monitoring of the freeze drying process. One noteworthy device that measures the product temperature and the electrical resistance of the sample is the **LyoRx** System, commercially available from Martin Christ (Smith and Polygalov 2019). The measurement involves the use of a PT100 RTD probe, located between the metal pin electrodes to track the changes in the product temperature and allow the determination of the freezing/eutectic point and process optimization. During freezing stage, the electrical resistivity of the formulation increases from 5% to 90% due to a phase transition from liquid to frozen solid respectively. This technique is similar to the off-line electrical resistance measurement approach, as both measure electrical resistivity at a fixed frequency (1 kHz).

Figure 12: Martin Christ LyoRx Sensor

The main drawback of the LyoRx sensor is its invasive measurement, as the electrodes have to be immersed into the sample and hence most likely to affect ice nucleation. It follows the LyoRx sensor is of limited use in recording the sublimation rates and the measurement of drying end points. In addition, since the individual vial is introduced with three probe system, these measurement pins are expected to provide additional path for the vapour flow during primary drying, resulting in drying rates higher than the vial without such perturbations.

Alternatively, **through vial impedance spectroscopy (TVIS)** has been used as non-invasive single vial technique at the laboratory scale for the monitoring of the different stages of the freeze-drying process (Smith and Polygalov 2019). In its current manifestation a pair of thin film or metal foil electrodes are attached on opposite faces of the glass wall and connected to a purpose built broad-band (10 Hz to 1 MHz) electrical impedance spectrometer. The object under test is, in effect, a composite capacitor comprising the glass vial and its contents. When filled with water, the complex capacitance spectrum is characterised by a peak in the imaginary part capacitance (dielectric loss) and a step in the real part capacitance (dielectric storage) as a result of the interfacial (or Maxwell-Wagner) polarization of the glass wall through the electrical conductance of the water. For frozen water (ice), there is also a peak in the imaginary part and the step in the real part but in this case, it is the manifestation of the dielectric relaxation of the ice (Smith and Polygalov 2019).

The application of TVIS for freeze-drying process development was first introduced by Smith et al. (2013). For a 2.5 % w/w sucrose solution, the authors demonstrated its potential for the in-line monitoring of the product temperature throughout the cycle, measure the sublimation rate and the primary drying endpoint, thereby being able to monitor the process without interfering with the product and the process kinetics. In subsequent studies, Smith et al. have used impedance based methods for: (i) the in-line characterisation of the glass transition temperature of maltodextrin solutions (Smith, Arshad, et al. 2013); (ii) the impact of annealing on sublimation rate (Smith, et al. 2014); (iii) prediction of the ice temperature at the sublimation interface (T_i) and at the vial bottom

(T_b), and sublimation rate and the vial heat transfer coefficient (Smith, et al. 2018). More recently TVIS has been shown to measure the time difference between the ice nucleation onset (i.e. the point when primary nuclei first form) and the point when ice solidifies completely, referred to as the solidification endpoint (Smith and Jeeraruangrattana 2019). Before this publication, the solidification endpoint was thought to be the point when the product temperature from a thermocouple equilibrates to the shelf temperature. However, the authors demonstrated that the ice solidification phase is completed well before a thermocouple equilibrates to the shelf temperature, as it continues to sense the evolution of the heat of crystallisation.

One potential drawback of the technique is that it requires a manual assembly of the cables to connect the electrodes and thus incompatible with automatic vial loading systems nor can it be sterilised. However, a "non-contact" TVIS system which involves placing a single electrode over a cluster of vials is under development, which would be compatible with automated loading systems (Smith and Polygalov 2019).

Near Infrared Spectroscopy (NIR) and Raman Spectroscopy

Near IR and Raman Spectroscopy are vibrational spectroscopy techniques based on the interaction between matter and the electromagnetic spectrum (Kauppinen 2015). In practice, in both cases, the sample is illuminated with a laser of a certain wavelength and a fibre optic probe. When the sample is illuminated with NIR light, the sample molecules with bonds containing OH, CH and NH absorb this energy and become excited to higher vibrational states; this reflected/transmitted radiation is collected by the probe and analysed to generate an NIR spectrum. In contrast, Raman spectroscopy is based on the principle of in-elastic light scattering, wherein the sample is illuminated with monochromatic radiation, and as a consequence, a small portion of the incident photons exchanges energy with the sample molecules with bonds containing CC, CN and CS; this inelastic scattering is known as the Raman effect (Kauppinen 2015).

Over the recent times, Near IR and Raman spectroscopy techniques have been applied in conjunction primarily at the laboratory scale, for the non-invasive and non-destructive monitoring of the freeze-drying process, particularly the freezing and the primary drying stages (Fissore, et al. 2018). For instance, De Beer et al. placed a Raman probe above the freeze-dried product (noncontact), coupled to Near IR and X-Ray powder diffraction, to monitor physical transitions during the freezing stage, namely ice crystallisation and mannitol crystallisation, endpoint of freezing and the evolution of mannitol solid state (De Beer, et al. 2007). In the same study, the application of the techniques was demonstrated for determining the primary drying endpoint. The end point of sublimation is characterized by an exponential drop in the intensity of absorption peaks relating to water (Brülls, et al. 2003). Other studies have demonstrated the successful implementation of the techniques for measuring other parameters such as the moisture content throughout the freeze drying process, the potential changes in the protein confirmation due the stresses induced during the drying stages as well as the secondary drying endpoint (De Beer, et al. 2009; De Beer, Burggraeve, et al. 2011; Kauppinen 2015). In addition, the techniques have also been used to characterise the changes in the protein conformational stability and liposomal structural integrity (Pieters, De Beer, Kasper, et al. 2012; Pieters, De Beer and Vander Heyden 2012; Sylvester, et al. 2018).

One significant advantage of Near IR spectroscopy over Raman Spectrosocopy is that Near IR has much stronger affinity to absorption of water (Water molecule has a weak Raman scatter) and hence it can determine the primary drying endpoint with more sensitivity (De Beer, et al. 2007). However, there is some evidence which suggests that certain excipients can absorb in spectral regions designated for water thereby carry the potential to affect the quantification of water in the case of NIR spectroscopy (Grohganz, et al. 2009). Further, residual moisture content estimated from Near IR has been known to be underestimated in relation to the off-line Karl-Fischer measurements performed on freeze-dried samples. Moreover, near IR and Raman Spectroscopy techniques are very powerful but are still under development and the data analysis is quite complex. (Fissore, et al. 2018).

1.4.2.2 Batch Monitoring Techniques

Batch monitoring tools are those that measure an average estimate of a given variable for the entire batch during freeze-drying and are in general, more readily applicable to scale up from pilot to production scale freeze dryers (Fissore, et al. 2018; Nail, et al. 2017; Patel and Pikal 2009). Some of the noteworthy technologies described in this section are based on the application of pressure monitoring (Comparative Pressure Measurement with Pirani Gauge and Capacitance Manometer; Pressure Rise Tests) and those that are based on the measurement of the gas composition or gas flow (Dew Point Sensor, Cold Plasma Ionization Device, TDLAS). The majority of the batch measurement tools are primarily used for the determination of the primary drying endpoint while others (Pressure Rise Tests, TDLAS) can also monitor the sublimation rate during the primary drying and secondary drying stages. Freeze drying exponents have combined different batch measurement techniques with the goal to achieve a more accurate estimation the evolution of the moisture content during the primary drying stage, more specifically to determine the primary drying endpoint (Fissore, et al. 2018).

Pressure Monitoring Sensors

Comparative Pressure Measurement: Pirani Gauge and Capacitance Manometer

The Pirani gauge senses the gas composition in the drying chamber; while the capacitance manometer controls the absolute pressure of the chamber, that is independent of the gas composition. The characteristics of the two pressure sensors can be used in conjunction to detect the primary drying endpoint; the methodology is referred to as the comparative pressure measurement, first introduced by Nail and Johnson (1992).

The **Pirani gauge** (Figure 13a) is a thermal conductivity-type gauge comprising a pair of filaments, the reference and the measurement filament, that form a “Wheatstone bridge” circuit (Liptak 2003). The reference filament is immersed in a constant gas pressure; whereas the measurement filament is exposed to the gas in the system. When both the filaments are heated at a constant temperature, the gas molecules that collide with the reference filament conduct the energy

away from it. This energy gap is detected by the measurement filament, which in turn, is filled by controlling the flow of current via a feedback loop. The amount of current needed to do so depends on the gas composition (Lesker 1996). This is important in freeze drying, where the gas composition is essentially 100 % water vapour at the beginning of primary drying phase, while it is 100 % inert gas (e.g. Nitrogen) at the end of secondary drying. The free molecular flow thermal conductivity of water vapour has been reported to be 6.34 x 10^{-3} cal. s^{-1} cm^{-2} $mmHg^{-1}$; while it is 3.98 x 10^{-3} cal. s^{-1} cm^{-2} $mmHg^{-1}$ for N_2, i.e. 60 % higher than N_2 (Amidon, et al. 1999).

In principle, the **capacitance manometer** (CM) works by measuring the pressure differential between two sides, isolated by a thin, flexible stainless-steel diaphragm as shown in (Figure 13b) (Liptak 2003). One side is evacuated to a very low pressure (1.3 x 10^{-7} mbar) and the other side is exposed to the system pressure. As the system pressure changes, the diaphragm deflects and the deflection is measured in terms of the electrical capacitance between the diaphragm and the electrodes, hence the name capacitance manometer. In this manner, the pressure of a system can be monitored and controlled by maintaining a constant geometry or a constant capacitance.

During the primary drying phase, when the gas composition is essentially water vapour, the apparent pressure detected by the Pirani increases sharply and reaches a pseudo steady-state value, while the Baratron (a brand name for CM) continues to maintain the absolute chamber pressure at the desired setpoint (Nail and Johnson 1992). This is illustrated in Figure 13(c). There comes a point when the Pirani pressure starts to decrease (onset point) as the partial pressure of the water vapour in the chamber decreases, which corresponds to a significant fraction of vials having completed ice sublimation. The Pirani gauge ultimately reads a value close to that of the CM (offset point), which corresponds to a second pseudo steady state value, which is taken as the endpoint Figure 13(c). In practice, primary drying stage may be switched to secondary drying after the difference between the Pirani reading and the CM reading has reduced to 6-13 µbar provided that their difference before the onset of the reduction in the Pirani pressure is more than 50 µbar (Nail, et al. 2017). The period

between the onset of reduction in the pirani reading and the offset point is characterised by large slope and the analysis of the shape of the decreasing curve can provide information on the intra-vial heterogeneity in the porosity of the dry layer, which can be linked back to the ice crystal structure which forms during the freezing stage (Fissore, et al. 2018).

The comparative pressure measurement method can also be applied for the detection of the secondary drying endpoint (Nail, et al. 2017). The Pirani pressure increases in response to the initial burst release of the water vapour from the product as unfrozen water from the formulation is released at elevated product temperatures (Figure 13c). Towards the end of secondary drying, the Pirani pressure returns to CM reading once again, indicating very little additional drying takes place at that shelf temperature, which is taken as the end of secondary drying.

There are three potential limitations of the method. First, there can be an inherent uncertainty in determining the primary drying endpoint, i.e. whether the pseudo-steady state value of the Pirani reading obtained at the end of the primary drying stage (offset point) corresponds to the removal of the last traces of ice from the bottom-centre of the vials or the sensor is erroneously registering any water vapour trapped in chamber (Fissore, et al. 2018). Second, there is an ongoing debate whether it is possible to steam sterilise the Pirani. Patel and Pikal reported no problems with sterilising the Pirani (Patel and Pikal 2009), while Nail et al. ascribe steriliability to the given model (Nail, et al. 2017). In general, the sterilisability could be improved by incorporating better quality parts (e.g. using a different filament material) and frequent recalibration and/or replacement with advanced sensors, such as those with radiation shields that stop the vapour from condensing onto the sensor (Fissore, et al. 2018). The other limitation is that Pirani is not safe to use in the presence of organic solvents. In fact, it is considered best practice not to use the Pirani when freeze-drying flammable solvents (e.g. ter-butanol). The Pirani gauge uses a hot filament, which may cause an explosion in coming in contact with the flammable mixture. Explosion occurs when there are enough molecules of the flammable vapour and oxygen. Therefore, the risk of explosion is particularly high from the point of the application of the

vacuum through to most part of the drying stage, when there is an abundance of water vapour/flammable gas mixture in the chamber. One solution to address the safety concern is to introduce Nitrogen gas before the freezing stage (Nail, et al. 2017) . Despite the concerns, the Pirani is still considered to be the most preferred PAT tool for monitoring the primary drying endpoint, also at larger scales (Fissore, et al. 2018).

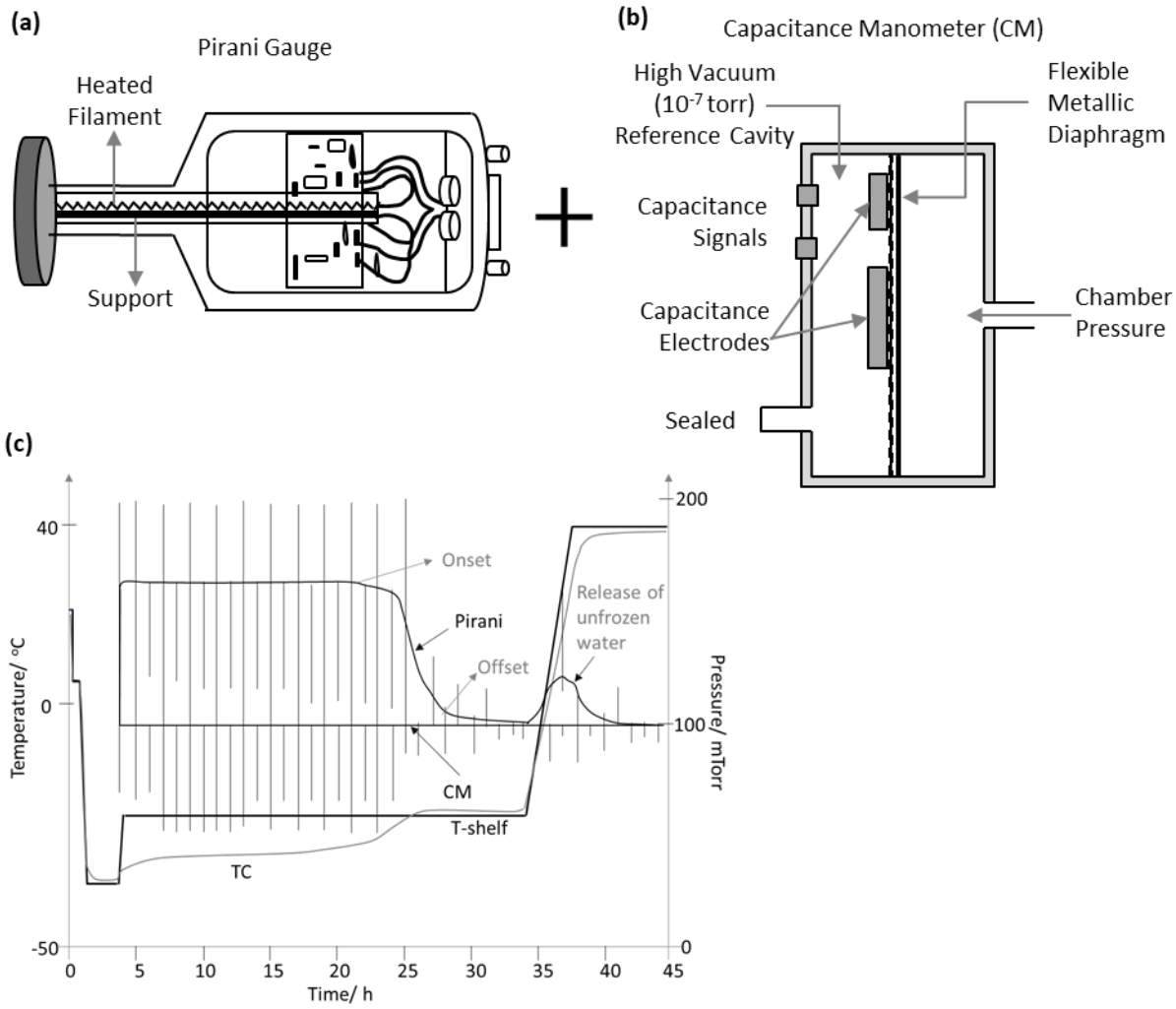

Figure 13: Comparative pressure measurement for the determination of the primary drying endpoint: (a) A schematic diagram of a Pirani gauge, adapted from Lesker (1996); (b) a schematic diagram of a capacitance manometer, adapted from literature (Liptak 2003); (c) Result reproduced from Schneid and Gieseler (2008) which shows the timelines of the product temperature from a thermocouple, the vapour pressure from the Pirani gauge and the absolute chamber pressure from a capacitance manometer- towards the end of primary drying, the Pirani pressure decreases abruptly as the product temperature from a thermocouple increases sharply before reaching a pseudo steady-state value, which is taken as the endpoint.

Pressure Rise Tests

The pressure rise test (PRT) is a general name for a range of methods performed in the drying chamber that involve a brief (up to 30 s) isolation of the valve between the drying chamber and the condenser (Figure 14a) which results in a characteristic rise in the vapour pressure during the drying stages (Fissore, et al. 2018; Nail, et al. 2017). For the determination of the primary drying endpoint, PRT is frequently performed in conjunction with the comparative pressure measurement as depicted in Figure 13c shown previously, wherein the spikes in the values of the Pirani and the CM correspond to the vapour pressure rise and the rise in the total pressure in the chamber, respectively. The pressure rise immediately after the isolation of the chamber can be correlated with the vapour flow rate, or rather the sublimation rate during primary drying. In practice, the point when the gradient of the PRT curve (Figure 14b) or the sublimation rate is below a certain threshold considered to be negligible or comparable to the leak rate of drying chamber is taken as the end of sublimation (Neumann 1961). In other words, the sublimation phase is assumed to be complete, when there is very little or no pressure rise, as depicted by the Pirani reading in Figure 13(c).

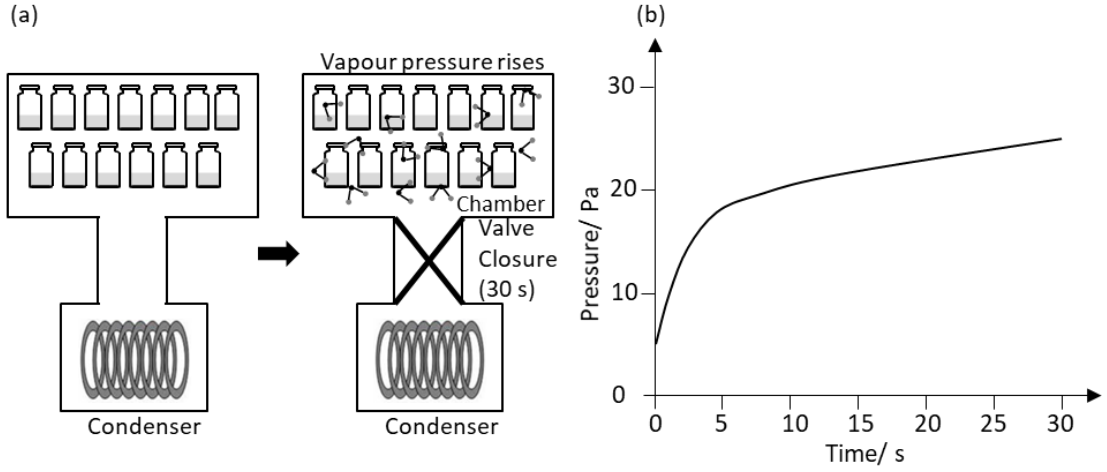

Figure 14: Demonstration of the Pressure Rise Test (PRT). Adapted from Schneid et al. (2008) for sucrose-based formulation in a laboratory freeze-dryer.

Over the past several decades, several other product and process related parameters have been monitored or estimated by fitting the pressure rise data to a set of equations or mathematical algorithms. These include the Barometic Temperature Measurement (BTM), Manometric Temperature Measurement (MTM), Dynamic Pressure Rise (DPR), Pressure Rise Analysis (PRA) and Dynamic Parameter Estimation (DPE and DPE+). The capabilities of these algorithms have been evaluated comprehensively by Fissore et al. (2011). In general, the method has been used to estimate the primary drying endpoint from the estimates of the sublimation rate and the evolution of residual ice content. Moreover, the use of PRT for the monitoring of the secondary drying stage, more specifically the desorption rate, has also been demonstrated using a mathematical model. The most accepted variations of the method are the MTM and DPE method. A brief overview of the key features and limitations have been described here.

It is well known that the product temperature increases during a PRT. Initially, when the valve is closed, the chamber pressure rises rapidly and then increases linearly with time (Figure 14b). The value of the pressure on the linear part of the curve strongly correlates with the vapour pressure of ice (P_o) and hence the temperature of ice at the sublimation front (T_i) (Neumann 1961). As a rough approximation, the higher the final value of P_0 at the end of the PRT (just before valve is opened) the higher is the value of T_i (Oetjen 1999). An increase in the total pressure in the drying chamber leads to an increase in the vial heat transfer coefficient from the shelf to the vial bottom (K_v) due to increased gas conduction to the vial bottom concavity and a decrease in the mass transfer rate (Pikal, et al. 1984). It follows that if the shelf temperature remains unchanged, while K_v increases and the mass transfer rate decreases, the product temperature increases during the PRT as per the classical steady state heat and mass transfer theory (Pikal, et al. 1984). Pisano et al. (2010) have reported that T_i increases by 1 to 3 °C during the valve closure of 30 s relative to that before the PRT. The temperature increase becomes a cause for concern in cases where the temperature at the vial bottom exceeds the maximum allowable temperature, which the method developed by Neumann and BTM method could not determine accurately, though BTM was an improvement over Neumann's method

(Fissore, et al. 2018). Then, Milton et al. (1997) developed a method, commonly known as a the **Manometric Temperature Measurement (MTM)** based on a mathematical model capable of determining more accurately, the temperature at the sublimation interface and at the vial bottom. Tang et al. and Gieseler et al. determined the values for P_{ice} and R_p directly from the MTM equation and further estimated the values for K_v, dm/dt, dq/dt, T_i and T_b as well as the thickness of the dry layer (l_{dried}) (Gieseler, Kramer, et al. 2007; Tang, et al. 2006; Tang, Xiaolin Charlie, Nail and Pikal 2006a; Tang, Xiaolin Charlie, Nail and Pikal 2006b). The MTM method has also been used for the detection of the primary drying endpoint and monitor the moisture content in-line (Tang, Xiaolin (Charlie), et al. 2005). Some of these studies by Gieseler et al. and Tang et al. employed a commercial freeze-dryer, termed SMART™, which uses the MTM method to automatically adjust the shelf temperature and chamber pressure to maintain the optimal product temperature. Further, the knowledge of R_p estimated from MTM has been exploited for investigating the impact of annealing (Lu and Pikal 2004), the degree of supercooling (Rambhatla, et al. 2004), cake shrinkage (Rambhatla, S., et al. 2005) and sublimation rates (Johnson, et al. 2010a; Parker, et al. 2010).

However, there are several limitations of the MTM method. First, the MTM method cannot account for the edge vial effects, as it assumes low non-uniformity and radiation effects and is thus biased towards the colder running core vials. Actually, the value of T_i varies from one vial to another (Tang, et al. 2006). Second, the estimates of the parameters are reliable only over the first ~60-70 % of the primary drying stage, as thereafter, the method systematically underestimates T_i as observed by Tang et al. (2005) and Fissore et al. (2011). The systematic decrease in T_i has been ascribed to faster drying of the edge vials, thereby resulting in a decreased area of the sublimation. Further improvements over the MTM method in regard to a more accurate estimation of the process parameters are the **DPE** and the **DPE+ method**, developed by Velardi et al. (2008) and Fissore et al. (2011) respectively. The DPE method has been shown to account for batch heterogeneity (Barresi, et al. 2010) and side wall radiation (Pisano, Barresi, et al. 2011) and is thus especially useful for the thermal mapping of lab scale dryers, where the edge/core vial ratio is higher as compared to that in

larger freeze-dryers (Fissore, et al. 2018). On the other hand, the DPE+ algorithm further simplifies the numerical complexities related to the DPE method (Fissore, et al. 2018).

The main advantage of the PRT method is that they are more readily amenable to scale up and are compatible with automated loading systems provided the dryers have a fast closing valve in the duct between the drying chamber and the condenser (Nail, et al. 2017). One limitation of the method is that all models underestimate the temperature of the sublimation interface and are reliable up to approximately two-thirds of the primary drying stage, though MTM method is worse out of PRA, DPE and DPE+ as evidenced by Fissore et al. (2011). It follows that PRT test cannot determine the true endpoint of the batch as it loses sensitivity towards the end of the primary drying stage. Second, there will always be a temperature increase (1-3 °C) during a PRT, which can impact product performance. Besides, repeated tests can interfere with the dynamics of the process. Third, the estimates of process parameters are unreliable when the method is applied to formulations with a high amorphous content (<150 mg/mL) (Schneid, Stefan C., et al. 2015). A similar observation was made by Johnson et al. (2010b) for a high protein sample (20 mg/mL) freeze dried at a high shelf temperature (25 °C). This has been attributed to moisture being re-adsorbed to the amorphous dry layer and is more pronounced at high fill volumes (Gieseler, et al. 2007).

Condenser Pressure

The increase in the condenser pressure at the end of the sublimation phase may be used as an indicator of the primary drying endpoint. For this purpose, usually, a capacitance manometer is placed in the condenser which detects an increase in the partial pressure of nitrogen as a consequence of a drop in the partial pressure water vapour (Fissore, et al. 2018). However, the major drawback of the method is its poor sensitivity due to the low levels of pressure increase, which is a problem particularly with slow sublimation rates of ice (Patel and Pikal 2009).

Gas Composition or Gas Flow Monitoring Sensors

Dew Point Sensor

A dew point sensor measures the changes in the relative humidity and hence the gas composition in the chamber to detect the primary drying endpoint (Roy and Pikal 1989). The sensor uses a thin film of a metal oxide whose capacitance changes depending on the extent of the absorption of water (like the capacitance manometer). The resulting capacitance is translated into an output voltage, which in turn is calibrated to obtain the partial pressure of the frost point: the temperature at which the equilibrium vapour pressure equals the partial pressure of water measured by the sensor. Similar to the Pirani output, the dew point sensor reading remains high initially and approximately equal to the frost point until the gas composition changes from water vapour to inert gas, which causes a decrease in the dew point temperature. A sensitivity of being able to detect the last ~1% of the vials still containing residual ice has been reported by Roy and Pikal (1989). In another study, a moisture sensor utilising a gold sputtered foil material remained sensitive until nearly all the water vapour (close to 0 %) was gone (Bardat, et al. 1993). The device used by Roy and Pikal was also used by Genin et al.(1996) and Rambhatla et al. (2004) for the determination of the endpoint. The dew point sensor has been widely adopted at the laboratory scale and has been tested at the manufacturing scale. However, it cannot withstand steam sterilization as reported by Roy and Pikal, though it is possible to use a sterilising filter and valve to isolate the sensor from the steam (Patel and Pikal 2009). The main drawback is its slow response time, leading to significantly longer drying times than those indicated by conventional thermocouples (Roy and Pikal 1989). Similar observations were made by Baressi et al. (2009b) and Hottot el al. (2009) who attributed the reason to the moisture sensor's high sensitivity to the residual vapour trapped in the chamber or slow desorption from the sensor itself or both.

Residual Gas Analyser (RGA)

The use of the Residual Gas Analyser (RGA), such as the Quadrupole Mass Spectrometer (QMS) has been investigated as a process sensor for monitoring both primary and secondary drying in conjunction with other process sensors (e.g. thermocouples, Pirani, Dewpoint, cold plasma) (Barresi, et al. 2009; Connelly and Welch 1993; Jennings, T. A. 1980; Roy and Pikal 1989; Wiggenhorn, et al. 2005; Willemer 1992). In principle, a QMS unit is placed in the duct connecting the chamber and the condenser, where it receives the incoming gas mixture. The gas molecules get sorted based on their mass to charge ratios, ionised and then accelerated in an electric field. The ions are then transferred to the detector which gives a signal based on the concentration and the type of molecules. A mass spectrum is thus obtained, which displays the output in terms of the current intensity v/s time, which when calibrated for gas composition or partial pressure can be used to detect the end of the sublimation phase, as a sharp drop in its signal has been reported to be consistent with ice sublimation being almost complete (Barresi, et al. 2009; Patel and Pikal 2009). However, the method is only qualitative with no numerical criterion for the true endpoint detection, and variations can occur depending on the batch size, scale, formulation type, each of them requiring a separate calibration routine, which must be repeated in every run, thereby making the calibration difficult to implement universally (Fissore, et al. 2018). Besides, the signal suffers from instability of the baseline, making the endpoint detection method less reliable than the comparative pressure measurement (Barresi, et al. 2009; Hottot, et al. 2009).

The partial pressure of water vapour can also be converted into residual moisture and this evolution of moisture can be monitored during both the drying stages but requires complex calibration. Further, QMS cannot be steam sterilised, but can only protected by using a sterile filter like the Pirani gauge (Patel and Pikal 2009). Some other applications of QMS include its use with organic solvents, as a leak detector, as Oxygen partial pressure sensor (thus useful for oxidative products) (Fissore, et al. 2018; Patel and Pikal 2009; Wiggenhorn, et al. 2005). QMS has been very expensive in the past, though more recently, the demand for small and cost-effective devices has increased (though

still more expensive than the Pirani), particularly at the production scale. LYOPLUS™ is a QMS, which has been incorporated as a PAT tool for routine monitoring and process control at the production scale.

Lyotrack (Cold Plasma Ionization Device)

LyoTrack is a type of a cold plasma ionisation detector based on optical emission spectroscopy (OES) which measures the water vapour to nitrogen ratio, i.e. the humidity in the drying chamber (De Beer, et al. 2009; De Beer, Wiggenhorn, et al. 2011; Hottot, et al. 2009; Mayeresse, et al. 2007). The instrument comprises two parts: A Quartz tube and an optical spectrometer (Figure 15). The quartz tube generates a high power radio wave (440 MHz) which results in a cold plasma of the gas in the drying chamber. The plasma thus contains a mixture of excited electrons and gas molecules which, on their return to their initial energy state, emit light of a characteristic wavelength. The spectrometer identifies the water vapour concentration based on the wavelength of the emitted light, which is translated into amount of moisture present in the chamber.

Like the Pirani, Dew point sensor and the RGA, the point where a sharp decrease in the humidity level from Lyotrack occurs indicates that the gas composition has changed from water vapour to nitrogen and ice sublimation is almost complete (Mayeresse, et al. 2007). Over the past, many researchers have reported Lyotrack to be the most sensitive when it was complimented with the Pirani/Baratron and Dew Point sensors, with the Lyotrack-Pirani-CM combination providing the best possible indication of the endpoint, and yet the determination is only qualitative like with the other sensors (Hottot, et al. 2009; Patel, Sajal M., et al. 2010). De Beer et al. complimented two batch measurement tools (NIR, and Raman spectroscopy) and one single vial tool (TEMPRIS®) for the in-line monitoring of the freeze-drying process and found Raman and Lyotrack to be the best method for monitoring the freeze-drying process. Lyotrack can also be used to monitor the secondary drying stage and for the analysis of the evolution of the residual moisture and the secondary drying endpoint, but

requires complex calibration (De Beer, et al. 2009; De Beer, et al. 2011; Hottot, et al. 2009; Mayeresse, et al. 2007).

Some of the drawbacks related to the use of Lyotrack have already been mentioned previously, but are reiterated here in addition to other limitations: uncertainty in the detection of the true endpoint, complex calibration, risk of product degradation via free radical oxidation (due to the ionisation of the chamber gas), and a potential concern associated with the measurement being impacted by probe location (Fissore, et al. 2018; Mayeresse, et al. 2007; Patel, et al. 2010). Further, Lyotrack is more expensive than the Pirani gauge, possessing no additional features in relation to the Pirani (Fissore, et al. 2018). The limitations far outweigh its potential advantages of being readily steam sterilisable, reproducible and compatible with in automated loading systems at the industrial scale.

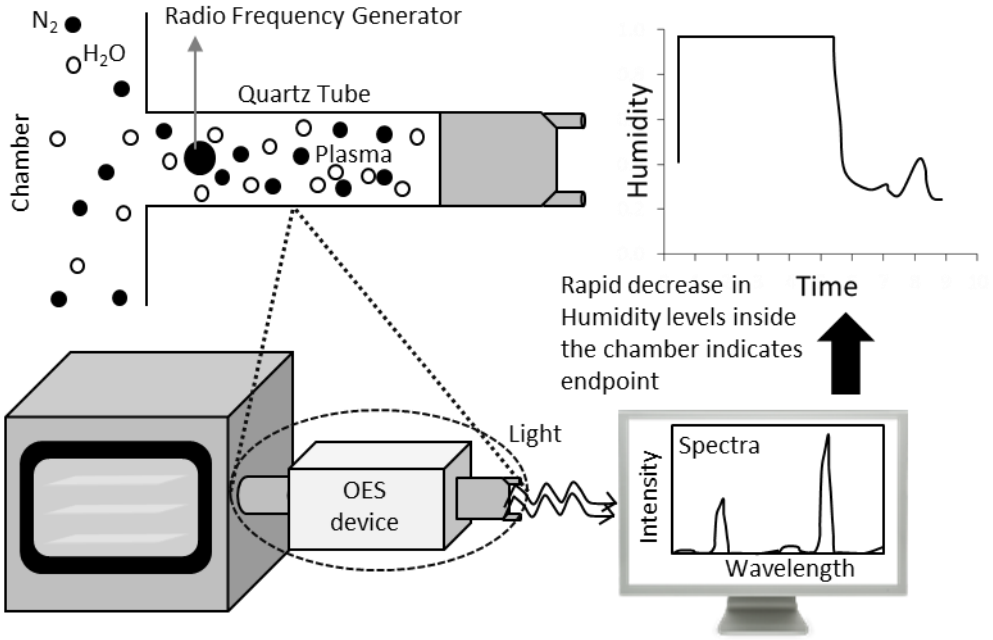

Figure 15: LyoTrack based on Optical Emission Spectroscopy for the determination of the primary drying endpoint. Adapted from Mayeresse et al. (2007)

Windmill

The windmill sensor is used to measure the flow of water vapor from the drying chamber to condenser (Tenedini and Jr. Bart 2001). Although a decrease in the vapour flow towards the end of primary drying indicates ice sublimation is complete, but the asymptote is only an approximation, being incapable of being sensitive to the true endpoint of the batch(Johnson, et al. 2009). Notwithstanding its poor sensitivity, Windmill has been tested at the manufacturing scale (Fissore, et al. 2018).

Tunable Diode Laser Absorption Spectroscopy (TDLAS)

TDLAS measures the water vapour composition profile in the duct connecting the drying chamber and the condenser (Figure 16) and can be used to determine a variety of parameters: vial heat transfer coefficient (K_v), batch average product temperature at the vial bottom (T_b), sublimation rate, primary drying and secondary drying endpoints, and dry layer resistance (R_p) (Fissore, et al. 2018). Typically, the TDLAS system comprises two diode laser beams that pass through the gas at an angle different from the direction of the vapour vapour (Figure 16a). The beam's wavelength is calibrated to the absorbance of the water vapour, from where the average concentration of water vapour per unit volume is determined by the amount of light absorbed at the wavelength characteristic of water absorption (Fissore, et al. 2018; Nail, et al. 2017).

Gieiseler et al. compared the sublimation rate determined gravimetrically and the vapour flow rate from TDLAS and found very good agreement between the two estimates for pure ice and 5 %w/w Mannitol-based formulations at the laboratory scale (Gieseler, et al. 2007). In the same study, TDLAS was applied to determine the K_v value for the batch, which first requires one to determine the sublimation rate and the batch average product temperature determined separately from thermocouples (Gieseler, et al. 2007). Alternatively, TDLAS has been proposed for the estimation of the batch average product temperature. This requires one to obtain K_v at different chamber pressures for pure ice. Once the K_v value is known, the batch average temperature can be determined for any

other lyophilization cycle (Kuu, et al. 2006). In one study, an agreement within 1-2 °C between the average product temperature measured with thermocouples and the one estimated from TDLAS was reported (Schneid, Stefan C., et al. 2009) . Further, TDLAS has been used for determining R_p from the knowledge of either (i) sublimation rate; (ii) product temperature or both. A simpler configuration of the instrument involving a single laser can also be used for the determination of the primary drying endpoint (Kuu, et al. 2011). TDLAS has also been to comparative pressure measurement for the monitoring of the evolution of vapour flow rate and vapour concentration to determine the primary drying endpoint (Patel and Pikal 2009). An example is presented in Figure 16(b to d) which shows that the signal of the water vapour concentration starts to decrease at the point which corresponds to (i) vapour flow rate from TDLAS is being approximately zero; (ii) the onset of the reduction in the Pirani pressure; (iii) a sharp increase in the product temperature registered by the thermocouple (Fissore, et al. 2018). This is generally assumed to be the point when the sublimation is almost complete.

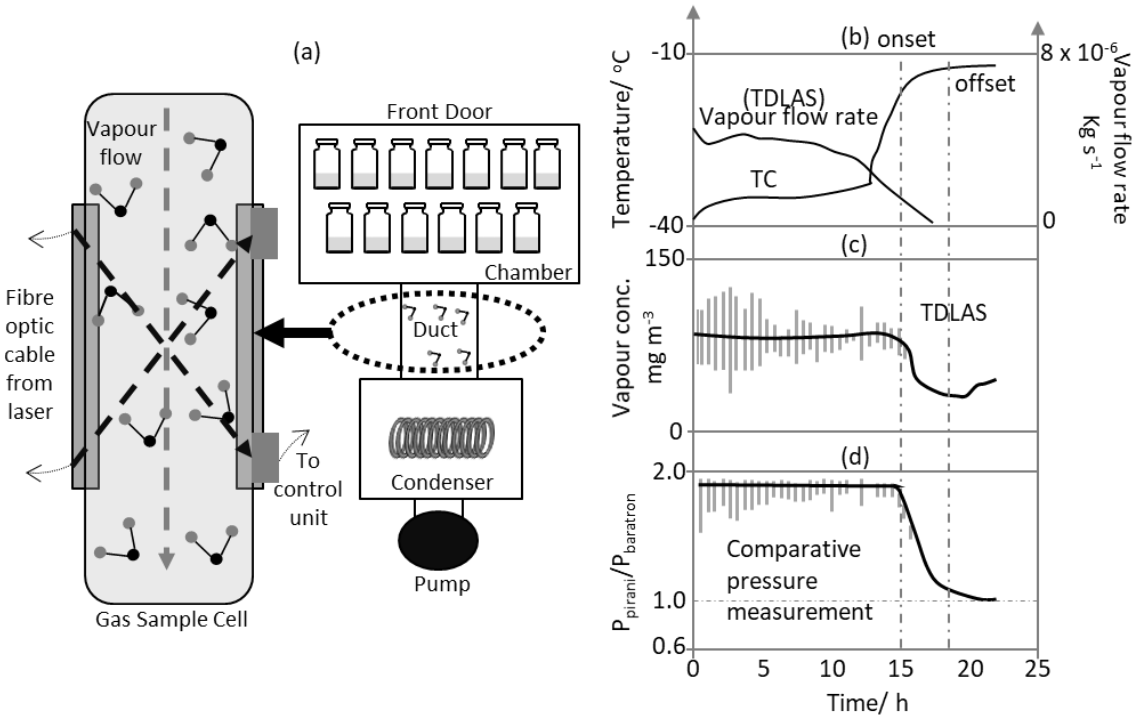

Figure 16: Tunable Diode Laser Absorption Spectroscopy instrument for the determination of the endpoint. Plots (a to c) have been reproduced from Fissore et al. (Fissore, et al. 2018)

There are a number of drawbacks of this TDLAS for its application in freeze-drying. First, TDLAS requires a freeze dryer with a sufficiently long duct between the chamber and the condenser so that the angle of the lasers can be significantly different from the direction of the vapour flow; but not all freeze dryers have the capability (Fissore, et al. 2018). Second, during steam sterilisation, the optical alignment of the sensor can drift thereby resulting in erroneous estimations of the mass flow rate (Fissore, et al. 2018; Nail, et al. 2017). Third, at the laboratory scale, the estimated value of the sublimation rate from TDLAS has been reported to agree within 5-7 % from that determined from a gravimetric measurement of the total water removed. However, this reasonable agreement translates to a discrepancy of up to 25 % at the manufacturing scale, which has been ascribed to the fluid velocity used for calculating the mass flow rate (Fissore, et al. 2018; Nail, et al. 2017).

1.4.3 Summary of Process Analytical Technologies

The main features of all the PAT tools described in this chapter are given in Table 3; the main features being (i) monitoring of phase behaviour and product temperature; (ii) determination of sublimation rate, primary drying endpoint, and moisture content; (iii) sterilisability; and (iv) compatibility with automated loading systems.

Since the introduction of the US Food and Drugs Administration (FDA) Process Analytical Technology (PAT) initiative in 2003 (FDA 2004) there has been much interest in the development of in-line measurement techniques for freeze-drying process development. These technologies have been comprehensively reviewed in the literature (Fissore, et al. 2018; Nail, et al. 2017; Patel and Pikal 2009). In-line Near IR and Raman Spectroscopy are very powerful techniques which provide a wide range of critical information (e.g. solid state evolution of the product during the freeze drying process). However, complex data analysis coupled with their nascency in freeze-drying process control renders them the tools to look out for in the future. The use of the freeze drying microbalance to determine the sublimation rate of an individual vial has been discussed. The method involves a disruption of the vial packing and subsequently an interruption to the process from a brief but repeated lifting of the vial from the heat source, i.e. shelf (Roth, et al. 2001). Both factors could easily result in a change to the drying process.

The most prevalent single vial monitoring techniques for product temperature measurement and the primary drying endpoint determination are the thermocouples and resistance temperature detectors (RTDs) (Nail and Johnson 1992) though more recently, there has been more widespread adoption of the wireless Temperature Remote Interrogation System (TEMPRIS®) (Schneid and Gieseler 2008). On the fringe of these technologies, in terms of adoption/usage rates, are the invasive Fibre Bragg Grating (FBGs) optical sensors, which are based on the measurement of the refractive index as a function of temperature and are more sensitive and responsive than the conventional thermocouples and RTDs (Kasper, et al. 2013).

All these technologies involve the insertion of a probe into the product to measure its ‘point’

temperature during the freeze drying cycle, more specifically the ice solidification endpoint being taken from the product temperature equilibrating with the shelf temperature at the end of the freezing stage; and the sublimation end point being taken from the product temperature increasing towards that of the shelf temperature as the process of sublimative cooling ends (Nail and Johnson 1992). However, a lack of representativeness in relation to the vials in the vicinity and the batch in general due to atypical freezing and sublimation kinetics is the main drawback of product-invasive probes (Nail, et al. 2017). This warrants the introduction of a soak period during primary drying to ensure all the ice has been removed (Tang and Pikal 2004).

The issues with these product-invasive probes has stimulated the development of non-product invasive, individual-vial sensors such as plasma-sputtered thermocouples deposited externally to the glass vial (Parvis, et al. 2012), the Bragg-grating sensors embedded in the shelf (Kasper, et al. 2013), soft sensors that utilise mathematical modelling to estimate in-line any variable (e.g. T_i, K_v, R_p) when combined with a prior knowledge of the product temperature from an invasive or non-invasive temperature sensor (Bosca, et al. 2014). However, at least for the freezing stage, the solidification endpoint is still taken as the point when the product temperature reaches that of the shelf temperature, though the ice nucleation onset itself is not impacted

The use of heat flux sensors has also been discussed. These utilise non-invasive thermocouple arrays that measure the heat flux from the shelf to the vial bottom, thereby being able to monitor the freezing kinetics (ice nucleation); and with the knowledge of the vial heat transfer coefficient, they can monitor the product temperature during primary drying and determine the primary drying endpoint (Chen, et al. 2008). However, these require careful positioning of the vial on the heat flux sensor to maintain a good thermal contact. Besides, the primary drying times obtained from heat flux monitoring have been reported to be shorter than those indicated by comparative pressure measurement (Vollrath, et al. 2017). Finally, Infrared thermography involving a novel IR camera system has been recently introduced by Fissore et al. which utilises a mechanistic model developed by Velardi et al. (2008) to predict the dry layer resistance at the end of the freezing process, thereby being able to

predict the primary drying time and the product temperature (Lietta, et al. 2019). The monitoring of the evolution of the temperature gradient and freezing front rate is also possible, which allow for the prediction of the ice crystal size distribution (Colucci, et al. 2019).

Another non-invasive technique is Through-Vial Impedance Spectroscopy (TVIS) introduced by Smith et al. which utilises electrodes attached externally to the glass wall (Smith, et al. 2013; Smith and Polygalov 2019), thereby being able to (i) monitor phase behaviour during the freezing stage such as ice nucleation onset and perhaps of equal importance, the ice solidification endpoint using a parameter which has almost no temperature dependence and is thus not sensitive to the release of the heat of crystallisation unlike a temperature sensor (Smith and Jeeraruangrattana 2019); (ii) assess the impact of annealing on the ice crystal structure and the subsequent primary drying time (Smith, et al. 2014); (iii) predict non-invasively, the product temperature at the sublimation interface and at the vial bottom during steady state primary drying and determine sublimation rate and vial heat transfer coefficient (Smith, et al. 2018).

All these non-invasive vial measurement techniques require either special vials or special shelves in order to perform measurements. Nevertheless, one common feature of all the single vial monitoring techniques is that they can provide an insight into the inter-vial variability in the critical process parameters and hence serve as invaluable tools for research in the early stages of process development. However, all of them require manual operation and are not compatible with the automatic vial loading and stoppering systems. Moreover, many of the vial techniques are not able to withstand sterilization (Fissore, et al. 2018). These requirements strongly limit their application at the manufacturing scale, which brings one to the application of batch monitoring techniques for freeze drying process control.

In general, the majority of the batch measurement tools are more readily applicable to larger scale sterile GMP freeze-drying than the vial monitoring techniques owing to their feasible scale-up without necessitating the need for manual operation, and other advantages such as being steam sterilizable and compatible with automated vial loading and stoppering systems (Fissore, et al. 2018;

Nail, et al. 2017). Despite the issues surrounding sterilisability and the performance of the Pirani gauge, the use of Pirani gauge in conjunction with the Capacitance Manometer (comparative pressure measurement) stands out as the most common method for the determination of the primary drying endpoint as far as the cost/performance ratio is concerned (Fissore, et al. 2018). Further, the dew point sensor and Lyotrack (cold plasma ionization device) are also used for the determination of the chamber gas composition, but not more sensitive than the Pirani, thereby providing one no significant advantage over the comparative pressure measurement method (Patel, et al. 2010). Besides, both dew point and cold plasma sensors are more expensive and have drawbacks such as the dew point sensor being extremely sensitive to the moisture (Roy and Pikal 1989), particularly the water vapour desorbed from the chamber walls (Fissore, et al. 2018); and the cold plasma detector being slow in response time, with the measurement being impacted by probe location and also carrying with it, a risk of ionization of the chamber gas (Hottot, et al. 2009; Mayeresse, et al. 2007). Besides, the quadruple mass spectrometer (QMS) is another device based on gas composition that is more applicable to the secondary drying stage. QMS is very expensive, has a long response time at low pressure and has issues with the stability of the baseline during primary drying, thereby introducing uncertainties in primary drying endpoint detection (Barresi, et al. 2009; Fissore, et al. 2018).

Some of the other batch sensors such as PRT, TDLAS are able to monitor the sublimation rate, moisture content and product temperature in addition to primary drying and secondary drying endpoints (Gieseler, et al. 2007; Milton, et al. 1997). However, the obtained value is a batch average, which cannot account for vial to vial non-uniformity. Besides, PRT causes a rise in the product temperature during the valve closure and also loses sensitivity during the terminal stages of primary drying when the water vapour pressure substantially low.

A common drawback of all these sensors is that they cannot determine the true endpoint of the batch, meaning the exact point when the last vestiges of ice sublimates from the batch. In practice, the midpoint point of their response curve (except for PRT) is frequently used an indicator of the point when ice sublimation is “essentially” complete as illustrated in Figure 17, although it is assumed that

the offset point should correspond to the true endpoint of the batch (Patel, et al. 2010). However, the observed offset value may could also be attributed to either a drift in the baseline of the sensor or the presence of residual water vapour trapped in the chamber (Fissore, et al. 2018). It follows even these methods will require an additional soak period to ensure 100 % ice sublimation before one switches to the secondary drying stage.

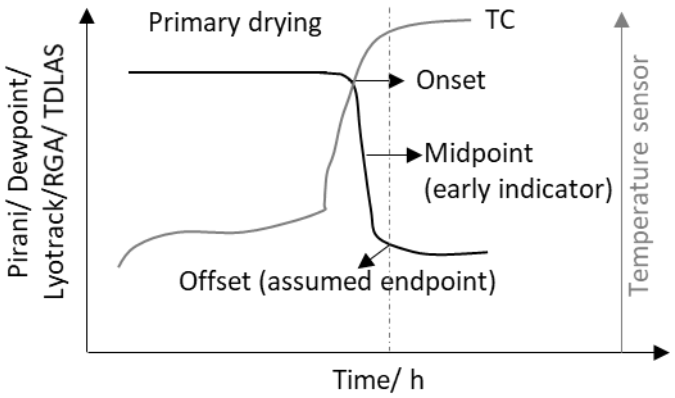

Figure 17: Determination of Primary drying Endpoint: batch v/s single vial

Table 3: Summary of PAT tools and their main features for freeze drying process control

	In-line PAT	Measurement Principle	Ice Nucleation onset	Ice solidification endpoint	Product Temperature	Primary Drying Endpoint	Product Moisture	Feasible Scale-Up	Sterilisability	Compatibility with automated loading systems
Single vial monitoring	Microbalance	Mass loss	No	No	No	No	Yes	No[1]	No	No
	TC and RTDs	Product temperature	Yes	No	Yes	Yes	No	No	No	No
	TEMPRIS	Product temperature	Yes	No	Yes	Yes	No	Yes	Yes	Yes
	Plasma Sputtered Thermocouples	Product temperature	Yes	No	Yes	Yes	No	No	No	No
	Invasive or Non-invasive Optical FBGs	Product temperature	Yes	No	Yes	Yes	No	No	No	No
	Heat Flux Monitors	Heat flow from the shelf to the product	Yes	No	Yes	Yes	No	No	No	No
	Soft Sensors	Product temperature	Yes	No	Yes	Yes	No	Yes	Yes	Yes
	Infrared Camera	Product temperature	Yes	No	Yes	Yes	No	No	No	No
	TVIS	Capacitance	Yes	Yes	Yes	Yes	No	No	No	No
	Near IR/ Raman Spectroscopy	Absorption of radiation (NIR)/Inelastic scattering (Raman) of radiation by product	Yes	Yes	No	Yes (NIR)/ No (Raman)	Yes	No[1]	No	No
	Photographic data	Visual observation of sublimation front	Yes	No	No	No	No	No[1]	Yes	No
Batch Monitoring	Pirani/CM	Water pressure (Pirani) v/s absolute pressure (CM) in the chamber	No	No	No	Yes	No	Yes	Yes and No (depends on the make)	Yes
	Condenser Pressure	Increase in Nitrogen pressure	No	No	No	Yes	No	No[2]	Yes	Yes
	Dew Point	Relative humidity	No	No	No	Yes	No	Yes[3]	Yes[2]	Yes
	Pressure Rise Tests (e.g. MTM)	Rise in absolute chamber pressure	No	No	Yes[4]	Yes	Yes[4]	No[2,5]	Yes	Yes
	Lyotrack (Cold Plasma)	Composition of chamber gas	No	No	No	Yes	Yes[4]	Yes	Yes	Yes
	Residual Gas Analyser (QMS)	Composition of chamber gas	No	No	No	Yes	Yes[4]	Yes	Yes[2]	Yes
	Windmill	Water vapour flow	No	No	No	Yes	No	No[2]	Yes	Yes
	(TDLAS)	Gas composition and flow	No	No	Yes[4]	Yes	Yes	No[2]	Yes	Yes

[1]requires line of sight of samples, [2]condenser external to chamber, [3]additional isolation, [4]batch average, [5]requires fast closing valve

1.5 Through Vial Impedance Spectroscopy

TVIS measures the electrical impedance of the product, contained within a standard freeze-drying vial that has been modified with electrodes placed on the outside of the glass wall (Smith and Polygalov 2019). TVIS has several advantages over the existing single vial PATs (viz. thermocouple and microbalances) (Smith, et al. 2017):

- the measurement electrodes are product non-invasive (unlike a thermocouple) which means that the system will not interfere with the processes of ice nucleation and growth.
- The measurement hardware has minimal thermal mass and volume (unlike the microbalance) which means that the impact on heat transfer is minimised whilst allowing the arrangement of TVIS vials in the usual hexagonal array.
- The TVIS instrument possesses multiple channels which enables the placement of TVIS vials at different positions across the shelf, as shown in Figure 18. This feature, in turn, could potentially be applied in the spatial mapping of the shelf providing information about the temperature distribution and the variations in the drying rates during the process.

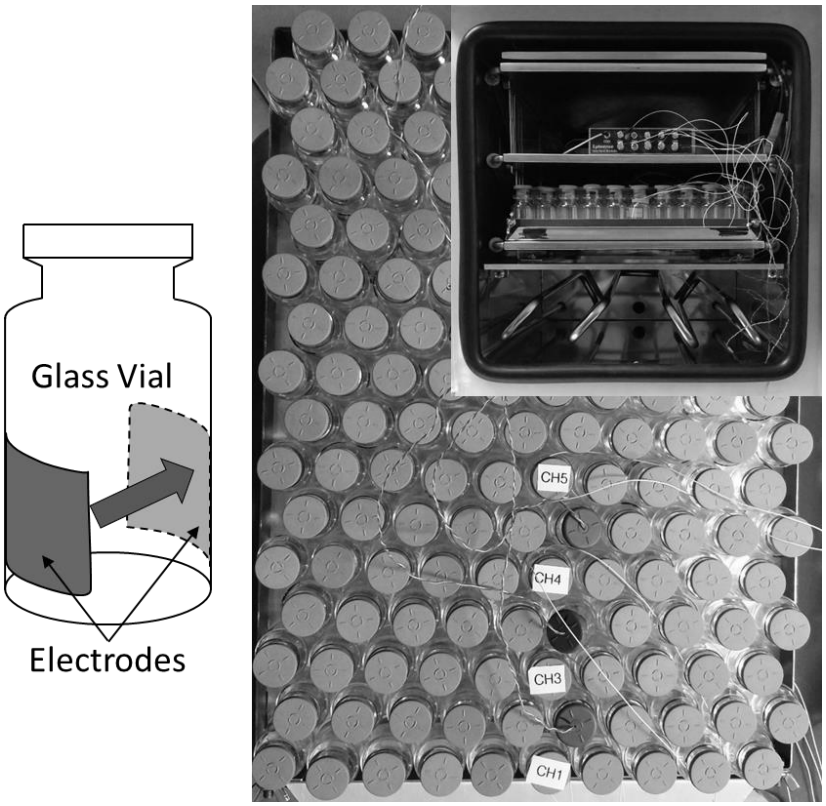

Figure 18: Demonstration of the placement of TVIS measurement vials in various locations of the shelf without perturbing the normal hexagonal arrangement of the vials on the shelf.

1.5.1 Description of the Measurement System

The details of the TVIS systems have been described comprehensively in a previous publication (Smith and Polygalov 2019). The majority of the data presented in the following chapter has been undertaken on a Virtis Advantage Plus laboratory freeze-dryer equipped with a five-channel TVIS system as shown in Figure 19(a). In brief, the TVIS system comprises:

- a bespoke five-channel impedance spectrometer placed externally to the dryer (Figure 19b)
- a passthrough mounted on one of the rubber manifolds of the freeze dryer (Figure 19c)
- a junction box, placed inside the dryer, usually on the top shelf (Figure 19d)
- a TVIS vial placed on the bottom shelf of the freeze dryer (Figure 19d)
- LyoDEA® real time monitoring software (Figure 19e) and LyoView™ analytical software (Figure 19f)

Co-axial cables take the stimulating voltage from the impedance spectrometer to the junction box via the passthrough. Inside the junction box, a splitter feeds the voltage simultaneously to 5 stimulating ports on the junction box in the top row. The TVIS vial comprises a pair of fine coaxial cables, one of which is connected to one of the stimulating ports of the junction boxes, and the other is connected to the corresponding sensing port in the bottom row of the junction box. The signals from the five sensing ports are then taken back to the impedance spectrometer, where the voltage is converted into current. The stimulating voltage and the resultant current are then compared to determine the impedance of the TVIS vial (and its contents).

To date, the majority of the studies have been undertaken on Type 1 glass vial (nominal capacity 10 mL) with a single pair of electrodes, 5 mm in height, each surrounded by a guard electrode) (Arshad, et al. 2014; Smith, et al. 2013; Smith, et al. 2013; Smith, et al. 2014; Smith, et al. 2014a; Smith, et al. 2017). In the following chapters, the data has been generated using Type I glass vials (nominal capacity 10 mL) with a single pair of electrodes, 10 mm in height, but without the guard electrode. This is exemplified in Figure 20, where two TVIS vials are shown, one connected to channel 3 and other to channel 4 of the junction box. The electrodes are formed from a 19 mm wide copper adhesive tape (1181 3M^{TM}) that consists of a soft copper foil backing (0.04 mm) and an electrically conductive pressure-sensitive acrylic adhesive (0.026 mm) attached to the outer wall of the vial.

(a) Virtis Advantage Plus freeze dryer with TVIS system

(b) Five-channel impedance spectrometer

(c) Passthrough

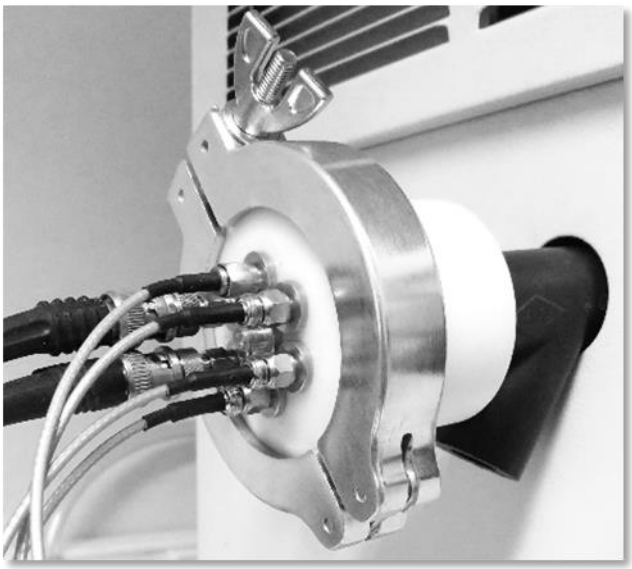

(d) TVIS vial connected to junction box

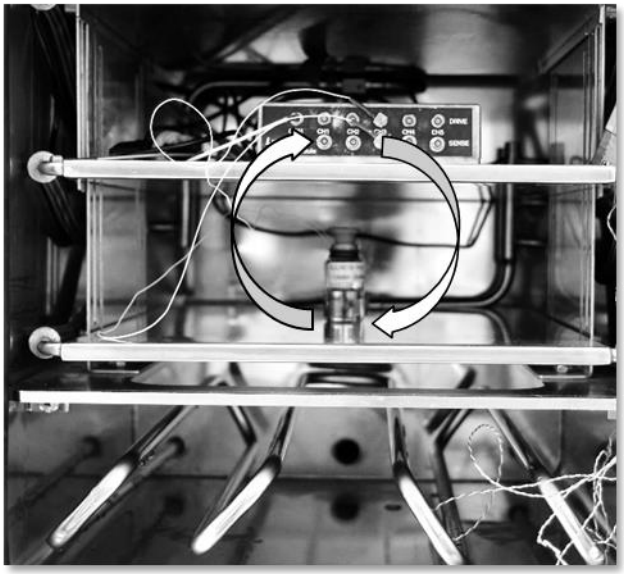

(e) LyoDEA™ monitoring software

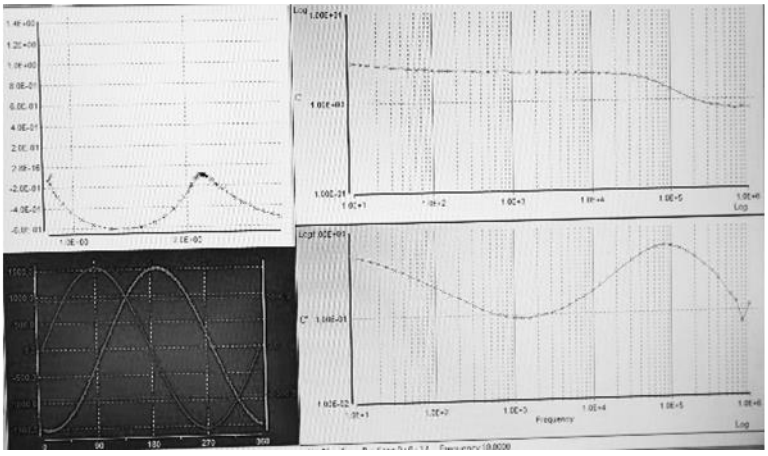

(f) LyoView™ Analytical Software

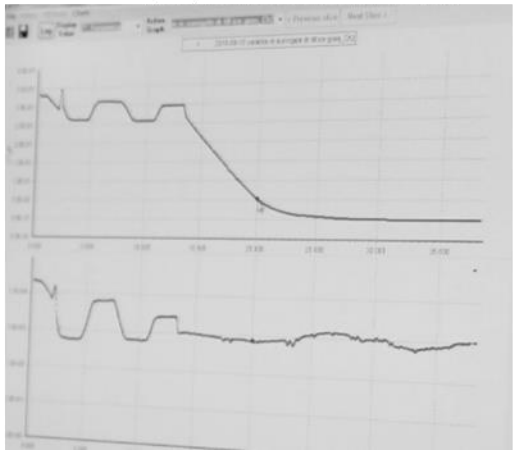

Figure 19: TVIS system for freeze-drying process development

Figure 20: TVIS vials connected to the junction box via the stimulating ports (top row) and the sensing ports (bottom row). Other nearest neighbour vials contain a thermocouple.

1.5.2 Measurement Principles

The electrical impedance of an object (e.g. glass vial and its contents) defines the total opposition to the flow of current when a sinusoidal alternating voltage is applied. On the application of a voltage in the frequency range 10 Hz to 1 MHz, the TVIS system generates an electrical impedance spectrum, which when expressed in terms of electrical capacitance, results in a step in the real part (dielectric storage) and a peak in the imaginary part (dielectric loss) (Smith and Polygalov 2019). For frozen water (ice), the dielectric loss peak and the step are positioned within the mid-range (~1 kHz) of the measured frequency range (10 Hz to 1 MHz). However, the exact position of the peak and its height depends on the physical state of the sample (liquid or frozen state) at any point during the freeze-drying process, the temperature of the sample in that phase and the height of the frozen layer within the region bounded by the electrodes on the outside of the vial. In other words, the progression of the freeze-drying cycle and the changes in the condition of the sample manifest as the changes in these electrical parameters of the sample being freeze-dried.

Figure 21 shows example spectra for the TVIS vial (Adelphi VC010-20C of nominal volume 10 mL) containing 3 g of double distilled water at 20 °C and 3.5 g of frozen water (ice at -20 °C). The capacitance spectra (bode plots of real and imaginary capacitance plotted against log frequency) illustrate how the position of the peak imaginary amplitude, $\boldsymbol{C''_{PEAK}}$, and the peak frequency, $\boldsymbol{F_{PEAK}}$ of the dielectric loss peak in the imaginary capacitance spectrum, and the step height ($\Delta C'$) and the value of the high frequency capacitance, $C'(\infty)$, in the real capacitance spectrum, change with those same transitions. It is evident that the peak for water contained in the TVIS vial shifts from ~25 kHz to a lower frequency (i.e. ~500 Hz) in the liquid state. A dramatic decrease in the magnitude of $C'(\infty)$ is also observed at the low temperature.

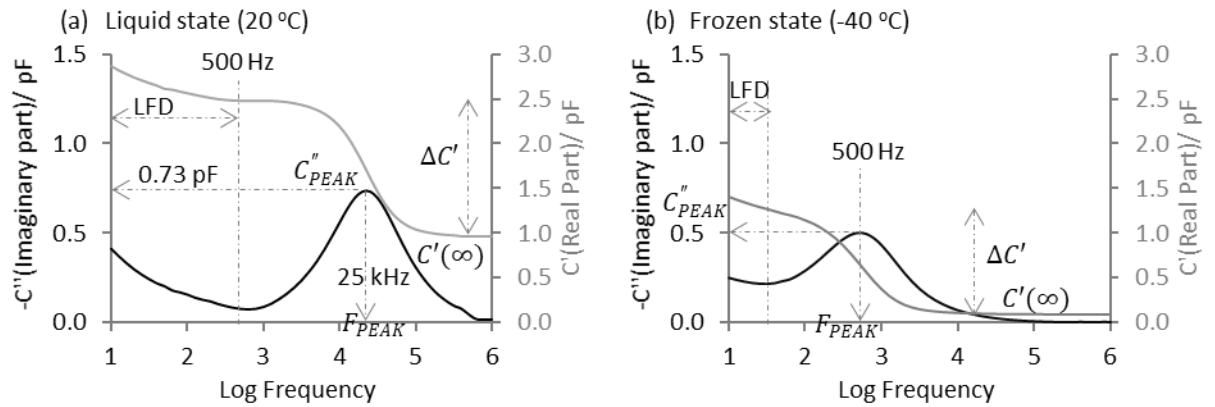

Figure 21: (a) Capacitance spectrum of 3 mL double distilled water at 20 °C in an Adelphi VC010-20C Type I glass tubing vial with a pair of electrodes (10 mm by 19 mm) attached externally to the glass wall at a distance of 3 mm from the vial base; (b) Capacitance spectrum of the same vial containing water but frozen to -20 °C; C' is the dielectric storage and C'' is the dielectric loss components of the complex capacitance, respectively. The vertical dot dashed line at the low frequency end of the spectrum, which reflects charge percolation through the porous glass microstructure. As consequence both the real and imaginary part capacitance increase with decrease in the frequency.

Furthermore, in the low frequency region of the capacitance spectrum (up to ~1 kHz) the magnitude of the real part and the imaginary part capacitance increase as the frequency decreases (Figure 21). This is due to charge percolation or space charge polarization through the porous glass microstructure. The low frequency response of the glass wall is often referred to as **Low Frequency Dispersion** (LFD). It must be stressed that the underlying mechanism behind the step and the peak in the real and imaginary part of the capacitance spectrum are not related to the dielectric properties of the liquid. For example, the dielectric permittivity of water remains constant in the frequency range 10 Hz to 10 MHz. In fact, the frequency dependent response of the composite object is attributed to the Maxwell-Wagner polarization of the glass wall, which is described in the next section.

1.5.2.1 Maxwell-Wagner Polarization of the Glass Wall in the Liquid State

In the case of a simple liquid like water, the step and the peak in the real and imaginary part, respectively, are due to a Maxwell-Wagner (MW) polarization process, also referred to as space charge polarization or interfacial polarization. This is attributed to the migration of charge carriers in the relatively conductive liquid to the intimate boundary between the poorly conductive glass and the liquid (or the glass-liquid interface) when a static voltage (V), is applied to the composite object (glass wall and the liquid). Figure 22 illustrates the concept of charge accumulation at the glass-liquid interface in a static electric field. When a voltage is applied to the electrodes attached externally to the glass wall, current starts to flow and the glass wall starts to accumulate charge at a rate determined by the resistance and the capacitance of the liquid. In other words, the ion concentration determines the resistance and the polarization capacity of the dipoles and other molecules of the liquid determines the dielectric storage (liquid capacitance); both will impact amount the and therefore the rate of charge accumulation at the glass wall-liquid interface (Equation 11):

$$\tau = R_s\ (C_g + C_s) \qquad \text{Equation 11}$$

where τ is the time constant of charge accumulation at the glass wall interface (C_g), which is impacted by resistance (R_s) and the capacitance (C_s) of the liquid. Note that the bulk of the liquid electrically remains electrically neutral when oppositely charged carries migrate to the either side of the glass wall. In effect, the net charge at the glass-liquid interface is neutralized by the glass wall capacitance, thereby resulting in a voltage drop. The accumulation of charge at the glass-liquid interface is often referred to as “double layer capacitance”.

The mechanism of the MW process described above considers a static applied voltage. Actually, TVIS measurements are performed by applying an oscillating sinusoidal voltage: $V = V_0\ sin\ (\omega t)$ to measure current $I = I_0\ sin\ (\omega t\ +\ \varphi)$, where ω is the angular frequency in radians and φ is the phase difference between voltage and current. The phase difference for a pure resistor is zero, but it is equal to -90 °C for a pure capacitor, meaning voltage lags behind current by 90

°C. The ratio of V_0 and I_0 is termed Impedance Magnitude ($|Z|$), whereas the inverse is termed admittance (Υ).

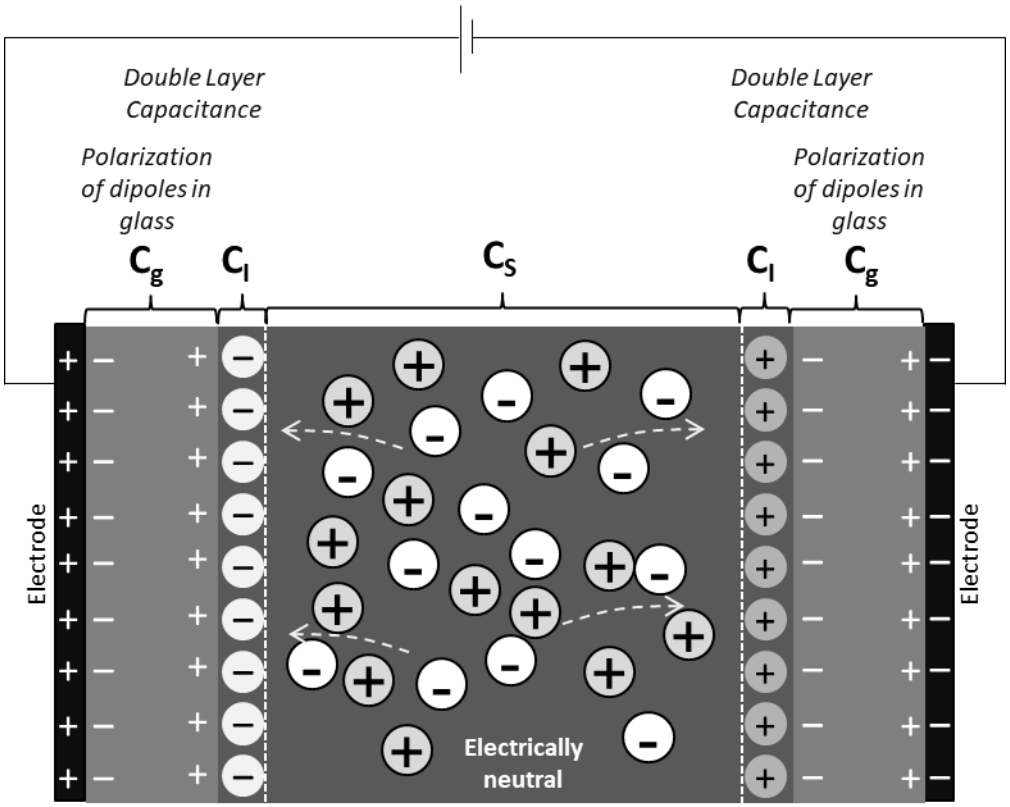

Figure 22: Maxwell-Wagner polarization of the glass wall in the liquid state. On application of an alternating voltage, charge carries in the liquid migrate to the glass-liquid interface, and the charge carries within the glass microstructure also polarise, leading to "double layer capacitance". C_g is the glass wall capacitance; C_i is the interfacial capacitance and C_s is the capacitance of the liquid, which also has a resistance. The net charge in the bulk is zero.

1.5.2.2 Dielectric Relaxation of Ice in the Frozen State

As water freezes to form ice, the dielectric loss peak shifts to a lower frequency. Figure 23 shows an example spectrum at -40 °C for frozen water contained in the TVIS vial. For ice, the electrical resistance is much higher and thus the MW peak shifts below the lower limit of the experimental frequency range (10 Hz to 1 MHz). The observed dielectric loss peak then, is due to dielectric relaxation of ice. The dielectric relaxation time of ice increases as the temperature is reduced and so the peak shifts to lower frequencies. The peak frequency (F_{PEAK}) therefore provides a surrogate measurement for the ice temperature (Figure 23).

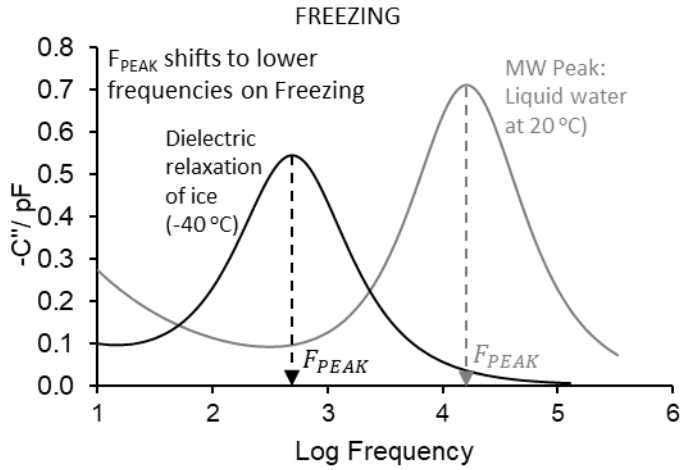

Figure 23: Two mechanisms underlying the observed dielectric loss peak in the imaginary part spectrum for water: Dielectric loss peak due to Maxwell-Wagner polarization peak in the liquid state (20 °C) and other due to dielectric relaxation of ice. An example of frozen spectrum taken at -40 °C is shown.

1.5.2.3 Equivalent Circuit Models for the TVIS spectrum for water in the liquid and in the frozen state

In order to explain the dielectric response of the object under test and rationalize its relationship with the physics of the system during freeze drying, an equivalent circuit model is used to model the TVIS spectrum. An equivalent circuit model comprises individual elements that model individual parts the observed shape/trajectory of the impedance spectrum as a function of applied frequency. For example, an insulator like the glass wall can be represented by a simple capacitor whereas a good conductor is represented by a resistor.

In the **liquid state** (Figure 24a), the electrical impedance of the object (glass vial and its contents) is represented by the solution capacitance C_S in parallel with the solution resistance R_S which together model the Maxwell-Wagner polarization in the glass-liquid interface in the high frequency end of the spectrum. The low frequency end of the spectrum then is represented by the glass wall capacitance, C_G in parallel with a constant phase element (CPE) that models the frequency dependent dispersive characteristics of the glass wall.

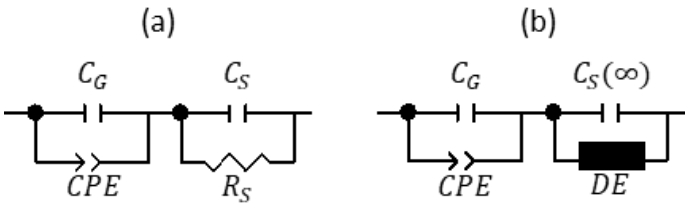

Figure 24: Equivalent circuit models for the TVIS spectrum for water contained in a TVIS vial: (a) In the liquid state, the impedance of the composite object (TVIS vial and the liquid) is represented by a parallel combination of the glass wall capacitance C_G and a CPE (which models the frequency dependent dispersive characteristics of the glass wall) which collectively model the low frequency end of the spectrum; whereas the high frequency end of the spectrum or the Maxwell-Wagner polarisation at the glass-liquid interface is represented by a parallel combination of the solution capacitance C_S and the solution resistance R_S. In the frozen state, the solutions capacitance takes on a frequency dependence such that it exhibits a step like decrease due to the dielectric relaxation of ice, which is can be modelled by a Cole Cole element (e.g. DE, Co) in parallel with the instantaneous solution capacitance $C_S(\infty)$. The low frequency end of the spectrum retails constant phase element behaviour, being modelled by the CPE in parallel with the glass wall capacitance C_G.

In the **frozen state**, the dielectric loss peak is due to the dielectric relaxation of the dipoles of water molecules within the ice crystal lattice. Dielectric relaxation of ice means that the solution capacitance is not constant over the experimental frequency range (10 Hz to 1 MHz) of the TVIS instrument. Actually, it takes on a frequency dependence, whereby the permittivity of frozen water (ice) changes from a value between 120 and 97 at low frequency (known as the static permittivity, ε_s of ice) to a value between 3.03 and 3.09 at high frequency (known as the instantaneous relative permittivity, ε_∞). The values of the static relative permittivity and the instantaneous relative permittivity are relevant in the freeze drying temperature range of interest (-70 °C to 0 °C).

Given the frequency dependent characteristics of the solution capacitance, the model in the frozen state for the TVIS spectrum at the high frequency end changes to a parallel combination of solution capacitance a Cole-Cole element, DE (which models dielectric relaxation) and C_∞ or instantaneous capacitance which now undergoes a step like change in the experimental frequency range of the TVIS instrument (10 Hz to 1 MHz). The low frequency end of the spectrum can still be represented by the glass wall capacitance C_G in parallel with a CPE. The model is shown in Figure 24(b).

It must be stressed that the low frequency dispersion observed for the glass wall is perturbing to the impedance spectrum in the sense that without the CPE, the low frequency dispersion can impact the spectrum up to frequencies as high as 10 kHz. In the context of freeze-drying, the glass wall is relevant to the estimation of the product temperature, given its close proximity to the product as shown by Velardi and Baresi (2008) and further studied by Fissore and co-workers (Colucci, et al. 2019; Lietta, et al. 2019). It follows that the understanding of the temperature dependency of the low frequency dispersive characteristics of the glass can allow for the development of an improved circuit model for the glass wall in the case of TVIS.

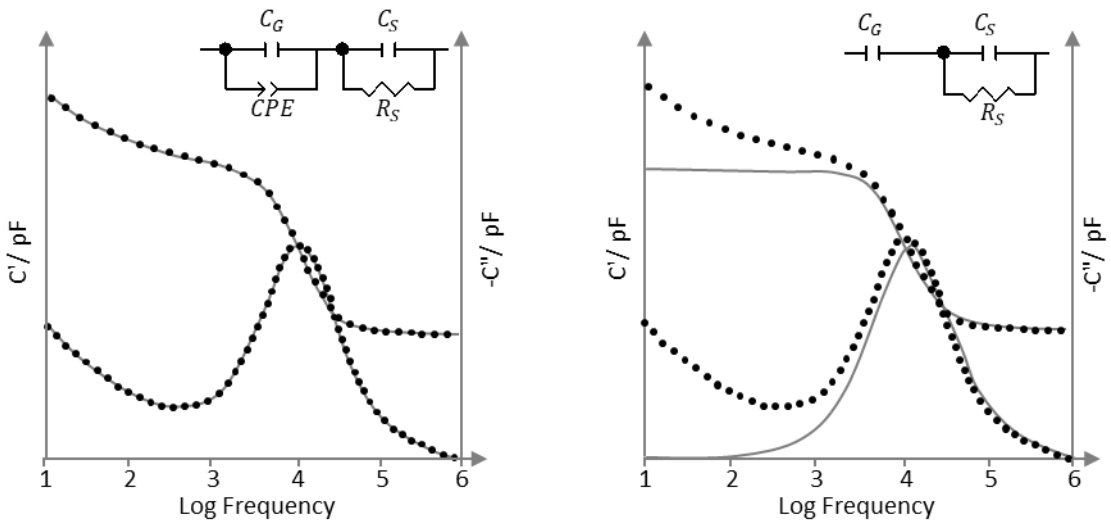

Figure 25: Illustration of the impact of the low frequency dispersion of the glass wall on the Maxwell-Wagner peak for water. Concept adopted from Smith et al. (2019).

1.5.2.4 Applications of TVIS parameters for Freeze Drying Monitoring

The various applications of TVIS have been mentioned previously (see the section on TVIS under Spectroscopic Methods for brief overview of all the developments). In this section, the key published methodologies pertaining to the prediction of the ice nucleation onset and ice solidification endpoint, product temperature and sublimation rate during primary drying and the primary drying endpoint have been conceptualized.

Ice Nucleation Onset and Ice Solidification Endpoint

The use of, $\boldsymbol{F_{PEAK}}$ and $\boldsymbol{C'(0.2MHz)}$ (or the real part capacitance measured at a frequency of 0.2 MHz) for the prediction of the ice nucleation temperature and the ice solidification endpoint respectively has been demonstrated previously (Smith and Jeeraruangrattana 2019). While $\boldsymbol{F_{PEAK}}$ has a strong positive temperature dependency, $\boldsymbol{C'(0.2MHz)}$ has a very low temperature coefficient, and therefore, it is largely sensitive to the time duration of ice solidification. As a result, the solidification endpoint predicted from $\boldsymbol{C'(0.2MHz)}$ occurs at some point before the one given by a thermocouple, which continues to sense the evolution of the heat of crystallization.

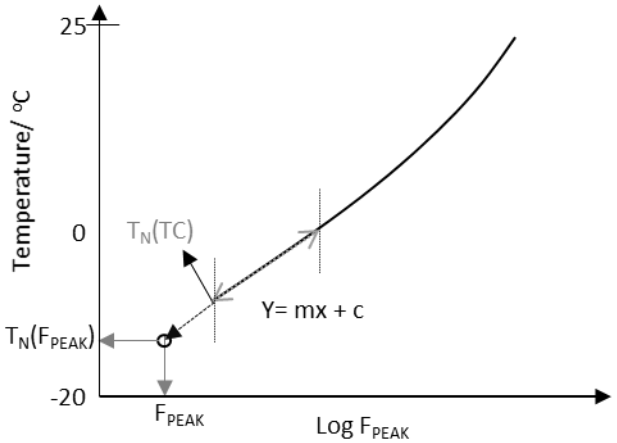

Figure 26: Use of $\boldsymbol{F_{PEAK}}$ and the ice nucleation temperature from a thermocouple to predict the Ice nucleation temperature $T_N(F_{PEAK})$ in the TVIS vial. Adapted from Smith and Jeeraruangrattana (2019).

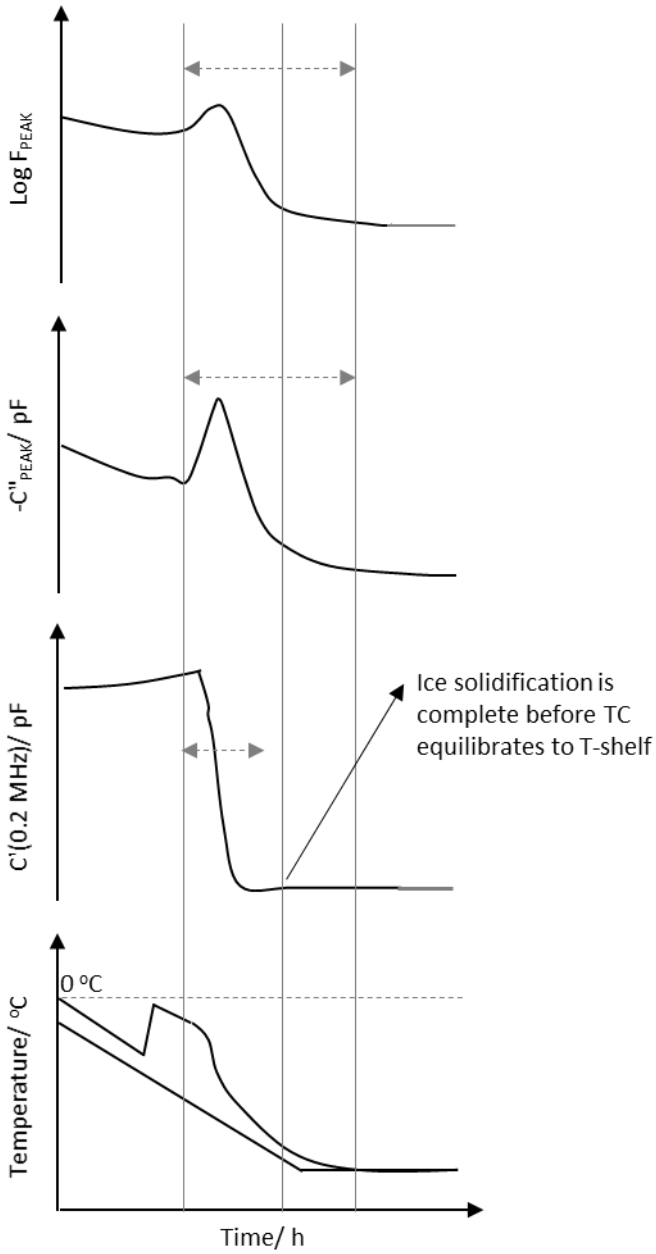

Figure 27: Sensitivity of TVIS parameters for the detection of ice solidification endpoint: The high frequency capacitance measured at 0.2 MHz or $\boldsymbol{C'(0.2MHz)}$ is a better indicator of the ice solidification endpoint than $\boldsymbol{C''_{PEAK}}$ and $\boldsymbol{F_{PEAK}}$ as well as the product temperature from a thermocouple, as all of them are sensitive to the release of heat; whereas $\boldsymbol{C'(0.2MHz)}$ has a very low temperature coefficient and is hence sensitive to the changes in the physical state of the sample. In this case it is the completion of the ice crystal growth. The concept has been adopted from from Smith and Jeeraruangrattana (Smith and Jeeraruangrattana 2019).

Prediction of Sublimation Rate and Product Temperature During Primary Drying

The peak frequency, $\boldsymbol{F_{PEAK}}$, provides a surrogate measurement of the ice temperature in primary drying because of its sensitivity to product temperature. The value of $\boldsymbol{F_{PEAK}}$ is most sensitive to the average temperature, i.e. at the midpoint of the ice cylinder bounded by the electrodes (known as the TVIS node). The method involves introducing a temperature cycling stage (of re-heating and re-cooling) once the ice has been frozen from the solution (Figure 28a) and then calibrating $\boldsymbol{F_{PEAK}}$ for temperature using the values of temperature obtained from a thermocouple in the nearest neighbour vial (Figure 28 b and c). The temperature coefficients from the temperature calibration curve and the values of $\boldsymbol{F_{PEAK}}$ measured during primary drying are then used to predict the product temperature in primary drying.

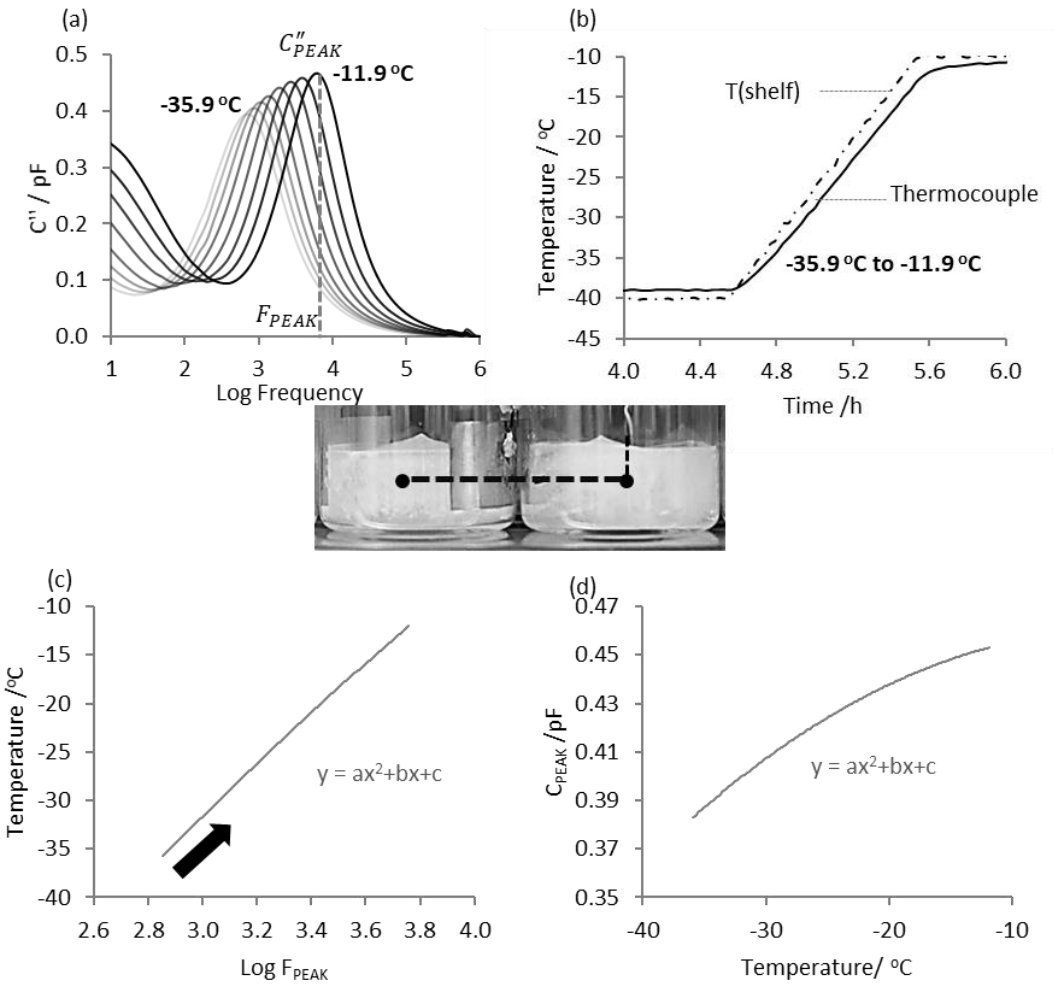

Figure 28: Methodology for Temperature calibration of $\boldsymbol{F_{PEAK}}$ during a re-heating ramp of a temperature cycling stage. The values of the ice temperature from a thermocouple in the nearest neighbor vial are plotted against the values of $\boldsymbol{F_{PEAK}}$ in the TVIS vial. The temperature coefficients and the values of $\boldsymbol{F_{PEAK}}$ during the primary drying stage are then used to predict the ice temperature during primary drying. The temperature dependency $\boldsymbol{C''_{PEAK}}$ is used to temperature compensate $\boldsymbol{C''_{PEAK}}$. The concept has been adopted from Smith et al. (2018) and the data correspond to 3 g of ice contained in an Adelphi VC010-20C vial of nominal volume 10 mL, with electrodes (10 mm by 19 mm) attached externally to the glass wall at a distance of 3 mm from the vial base.

The magnitude of $\boldsymbol{C''_{PEAK}}$ is sensitive to the ice mass in intimate contact with the glass wall in the region bounded by the electrodes (and therefore the ice cylinder height) During primary drying, when the height of the ice cylinder decreases(Figure 29a), the rate of decrease in $\boldsymbol{C''_{PEAK}}$ can be used as a surrogate for drying rate in primary drying. The methodology involves two stages: First, $\boldsymbol{C''_{PEAK}}$ is calibrated for ice cylinder height by constructing a calibration plot at a range of fill heights at a constant temperature (e.g. -20 °C) (Figure 29). Second, the temperature dependency of $\boldsymbol{C''_{PEAK}}$ (Figure 28d) obtained during a re-heating ramp of the temperature cycling stage (once the ice is frozen) is removed

(method not shown). That then allows for the prediction of the loss in height of the ice cylinder and therefore the loss in ice mass during primary drying. The loss in mass over a given period can then be used to obtain an estimate of the drying rate.

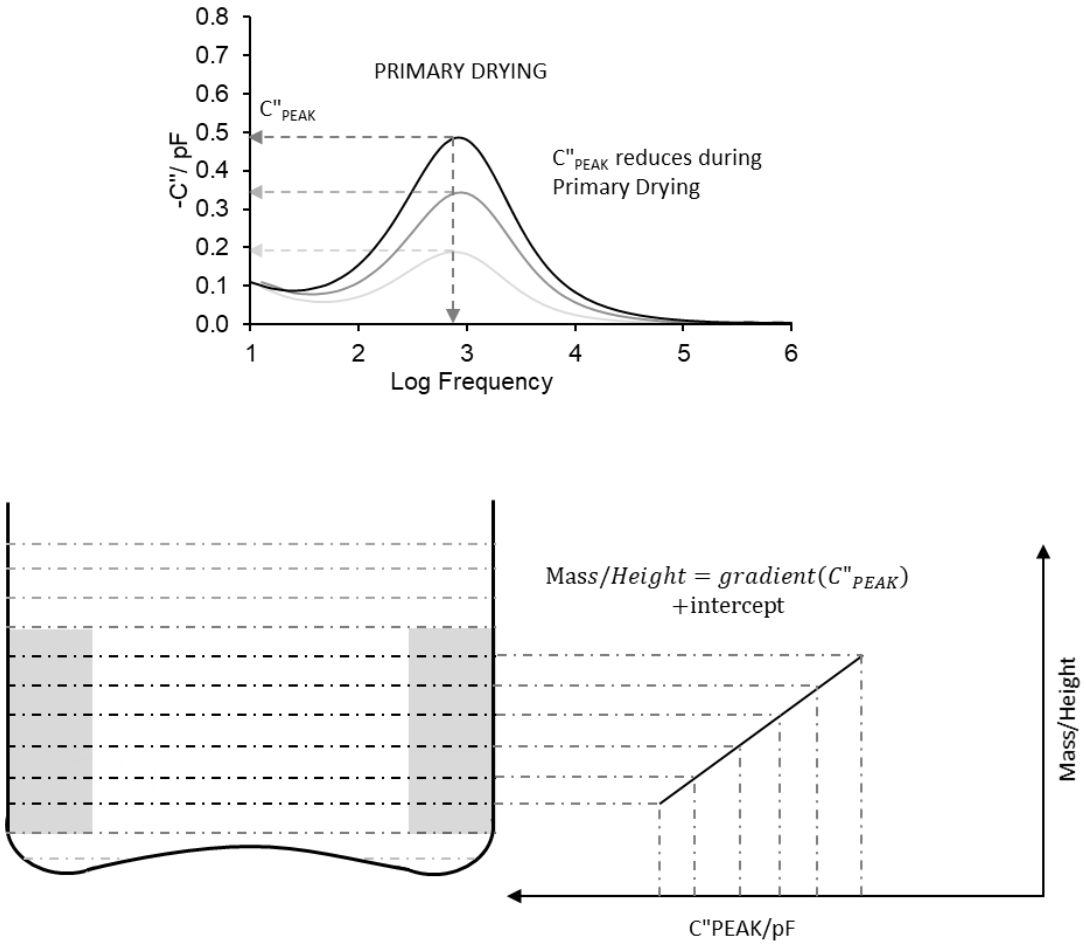

Figure 29: Sensitivity of $\boldsymbol{C''_{PEAK}}$ to the height of the ice cylinder in the region bounded by the electrodes. This feature is exploited to use the rate of change in the magnitude of $\boldsymbol{C''_{PEAK}}$ as a surrogate for the sublimation rate in the primary drying stage. The concept has adopted from Smith et al. (2018).

Primary Drying Endpoint Detection

Previously, Smith et al. (2013) used the time-lines of $\mathrm{d}(\mathrm{C'}_{1\mathrm{kHz}})/\mathrm{dt}$ (i.e. derivative of the real part capacitance measured at 1 kHz) and $\mathrm{d}(\mathrm{C"}_{1\mathrm{kHz}})/\mathrm{dt}$ (i.e. the derivative of the imaginary part capacitance measured at 1 kHz) for the estimation of the primary drying endpoint for a 2.5 % w/w sucrose solution. The methodology has been conceptualised in Figure 30, which shows the time-lines of $\mathrm{d}(\mathrm{C'}_{1\mathrm{kHz}})/\mathrm{dt}$ (plot a), $\mathrm{d}(\mathrm{C"}_{1\mathrm{kHz}})/\mathrm{dt}$ (plot b) and the product temperature from a thermocouple in the nearest neighbour vial at the bottom centre of the vial base (plot c). It was evidenced that the inflection in the magnitude $\mathrm{d}(\mathrm{C"}_{1\mathrm{kHz}})/\mathrm{dt}$ $\mathrm{d}(\mathrm{C'}_{1\mathrm{kHz}})/\mathrm{dt}$ coincided with the point when the product temperature value reached that of the shelf temperature. In contrast, the endpoint estimated by $\mathrm{d}(\mathrm{C'}_{1\mathrm{kHz}})/\mathrm{dt}$ occurred much earlier, indicating that the imaginary part capacitance at 1 kHz was more sensitive to the amount of ice in the vial.

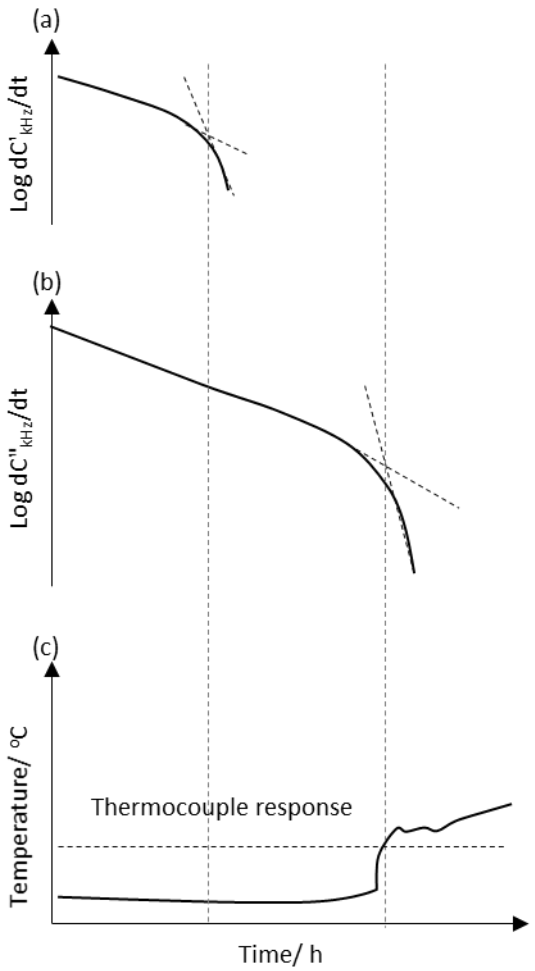

Figure 30: Use of the gradient of the log real part and log imaginary part capacitance measured at 1 kHz, $\mathrm{d}(\mathrm{C'_{1kHz}})/\mathrm{dt}$ an $\mathrm{d}(\mathrm{C"_{1kHz}})/\mathrm{dt}$, respectively, for the estimation of the primary drying endpoint for a 2.5 % sucrose solution contained in a TVIS vial with electrodes 5 mm in height and 18 mm in width, including a guard electrode. The concept has been illustrated using the method described by Smith et al. (2013): (a) primary drying timelines of log $\mathrm{d}(\mathrm{C'_{1kHz}})/\mathrm{dt}$; (b) log $\mathrm{d}(\mathrm{C"_{1kHz}})/\mathrm{dt}$; and (c) product temperature from a thermocouple at the bottom centre of the nearest neighbour vial.

2 Preface to the Experimental Work

The experimental chapters are devoted to the study of three applications of TVIS for freeze drying process development:

- Freezing, in particular, the ice nucleation onset and its influence on the stability of the ice microstructure
- Prediction of the primary drying endpoint
- Dielectric properties of the glass wall

Freezing

The first experimental study (Section 4) was undertaken to assess the impact of the ice nucleation temperature on the ice solidification endpoint and ultimately the stability of the ice crystal structures that result from different methods of freezing. It was found that the ice structures formed from controlled nucleation were more stable than that formed when the ice was allowed to form stochastically. Previously, it was shown that a change from a Maxwell-Wagner (MW) polarization process in the liquid state to a dielectric relaxation process in the frozen state (during ice formation) can be characterized using the time dependencies of the peak imaginary amplitude, $\boldsymbol{C''_{PEAK}}$, and the peak frequency, $\boldsymbol{F_{PEAK}}$, of the dielectric loss peak in the imaginary part (Smith and Jeeraruangrattana 2019). In effect, it is possible to determine the ice nucleation temperature for a simple system like water. However, for real systems (e.g. salt solutions) $\boldsymbol{C''_{PEAK}}$ is not a universal parameter for monitoring the ice nucleation process which is ascribed to the Maxwell-Wagner peak falling outside the experimental frequency range (10 Hz to 1 MHz) of the TVIS system. Nevertheless, it has been possible to use $\boldsymbol{F_{PEAK}}$ and $\boldsymbol{C'(0.2MHz)}$ (or the real part capacitance measured at a frequency of 0.2 MHz) for the prediction of the ice nucleation temperature and the ice solidification endpoint respectively (Smith and Jeeraruangrattana 2019). This is because, while $\boldsymbol{F_{PEAK}}$ has a strong positive temperature dependency, $\boldsymbol{C'(0.2MHz)}$ has a very low temperature coefficient, and therefore, it is

largely sensitive to the time duration of ice solidification. As a result, the solidification endpoint predicted from $\boldsymbol{C'(0.2MHz)}$ occurs at some point before the one given by a thermocouple, which continues to sense the evolution of the heat of crystallization.

Once the sample is in the frozen state, then the applications of $\boldsymbol{F_{PEAK}}$ and $\boldsymbol{C''_{PEAK}}$ become important because $\boldsymbol{F_{PEAK}}$ is employed in the prediction of the product temperature, $T(F_{PEAK})$ during primary drying, using a temperature calibration of $\boldsymbol{F_{PEAK}}$ during a re-heating ramp; whereas $\boldsymbol{C''_{PEAK}}$ has been shown to be sensitive to the amount of ice in the vial, which, when calibrated for ice mass, can then be used for determining the sublimation rate. However, it is first necessary to compensate $\boldsymbol{C''_{PEAK}}$ for temperature, which has been shown to change by ~4 % in the temperature range -40 °C to -20 °C (Smith, et al. 2018).

Unlike the studies on the bulk dielectric properties of ice involving a single electrode-ice interface (Johari 1976; Johari and Whalley 1981; Popov, et al. 2017), the properties of the dielectric relaxation process measured by TVIS are impacted by the inclusion of an additional glass-ice interface due to the glass wall, forming an electric double layer akin to a system with ion blocking electrodes (Orazem and Tribollet 2017). The impact of the glass wall is such that the measured relaxation process is smaller in height and is shifted to higher frequencies (Smith and Polygalov 2019).

It is also well established that the dielectric relaxation of ice occurs via two types of mechanisms of charge propagation depending on the temperature: the L-D orientation defects and the ionic (H_3O^+ and OH^- pairs) defects (Popov, et al. 2017), the relative proportions of which are likely to depend on the structural stability of the ice crystal lattice, which in turn is dependent on the way ice forms. Previously, the mechanisms for ice re-structuring on annealing of a 10 %w/w Maltodextrin were unraveled by developing an equivalent circuit model and using resistance as a parameter for studying the ice crystal stability. In this work, the unique sensitivity of the $\boldsymbol{C''_{PEAK}}$ parameter to the micro-structural features of the ice has been exploited.

Primary Drying Endpoint

Previously (Smith, et al. 2013) the log of the derivative of the real and the imaginary part capacitances at 1 kHz, i.e. $\log \mathrm{d}(\mathrm{C}'_{1\mathrm{kHz}})/\mathrm{dt}$ and $\log \mathrm{d}(\mathrm{C}''_{1\mathrm{kHz}})/\mathrm{dt}$ were investigated in an application for determining the primary drying endpoint (for the particular example of a 2.5% sucrose solution). Note that the electrode system used in that study was designed with a 5 mm (high) and 19 mm (wide) electrode surrounded by a guard electrode. The conclusion then was that a downward inflection in the time-line of $\log \mathrm{d}(\mathrm{C}''_{1\mathrm{kHz}})/\mathrm{dt}$ was thought to be an indicator of the primary drying endpoint, as it coincided with the time point at which the thermocouple temperature experienced a step-like increase in value which increased above the shelf temperature (see Fig. 14 in ref. Smith et al. (2013)). On reflection, given the dramatic step in the thermocouple temperature, rather than a gradual increase towards the shelf temperature, it must be recognised that this supposed thermocouple derived end point might be in fact due to the loss of contact between the thermocouple and the ice mass rather than the true end point of sublimation. Moreover, the probability that both the TVIS vial and the thermocouple containing vial would have the same primary drying end point would be quite low and therefore the inference of the end point from the nearest neighbour thermocouple containing vial is fundamentally flawed. An alternative method for assessing the true sublimation end point of the TVIS vial is needed in order to be able to isolate a TVIS parameter that could independently assess the end point. The method that has been chosen here is to use photographic evidence to capture the time point when the last vestiges of ice can be observed in the vial.

In the article by Smith et al. (2013) the rationale for choosing 1 kHz was that it is within the range of peak frequencies of the loss process and that the dielectric loss mechanism was assumed to be due to the charging the glass wall capacitance through the conductivity of the ice mass. In other words, the dielectric loss process in the frozen state was thought to be due to an interfacial (i.e. Maxwell-Wagner) process rather than due to the dielectric relaxation of ice. In the new study (Section 5), two modifications have been made:

Firstly, the electrode design was changed by removing the guard electrode used by Smith et al. (2013) and the electrode height was increased from 5 mm to 10 mm. In addition, two electrode positions were considered, one where the lower edge of the electrode was positioned close to the base of the vial (what is referred to as the 0 mm separation) and the other positioned at a height of 3mm from the base of the vial, in order to establish which more reliably identifies the end point. The hypothesis is that the electrode system close to the base (i.e. 0 mm separation) rather than at a height of 3 mm, would be the one which is most sensitive to the sublimation end point as one might expect that the closer proximity to the last vestiges of ice would provide increased sensitivity. However, it was found that the closer the electrode is to the base (and hence the grounded shelf) the greater the distortion there was to the relaxation spectrum.

Secondly, the real part capacitance was chosen for the assessment of the end point with this new electrode system (rather than the imaginary part capacitance at 1 kHz that was chosen for the 2013 article). The rationale for the change is that it is now recognised that (i) the dielectric loss process is not due to a Maxwell-Wagner/interfacial polarization of the glass wall capacitance, when water was in the frozen state, but rather it was due to the dielectric relaxation of ice, and (ii) the permittivity of ice on the high frequency side of the loss peak (which is known as the instantaneous relative permittivity, ε_∞, of ice) has almost zero temperature dependence (Johari and Whalley 1981). However, it was found that even the electrode system with the 3 mm spacing could be used to detect the sublimation of the last ice crystal.

For both electrode spacings, the TVIS parameter, $C'(100kHz)$ (or the part capacitance measured at 100 kHz) was shown to be sensitive to the amount of ice in the vial and its trajectory during the primary drying stage was characterized by a decrease in the values of $C'(100kHz)$ and its recovery to a plateau which corresponds to the end of ice sublimation as confirmed by the visual examination of a TVIS vial located in the line of sight of the camera. But it is recognised that the photographic observation is not possible for the vials surrounded by their nearest neighbours. To

account for this, a methodology based retrospective and real-time prediction of the endpoint was proposed that could be applied to a TVIS vial positioned at any location on the shelf.

Given the opacity of the dry layer, it is all the more important detect the removal of the last traces of ice from the vial bottom (where the risk of melt-back is the highest) before switching to the secondary drying stage. Subsequently, the methodology was extended to a simple sucrose solution (Section 6) for the prediction of the endpoint. Finally, TVIS was multiplexed with comparative pressure measurement and a PRT to monitor the primary drying and the secondary drying stages (Section 7). The main objective of the study was to determine to what degree do the predicted primary drying endpoints in TVIS vials located at the edge and the core agree with the endpoint detected by the batch sensors. Given that none of the current batch technologies in the market are capable of detecting the last vestiges of ice from the batch and single vial technologies being non-representative of the batch, the hypothesis then was that the detection of the true endpoint may not be realised.

Dielectric properties of the glass wall

Fissore and co-workers (Colucci, et al. 2019; Lietta, et al. 2019) have developed an infrared camera and used a mathematical model developed by Velardi and Baresi (2008) to monitor the temperature of the glass wall and therefore temperature of the product (which is in close proximity to the glass wall) during a freeze drying process. With TVIS, it is possible to potentially monitor the product temperature using the temperature dependency of the glass wall. While it has been established previously that the impedance response of the TVIS vial and its contents is perturbed by the presence of the glass wall between the electrodes and the sample (Smith and Polygalov 2019) the dielectric properties of the glass wall alone have not been studied. The current study (Section 8) explores the dielectric properties of the glass wall *per se* as a function of a broad range of frequencies (10^{-2} -1 MHz) and temperatures (-90 °C to 40 °C) which are of a particular relevance to a freeze-drying process, with an end goal of developing a model for the glass wall, which can ultimately be used for predicting the product temperature from the temperature dependency of the glass wall.

A part of the work involved using equivalent circuit models for visualising how mobile species within the glass microstructure (protons, dipoles, ions) choose various levels of migratory paths (known as percolation) to traverse through the microstructure as a function of applied frequency and temperature (Feldman, Yu, et al. 2012). It is recognised that glass composition plays a major role in molecular motion within the glass microstructure. Further, the value of the relative permittivity (also known as the dielectric constant) of a material is considered to be a direct measure of the extent to which charged species get polarised as function of frequency and migrate as a function of temperature; both are related to gas composition (Ehrt and Keding 2009; El-Egili 1996; Grandjean, et al. 2006). In the current study, the Adelphi VC010-20C glass vial has been used as a model sample for experimentation, where the relative permittivity of the glass vial as reported by Schott (5.7) has been compared with that obtained after measuring glass segments extracted from the vial using Broadband

Dielectric Spectroscopy (BDS). The measured value was found to be in good agreement with the one reported by Schott. This result served as a way of qualifying the proposed circuit models.

The other part of the study was to investigate the physical relevance of the Constant Phase Element, which is used to model the frequency dependent dispersive characteristics of the glass wall at low frequencies (Smith and Polygalov 2019). Given that TVIS, in its current manifestation, can only operate between 10 Hz and 1 MHz (Smith and Polygalov 2019) the present work involved investigating the dielectric behaviour of the glass wall over a broader frequency range (10^{-2} to 1 MHz) using Broadband Dielectric Spectroscopy (BDS). BDS has long been known to be a powerful tool for investigating the dielectric behaviour of solids and liquids at various levels (e.g. macroscopic, mesoscopic, microscopic). Further, the dielectric response can be measured over a broad frequency range (10^{-6} to 10^{12} Hz) hence the term broadband dielectric spectroscopy (Kremer and Schönhals 2003).

3 Aim

The present work aims to propose an application of Through Vial Impedance Spectroscopy as a non-product invasive single vial process analytical technology for the in-line monitoring of the freeze drying process. TVIS was employed to (1) monitor the freezing stage, in particular, investigate the impact of ice nucleation temperature on the ice growth time and subsequently, the resulting stability of the ice crystal structures; (2) predict the primary drying endpoint for pure ice, a 5%w/w/ sucrose solution and Immunoglobulin G containing formulations contained in TVIS vials positioned at various shelf locations. Finally, Broadband Dielectric Spectroscopy (BDS) was employed to study the dielectric properties of an Adelphi VC010-20C glass vial routinely used in TVIS studies at a range of frequencies and temperatures. This study partly addresses the end goal to exploit the temperature dependency of the glass wall for the prediction of the product temperature during the critical stages of the freeze drying process.

4 A Study of Ice Nucleation and the Stability of Ice Crystal Structures

4.1 Objectives

The objective was to form ice in three ways as shown in Figure 31. The **first method** is referred to as the "uncontrolled ice nucleation" method, wherein, the ice was allowed to form stochastically. Here, we expected to find (i) a low ice nucleation temperature (high degree of supercooling) predicted from $\boldsymbol{F_{PEAK}}$ and a short solidification time determined from $\boldsymbol{C'(0.2MHz)}$**,** reflective of a small, non-uniform ice crystal size distribution and therefore, (ii) the highest % change in $\boldsymbol{C''_{PEAK}}$, suggestive of the least stable ice crystal microstructure at the end of freezing.

The second and the third methods are based on controlled ice nucleation. The **second method** has been termed "re-pressurisation-induced ice nucleation", wherein, the chamber was re-pressurised from partial vacuum of ~300mbar to the atmospheric pressure and ice nucleation was induced at an intermediate shelf temperature. Here, we expected to obtain (i) an intermediate ice nucleation temperature induced simultaneously in the monitored vials and an intermediate solidification time (hence relatively larger ice crystals), and therefore, (ii) an intermediate % change in $\boldsymbol{C''_{PEAK}}$ indicating a relatively more stable ice microstructure. The **third method**, "de-pressurisation & re-pressurisation-induced ice nucleation", involved using a higher shelf temperature (than for method 2), and first de-pressurisation from partial vacuum (~300 mbar) to a pressure in the order of a few millibars and then quickly re-pressurisation of the chamber to the atmospheric pressure. Here, it is important to recognise that we changed both the shelf temperature and the technique for forming ice with the anticipation of obtaining a relatively higher ice nucleation temperature and the longest ice solidification time, which then was most likely to give us the most stable ice crystal structure at the outset. That then allowed for a back to back comparison of the relative ice crystal stabilities from the controlled nucleation methods with the baseline ice crystal stability from the uncontrolled nucleation.

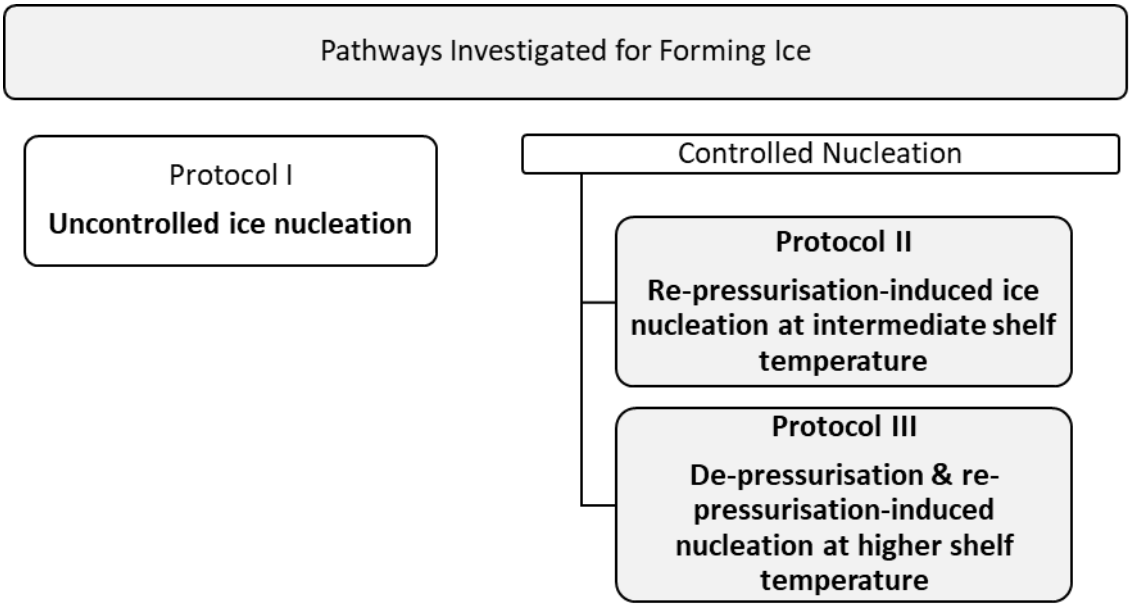

Figure 31: Three freezing methods for forming ice

4.2 Materials and Methods

4.2.1 Equipment

Water was double-distilled from an all glass apparatus. All freezing studies were carried out in a Virtis Advantage Plus freeze-dryer equipped with a five channel TVIS system (Figure 32a). The passthrough shown in Figure 32b) allows for a wired connection to be established between the impedance spectrometer (placed externally to the dryer) and a junction box (placed inside the dryer), to which the TVIS vial is connected: the TVIS vial is standard Adelphi (VC010-20C) vial modified with copper electrodes (copper adhesive tape 1181 3M), of dimensions 10 mm by 19 mm, attached externally to the glass wall at a distance of 3 mm from the vial baseline. Three grams of double distilled water was filled in the the TVIS vial and two nearest neighbour vials, each containing a type T thermocouple, with its sensing element at a height that corresponds to the midpoint of the sample bounded by the electrodes as shown in Figure 32(c). The midpoint is called the TVIS node. A second thermocouple vial was included so that if one of two thermocouple containing vials nucleated stochastically before controlled nucleation was performed, the second thermocouple containing vial would then be used for monitoring the ice nucleation temperature.

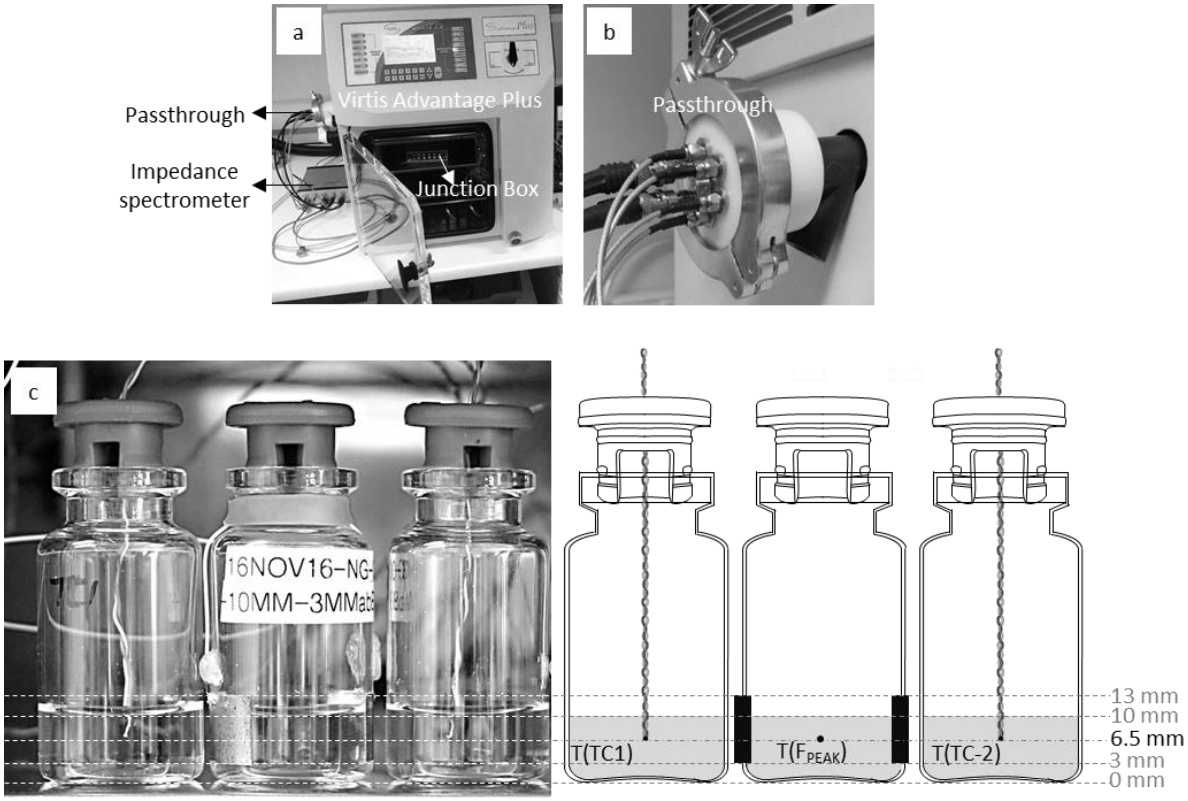

Figure 32: Experimental set-up: (a) A Virtis Advantage Plus freeze dryer equipped with a five channel TVIS system; (b) The passthrough for establishing a wired connection between the impedance spectrometer and the TVIS vial; (c) 3 g of double distilled water filled in a TVIS vial with copper electrodes (19 mm wide & 10 mm high) attached externally to the glass wall at a distance of 3 mm from the vial base, and two nearest neighbour vials, each containing a type T thermocouple (TCs) submersed in the liquid at a height of 6.5 mm, which corresponds to the height of the TVIS node, i.e. midpoint of the 7 mm sample height bounded by the electrodes (3.5 mm) added to the liquid height from the vial base to the lower edge of the electrode (3 mm). Note the nomenclature of the product temperature, T(TC1) and T(TC2).

4.2.1 Design of the Freezing Protocols

The various process steps for each protocol are detailed in Figure 33, where the time-lines of the shelf temperature and the chamber pressure are shown on the primary Y-axis and the secondary Y-axis respectively. It is worth noting that the dryer used in this study operates at a partial vacuum of ~300 mbar during freezing. Each protocol has a **thermal treatment** phase and an **analytical phase**. In the thermal treatment phase, the ice was formed either by uncontrolled nucleation (Figure 33a), or by inducing nucleation at a shelf temperature of -10 °C (Figure 33b) and -5 °C (Figure 33c). The principle difference between the two controlled nucleation approaches is that in protocol 1, once the vials had been equilibrated to -10 °C under the partial vacuum, the chamber was re-pressurised to atmospheric

pressure (Figure 33d). In contrast, protocol 3 involved equilibrating the vials at the shelf temperature of -5 °C and pulling a vacuum of ∼5 mbar for 5 min, and then re-pressurising the chamber to atmospheric pressure (Figure 33e). The rationale for changing the method and the shelf temperature in protocol 3 has already been discussed earlier in the objectives section (Section 4.1) but is re-iterated here in the sense that we expected to get a most stable ice crystal structure from protocol 3. After each thermal treatment phase, an **analytical phase** was imposed, where the shelf temperature was ramped to an elevated temperature and then held for 2 h. Over this period, the time-line of the $C"_{PEAK}$ parameter is followed to determine the relative stability of the ice crystal structure that results from the respective thermal treatments.

Each process step is described as follows. In protocol 1, the thermal treatment phase involved the equilibration of the shelf temperature to 20 °C within 30 min and a freezing ramp to -45 °C at 0.5 °C/ min with a hold period of 3 h. That then followed the analytical phase, wherein the shelf temperature was ramped from -45 °C to -10 °C at 0.5 °C and subsequently held at -10 °C for 2 h.

In protocol 2, the thermal treatment phase was comprised of an equilibration of the shelf temperature to 20 °C within 30 min, a freezing ramp from 20 °C to -10 °C at 0.5 °C/ min with a hold period for 2 h. The chamber was then re-pressurised from the partial vacuum to atmospheric pressure to induce ice nucleation. Once the ice nucleation occurred, the partial vacuum was re-established within 2 min and an ice solidification phase for 2 h at the shelf temperature of -10 °C was begun. That then followed a re-cooling ramp to -40 °C at 0.5 °C with a 2 h hold phase at -40 °C. The analytical phase was then started, wherein the shelf temperature was raised from -40 °C to -10 °C and held at -10 °C for 2 h.

In protocol 3, the shelf temperature was brought to -5 °C from a value of ∼10 °C (pre-cooled shelf) within 20 min and then held at -5 °C for 2 h. The chamber pressure was then de-pressurised from partial vacuum to ∼5 mbar within 2 min, followed by a quick re-pressurisation to the atmospheric pressure to induce ice nucleation. The partial vacuum was re-established within 2 min and then a

solidification phase was begun at a shelf temperature -5 °C for ~2.7 h. The shelf temperature was then ramped down to -40 °C at 0.5 °C/min and then held at -40 °C for 2 h. That then followed an analytical phase wherein the shelf temperature was re-heated to -5 °C at 0.5 °C and subsequently held at -5 °C for 2 h.

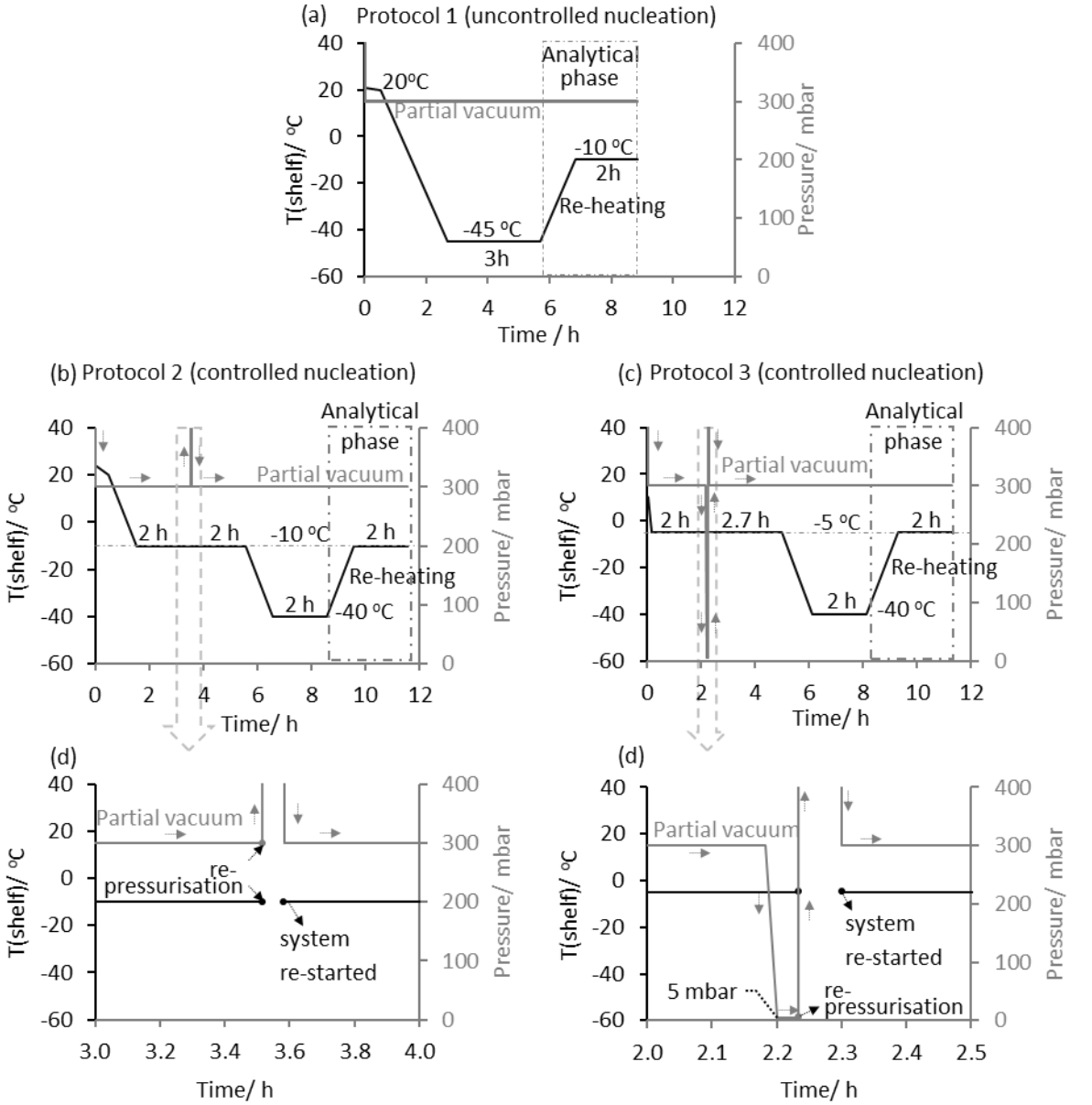

Figure 33:Sequence of steps for three freezing methods investigated: (a) Protocol 1 for uncontrolled ice nucleation; (b) Protocol 2 for re-pressurisation-induced ice nucleation; (c) protocol 3 for de-pressurisation & re-pressurisation-induced ice nucleation; (d) a closer look at the re-pressurisation event in protocol 2; (e) a closer look at the de-pressurisation and re-pressurisation events in protocol 3. Each thermal treatment phase follows an analytical phase (the period enclosed in a dashed box) which includes a re-heating ramp and an annealing phase.

4.2.2 Results

Determination of Ice Nucleation Temperatures

Figure 34(a) shows the time-lines of the shelf temperature, the chamber pressure and the product temperatures from the two thermocouples, T(TC1) and T(TC2) over the first 3 h of the thermal treatment phase. Figure 34(b) shows the time-line of log F_{PEAK} during the same period. The shaded regions in plot a and b are presented on an enlarged scale in Figure 34(c) & (d), which clearly demonstrate the TC vials nucleated at -9.4 °C (1.73 h) and -12.3 °C (1.90 h), and the TVIS vial nucleated at 1.77 h, which is the last time-point before the inflection in the time-line of log F_{PEAK} associated with the ice nucleation event.

Given that the first TC vial nucleated 2 min prior to the TVIS vial, it was possible to employ the T(TC1) to predict a value of the ice nucleation temperature in the TVIS vial, hence termed $T_{N(TC1)}(F_{PEAK})$, as plotted in Figure 34(e). Further, since the TC2 vial nucleated after the TVIS vial, it was possible to obtain another estimate of the nucleation temperature for the TVIS vial by simply reading off the temperature value at 1.77 h from the time-line of T(TC2), hence termed $T_{N(TC2)}(F_{PEAK})$ (also marked in Figure 34e). For a closer inspection of the two estimates, the reader is directed to Figure 34(f), which clearly shows the values of $T_{N(TC1)}(F_{PEAK})$ and $T_{N(TC2)}(F_{PEAK})$ to be -10.7 °C and -10.4 °C respectively. Note that the relationship between the product temperature and log F_{PEAK} in the liquid state follows a 2nd order polynomial when the shelf temperature is ramped down at a constant rate until ice nucleation occurs. That then allows for the construction of the temperature calibration curve as shown in Figure 34(g), where the values of T(TC1) have been plotted against the those of log F_{PEAK} obtained between 0.57 h and 1.73 h in the temperature range 18.6 °C to -9.4 °C. The value of log F_{PEAK} at 1.77 h and the temperature coefficients from the calibration curve (given in Table 4) are then used to obtain the value for $T_{N(TC1)}(F_{PEAK})$, i.e. -10.7 °C, which is also presented on an enlarged scale in Figure 34(h) for demonstration purposes. Given that the estimates of $T_N(F_{PEAK})$

from the two thermocouples are in excellent agreement, one may use either of those values moving forward. However, an average of the two values (i.e. -10.5 °C) has been considered.

Table 4: the calibration coefficients for T(TC1) and Log F_{PEAK} between 0.57 h and 1.73 h in the liquid state in the temperature range 18.6 °C to -10.7 °C, to be used for the prediction of the ice nucleation temperature for the TVIS vial

Order	**2**	**1**	**0**
Temperature coefficients	11.1	-21.9	-83.5

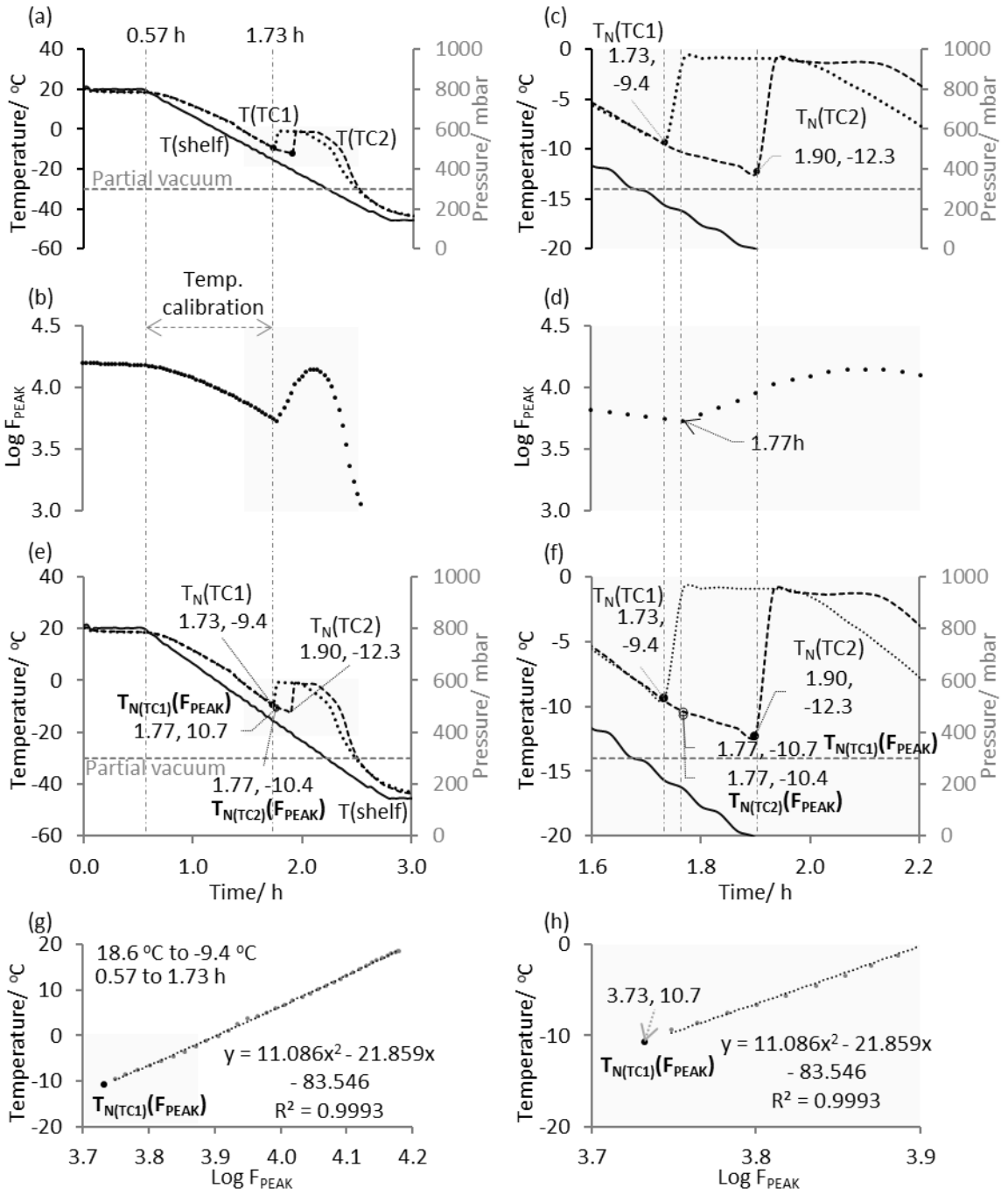

Figure 34: Determination of the ice nucleation temperatures during the uncontrolled nucleation event (protocol 1): (a) time-lines of the shelf temperature, the chamber pressure and the product temperature from the two thermocouples in the nearest neighbour vials over the first 3 h of the freezing step; (b) time-line of log F_{PEAK} for the TVIS vial over the first 3 h; (c) the shaded region in plot a on an enlarged scale shows the ice nucleation temperatures, $T_N(TC1)$ of -9.4 °C at 1.73 h and $T_N(TC2)$ of -12.3 °C at 1.9 h; (d) shaded region in plot c on an enlarged scale shows the TVIS vial nucleated at 1.77 h (i.e. 2 min after the TC1 vial and 8 min prior to TC2 vial; (e) The two estimates for $T_N(F_{PEAK})$ determined using T(TC1) and T(TC2) along with the previously identified values for $T_N(TC1)$ and $T_N(TC2)$ are shown; (f) shaded region in plot e on an enlarged scale shows the values of $T_N(TC1)$, $T_{N(TC1)}(F_{PEAK})$ predicted using T(TC1), and $T_N(TC2)$. The value of $T_{N(TC2)}(F_{PEAK})$ (i.e. -10.4 °C) was read off, from the time-line of T(TC2) at 1.77 h; (g) The temperature calibration curve in the liquid state for predicting $T_{N(TC1)}(F_{PEAK})$ was constructed using the values of T(TC1) and the values of Log F_{PEAK} between 0.57 h and 1.73 over the temperature range 18.6 °C to -9.4 °C; (h) shaded region in plot g on an enlarged scale highlights the position of $T_{N(TC1)}(F_{PEAK})$ on the calibration curve. Note an average of $T_{N(TC1)}(F_{PEAK})$ and $T_{N(TC2)}(F_{PEAK})$ was taken, i.e. -10.5 °C, termed $T_N(F_{PEAK})$.

Controlled ice nucleation

For protocol 2, the time-lines of the process parameters (shelf temperature, chamber pressure and product temperature from a thermocouple) and the TVIS parameter, Log F_{PEAK}, are presented in Figure 35(a) & (b) respectively, which clearly show the changes in the magnitude of log F_{PEAK} from the TVIS vial almost mirroring the changes in the product temperature in the TC vial in response to the changes in the programmed shelf temperature. The regions enclosed in dashed boxes within plots a and b are presented in Figure 35(c) & (d), which demonstrate that the product temperature (∼-9.3 °C) and the magnitude of log F_{PEAK} were constant over the last 50 min (2.73 h to 3.53 h) of the equilibrium phase at T(shelf) of -10 °C.

Furthermore, two photographs of the samples contained in the TVIS vial and the neighbouring TC vial are shown in Figure 35. Photograph i was taken at 3.53 h which corresponds to the last time-point before the process was terminated to allow the chamber to be re-pressurised to atmospheric pressure. As soon as the chamber was re-pressurised, both the vials nucleated simultaneously which is evident from photograph ii. Once the nucleation was induced, the dryer (and the TVIS system) was re-started within 2-3 min to prevent melting and resume the remaining part of the freezing protocol. It is clear from Figure 35(c) and photograph i that the vials were in a supercooled state until 3.53 h, which corresponds to the last time-point before the chamber was re-pressurised. The value of the product temperature in the TC vial at 3.53 h was -9.4 °C. Given that the value of T(TC) was found to be close to the equilibrium freezing point (0 °C) when the system was re-started, it implies that TC vial nucleated on re-pressurisation and the rise in temperature must be due to the release of the heat of crystallisation. Likewise, the value of log F_{PEAK} was higher (Figure 35d) when the system was re-started compared to the value at 3.53 h, which implies the TVIS vial also sensed the evolution of the heat of crystallisation. Given that both the vials nucleated at the same time-point, the value of ice nucleation temperature in the TVIS vial was assumed to be ∼-9.4 °C.

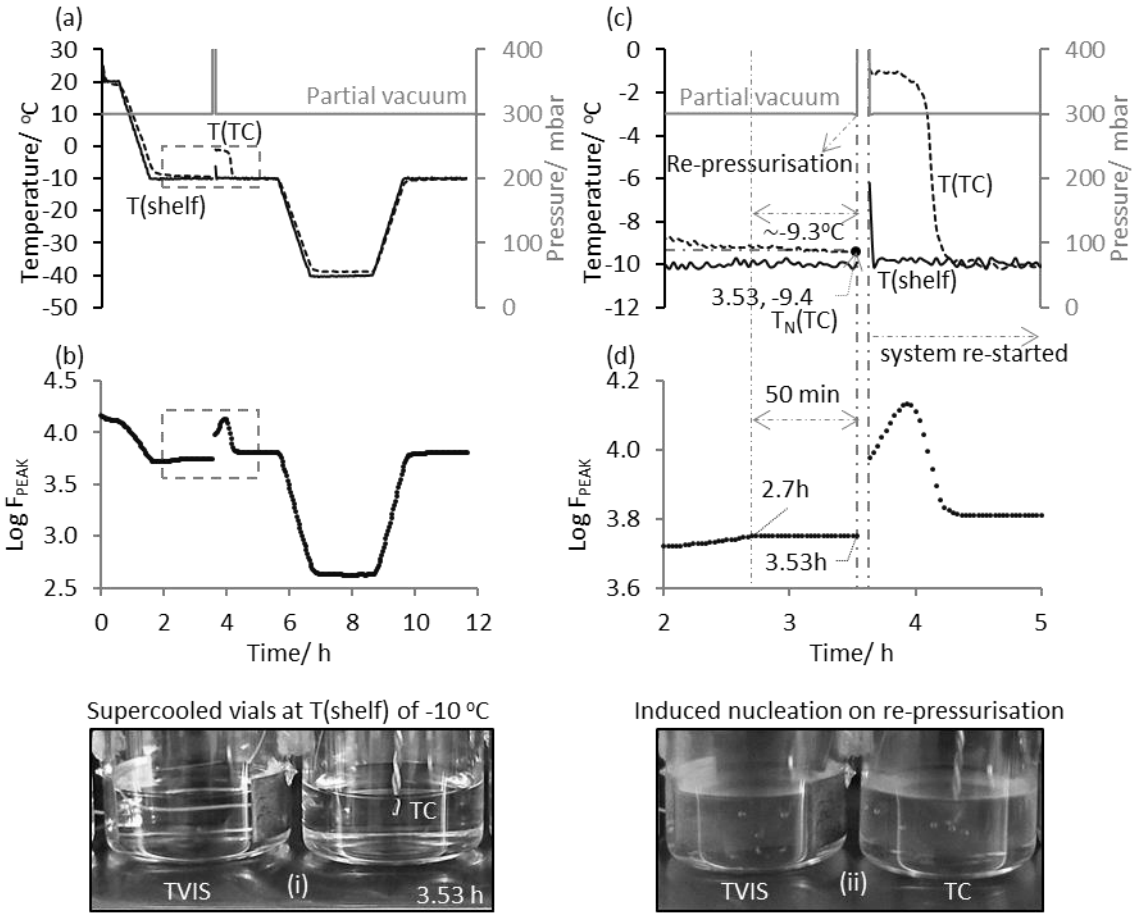

Figure 35: Evidence for the re-pressurisation-induced ice nucleation (Protocol 2) in the TVIS vial and the TC vial: (a) time-lines of the shelf temperature (solid black line), the chamber pressure (solid grey line) and the product temperature (dashed black line) from a thermocouple in the nearest neighbour vial during the entire freezing cycle; (b time-line of log F_{PEAK} response from the TVIS vial, mirroring the product temperature from the TC vial during the same period; (c) & (d) the regions enclosed in the dashed boxes have been enlarged to highlight that the TC vial and the TVIS vial nucleate at the same time (i.e. 3.53 h) on re-pressurisation of the chamber to atmospheric pressure. The value of the nucleation temperature for the TC vial was -9.4 °C, which is assumed to be the same for the TVIS vial. Photograph i shows both the vials were in a supercooled liquid state at 3.53 h. Photograph ii was taken immediately after ice nucleation occurred on re-pressurisation to atmospheric pressure. The system was re-started within the next 2-3 min to initiate the remaining part of the freezing protocol.

The time-lines of the process parameters and log F_{PEAK} for protocol 3 are presented in the same manner in Figure 36(a to d) as previously presented for protocol 2. Two photographs of the samples contained in the TC and the TVIS vials are also included in Figure 36, where photograph i shows the vials were in a supercooled liquid state during de-pressurisation; whereas photograph ii captures the induced nucleation event that occurred as soon as the chamber was re-pressurised to atmospheric pressure. This is clearly observable from the time-lines of T(TC) and log F_{PEAK} which responded to the release of the heat of crystallization after ice nucleation had occurred. Furthermore, Figure 37 comprises a series of screen-shots from a video taken during the de-pressurisation and re-pressurisation events. Although it was not possible to obtain superior quality pictures due to a lot of vibration occurring in the dryer, the pictures clearly demonstrate the progression of the ice nucleation from the top to the bottom of the vials within 1 second.

A closer inspection of the de-pressurisation event in Figure 36c reveals that by the time the 2 min depressurization step was concluded, the value of T(TC) had decreased from ∼-4.5 °C to -7.9 °C over a 6 min period (marked with an alphabet A in Figure 36c) starting from 4 min before the application of the vacuum to the end of the 2 min de-pressurisation step. The drop in the temperature before the application of vacuum is due to an inherent perturbation in the condenser of the dryer which is routinely observed and that causes a reduction the shelf temperature and, in turn, leads to a decrease in the product temperature. However, the drop in the temperature during the de-pressurisation step may be attributed to evaporative self-cooling. Therefore, it must be noted that the value of $T_N(TC)$ just before the re-pressurisation event was -7.9 °C (and not -4.5 °C). Further, given that even log F_{PEAK} decreases during de-pressurisation (Figure 36d), the nucleation temperature in the TVIS vial was assumed to be ∼8 °C.

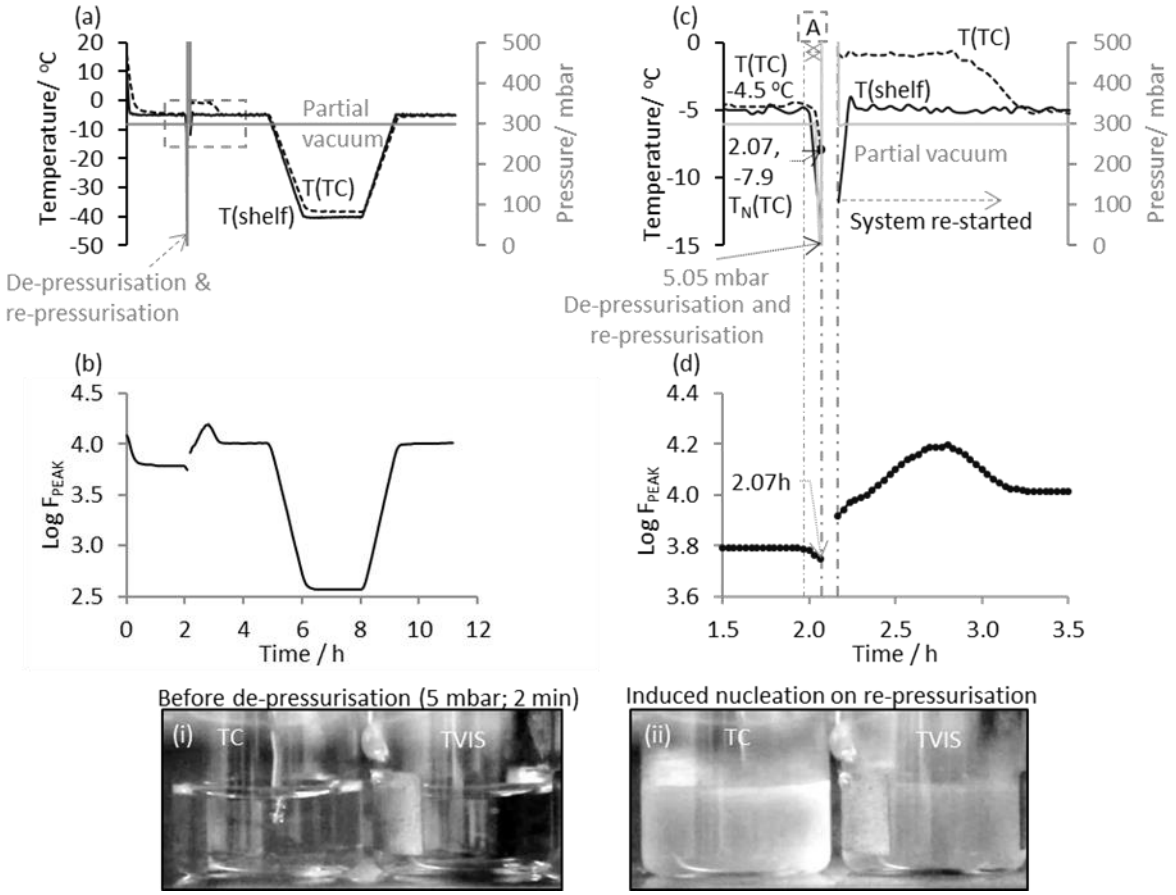

Figure 36 Evidence for the de-pressurisation- re-pressurisation-induced ice nucleation (Protocol 3) in the TVIS vial and the TC vial: (a) time-lines of the shelf temperature, the chamber pressure and the product temperature from a thermocouple in the nearest neighbour vial during the entire freezing cycle; (b) time-line of log F_{PEAK} response from the TVIS vial, mirroring the product temperature from the TC vial during the same period; (c) & (d) the regions enclosed in the dashed boxes have been enlarged to highlight that the TC vial and the TVIS vial nucleated at the same time (i.e. 2.07 h) on re-pressurisation of the chamber to atmospheric pressure following a 2 min depressurisation step at ~5 mbar. The value of T(TC) decreased from -4.5 °C 4 min before the application of vacuum to -7.9 °C by the end of the 2 min de-pressurisation step. The value of the nucleation temperature for the TC vial, $T_N(TC)$, was thus -7.9 °C, assumed to be approximately the same for the TVIS vial. The photographs shown below are captured from a video taken before depressurisation and on re-pressurisation. Photograph i shows both the vials were in a supercooled liquid state until depressurisation. Photograph ii shows both vials nucleated simultaneously on re-pressurisation to atmospheric pressure. The system was re-started within the next 2-3 min to initiate the remaining part of the freezing protocol.

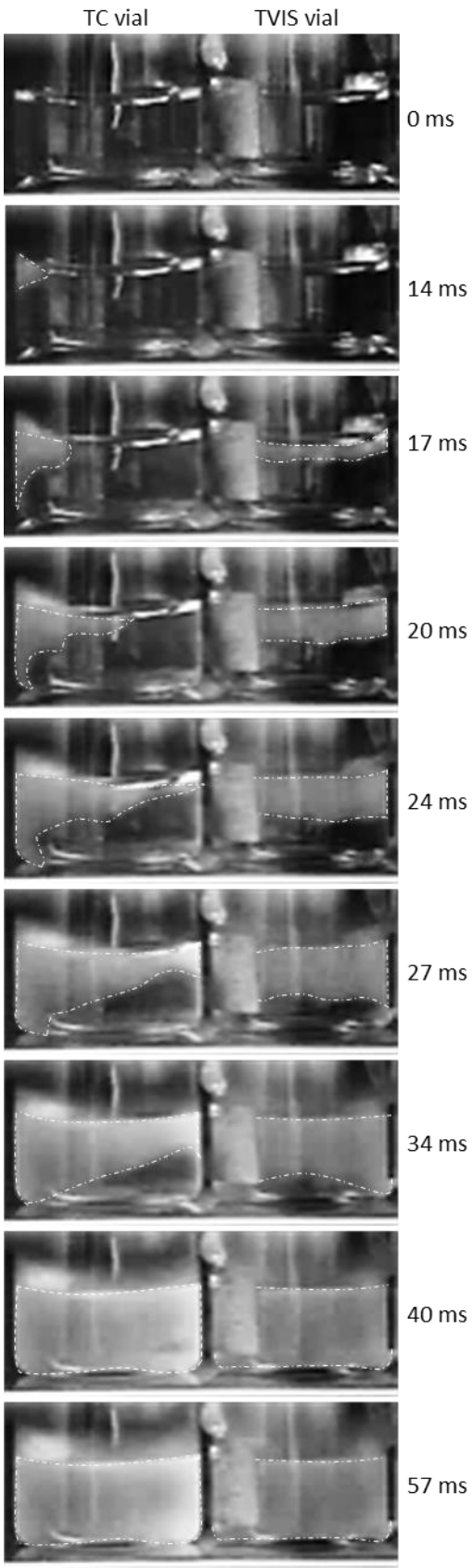

Figure 37: Progression of controlled ice nucleation in the TC vial and the TVIS vial from top left to bottom right of the vials within ~1 second of the re-pressurisation of the chamber to atmospheric pressure, following a 2 min de-pressurisation step at ~5 mbar. The pictures are screenshots captured at the specific time-points from a video filmed during the process.

Impact of Ice Nucleation Temperature on Ice Solidification Time

The relationship between ice nucleation temperature and ice solidification time determined from a thermocouple and the TVIS parameter, $C'(0.2MHz)$ is demonstrated in plots a, c and e of Figure 38, which show the time lines of the T(shelf) and T(TC), and plots b, d and f Figure 38, which show the time-line of $C'(0.2MHz)$ during the solidification phase that followed the respective thermal treatments. For the TC vial, the ice solidification times were determined by marking the onset of solidification on the time-line of T(TC) close to 0 °C and the point when T(TC) decreased to a pseudo steady state value close to that of T(shelf); whereas for the TVIS vial, the ice solidification times were determined from the beginning of the decrease in $C'(0.2MHz)$ immediately after nucleation to the point when it drops abruptly to a pseudo steady state value, as shown by dashed vertical time-markers. The values of the ice nucleation temperatures and the corresponding ice solidification times for the TVIS vial are given in Table 5. It is evident from Figure 38 that the ice solidification time increased with a decrease in the ice nucleation temperature (low degree of supercooling) which was expected because a higher nucleation temperature implies more time is given for ice crystal growth. It is worth noting that the solidification endpoints from TVIS were estimated well before that determined from a thermocouple for each method. This is due to the fact that $C'(0.2MHz)$ is much more sensitive to phase change than product temperature and hence it was able to detect the point of complete ice solidification even as a thermocouple continued to register the evolution of the heat crystallisation well after $C'(0.2MHz)$ had reached a plateau.

Table 5: Relationship between ice nucleation temperature and ice solidification time determined for the TVIS vial using the time-line of $C'(0.2MHz)$

	High T_N	**Intermediate T_N**	**Low T_N**
Long solidification time	Depress-repress-induced	-	-
Short solidification time	-	Repress-induced	Uncontrolled

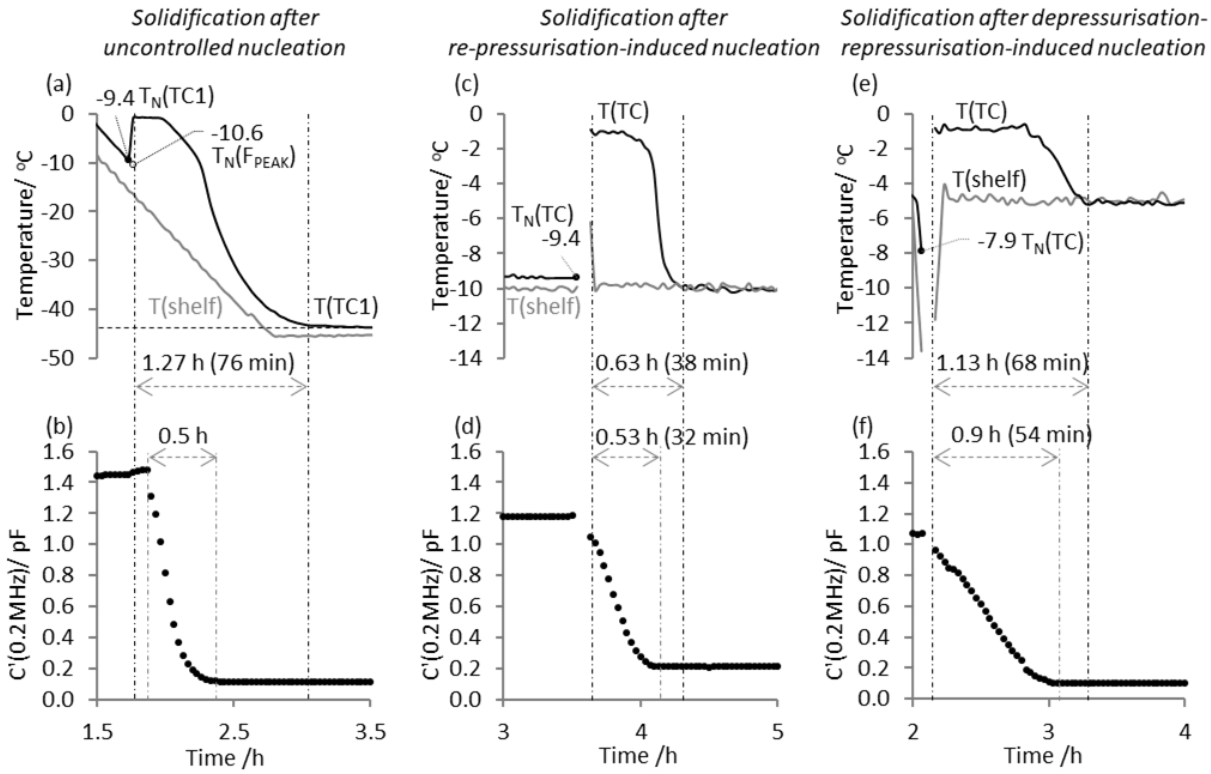

Figure 38: Impact of ice nucleation temperature on ice solidification time: (a) the time-lines of T(shelf) and T(TC) during the ice solidification phase following uncontrolled nucleation; (b) the time-line of $C'(0.2MHz)$ during the ice solidification phase following uncontrolled nucleation in the TVIS vial; (c) & (d) the time-lines of the process parameters, and $C'(0.2MHz)$, respectively, during the ice solidification phase following the controlled re-pressurisation-induced nucleation; (e) & (f) the time-lines of the process parameters with and $C'(0.2MHz)$, respectively, during the ice solidification phase following the controlled de-pressurisation-re-pressurisation-induced nucleation. The values of the ice nucleation temperatures are plotted as datapoints in each case.

Determination of the Relative Stability of the Ice Crystal Structures

Having established a direct relationship between ice nucleation temperature and ice solidification time (i.e. the higher the nucleation temperature, the longer the solidification time), the next part of the investigation involved determining using TVIS, whether a higher ice nucleation temperature translates to a more stable ice crystal structure and vice versa. For this purpose, an analytical phase constituting a shelf temperature ramp to an elevated temperature and a 2 h annealing period was imposed. The relative changes in the magnitude of C''_{PEAK} were then compared among the three nucleation methods during the 2 h annealing period. The results are presented in Figure 39, where plots a, c and e show the time-lines of the shelf temperature and the product temperature; and the plots b, d and f show the time-line of C''_{PEAK} during the 2 h annealing phase for the first, the second and the third ice nucleation methods respectively.

Over the initial period of the annealing phase (shown as dashed vertical lines in Figure 39a to c), the product temperature was found to be increasing towards a pseudo-steady state value, even as the shelf temperature was constant. This is routinely observed for a thermocouple response which lags behind the shelf temperature at the beginning of a hold step. At first glance, the trajectory of C''_{PEAK} in the first case differs remarkably from the trajectories of C''_{PEAK} in the second and the third case in two ways: (i) an increase in the magnitude of C''_{PEAK} was observed for the ice formed with the two controlled nucleation methods during the initial period of the annealing phase (when the product temperature was still increasing); whereas no such increase was observed for C''_{PEAK} in the first case; (ii) the % decrease in the magnitude of C''_{PEAK} follows the rank order uncontrolled (0.6 %) > repress-induced (0.4 %) > depress-repress-induced (0.08 %).

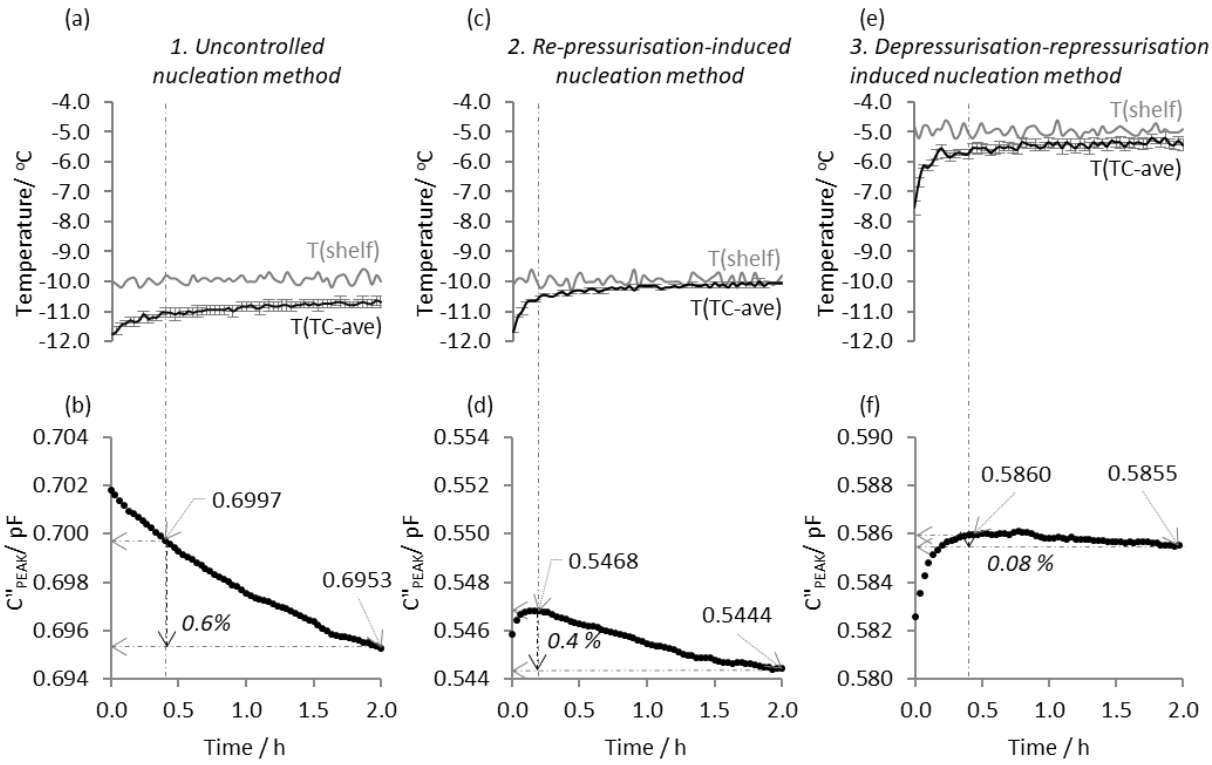

Figure 39 Use of $C"_{PEAK}$ parameter to determine the relative ice crystal structural stability: (a) & (b) the time-lines of the shelf temperature and the product temperature, and the time-line of $C"_{PEAK}$ respectively, during the 2 h annealing period of the analytical phase for the ice structure formed from the uncontrolled nucleation method; (c) & (d) the time-lines of the same process parameters during the 2 h annealing period of the analytical phase for the ice structure formed from the re-pressurisation-induced nucleation method; (e) & (f) the time-lines of the same process parameters during the 2 h annealing period of the analytical phase for the de-pressurisation-re-pressurisation-induced nucleation method. The dashed vertical lines correspond to the beginning of the constant product temperature period when the % change in $C"_{PEAK}$ decreased in the rank order uncontrolled (0.6 %, least stable) > repress-induced (0.4 %) > depress-repress-induced (0.08 %, most stable).

In order to understand these relative differences, it is important to recognise that $C"_{PEAK}$ is sensitive to both the product temperature and the changes in the double layer capacitance (or charge accumulation) at the electrode-glass-ice interface, which has a positive temperature dependency, unlike the bulk dielectric properties of ice (particularly the static permittivity, ε_s, of ice) which have a negative temperature coefficient (Johari and Whalley 1981).

A consequence of the positive temperature dependency of $C"_{PEAK}$ is evident for the ice structures formed from the controlled nucleation methods in Figure 39(d) and (f), where, as expected, the magnitude of $C"_{PEAK}$ increased with temperature over the initial period of the annealing phase. However, the relative differences in the step change in $C"_{PEAK}$ with temperature amongst the controlled nucleation methods notwithstanding a similar temperature increment (∼1 °C) over the initial phase of annealing and no increase observable at all in the first case, and the fact that the % change in $C"_{PEAK}$ at a constant temperature became increasingly less significant from method 1 to method 3, may be explained by the other property of $C"_{PEAK}$, i.e. its sensitivity to charge accumulation at the interface. As discussed previously, dielectric relaxation of ice occurs by charge propagation via crystal defects (Popov, et al. 2017) and the extent of this migration is likely to depend on the number of defects in the crystal lattice. In other words, the larger the number of defects, the greater the charge migration. It follows that the higher the structural stability, the fewer the number of defects, the fewer the opportunities for charge migration to the interface, hence the lower the value of $C"_{PEAK}$ for the same ice mass bounded by the electrodes. Given that the % change in $C"_{PEAK}$ at a constant product temperature was the greatest for the ice structure that resulted from the uncontrolled nucleation method, it implies that the ice structure was highly unstable with significantly larger defects at the beginning of annealing. Further, the annealing effect was so predominant that the temperature dependency of $C"_{PEAK}$ was supressed over the initial period of the annealing phase. On the other hand, given that the % change in $C"_{PEAK}$ was more gradual in the second case and the least significant in the third case, it implies the ice structures were already much more stable before the analytical phase was imposed. That then allowed for the temperature effect on $C"_{PEAK}$ to be observable.

4.2.3 Discussion

There were two parts to the presented study: (i) forming ice at different ice nucleation temperatures and determining the relationship between ice nucleation temperature and ice solidification time; (ii) investigating the impact of ice nucleation temperature on the ice structural stability. The key steps of the thermal treatment and the key findings have been summarised in Table 6. In the first part of the study, it was demonstrated that the time taken by $C'(0.2MHz)$ to reach a plateau was the shortest when the ice nucleation temperature was the lowest. In other words, the lower the ice nucleation temperature, the shorter is the ice solidification time. For example, in Table 6, when the value of $T_N(F_{PEAK})$ was -9.5 °C (protocol 1: uncontrolled nucleation), the ice solidification time was 30 min; whereas when nucleation occurred at ~-8 °C (protocol 3: controlled nucleation), the solidification time was 54 min. Further, a thermocouple could not be used to qualify the relationship between ice nucleation temperature and ice solidification endpoint because it was sensitive to the release of heat of crystallisation during ice formation (which is released relatively slowly), but not phase change. For example, between protocol 1 and 3, the ice solidification times suggested by a thermocouple were similar (76 min and 68 min) despite the fact that the nucleation temperatures were different. Consequently, the ice solidification endpoints estimated from a thermocouple were also found to be relatively longer as opposed to those estimated by $C'(0.2MHz)$.

The second part of the study was focussed on demonstrating how ice nucleation temperature has a bearing on the final ice crystal structural stability. This was demonstrated by forming ice in three different ways and imposing an analytical phase where the solidified ice was re-heated to an elevated temperature and then annealed for 2 h. Table 6 shows how TVIS confirms that a lower ice nucleation temperature (-9.5 °C) lead to a shorter ice solidification time (30 min), which ultimately resulted in a higher percentage change in $C"_{PEAK}$ (0.6 %) over the constant temperature period of the analytical phase. As the ice nucleation temperature was increased (protocol 2 and 3), there was an increase in the ice solidification time and consequently, a smaller % change in $C"_{PEAK}$.

Table 6: The key outcomes for the three methods of forming ice, ice nucleation temperature, ice solidification time and the final ice crystal stability for the thermocouple containing vial and the TVIS vial.

	Thermal Treatment	Outcomes for the thermocouple containing vial and the TVIS vial		
		Nucleation temperature (T_N)	Solidification time	Ice crystal stability*
1	• Default partial vacuum established (~300mbar) • Shelf freezing to -45 °C to allow for a stochastic ice nucleation event • Equilibrium phase at T(shelf) of -40 °C	• Intermediate to low, and variable; • T_N(TC) -9.4 °C & -12.3 °C • **Average $T_N(F_{PEAK})$ -9.5 °C**	• 76 min taken for T(TC) to equilibrate to T(shelf) of -45 °C as it continues to sense evolution of heat of crystallisation • **Short, i.e. 30 min** taken for $C'(0.2MHz)$ to drop to plateau	• Temperature dependency of C''_{PEAK} is suppressed during the temperature effect phase due to a predominant annealing effect. • **Least stable** structure: 0.6 % reduction in C''_{PEAK} at constant product temperature during annealing
2	• Default partial vacuum established • T-shelf equilibrated to -10 °C for 2 h • Re-pressurisation of the chamber to atmospheric pressure • Ice solidification at T-shelf of -10 °C for 2 h	• Intermediate; • **Same T_N i.e. ~-9.3 °C**	• **Intermediate** • **38 min** from T(TC) & **32 min** from $C'(0.2MHz)$	• Small increase in C''_{PEAK} during the temperature effect phase; annealing effect more gradual • **More stable than 1** 0.4 % reduction in $\boldsymbol{C''_{PEAK}}$ at constant product temperature during annealing
3	• Default partial vacuum established • T-shelf equilibrated at -10 °C • De-pressurisation to ~5 mbar for ~2 min • Re-pressurisation to atmospheric pressure • Ice solidification at T(shelf) of -5 °C (2.7 h)	• High • **Same T_N, i.e. ~-8 °C**	• Long • **68 min** from T(TC) & **54 min** from $C'(0.2MHz)$	• Greater increase in C''_{PEAK} (than in 2) during the temperature effect phase; annealing effect least significant • **Most stable**: 0.08 % reduction in C''_{PEAK} at constant product temperature during annealing

*indicated by $\boldsymbol{C''_{PEAK}}$ during the 2 h annealing period of the analytical phase

In the case where there was a higher change in $C"_{PEAK}$ (uncontrolled nucleation method), i.e. more charge propagation, the ice microstructure was less stable compared to the microstructures that resulted from the controlled nucleation methods. Furthermore, the temperature dependency of $C"_{PEAK}$ over the initial part of the analytical phase was suppressed by the annealing effect for the ice structure formed from the uncontrolled nucleation method (Figure 39b). In contrast, the temperature effect was clearly visible for the ice structure formed from the de-pressurisation-re-pressurisation-induced nucleation (Figure 39f) owing to the fact that the annealing effect was much less significant in the latter as the ice structure appeared to be more stable.

The competition between the temperature and the annealing effects has been conceptualised in Figure 40, where two scenarios are presented: (i) Annealing of an ice crystal structure pre-stabilised with controlled nucleation, and (ii) Annealing of an unstable ice crystal structure formed with uncontrolled nucleation. In the first scenario (Figure 40a) when the ice is annealed, the anticipated response of annealing is shown as a solid black line and the anticipated response of the temperature effect is shown as a solid grey line. Since the ice structure is already stable, annealing is more gradual and hence the combined effect on $C"_{PEAK}$ is expected to be dominated by temperature (the predicted response shown as a dashed black line). On the other hand, for an unstable ice crystal structure, the anticipated annealing effect is shown as a solid black line and the anticipated temperature effect remains the same as scenario 1 (Figure 40b). Because the ice structure is less stable compared to that in scenario 1, annealing has a more dramatic impact on $C"_{PEAK}$ such that the temperature effect is supressed. In effect, the predicted $C"_{PEAK}$ response is dominated by the annealing effect (shown as a dashed grey line).

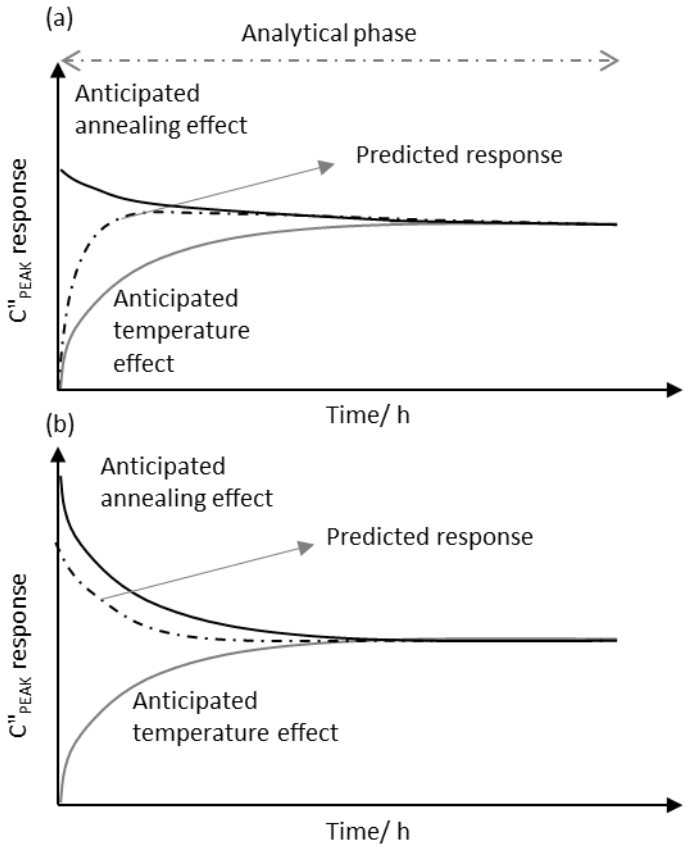

Figure 40: The concept of the combined effect of temperature and annealing on the $C"_{PEAK}$. Solid black line is the anticipated annealing effect on $C"_{PEAK}$; solid grey line is the anticipated temperature effect on $C"_{PEAK}$; and the dashed black line is the predicted response when (a) ice structure is stable and the annealing effect is more gradual and therefore, the temperature effect is more dramatic; (b) ice structure is unstable, hence annealing effect is more dominant which supresses the temperature effect.

4.2.4 Chapter Conclusion

The present study demonstrates two useful applications of TVIS for the characterisation of the freezing stage. First, it has been established that there is a direct relationship between the ice nucleation temperature and the ice growth time: the higher the ice nucleation temperature the longer is the ice growth time. Second, TVIS is sensitive to the relative differences in the ice crystal structural stability at the electrode-glass-ice interface. The double layer capacitance as studied with the C''_{PEAK} parameter is a function of very small conductivity defect type processes to which TVIS is highly sensitive, unlike the bulk dielectric properties of ice. These relative differences demonstrate how the controlled nucleation methods are better at creating more stable ice structures than the uncontrolled nucleation method. Moving forward, when multiplexed with an advanced controlled nucleation technology, TVIS can be used to ascertain the optimal condition of the ice crystal structure across the batch before the primary drying phase is initiated, thereby allowing for a more efficient primary drying and secondary drying process.

5 Prediction of the Primary Drying Endpoint of Ice

5.1 Objectives

The aim of this work is to develop an application for TVIS for determining the single-vial primary drying endpoint at any position on the shelf of a small-scale development dryer. The **first objective** is to identify a qualitative characteristic in the time profile of the high frequency capacitance measured 100 kHz[1] that corresponds to the time point at which the photographic evidence shows that last residues of the ice mass has disappeared from the vial. This study was undertaken using isolated vials, i.e. single TVIS vials placed alone on the freeze-dryer shelf. Two positions of the electrode were investigated in separate lyophilization cycles (Methods Section 5.2) and one of these selected for the remainder of the study. The **second objective** is to establish a mathematical method for identifying that characteristic and hence predicting the endpoint in TVIS vial located in front of the dryer door, and thereby obviating the requirement for the photographic evidence. The **third objective** is to extend the mathematical prediction so that could be applied to any vial which is not within the line of sight of the camera, i.e. any vial that is behind the front row of vials. This would then provide for a universal method for predicting the end point in any of the TVIS-enabled vials, located at chosen positions across the dryer.

[1] We have adopted the term $C'(100kHz)$ for the real part capacitance measured at an excitation frequency of 100 kHz.

5.2 Materials and Methods

5.2.1 Isolated TVIS vials with electrode positions of 0 mm and 3 mm from the base

Two (Adelphi VC010-20C) vials were modified with copper electrodes (copper adhesive tape 3M 1181) of dimensions 10 mm by 19 mm attached externally to the glass wall. On one vial the distance between the bottom of the electrode and the base of the vial was close to 0 mm (Figure 41a). On the other vial the bottom of the electrode was positioned 3 mm from the base of the vial (Figure 41b). The vials were filled with 2 g and 3 g of double-distilled water, respectively. Each TVIS vial was placed at the front of the shelf of a Virtis Advantage Plus freeze-drier equipped with a five-channel TVIS system and was freeze-dried separately using the lyo-cycle shown in Table 7, until all the ice disappeared. TVIS spectra, the freeze-drying process parameters and the photographic images (Canon DSLR camera with a self-timer option) were obtained every 2 min throughout the freeze-drying cycle.

Table 7: Freeze-drying cycle for the two TVIS vials with 0 mm and 3 mm electrode spacing, containing 2 g and 3 g of double distilled water, respectively.

Step	Start Temperature (°C)	End Temperature (°C)	Ramp rate (°C/ min)	Duration (min)	Cumulative Time (h)	Set pressure (mbar)
Equilibrium phase	RT	20	-	15	0.3	-
Freezing	20	-40	0.6	100	1.9	-
Hold	-40	-40	-	120	3.9	-
Re-heating	-40	-10	0.5	60	4.9	-
Hold	-10	-10	-	60	5.9	-
Re-freezing	-10	-40	0.5	60	6.9	-
Hold	-40	-40	-	60	7.9	-
Re-heating	-40	-15	0.6	40	8.6	-
Hold	-15	-15	-	40	9.3	-
Primary drying	-15	-15	-	506	17.7	0.4

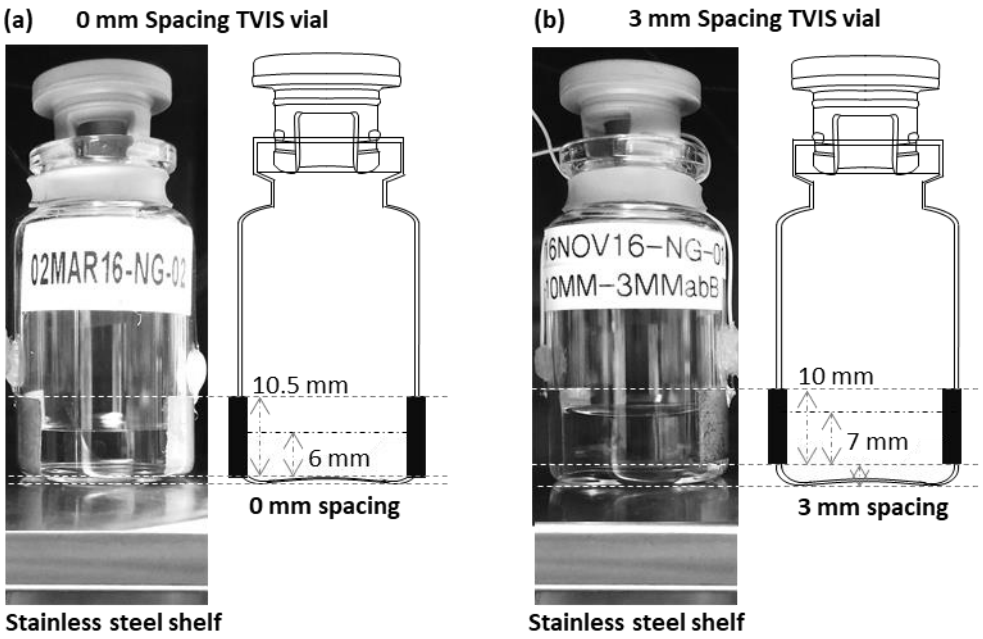

Figure 41: Details of the isolated vials: (a) TVIS vial containing 2 g of double distilled water (Φ = 0.6), with copper electrodes (10.5 mm by 19 mm) positioned at 0 mm from the vial base; (b)TVIS vial containing 3 g of double-distilled water (Φ = 0.7) , with copper electrodes (10 mm by 19 mm) positioned at 3 mm from the vial base.

5.2.2 Freeze-drying of a batch of vials, including three TVIS vials

A batch of 160 x 10 mL vials (Adelphi VC010-20C) was filled with ~4 g of double distilled water. Out of the 160 vials, three were TVIS vials with copper electrodes (19 mm by 10 mm) positioned at 3 mm from the base of the vial and hence freeze-drying shelf. These TVIS vials were placed in the front row (edge), the ninth row (i.e. core region) and the last row (edge) of the batch as shown in Figure 42a. Hereafter these vials are referred to as the front TVIS vial, the core TVIS vial, and the back TVIS vial. Each TVIS vial was accompanied by a nearest neighbour vial containing a Type-T thermocouple with the sensing element positioned in contact with the bottom-centre of the vial base. A photograph of the front TVIS vial next to the nearest neighbour TC vial is shown in Figure 42b. Freeze drying was carried out in a Virtis Advantage Plus freeze dryer equipped with a five-channel TVIS system. The stages of the lyo-cycle are given in Table 8.

Table 8: Freeze-drying protocol for 4 g of double distilled water in 160 x 10 mL Adelphi (VC010-20) vials

Step	Start Temperature (°C)	End Temperature (°C)	Ramp rate (°C/ min)	Duration (min)	Cumulative Time (h)	Set pressure (mbar)
Equilibrium	RT	20	1	20	0.3	-
phase	20	20	-	10	0.5	
Freezing	20	-45	0.5	130	2.7	-
Hold	-45	-45	-	120	4.7	-
Re-heating	-45	-5	0.5	80	6.0	-
Hold	-5	-5	-	120	8.0	-
Primary drying	-5	-5	-	1928	40.1	0.4

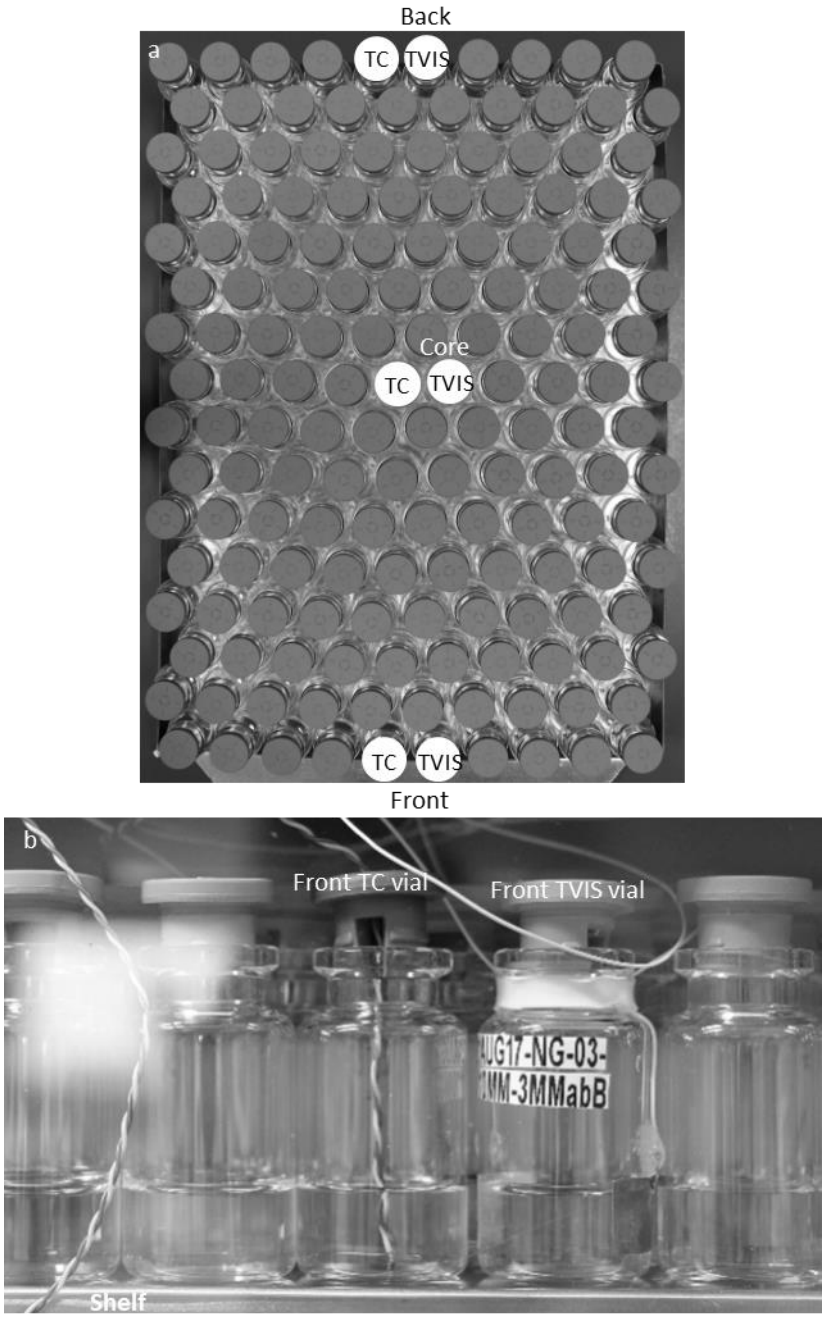

Figure 42: Batch freeze-drying of double distilled water in 160 x 10 mL Adelphi (VC010-20C) vials: (a) Top view of the vial batch showing the position of the measurement vials; (b) the front TVIS vial and the nearest neighbour vial containing a Type T thermocouple with its sensing element in contact with the bottom centre of the vial base.

5.3 Results

5.3.1 A Comparison of the Electrode Spacings on the Isolated TVIS Vials

Figure 43 shows the bode plots of log real part capacitance plotted against log frequency for the TVIS vials, containing ice, with a 0 mm and a 3 mm spacing of the bottom of the electrode from the base of the vial (left and right column respectively) at two similar temperatures, -39 ±0.5 °C (Figure 43a & b) and -20 ±0.5 °C (Figure 43c & d) during the re-heating ramp. The spectra (data points) have been fitted with an equivalent circuit of a constant phase element (CPE_G) in parallel with a capacitance C_G (which collectively model the glass vial impedance) which is in series with a Cole-Cole relaxation function in parallel with a capacitance, which model the relaxation behaviour and the instantaneous capacitance of the ice, respectively. In text format we define this model as "$CPE_G = C_G - C_S = Co$" and the line fit is shown as a solid line. This serves as the best possible approximation to the dielectric properties of the electrode-glass wall-ice composite over the frequency range 10 Hz- 1MHz (Smith and Polygalov 2019).

In the present case, the model is useful for demonstrating the atypical dielectric response, namely a distortion, or more specifically a dip in the spectra centred on ~1 kHz. This is clearly worse for the 0 mm spacing and more so at the higher temperature (Figure 42c). It suggests that there is a coupling between the electrode and the shelf via the conductivity of the ice. In other words, there is a shunt to a capacitance to ground (i.e. the shelf) which has a time constant in the region of ½ πf where f is the approximated from the experimental data as the dip frequency. While it appears that the capacitance recovers as the frequency is increased further it is likely that the values of capacitance across the whole spectrum are lower than they would otherwise be if the shelf was not in close proximity. The evidence for this is that values for the real capacitance spectrum for the 0 mm spacing of the electrode from the base of the vial are lower than the corresponding values for the 3 mm spacing. We refer to this as the lost capacitance. As the ice is removed the coupling to ground decreases and allows the capacitance to start recovering to a value that it would otherwise have

without the shunt capacitance to ground. We have used this phenomenon to explain the characteristic shape of the time profile of the real part capacitance during the sublimation phase.

. In the present case, the model is useful for demonstrating an atypical dielectric response at ~1 kHz, namely a distortion in the spectra, which is clearly worse for the 0 mm spacing particularly at the higher temperature (Figure 43c). In other words, the measured values of the capacitance appear to be lower than they should be at ~1 kHz, when the model clearly suggests that they should be higher than the values at the high frequencies. The reason why they should be higher is that the dielectric relaxation of ice in the TVIS vial is characterised by a step in the real part, i.e. a decrease in the values of the capacitance as per a fixed time-constant. The consequence of that is that for frozen water, the relaxation process finishes after 1 kHz and therefore, any values around 1 kHz must be higher than the values at the high frequency. However, there is clearly a depression in the values of the capacitance at 1 kHz. Further, this distortion appears to impact the high frequency part of the spectra and since the objective of the present study is to use $C'(100kHz)$ as a TVIS parameter to monitor the primary drying stage, it would be interesting to know the extent of the distortion in the spectra and how this distortion impacts the values of $C'(100kHz)$ during primary drying.

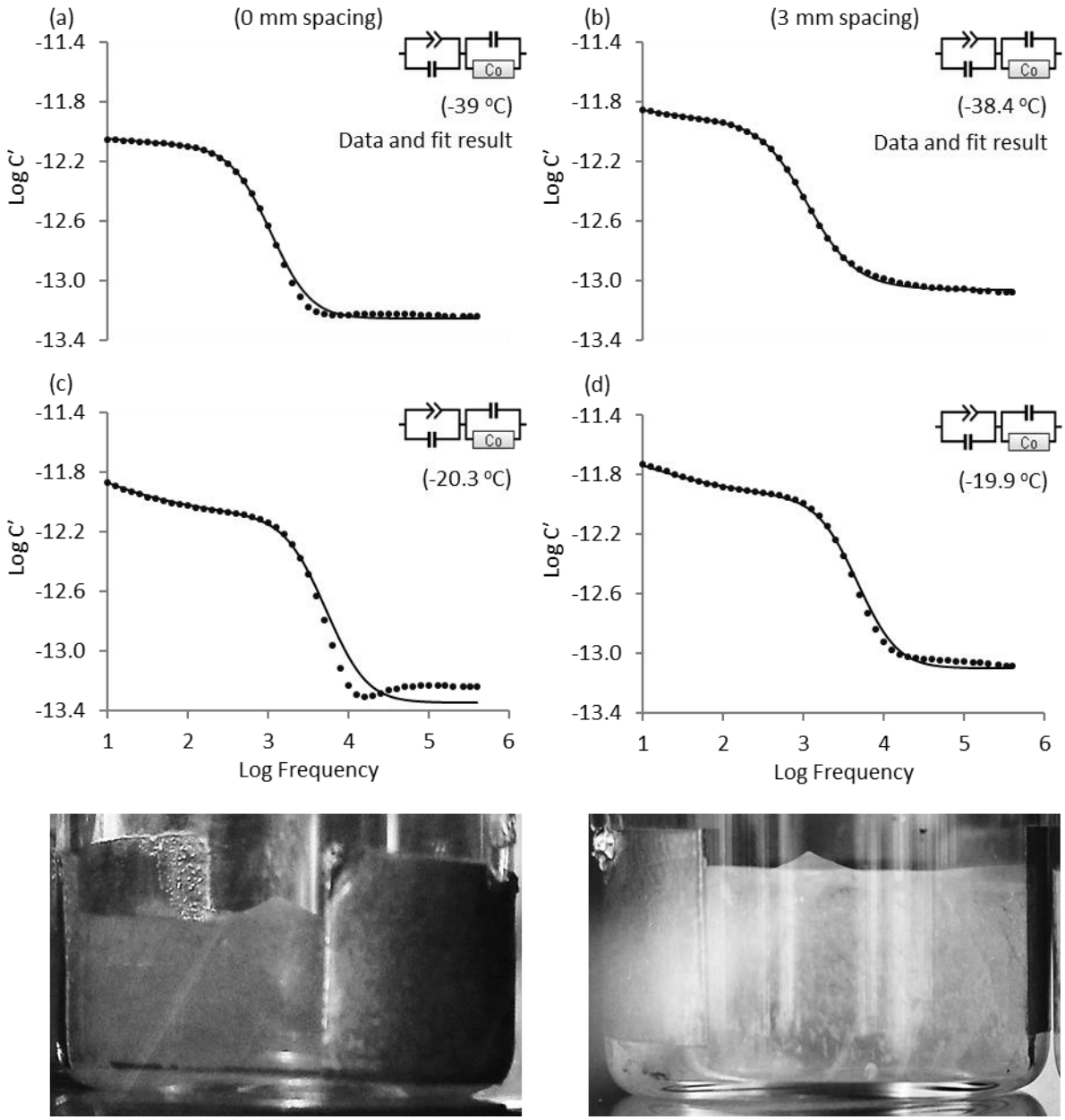

Figure 43 A qualitative comparison between spectra and a CPE=CG-Cs=Co model fit for the TVIS vials with a 0 mm spacing and a 3 mm spacing containing ice at two similar temperatures during a re-heating ramp: (a) & (b) log of real part capacitance plotted against log frequency at -39 ±0.5 °C for the 0 mm spacing and the 3 mm spacing respectively; (c) & (d) log of the real part capacitance plotted against log frequency at -20 ±0.5 °C for the 0 mm and the 3 mm spacing respectively. Experimental data and the model fit are shown as datapoints and lines respectively. A photograph of each vial full of ice, taken during re-heating is shown below the plots.

Figure 44 shows the real part spectra (a to j) of ice in the TVIS vial with the 0 mm spacing obtained at various time-points over the first ~5 h of primary drying, along with the fit results from the enhanced model for the TVIS vial. It is evident that the spectra are severely distorted over the first 1.8 h of primary drying (plots a to e); however, as the dielectric relaxation process becomes smaller through the course of ice sublimation, the distortion appears to have minimised until it is not visible (plots f to j).

A composite of real part spectra is also presented for the 3 mm spacing in Figure 45 over the first ~6.5 h of primary drying. Clearly, there is no distortion visible over the first ~2.4 h of primary drying (plots a to c); however, it appears that a small degree of distortion becomes apparent as the strength of the dielectric relaxation process reduces. In general, it can be concluded that the distortion in the spectra and the fitting of the model are worse for the 0 mm spacing.

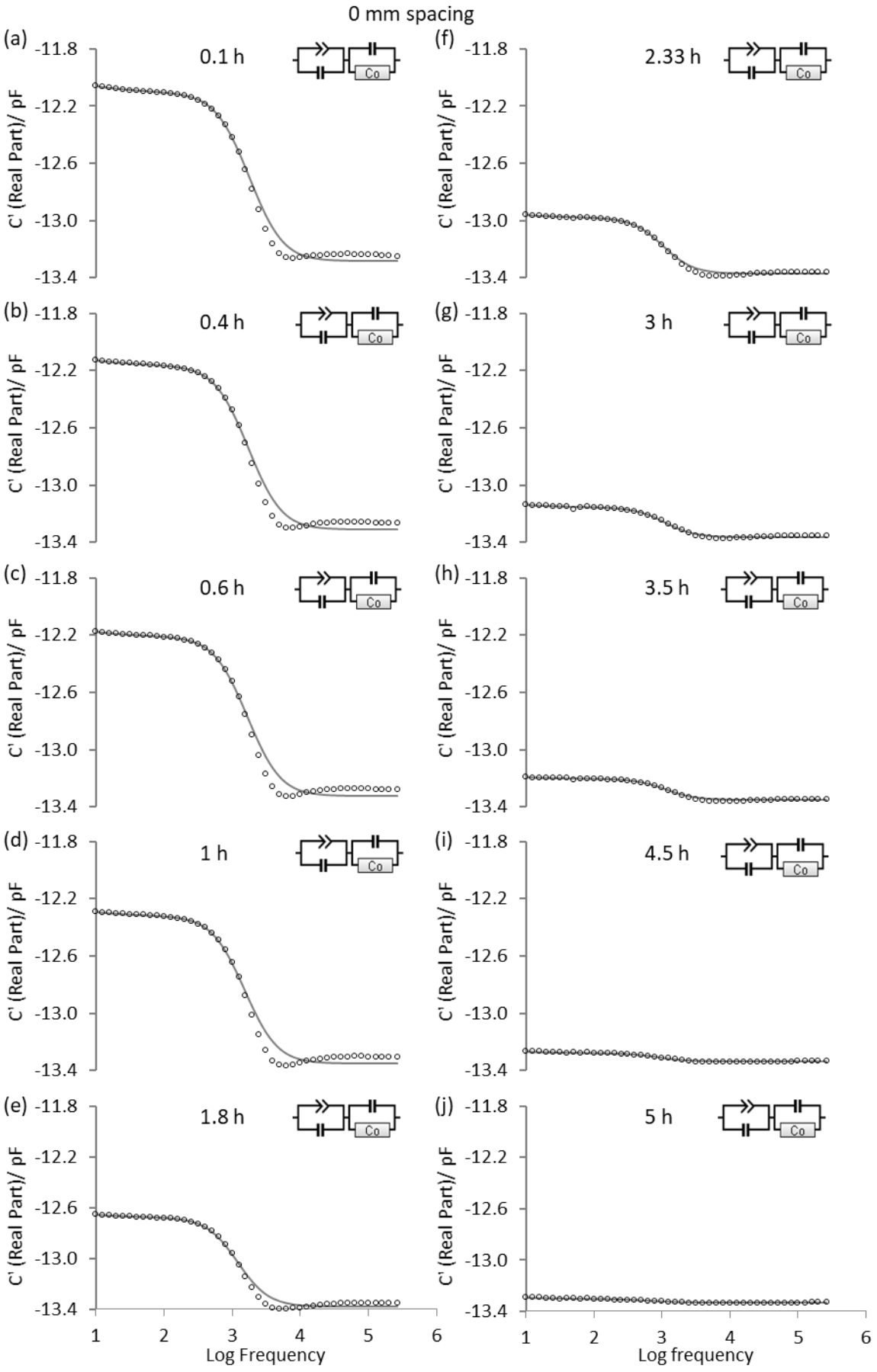

Figure 44: Bode plots (a to j) showing the real part spectra of ice obtained at various time-points during the primary drying phase for the 0 mm spacing. These have been fitted with the enhanced model for the TVIS vial to highlight the distorted part of the spectra

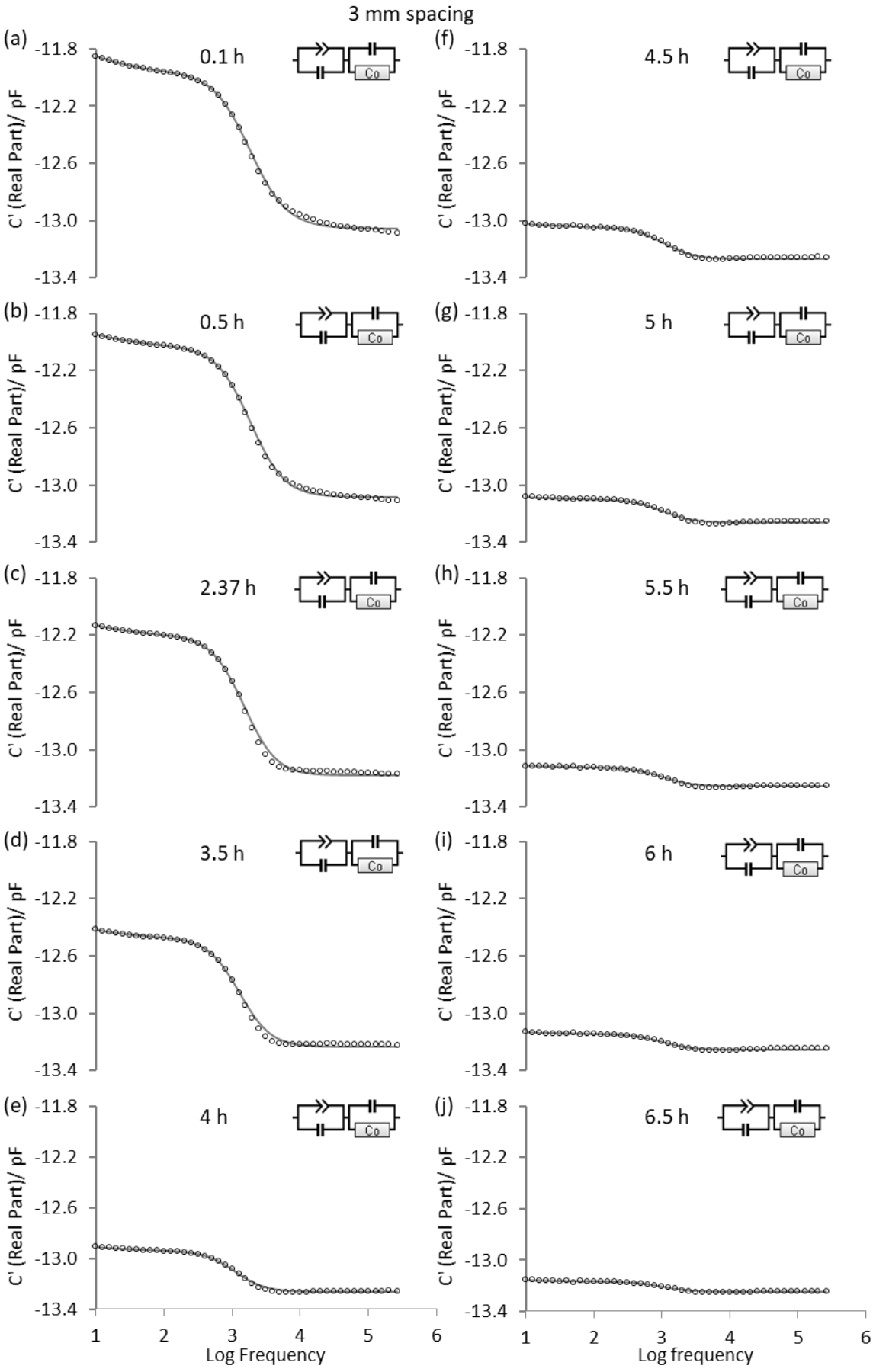

Figure 45 Bode plots (a to j) showing the real part spectra of ice obtained at various time-points during the primary drying phase for the 3 mm spacing. These have been fitted with the enhanced model for the TVIS vial to highlight the distorted part of the spectra.

From a quantitative viewpoint, the impact of the distortion in the spectra on the values of $C'(100kHz)$ may be better understood if the time-line of $C'(100kHz)$ is compared with the time-line of the lowest value of the capacitance in the distorted part of the spectrum during primary drying. Therefore, in Figure 46(a) & (b), the primary drying time-lines of $C'(100kHz)$ or C_H, and the lowest value of the real part capacitance in the distorted part of the spectra or C_D have been plotted on the primary Y-axis; and on the secondary Y-axis, the percentage distortion calculated over the same period using Equation 12, i.e.

$$\%\ distortion = \frac{C_H - C_D}{C_H} \times 100 \qquad \text{Equation 12}$$

where C_H is the value of $C'(100kHz)$ and C_H is the lowest value of the capacitance in the distorted part of the spectrum at any given time during primary drying.

It is clear from Figure 46(a) & (b) that the shapes of C_H and C_D are similar in the sense that their time-lines "dip" to a minimum value and then recover. Further, the difference between C_H and C_D increases until ~1 h of primary drying which manifests as a peak in the % distortion for the 0 mm spacing. Thereafter, C_D starts to approach C_H, hence a decrease in the % distortion. In contrast, in the case of the 3 mm spacing (Figure 46b), the values of C_D are higher than C_H because there is no distortion in the spectra, and therefore, % distortion is negative. However, a small degree of distortion surfaces after ~2 h of primary drying as the value of C_D goes below C_H which amounts to a % distortion of ~5 %. Nevertheless, even this small percentage decreases to zero by 10 h as C_D approaches C_H. The key observation here is that the distortion in the spectra may not be strongly impacting the observed dip and recovery of $C'(100kHz)$ because even the time-line of C_D has a dip and recovery. It would be interesting to investigate how the shape of the ice sublimation front might throw some light on the observed trajectory of $C'(100kHz)$.

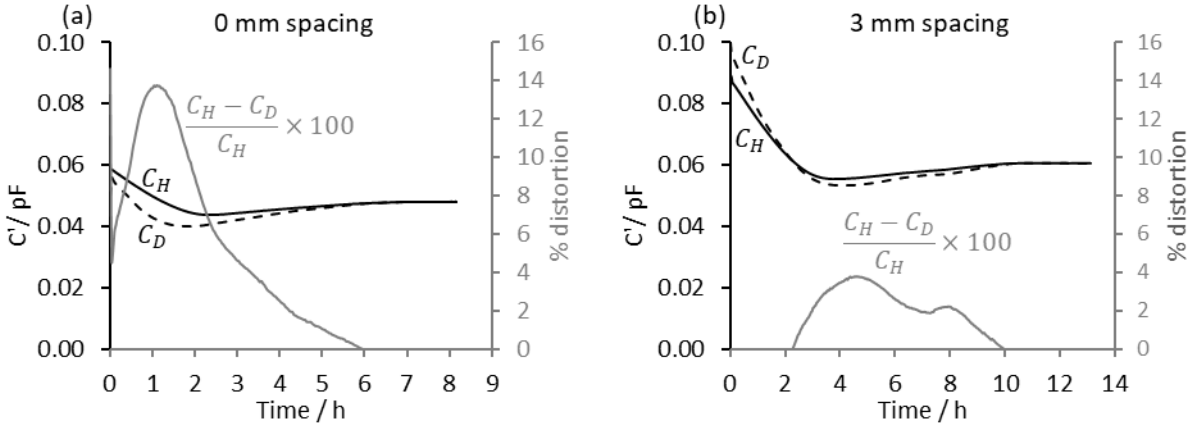

Figure 46: Determination of % distortion in the spectra in the real part during primary drying: (a) & (b) On the primary Y axis are the time-lines of $C'(100\text{kHz})$ or C_H, and the lowest value of real part capacitance in the distorted part of the spectrum, C_D for the 0 mm and the 3 mm spacing respectively. On the secondary Y-axis are shown the time-lines of the % distortion in the spectra for the 0 mm and the 3 mm spacing respectively.

5.3.2 The Features of the Primary Drying Curve of $C'(100kHz)$

Figure 47(a) & (b) show the time-lines of $C'(100kHz)$ and the process parameters (shelf temperature and chamber pressure) respectively during the primary drying stage for the 0 mm electrode spacing. A composite of the photographs of the sublimation front taken at various time-points during primary drying is presented below the time-line of $C'(100kHz)$ in order to map the changes in the shape of the sublimation front onto the different facets of the $C'(100kHz)$ time-line. The key stages and the corresponding photographs have been marked by letters enclosed within boxes. It is clear from Figure 47(a) that the magnitude of $C'(100kHz)$ decreases linearly over the first $\sim$1 h of primary drying, i.e. from point A (0 h) to B (1 h), referred to as the **linear drying phase**. The photograph (i to v) taken during this period demonstrate that the sublimation interface, initially comprising largely of an ice cylinder (and a cone above the cylinder) in intimate contact with the glass wall dries in a horizontal plane parallel to the vial base. This is usually observed when the relative heat contributions from the various heat sources do not change (Pikal, et al. 1984).

However, from point B (1 h) to C (2.33 h), the trajectory of $C'(100kHz)$ becomes non-linear as the rate of change in $C'(100kHz)$ decreases. Over this **non-linear drying phase**, some dramatic

changes in the shape of the sublimation interface occur as demonstrated in the photographs v to x: the preferential removal of the ice mass from the sides resulting in the loss of the glass wall-ice contact as well as the ice cylinder decreasing in height which is owed to a greater heat contribution via heat radiation from the dryer door (Pikal, et al. 1984) and possibly a small contribution via the conduction of air surrounding the vial (Scutella, et al. 2017). It is clear from the photograph x at 2.33 h that the ice cylinder disappears leaving behind an ice dome that is still in contact with point where side wall meets the vial base. This is also the point (C) when the drying curve of $C'(100kHz)$ reaches a minimum (~44 fF), hereafter referred to as the "**dip**" in the time-line of $C'(100kHz)$.

During the period between point C (2.33 h) and D (10.4 h), the drying curve changes its course as the magnitude of $C'(100kHz)$ increases from 44 fF to ~48 fF, hence termed as the **recovery phase**. The photographs x to xv show how the ice dome shrinks towards the centre of the vial base. It is interesting to note that $C'(100kHz)$ continues to recover until the last trace of ice is left in the vial (picture xiv at 6.37 h) and the recovery is completed when $C'(100kHz)$ reaches a **plateau** (10.4 h), which is synchronous with the visual endpoint of ice sublimation as seen in photograph xv.

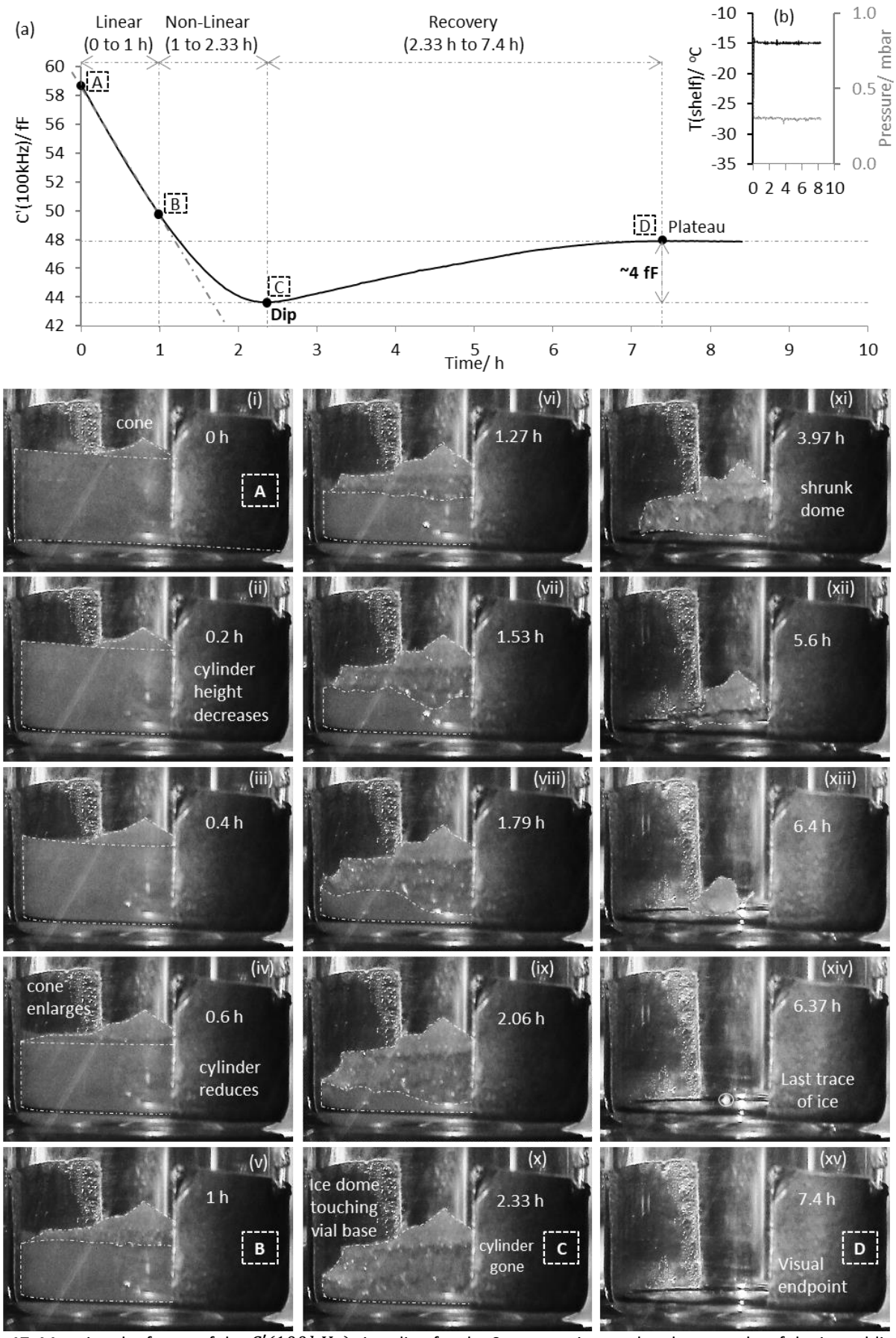

Figure 47: Mapping the facets of the $C'(100kHz)$ time-line for the 0 mm spacing on the photographs of the ice sublimation interface during the primary drying phase: (a) Time-line of $C'(100kHz)$ with phases marked A to B, B to C and C to D, which correspond to the linear drying phase, non-linear drying phase and the recovery phase respectively. Shown below are the photographs of the sublimation front at various time-points, where i to v, vi to x and xi to xv were taken during the linear phase, non-linear phase and the recovery phase respectively. Point D, termed "plateau" corresponds to the visual endpoint of ice sublimation (7.4 h); (b) time-line of the shelf temperature and the chamber pressure during primary drying.

Figure 48 demonstrates the features of the ice sublimation front mapped onto the trajectory of $C'(100kHz)$ for the 3 mm spacing, which in many respects are similar to the features observed for the 0 mm spacing. The drying curve of $C'(100kHz)$ as in Figure 48(a) consists of three distinct phases, i.e. the linear drying phase from point A to B (0.1 to 1.5 h), the non-linear phase from point B to C (1.5 h to 3.5 h) and the recovery phase from point C to D (3.5 h to 10.7 h). It is interesting to note that just like the dip in $C'(100kHz)$ for the 0 mm spacing as previously identified in Figure 47(a), the dip in the time-line of $C'(100kHz)$ at 3.5 h for the 3 mm spacing also corresponds to the point when the ice cylinder transforms completely into an ice dome with its sides still in contact with the point where side wall meets the vial bottom (picture x). From a freeze-drying modelling perspective, this is an important result because it suggests that the position of the dip in the time-line corresponds to an ice dome that touches the point where the side wall meets the vial base irrespective of the electrode position on the vial.

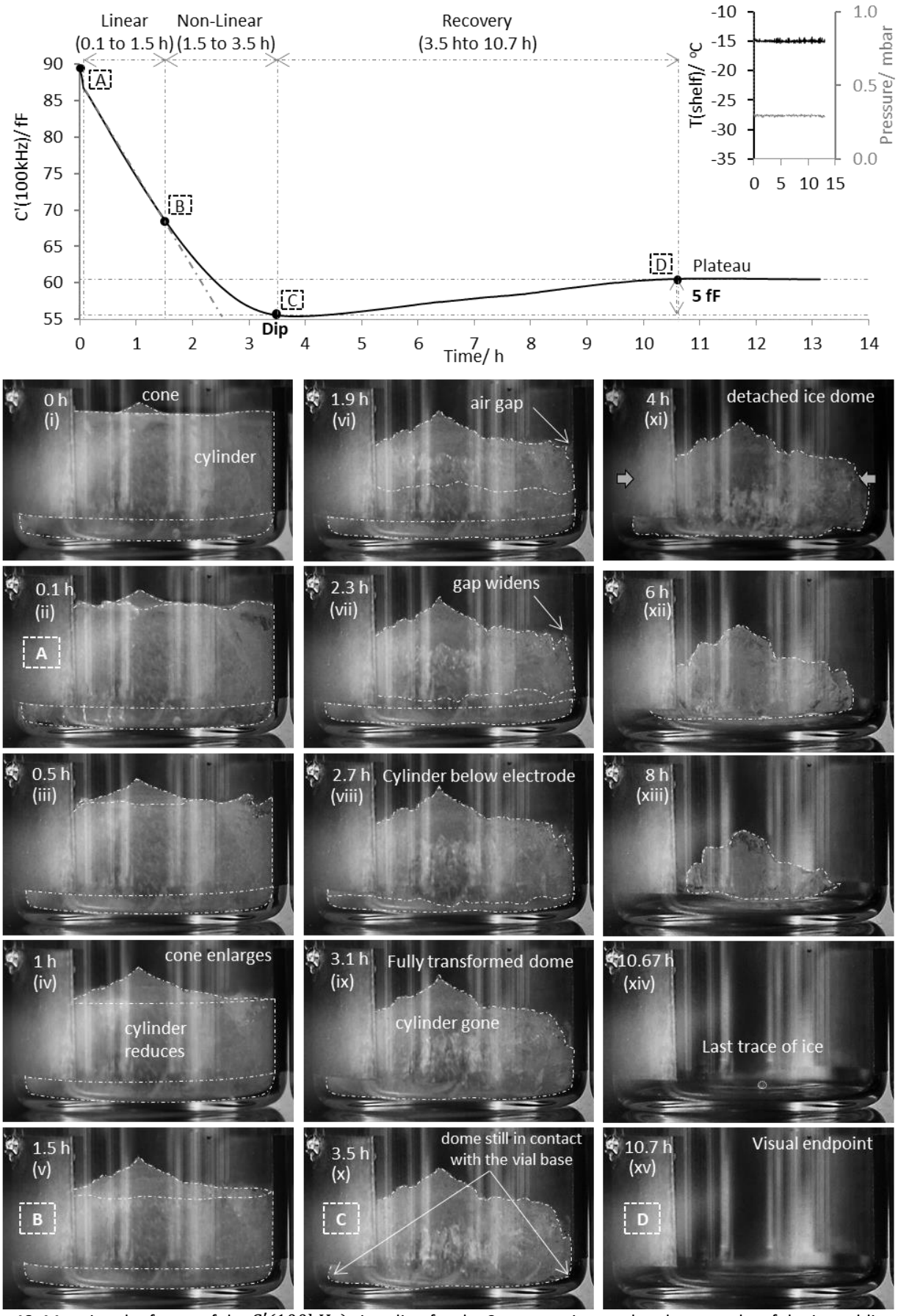

Figure 48: Mapping the facets of the $C'(100\text{kHz})$ time-line for the 3 mm spacing on the photographs of the ice sublimation interface during the primary drying phase: (a) Time-line of $C'(100\text{kHz})$ with the phases marked A to B, B to C and C to D correspond to the linear drying phase, non-linear drying phase and the recovery phase respectively. Shown below are the photographs of the sublimation front at various time-points, where i to v, vi to x and xi to xv were taken during the linear phase, non-linear phase and the recovery phase respectively. Point D, termed "plateau" corresponds to the visual endpoint of ice sublimation (10.7 h); (b) time-line of the process parameters.

5.3.3 The Mechanisms Underlying the Distortion in the Spectra and the Trajectory of $\mathbf{C'(100kHz)}$

The key observations that can be made on the quality of the spectra and the time-line of $\mathrm{C'(100kHz)}$ include: (i) the distortion in the spectra and model fit are worse for the 0 mm spacing when the vial is full of ice; (ii) the spectra during primary drying are more distorted when the electrodes are in close proximity to the shelf (0 mm spacing) than when they are placed 3 mm above the vial base; (iii) there is a systematic decrease in the distortion as more ice mass sublimates; (v) the time-line of $\mathrm{C'(100kHz)}$ can be divided into a linear phase, non-linear phase that ends in a dip followed by plateau through a recovery phase. These observations may be explained by a contribution from two competing mechanisms: (A): coupling between the electrode-glass-ice composite with the grounded shelf, and (B): an ever-decreasing contribution from an interfacial capacitance to the overall measured capacitance. In order understand the electrode-shelf coupling mechanism, it is important to take note of Equation 13 which describes the relationship between the electric field strength and the charge density between the electrodes of a parallel plate capacitor (Cutnell and Johnson 2012),

$$E = \frac{\sigma}{\varepsilon_0} \qquad \text{Equation 13}$$

where σ is the charge density (charge per unit area) and ε_0 is the permittivity of free space.

It is known that for a capacitor with infinitely long parallel plates placed in an electric field, the electric field strength is represented by parallel field lines which are equidistant from each other, which is reflective of the same magnitude and direction at all points (strong field strength). In contrast, for a capacitor with parallel plates having a finite length (Cutnell and Johnson 2012) the field strength increasingly weakens as one approaches the periphery of the electrodes, which is represented as curved field lines with an ever-increasing distance from one peripheral field line to the next, also referred to as the fringing field lines.

The two isolated TVIS vials are simplified parallel plate electrode-glass composite capacitors with copper electrodes of a finite length (10 mm). It has been established previously that the electrodes are most sensitive in the region bounded between the distance of 2 mm and 8 mm from

the bottom edges of the electrodes (Smith and Polygalov 2019). This is demonstrated in Figure 49, where a pair of oppositely charged electrodes (enlarged for clarity) are positioned in close proximity to the shelf (0 mm from the vial base), and in Figure 50, where the electrodes have been placed further away from the shelf to represent a 3 mm electrode gap. The electric field strength between the 2 mm and the 8 mm positions from the bottom edge of the electrodes (see marking on the electrodes) can then be represented as parallel field lines, and those closer to the periphery can be represented as fringing field lines.

The mechanism of interfacial capacitance is based on the theory of double layer capacitance which is demonstrated in Figure 49. An application of an alternating voltage to the TVIS vial containing ice, results in a charge accumulation at the electrode-glass interface (electrode polarisation), denoted by C_g and a dielectric relaxation of ice (~1 kHz), denoted by C_s. In addition, due to the blocking nature of the electrodes, some of the oppositely charged carriers in ice are attracted to the positively charged glass-ice interface, in a region referred to as the stern layer (Orazem and Tribollet 2017). This charge accumulation at the glass-ice has been referred to as the interfacial capacitance, C_i.

It has been established previously that the high frequency capacitance is an inverse sum of the glass wall capacitance, C_g, in series with the sample capacitance, C_s. Thus, the real part capacitance at high frequencies is (Smith and Polygalov 2019):

$$\mathrm{C}'(\infty) = \frac{C_g . C_s}{C_g + C_s} \qquad \text{Equation 14}$$

However, it is also true that when the ice cylinder is in intimate contact with the glass wall, there is a contribution from C_i, which when added in series with C_g, will potentially reduce the effective glass wall capacitance as per Equation 15, i.e.

$$C_g^{effective} = \frac{C_g . C_i}{C_g + C_i} \qquad \text{Equation 15}$$

where $C_g^{effective}$ is the net glass wall capacitance, which is lower than the value of C_g. As a consequence, the value of $\mathrm{C}'(\infty)$ in Equation 14 is going to decrease.

5.3.4 Relative contribution from the mechanisms when the vial is full of ice

As shown previously, when the TVIS vials are full of ice (beginning of primary drying), the ice cylinder is in intimate contact with the glass wall. For the 0 mm spacing, most of the fringing field lines are thought to become distorted as they pass through the ice cylinder in intimate contact with the glass wall/vial base which in turn, is coupled to the grounded shelf (Figure 49). As a result, some of the charge is able to migrate through the vial base into the grounded shelf, hence the term lost capacitance to ground, denoted by C_{gr} in Figure 49. In contrast, most of the fringing field lines are thought to be confined within the vial base for the 3 mm spacing (Figure 50) and therefore, there doesn't appear to be a strong conductive pathway between the electrodes and the shelf. Thus, the lost capacitance to ground manifests as differing degrees of distortion amongst the two electrode spacings, which in turn manifests as a decrease in the magnitude of $C'(100kHz)$ during the linear drying phase. Further, it is important to recognise that the decrease in the dielectric strength of the relaxation process during primary drying will itself lower the magnitude of $C'(100kHz)$. As the magnitudes of C_g, C_i and C_s are expected to decrease at a constant rate, so does the magnitude of $C'(100kHz)$.

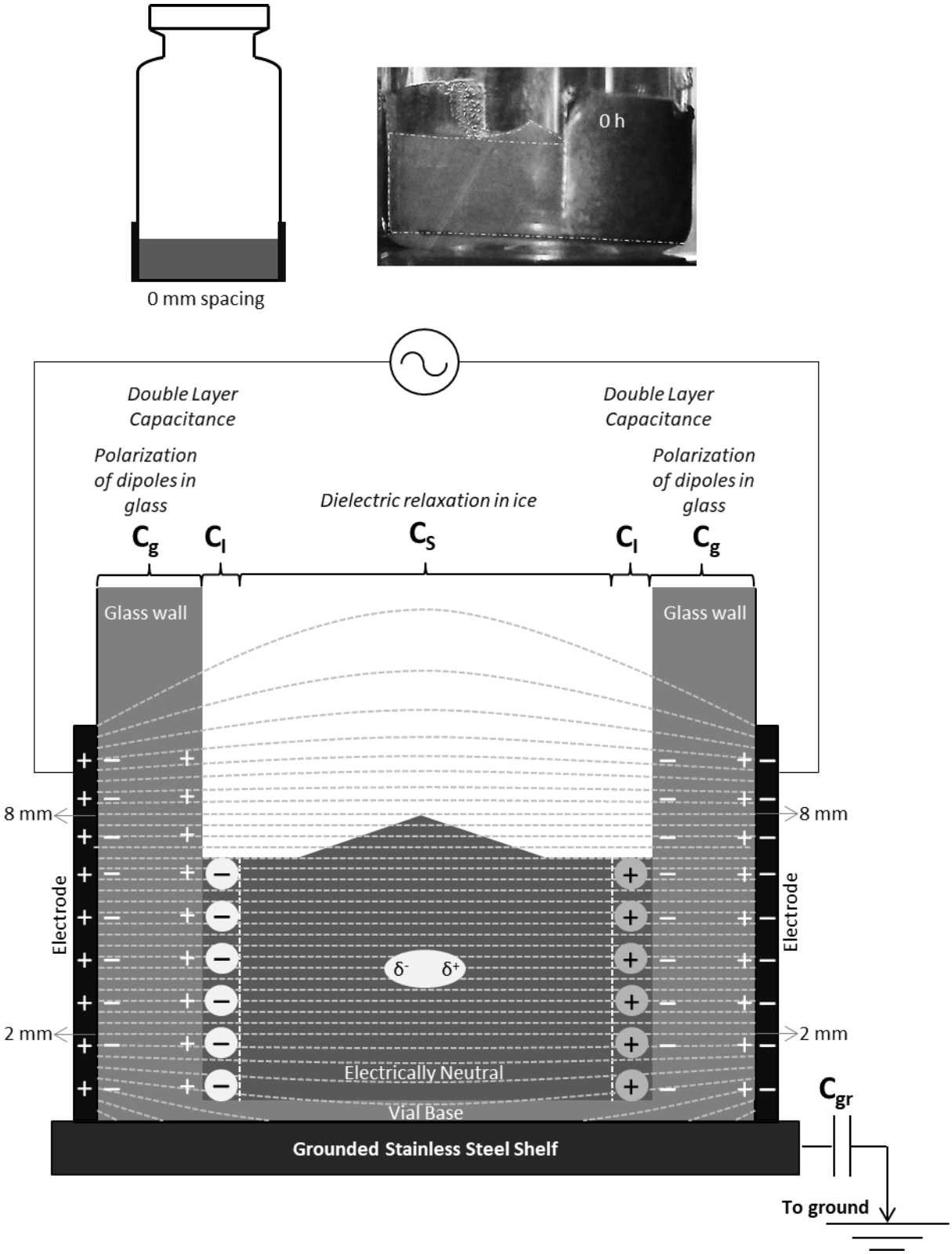

Figure 49: An illustration of the observed distortion in the spectra for ice contained in the TVIS vial with electrodes positioned in close proximity to the grounded shelf (0 mm spacing). The region of high electric field strength represented by parallel field lines starts 2 mm from the bottom edge and finishes at 8 mm from the bottom edge. The electric field above 8 mm and below 2 mm is represented by fringing field lines. Most of the fringing field lines near the lower edge pass through the electrode-glass composite allowing for a conductive path for current to leak through the grounded shelf, termed lost capacitance to ground or C_{gr}. Also shown are different types of polarisation phenomena that manifest when the vial is full of ice, i.e. charge accumulation at the electrode-glass wall interface (C_g) and a double layer capacitance (C_i) at the glass-ice interface, and the dielectric relaxation of water molecules in the electrically neutral ice bulk, represented by C_s.

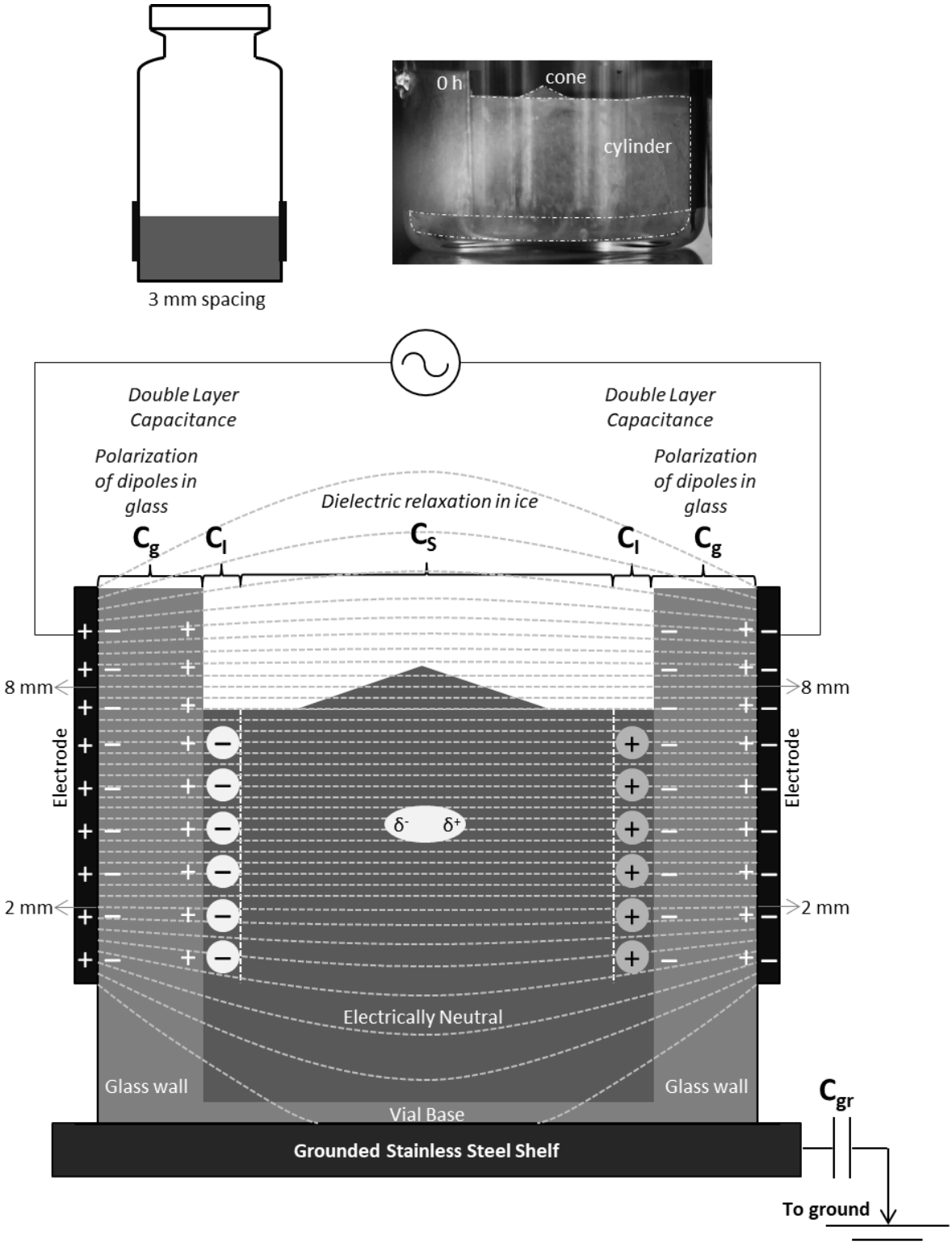

Figure 50: An illustration of the method for reducing the distortion in the real part spectra by positioning the electrodes 3 mm from the vial base. The region of high electric field strength represented by parallel field lines starts 2 mm from the bottom edge and finishes at 8 mm from the bottom edge. The electric field above 8 mm and below 2 mm is represented by fringing field lines. Most of the fringing field lines are confined within the vial base thereby allowing less charge migration through the grounded shelf, termed lost capacitance to ground or C_{gr}. Also shown are different types of polarisation phenomena that manifest when the vial is full of ice, i.e. charge accumulation at the electrode-glass wall interface (C_g) and a double layer capacitance (C_i) at the glass-ice interface, and the dielectric relaxation of water molecules in the electrically neutral ice bulk, represented by C_s.

5.3.5 Relative contribution from the mechanisms during the non-linear and the recovery phases

During the non-linear drying phase, the ice cylinder reduces in height faster than the ice mass in the centre leaving behind an ice dome which results in air gaps appearing between the glass wall and the ice dome; in effect that is likely to change the effective dielectric constant of the medium which now has a contribution from the air fraction as well. This situation may be analogous to spheres in a homogenous medium where the overall dielectric response is governed by the dielectric properties of the spheres, the dielectric properties of the medium, and the relative proportions of each (i.e. volume fraction) as per the effective dielectric medium theory (Giordano 2003).

Further, the observed curvature in the time-line of $\mathrm{C}'(100\mathrm{kHz})$ might be related to a lesser contribution from C_i as the area of the contact between the glass wall and the ice mass decreases, which in turn is expected to increase the measured capacitance. This is illustrated in Figure 51(a), where an ice dome over a small ice cylinder in contact with the side wall is drawn. However, it could be argued that there is also a contribution from the leakage capacitance to the ground, particularly in the case of the 0 mm spacing, since the ice mass is still in contact with the glass wall/vial base.

The last time-point of the non-linear phase is the dip in the time-line of $\mathrm{C}'(100\mathrm{kHz})$ for both the electrode spacings which corresponds to the point when the ice dome is no longer in an intimate contact with the side wall. At this point, it is expected that the contribution from C_i is non-existent (no side wall interface) and the effective dielectric medium has a greater contribution from air. Finally, as the ice mass shrinks away from the circumference of the vial base, the distortion in the spectra decreases which suggests the conductive pathway to ground is lost as demonstrated in Figure 51(b).

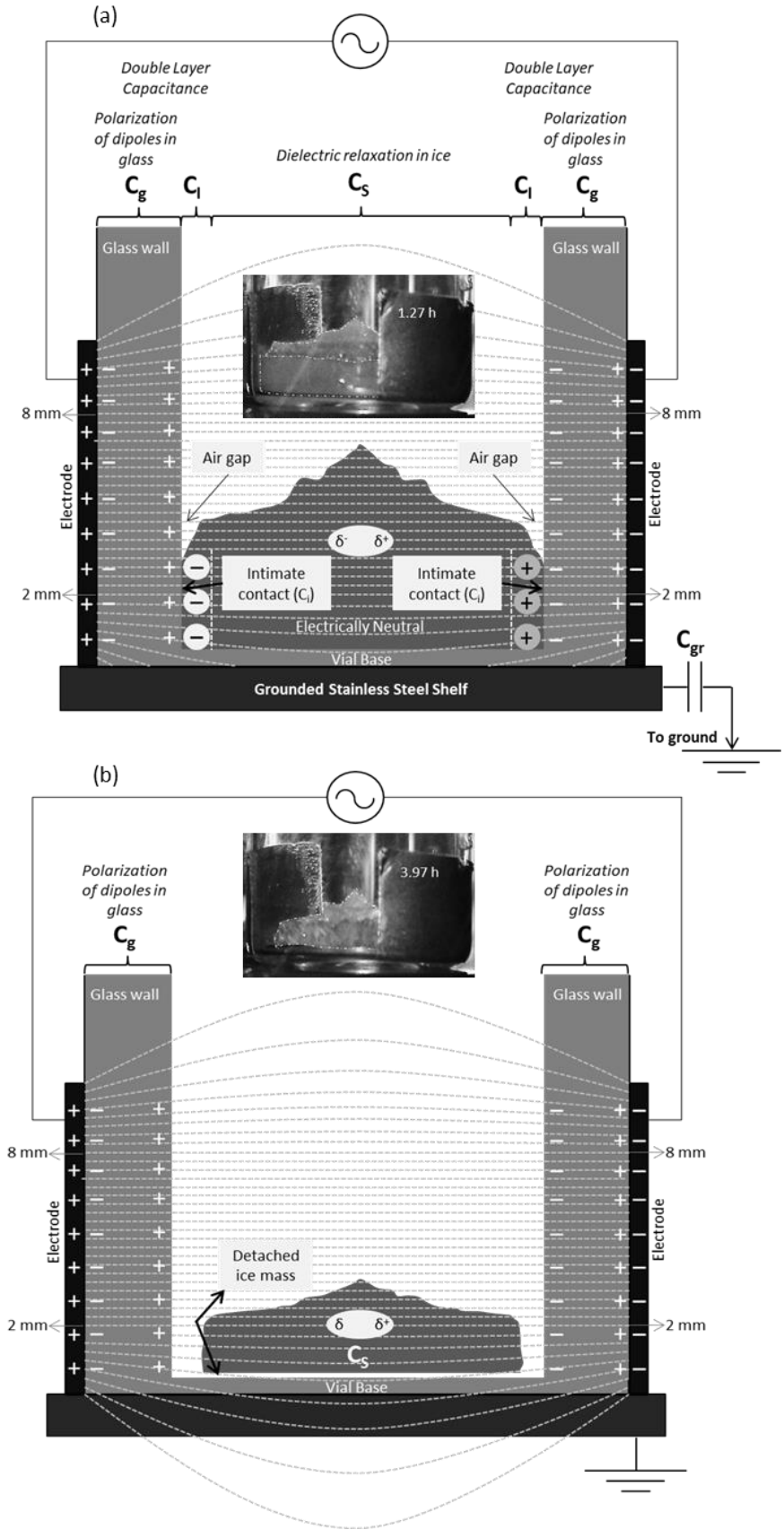

Figure 51: An illustration of the contributions from two competing mechanisms to the observed shape of the trajectory of $C'(100kHz)$ for the 0 mm spacing during (a) the non-linear phase: the ice cylinder height has reduced but it is still in intimate contact with the side wall. Possible mechanisms include charge leakage through the grounded shelf (i.e. C_{gr}) as the intimate contact is still present and a lesser contribution from the interfacial capacitance, C_i, as the area of intimate contact reduces; (b) Recovery phase: ice mass shrinks away from the side wall losing intimate contact, i.e. C_i is non-existent and C_{gr} almost negligible.

5.3.6 Summary on the Contributing Mechanisms

Two possible competing mechanisms have been identified which contribute to the shape of the trajectory of $C'100kHz$ which mirrors the changes in the shape of the ice sublimation front during primary drying. The first is the lost capacitance to ground that manifests as a distortion in the spectra, and other is the presence of an interfacial capacitance at the glass-ice interface. The extent of distortion seems to depend on two factors: (i) the distance between the electrodes and the vial base, and (ii) the intimate contact between the glass wall and the ice cylinder. During the first few hours of primary drying, when the ice cylinder height decreases in a linear fashion and continues to maintain an intimate contact with the glass wall, the distortion in the spectra is worse for the 0 mm electrode spacing (no distortion in the 3 mm spacing), which is a consequence of a stronger conductive pathway for charge migration through the ice cylinder-glass-electrode composite to the grounded shelf. The fact that the magnitude of $C'100kHz$ decreases linearly with time (linear drying phase) in the case of both the electrode spacings may be solely attributed to the reduction of the dielectric strength as the ice cylinder reduces in height.

During the non-linear phase, when the ice cylinder decreases in height faster than the ice mass in the centre, the surface area of the intimate contact between the ice cylinder and glass wall continuously reduces which is expected to bring down the magnitude of the interfacial capacitance. In effect, the effective glass wall capacitance increases (Equation 15) and therefore, net capacitance of the system increases (Equation 1), hence a slower the rate of reduction in $C'100kHz$ during the non-linear phase. Over the same period there is some indication that the distortion in the 3 mm electrode spacing appears briefly and that may be attributed to the weakening of the strength of the dielectric relaxation process of ice. By the time $C'100kHz$ reaches a minimum or what has been referred to as the dip in the time-line, the ice cylinder has already transformed into an ice dome with its sides touching the point where the glass wall and the vial base meet. From this point forward, the contribution from the lost capacitance to ground and the interfacial capacitance are non-existent due to no side wall-ice contact. As the ice mass starts to shrink towards the centre of the vial base, it implies

that the vial base-ice contact area also decreases which then allows for the lost capacitance to recover, hence a continuous reduction in the % distortion as $C'100kHz$ increases (recovery phase) until it reaches a pseudo-steady state plateau which corresponds to the visual endpoint of ice sublimation.

5.3.7 Primary Drying Endpoint in Vials with Thermocouples

Figure 52(a) shows the primary drying time-line of the shelf temperature, the chamber pressure and the centre-bottom product temperature from a thermocouple (TC) in each of the vials adjacent to the front, the back and the core TVIS vials that were freeze-dried as part of the batch study. Note the nomenclature of the product temperature profiles T(TC-front), T(TC-back) and T(TC-core). The photographs of the ice mass (i to ix) in the front vial TC vial captured at various time-points during primary drying presented below the process parameter plot demonstrate that the ice mass along the side walls of the glass wall sublimates faster than the ice mass in the centre.

The time-profile of T(TC-front) has three distinct inflections, i.e. 0.57 h (A), 10.8 h (B) and 12.47 h (C). The photograph vii captured at 10.8 h reveals how the sensing element is exposed to the ambient environment in the TC vial, which manifests as the second inflection in T(TC-front) at B as the thermocouple starts to register the air temperature which is warmer than the ice temperature. It follows that the infection at A (0.57 h) must be the first indication of the point when the ice mass loses thermal contact with the sensing element.

The third inflection in T(TC-front) at C (12.47 h) corresponds to the visual endpoint as demonstrated in photograph ix. An increase in temperature from 12.47 h to 17.67 h is due to the thermocouple approaching the ambient air temperature of the empty vial or what is referred to as the pseudo-steady state plateau for the primary drying endpoint. However, it is clear that the product temperature profile of an edge vial is not representative of the profiles of the internal TC vials. For instance, although the nature of the first inflection in the time profiles of T(TC-back) and T(TC-core) at ~1 h and ~4 h respectively is similar to that of T(TC-front), the second inflection for the internal TC vials is clearly not discernible. The third inflection for both the internal TC vials occurs at 17.67 h which

suggests that the ice sublimation is complete and yet the ice sublimation is completed in the TC containing vial ∼1 h 22 min earlier than in the vials in its immediate vicinity (Figure 53), which is consistent with the fact that probe containing vials dry faster than the vials without probes. Therefore, a few more hours of primary drying after reaching the plateau are recommended to account for this period of uncertainty.

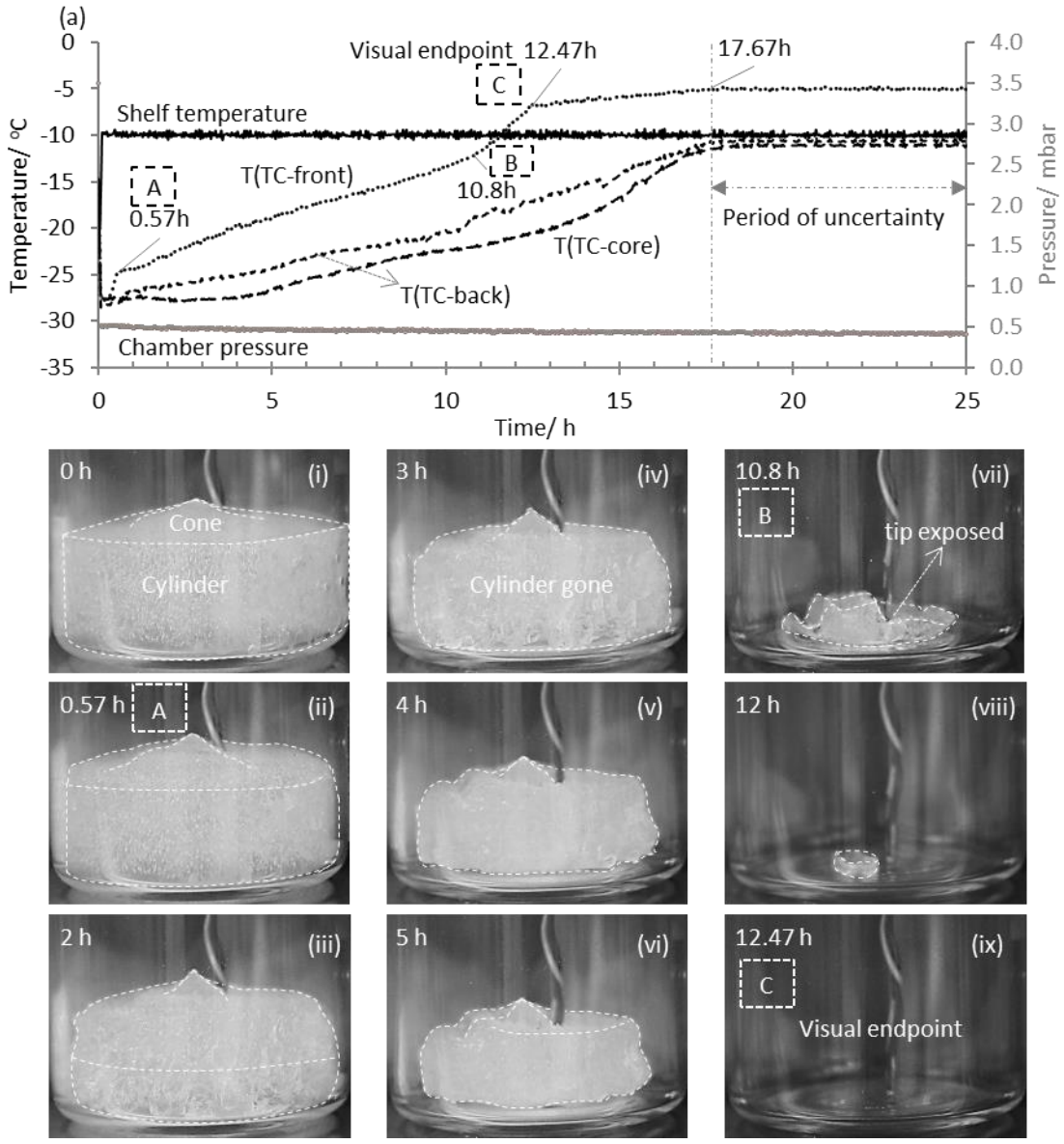

Figure 52: Determination of the primary drying endpoint in vials containing thermocouples: (a) time-lines of the process parameters, namely the shelf temperature, the chamber pressure and the product temperature, T(TC-front), T(TC-back) and T(TC-core), at the bottom-centre of the vial adjacent to each of the three TVIS vials located at the front edge of the shelf, the back edge of the shelf and in the core. Also shown below are the photographs of the ice mass in the front TC vial taken at various time-points during primary drying. The key events correspond to three inflections in the time profile of (TC-front) that have been time-marked and labelled with alphabets enclosed in dashed boxes, which are also annotated on the corresponding photographs at these time-points. An inflection at 0.57 h (A) corresponds to first indication of the loss of thermal contact between the ice mass and the sensing element of the thermocouple; the second inflection at 10.8 h (B) corresponds to the point when the thermocouple begins to register the ambient air temperature instead of the colder ice; and the inflection at 12.47 h (C) corresponds to the visual endpoint of ice sublimation. An inflection in the time profiles for the internal TC vials occurs at 17.67 h which corresponds to the beginning of a pseudo-steady state plateau. A double headed arrow is marked beyond 17.67 h in order to highlight the period of uncertainty in detecting the primary drying endpoint in the internal TC vials.

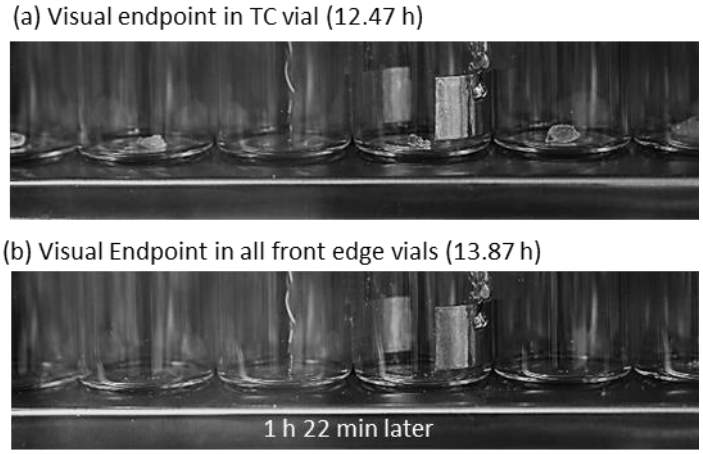

Figure 53: Photographs of the front edge vials showing that ice sublimation is completed in the TC vial 1 h 22 min earlier than the visual endpoint of ice sublimation in all front edge vials.

5.3.8 Primary Drying Endpoint in TVIS vials

In this part of the study, the primary drying stage is monitored for the TVIS vials with a 3 mm electrode spacing, at three shelf locations (the front, the back and the core) and the front TVIS vial is visually examined to track the visual endpoint. Further, a methodology for predicting the endpoint is described, which may be applied to a TVIS vial at any shelf location. The primary drying endpoint predicted from TVIS is hereafter simply referred to as the TVIS endpoint.

5.3.8.1 Criteria for Determining the Visual Endpoint in the Front TVIS Vial

A series of photographs (i to xi) taken at various time-points during the primary drying stage (Figure 55) demonstrate that the initial ice mass (4 g) reduces to a tiny ice crystal by 12 h and 54 min of primary drying. Finally, within the next 2 min (12:56), the ice is no longer visible in the photographs of the vial. It is worth noting that the ice may have disappeared at any point over this 2 min time interval. Since the time resolution of the photographic method is 2 min, the visual endpoint has been defined as the point when one doesn't see the ice, i.e. at 12:56.

Having determined the visual endpoint, it allows one to estimate a limit of detection of the ice mass. For this purpose, the ice mass captured at 12:42 (photograph ix) is assumed to be sphere. That then allows for the estimation of the sphere's diameter, $D_{sphere}^{estimated}$ (0.13 cm) using Equation 16, i.e.

$$D_{sphere}^{estimated} = \frac{H_{electrode}^{reference}}{H_{electrode}^{image}} \times D_{sphere}^{Image} \qquad \text{Equation 16}$$

where, $H_{electrode}^{reference}$ is the measured height of the electrode (1 cm), $H_{electrode}^{image}$ is the height of the electrode on photograph ix (i.e. length of the line drawn on the electrode is 1.5 cm) and D_{sphere}^{image} is the image diameter of the sphere denoted on photograph ix (i.e. 0.19 cm). The value of $D_{sphere}^{estimated}$ is then used to obtain an estimate for the sphere's volume (0.00106 cm^3). The sphere's volume and the density of ice (0.92 g cm^{-3}) are then used to calculate the ice mass (i.e. ~1 mg). Note that this value of the ice

mass (1 mg) was estimated 12 min (12:42; photograph ix) before the last ice crystal was still visible to the naked eye, i.e. at 12:54 (photograph x), which reduces the limit of detection from the photographic method to less than 1 mg.

5.3.8.2 Methodology for Predicting the TVIS Endpoint

An overview of the methodology is given in Figure 54, where the endpoint has been predicted using two methods. The first method is referred to as the retrospective method, wherein the data is analysed going forward in time. In other words, the endpoint is predicted retrospectively after reaching a point on the plateau, where it is safe to assume that all the ice has sublimated. In the second method, referred to as the real time method, can be applied in a situation where the endpoint is predicted by using the available data as one approaches the $\mathrm{C}'(100\mathrm{kHz})$ plateau. The methodology for defining the criteria for the prediction of the TVIS endpoint has been described in a number of steps and the results are presented in the order: front, back and core TVIS vial. The time-line of $\mathrm{C}'(100\mathrm{kHz})$ for the front TVIS vial during the primary drying stage (33 h 8 min) is presented on the primary Y-axis (solid black line) in Figure 55(a). The visual endpoint (12:56) has been marked with a dashed grey vertical line on the time-line of $\mathrm{C}'(100\mathrm{kHz})$ which appears to correspond to the end of the recovery phase, when the value of $\mathrm{C}'(100\mathrm{kHz})$ is constant at $\sim$71 fF.

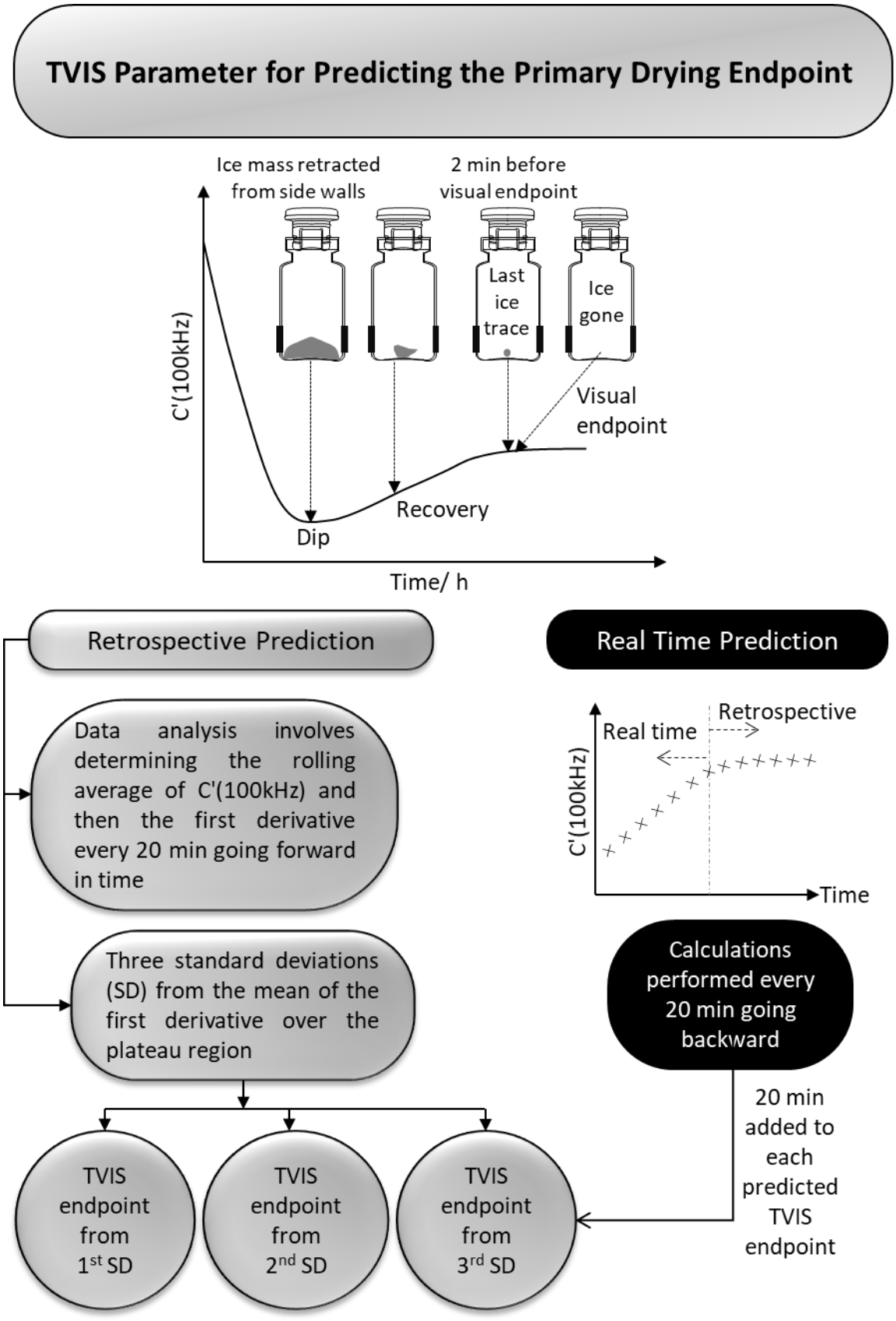

Figure 54: Overview of the methodology for the prediction of the primary drying endpoint using the TVIS parameter, $C'(100kHz)$.

Retrospective Prediction of the TVIS endpoint

Step 1: Determination of the rolling average of $C'(100kHz)$ and its first derivative

The **first step** is to determine the point when $C'(100kHz)$ reaches a plateau. For this purpose, a rolling average of $C'(100kHz)$ is determined retrospectively over every 20 min from the middle of the recovery phase (~8 h) until approximately the end of the process (32:50). Given the time resolution of the TVIS measurement is 2 min, the retrospective calculation involves the use of every 10 data points going forward in time. The time profile of the rolling average is shown as a solid grey line on the primary Y-axis in Figure 55(a). Of course, the reason for choosing 32:50 as the last datapoint is that the value of the rolling average at this time-point corresponds to the average of the last 10 measured values of $C'(100kHz)$**.** The above method is demonstrated in Figure 56(a), which shows two values, 67.4 fF and 69.5 fF, labelled on the time-line of $C'(100kHz)$ as examples, each of which is an average of the next 10 datapoints captured every 2 min from 9 h onwards and from 11 h onwards (shown as solid black lines), respectively. From the above discussion, one can imagine that the overall effect of having the rolling average determined retrospectively is that the time-line of rolling average shifts backward relative to that of $C'(100kHz)$ by 20 min.

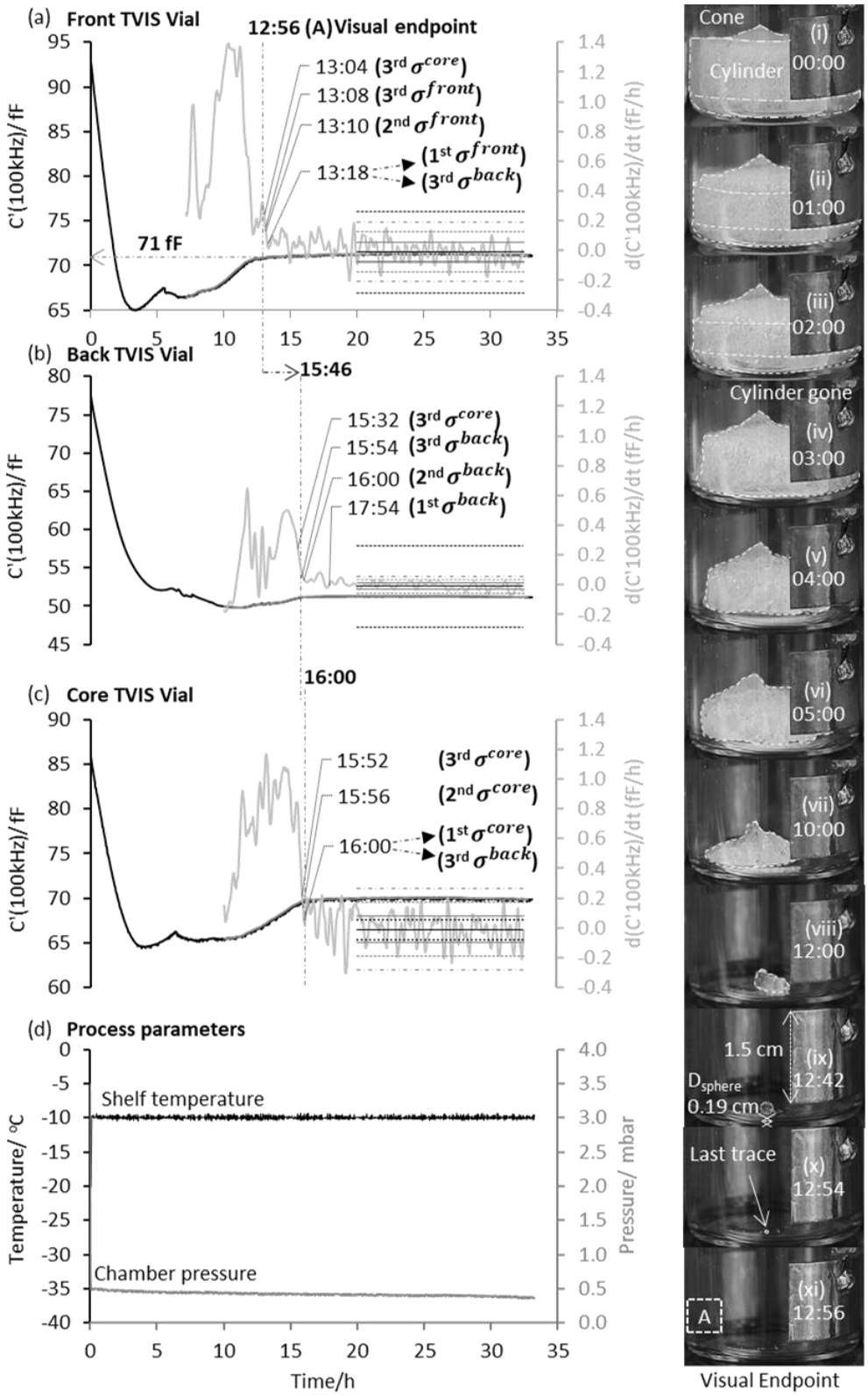

Figure 55: Determination of the visual endpoint and the prediction of TVIS endpoint: On the right: photographs of the front TVIS vial taken at various time-points with the visual endpoint at 12:56. The sphere of ice at 12:42 (photograph ix) corresponds to ~1 mg of ice, i.e. the limit of detection from the visual method. On the primary Y-axis (a) to (c) are the primary drying time-lines of $C'(100kHz)$ for the front, the back and the core TVIS vials respectively (solid black lines) with the rolling average determined retrospectively over every 20 min (solid grey lines); on the secondary Y-axis (a) to (c) are primary drying time-lines of the 1st derivative of the rolling average of $C'(100kHz)$, or $d(C'100kHz)/dt$ (also determined retrospectively over every 20 min). Also plotted are the values of the mean of $d(C'100kHz)/dt$ (solid black line passing through the scatter) for each vial, the upper and the lower limits of the 1st, 2nd and 3rd standard deviations (σ) from the mean (solid, dashed and dot-dashed grey lines). Finally, the values of the bands of the greatest variability from the core vial (3rd σ^{core}) have been applied to the front TVIS vial and the back TVIS vial (black dashed bands); and the least variability from the back TVIS vial (3rd σ^{back}) has been applied to the front TVIS vial and the core TVIS vial (dotted black bands). The labelled time-points are the predicted TVIS endpoints corresponding to each limiting criterion.

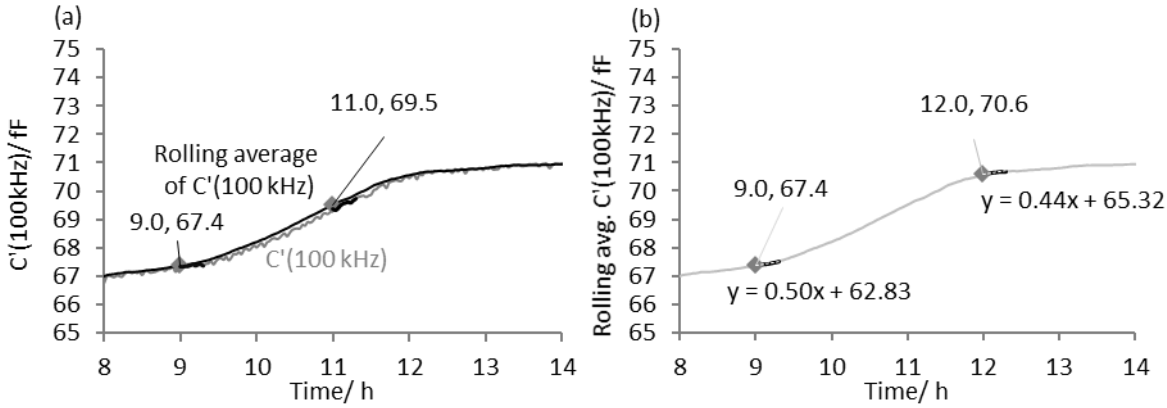

Figure 56: Demonstration of the method for determining the rolling average and the gradient of $C'(100kHz)$: (a) A part of the primary-drying time-line of $C'(100kHz)$ (light grey line) and its rolling average (black line) taken over every 20 min (10 datapoints). For illustration purposes, the datapoints shown as filled grey diamonds on the time-line of the rolling average at 9 h and 11 h are the averages of the datasets shown as solid black lines on the time-line of $C'(100kHz)$; (b) demonstration of a method for calculating the gradient of the rolling average, $d(C'100kHz)/dt$, taken over every 20 min (20 datapoints) at two time-points 9 h and 12 h shown as filled grey diamonds. The values of the gradient at these time-points have been derived from the datasets of the rolling average shown as solid black lines.

Thereafter, the first derivative of the rolling average, $d(C'100kHz)/dt$, is determined retrospectively over every 20 min from ~8 h of primary drying until the last available data-point (i.e. 32:32), which lies 20 min earlier than 32:50. The time-line of the first derivative (solid black line) is presented on the secondary Y-axis in Figure 55(a). Finally, Figure 56(b) shows the method for determining the value of the first derivative at two representative time-points. The Y-values corresponding to these time-points are the first derivatives of the next 10 datapoints on the time-line of the rolling average.

Step 2: Establishing the Limiting Criteria using the Three-Sigma Rule

It is clear from Figure 55(a) that the rate of change in $C'(100kHz)$ or the magnitude of the first derivative is much greater during the recovery than at beginning of the plateau, where it decreases to approximately zero, i.e. a few minutes after the visual endpoint (12:56). Thereafter, one cannot be certain about the point when $d(C'100kHz)/dt$ is equal to zero due to the fluctuation in the signal around zero over the remainder of the primary drying stage. The premise then is that once the first derivative drops below a threshold of variability around the scatter, it can be considered to be zero.

In **second** step, the general 68-95-99 rule or the three-sigma rule for a normal distribution (Trochim, et al. 2014) is applied to obtain the confidence limits of 68 %, 95 % and 99 %, which are within 1, 2 and 3 standard deviations (1st σ, 2nd σ and 3rd σ) respectively, from the mean (μ) value of the variability in the $d(C'100kHz)/dt$ signal measured between the time-points 20:00 and 32:32. Thus, in order to determine the upper and lower limit of 1st σ, the value of $1 \times RMSD$ is added to and subtracted from μ, respectively. Likewise, to determine the upper and lower limit of 2nd σ, the value of $2 \times RMSD$ is added to and deducted from μ, respectively. Finally, the upper and lower limit of 3rd σ determined by adding $3 \times RMSD$ to μ and deducting it from μ, respectively. The above calculations then allows for predicting a time point when the first derivative drops below the limiting criteria defined by the value (or number) of the standard deviation. For example, if the first derivative drops below the value of 2nd σ, then it is assumed that the probability of the first derivative being equal to zero is 95 %. In Figure 55(a), the value of μ is shown as a solid black line passing through the scatter, and the upper and the lower limits of the 1st σ, 2nd σ and 3rd σ for the front TVIS vial are shown as solid grey lines, dashed grey lines and dashed-dot grey lines respectively. Note the reason for establishing the limiting criteria over the last ~12.5 h period, is that this period corresponds to the plateau regions for all the TVIS vials, which allows one to assume that all the ice is removed by 20 h of primary drying.

Impact of the limiting criteria on the predicted TVIS endpoint

Having established the three sets of limiting criteria, the next stage of the second step is to explore the impact of the standard deviations on the predicted TVIS endpoint. As discussed previously, the point at which the value of $d(C'100kHz)/dt$ drops below a threshold, as defined by the three standard deviations, has been considered to be the beginning of "no change" or equal to zero. Thus, the predicted TVIS endpoint corresponding to 1st σ, 2nd σ and 3rd σ lies at 13:18, 13:10 and 13:08, respectively. These time-points have been marked on the time-line of the first derivative in Figure 55(a) and given in Table 9, which also includes the values of each standard deviation (upper limit) determined for the front TVIS vial. Note the nomenclature of these standard deviations for the front TVIS vial: 1st σ^{front}, 2nd σ^{front} and 3rd σ^{front}.

Table 9: The TVIS endpoints for the front, the back and the core TVIS vials defined by the individual TVIS criteria defined by three standard deviations determined using the retrospective and the real time prediction methods. For comparison, the visual endpoint for the front TVIS vial and the points when $C'(100kHz)$ reaches a plateau in the case of the back and the core TVIS vials are also included.

TVIS vial location on the shelf	Retrospective Methodology								
	Mean (μ) of $\frac{d(\mathrm{C}'(100\mathrm{kHz})}{dt}$	RMSD	1st σ	2nd σ	3rd σ	TVIS Endpoint (h:min)			Time at plateau (h:min)
						1st σ	2nd σ	3rd σ	
Front	-0.00833	0.067	0.058	0.120	0.190	13:18	13:10	13:08	**12:56 (visual)**
Back	-0.00978	0.023	0.013	0.036	0.058	17:54	16:00	15:54	15:46
Core	-0.00101	0.091	0.081	0.170	0.260	16:00	15:56	15:52	16:00
	Real Time Methodology								
Front	Addition of 20 min to the TVIS endpoints predicted from the retrospective method					13:38	13:30	13:28	**12:56 (visual)**
Back						18:14	16:20	16:14	15:46
Core						16:20	16:16	16:12	16:00

It is clear from the predictions for the front TVIS vial that the greater the number of standard deviations, the earlier the TVIS endpoint is predicted in relation to the visual endpoint (12:56). For example, if the 3rd σ gives a predicted TVIS endpoint at 13:08, one can be 99 % confident that the $d(C'100kHz)/dt$ is equal to zero 12 min after the visual endpoint (12:56). The next step is about exploring whether the methodology is applicable to those vials that cannot be visually examined, viz. the back and the core TVIS vials.

Step 3: Extension of the methodology to the internal TVIS vials

The time-lines of $C'(100kHz)$, the rolling average and the first derivative for the back and the core TVIS vials are presented in Figure 55 (b and c), respectively, in the same manner as shown previously for the front TVIS vial. The vertical time-markers in Figure 55 (b and c) show the point when the recovery phase ends and the plateau begins, i.e. 2 h 50 min later for the back TVIS vial (15:46) and 3 h 14 min later for the core TVIS vial (16:10), in relation to the visual endpoint (12:56) in the front TVIS vial. The **third step** then is to apply the limiting criteria as per the methodology discussed previously (Step 2). Note the nomenclature for the standard deviations determined for the two internal vials: 1st σ^{back}, 2nd σ^{back} and 3rd σ^{back} for the back TVIS vial and 1st σ^{core}, 2nd σ^{core} and 3rd σ^{core} for the core TVIS vial. The predicted endpoints corresponding to each of these standard deviations are marked in Figure 55 (b and c) and also given in Table 9.

As expected, with the increase in the number or the value of the standard deviation, the TVIS endpoint is predicted closer to the plateau. However, in some cases, it is under-predicted. For example, in the case of the core TVIS vial (Figure 55c), the TVIS endpoint is under predicted by 4 to 8 min in relation to the beginning of the plateau (16:10), depending on whether one uses 2nd σ^{core} or 3rd σ^{core} for establishing the limiting criteria. Furthermore, it is clearly observable that the inherent variability in $d(C'100kHz)/dt$ in the plateau region differs among the three TVIS vials, with the least variability found for the back TVIS vial and the worse variability found for the core TVIS vial.

It follows that the differences in the inherent variability in the signal presents one with two possibilities for predicting the TVIS endpoint: (1) apply the threshold defined by the signal with the least variability to all the vials; or (2) apply the limiting criteria defined by the worst variability to all the vials. The implication of applying the above cases to the front TVIS vial is clear from Figure 55(a), where the TVIS endpoint predicted using the bands defined by 3rd σ^{back} and 3rd σ^{core} are marked. If 3rd σ^{core} is considered, then the TVIS endpoint is predicted (13:04) 4 min closer to the visual endpoint as compared to when it is predicted using 3rd σ^{front} (13:08). In contrast, the TVIS endpoint predicted

from 3rd σ^{back} remains the same as predicted from 1st σ^{front} (13:18). When 3rd σ^{core} is used to predict the endpoint in the back TVIS vial (Figure 55b), it is under predicted (15:32) in relation to the beginning of the plateau (15:46). Further, when 3rd σ^{back} is used to predict the endpoint in the core TVIS vial, the predicted TVIS endpoint is the same as that predicted using 1st σ^{core} (16:00).

It appears that there is no single universal criterion that can be applied to all the vials. Nevertheless, it is possible to tune the system and choose the limiting criteria according to the situation. It is worth reiterating here that since the retrospective method involves determining the first derivative over every 10 data points going forward in time, it invariably shifts the analysis time point backward by 20 min. As a consequence, depending on the value of the standard deviation, the predicted TVIS endpoint can be under predicted or over predicted. In general, it can be stated that if the retrospective method is used, then one can set the limiting criteria in a way that the predicted endpoint lies after the beginning of the plateau rather than before the plateau to ensure all the ice is removed before the decision is made that sublimation has finished. Alternatively, it is also possible to use a real time prediction method (instead of a retrospective method) to allow for the addition of a soak period to ensure that TVIS overpredicts the endpoint for a given vial. The methodology is described as follows.

Prediction of the TVIS Endpoint in Real Time

In contrast to a retrospective method, where the rolling average and the 1st derivative are determined going forward in time, the method for real time prediction involves determining the rolling average and the first derivative over every 10 datapoints, going back in time. The concept has been demonstrated in Figure 57, which shows a time-period during which $C'(100kHz)$ transitions from the recovery phase to a plateau. On application of the real time method, the analysis period effectively shifts the TVIS endpoint forward by 20 min. In other words, the TVIS endpoint will now lie 20 min later in relation to the endpoint predicted from the retrospective method because the real time analysis will offset the impact of the standard deviations determined using the retrospective method. As a

consequence, in all the cases, the TVIS endpoint will be over predicted in relation to the beginning of the plateau. For example, for the core TVIS vial, the TVIS endpoint predicted using the biggest standard deviation will shift from an under predicted value (15:52) to an over predicted value (16:12) in relation to the beginning of the plateau (16:00). Hence, it is not clear whether there is an optimum method; however, it a real time method appears to be practical given that it does not under-predict the endpoint.

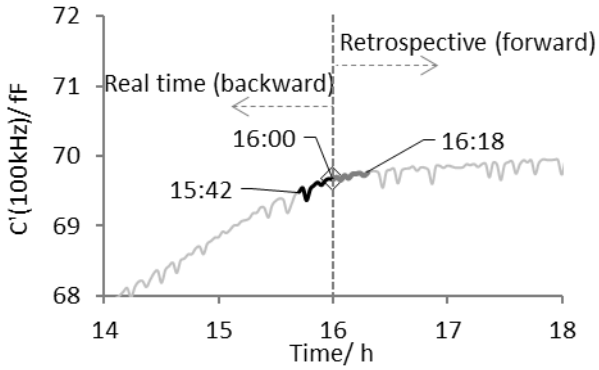

Figure 57: Two methods for the prediction of the TVIS endpoint. The time-line of $C'(100kHz)$ is shown as a solid light grey line. As an example, the point at the beginning of the plateau (16:00) for the core TVIS vial has been considered for demonstration. The retrospective method involves the analysis of 10 datapoints from 16:00 to 16:18 (20 min), shown as the dataset in dark grey line. The real time method involves analysis of 10 datapoints from 16:00 to 15:42 (20 min), shown as a solid black line.

5.4 Discussion

With the photographic method, it has been possible to detect a transition from being able to detect the last ice crystal at 12:54 to not being able to see the ice at 12:56, i.e. within a time-resolution of 2 min. This translates to a limit of detection of less than 1 mg of ice (or to less than 0.025 % of the initial ice mass) as discussed in section 5.3.7.1

Further, by using two methods: (1) retrospective, and (2) real time method, it has been possible to define three limiting criteria for the prediction of the TVIS endpoint. In the retrospective method, the rolling average of $C'100kHz$ and its first derivative are determined over every 20 min going forward in time. Then, by determining three standard deviations of the mean of the first derivative in the plateau regions, it has been possible to predict the TVIS endpoint, the position of which depends on the value of the limiting criteria chosen. An implication of retrospective prediction is that the greater the value or the number of the standard deviations, the earlier is the predicted endpoint in relation to either the visual endpoint in the case of the front TVIS vial or in relation to the point of the beginning of the plateau in the case of the internal TVIS vials. Likewise, reducing the number or the value of the standard deviation results in the TVIS endpoint being predicted at a later time-point. However, whether the same rule applies in a real system (e.g. sugar solution, protein solution) remains to be seen. This will be explored in the subsequent chapters.

Furthermore, when the retrospective method is extended to the internal TVIS vials, it is revealed that the inherent variability in the first derivative differs from one TVIS vial to another. This is ascribed to small variations in the signal from different channels of the TVIS system, differences in the quality of the electrical connections of the TVIS vial and potentially the variations arising from different shelf locations. That leaves one with two possibilities. The first possibility is that one applies the threshold defined by the smallest variability (back TVIS vial) to all the vials and the second possibility is the threshold defined by the largest variability (core TVIS) is applied to all the vials. The

consequence of choosing the largest variability is that there is a potential to under-predict the TVIS endpoint because of an increase in the limits of the larger threshold. However, the consequence of considering the least variability is that TVIS potentially over-estimates the endpoint in relation to the visual endpoint because the limits of the threshold decrease in value. Finally, the analysis is performed going back in time in order to predict the TVIS endpoint in real time, which invariably shifts the analysis period forward by 20 min in relation to that of the retrospective method.

From the above discussion, it is important to recognise that prediction of the TVIS endpoint is dependent on the method of data processing (retrospective or real time). In general, it appears that three standard deviations may be required in order to predict the endpoint as close as possible to the visual endpoint. In addition, by considering both the retrospective and real time methods of prediction, it may be possible to predict the TVIS endpoint later than the visual endpoint, which is, of course, preferable in order to ensure all the ice is removed.

One important aspect of the primary drying endpoint is that there is always a potential of a single vial technique to predict an endpoint which is non-representative of the true batch endpoint. Recently, Scutella and co-workers established a link between the variability in vial geometry and its impact on the variability in the vial heat transfer coefficient and therefore, a variability in the product temperature (Scutella, et al. 2017). In general, they concluded that not all vials of the same batch have the same geometry, in particular, the vial bottom contact area and the vial bottom concavity, due to the variations in the vial dimensions, which can change as a function of model and the manufacturer. The impact of variability in the vial bottom concavity becomes more significant at high chamber pressures, which in turn results in an increase in the variability of the vial heat transfer coefficient and a decrease in the variability in product temperature. For example, the authors found that the variability in the heat transfer coefficient and the product temperature was 1.78 W/ m^2/ K and 0.9 °C respectively, at 15 Pa (0.15 mbar) and 0.84 W/ m^2/ K and 2.2 °C respectively, at 4 Pa (0.04 mbar). This implies that

the greater the variability in the heat transfer coefficient at high chamber pressures, the lower the variability in the product temperature as per the classical heat transfer equation (Pikal, et al. 1984).

The average chamber pressure recorded in this study was approximately 40 Pa (0.4 mbar). Although the dryer and the processing conditions were different from those in the experimental study conducted by Scutella et al., it can be assumed that there is an inherent variability in the geometry of the vials used in this study. At present, it is not possible to determine the variability in the vial geometry as it requires additional equipment. But, if one were to determine that, then it is possible that one will find the variability in the product temperature as well (due to the variability in the vial heat transfer coefficient).

It follows that a variability in the product temperature among a core vial population will directly impact the primary drying rate, hence the primary drying time. One study states that with every 1 °C increase in the product temperature, the primary drying time is decreased by 13 % (Pikal 1985). However, not knowing the variation in the drying times of the vials used in this study, if one were to assume that the variability in the product temperature is going to follow a normal distribution and further assume that the variability in the true batch endpoint is 1 h, then this error must be added to the predicted TVIS endpoint. An example of this concept is presented in Figure 58, which shows a typical normal distribution with three confidence limits defined by three standard deviations from the mean. If the black dot circle on the left side of the bell curve is assumed to be the TVIS endpoint, then that prediction is underestimated by an hour, which is assumed to be the variability in determining the true endpoint of the batch with 95 % confidence. It will not be surprising to find a similar scenario in reality, which is a problem with single vial measurements. However, it is also true that batch sensors are less sensitive towards the end of primary drying. Nevertheless, batch techniques remain a preferred choice over single vial techniques despite the fact they might underestimate the true endpoint of the batch. As far as TVIS is concerned, the study demonstrates that the predicted TVIS endpoint for a given vial lies very close to the visual endpoint, which is a significant improvement over

the endpoint predicted from product invasive probes like thermocouples, for which a soak period of 10-30 % is often added after the product temperature reaches the shelf temperature in order to ensure the ice is removed from the entire batch of vials (Patel, et al. 2010).

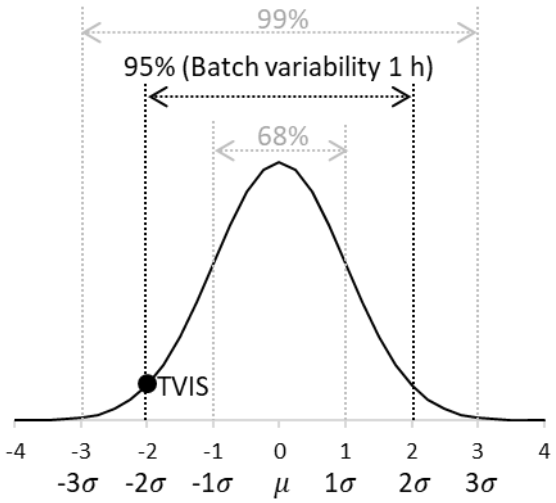

Figure 58: Normal distribution of a population with confidence limits defined by three standard deviations from the mean. Two assumptions have been made with respect to the primary drying endpoint in a single TVIS vial and the batch endpoint. The first assumption is that the variability in the true endpoint of a batch of core vials is 1 h. The second assumption is that the confidence of detecting the TVIS endpoint is 95 %, i.e. 2 standard deviations from the mean. In this situation, the predicted TVIS endpoint occurs 1 h earlier than the true endpoint of a batch.

5.5 Chapter Conclusion

Within the frequency range of the TVIS spectrometer, an excitation frequency of 100-200 kHz is sufficient to be on the high frequency side of the ice relaxation peak. A measurement of the time profile of the real part capacitance at 100 kHz (for example) would in effect be largely insensitive to the temperature of the ice and thereby provide an opportunity for tracking the reduction of the ice mass during the sublimation process.

The study on the isolated TVIS vials demonstrates that the area of ice-glass wall contact and the position of the electrodes on the vial appear to significantly impact the primary drying time-profile of the high frequency capacitance measured at 100 kHz, $C'100kHz$. It has been demonstrated that the point where the magnitude of $C'100kHz$ reaches a constant value at the end of the recovery phase corresponds to the visual endpoint. While the determination of the visual endpoint relies on the visual examination of the front TVIS vial undergoing ice sublimation and depends on the time resolution of the photographic method (limit of detection <1 mg), the methodology for predicting the TVIS endpoint involves a retrospective method and a real time method of data analysis. With these methods, it has been possible to establish the individual vial limiting criteria based on three standard deviations of the mean of the first derivative of the rolling average of the $C'100kHz$, that can be used to predict the TVIS endpoint. It is also recognised that there can be a variability in the signal depending on the channel, the vial and/or the shelf location. Depending on the method of data analysis and the value/number of the standard deviations chosen, there are opportunities with TVIS to tune the system according to the situation as there does not appear to be universal TVIS criterion that applies to all the vials. However, whichever method is chosen, there is always a potential variability in the detecting the true endpoint of a batch owing to the variability in the vial geometry which has a bearing on the vial heat transfer coefficient and the product temperature, and therefore, on the primary drying time. Nevertheless, the accuracy with which TVIS predicts the endpoint is a significant improvement over that determined by probe-based single vial sensors, for which a soak period of 10-30 % must be added to ensure 100 % ice sublimation across the batch. Moving forward, the potential for predicting the TVIS

endpoint in vials containing simple sugar solutions and protein solutions will be explored in conjunction with batch monitoring techniques.

6 Prediction of the Primary Drying Endpoint for a 5 %w/w Sucrose Solution

6.1 Objectives

It is recognised that the photographic method for the detection of the primary drying endpoint for pure ice is not applicable to a solution owing to the opacity of the dry layer as it forms above the sublimating interface. However, given that the TVIS parameter, $C'100kHz)$ is sensitive to the amount of ice in the vial, it is hypothesised that it should be possible to predict the endpoint for a simple sugar solution. The objective of the study then is to extend the methodology described for pure ice in the previous chapter to a 5 %w/w/ sucrose solution contained in the TVIS vials positioned at various shelf locations using the same methodology as described for ice in the previous chapter.

6.2 Materials and Methods

A batch of 160 x 10 mL vials (Adelphi VC010-20C), each containing 3 g of 5% w/v sucrose solution in Ultrapure water (Triple Red Duo™ Two-In-One Water Purification System) were freeze dried in a Virtis Advantage Plus freeze drier equipped with a five-channel TVIS system. Out of the 160 vials, four were modified with a pair of copper electrodes (copper adhesive tape 3M 1181) of dimensions 19 mm by 10 mm attached externally to the glass wall at a height of 3 mm from the vial base. The details of the identification label on each TVIS vial are given in Table 10. These TVIS vials were placed on 4 different shelf locations, hereafter referred to as the front TVIS vial, the left TVIS vial, the back TVIS vial and the core TVIS vial; each accompanied by a Type T thermocouple in the immediate neighbour vial as shown in Figure 59(a). The tips of the thermocouples in the immediate neighbour vials were in contact with the bottom centre of the vial base. An example is shown in Figure 59(b) for the vial next to the front TVIS vial. The TVIS spectra, the measurement of process parameters and the photographs of the front row of measurement vials were obtained every two minutes throughout the freeze-drying process. The TVIS parameters are given in Table 10 and the various stages of the lyo-cycle are given in Table 11.

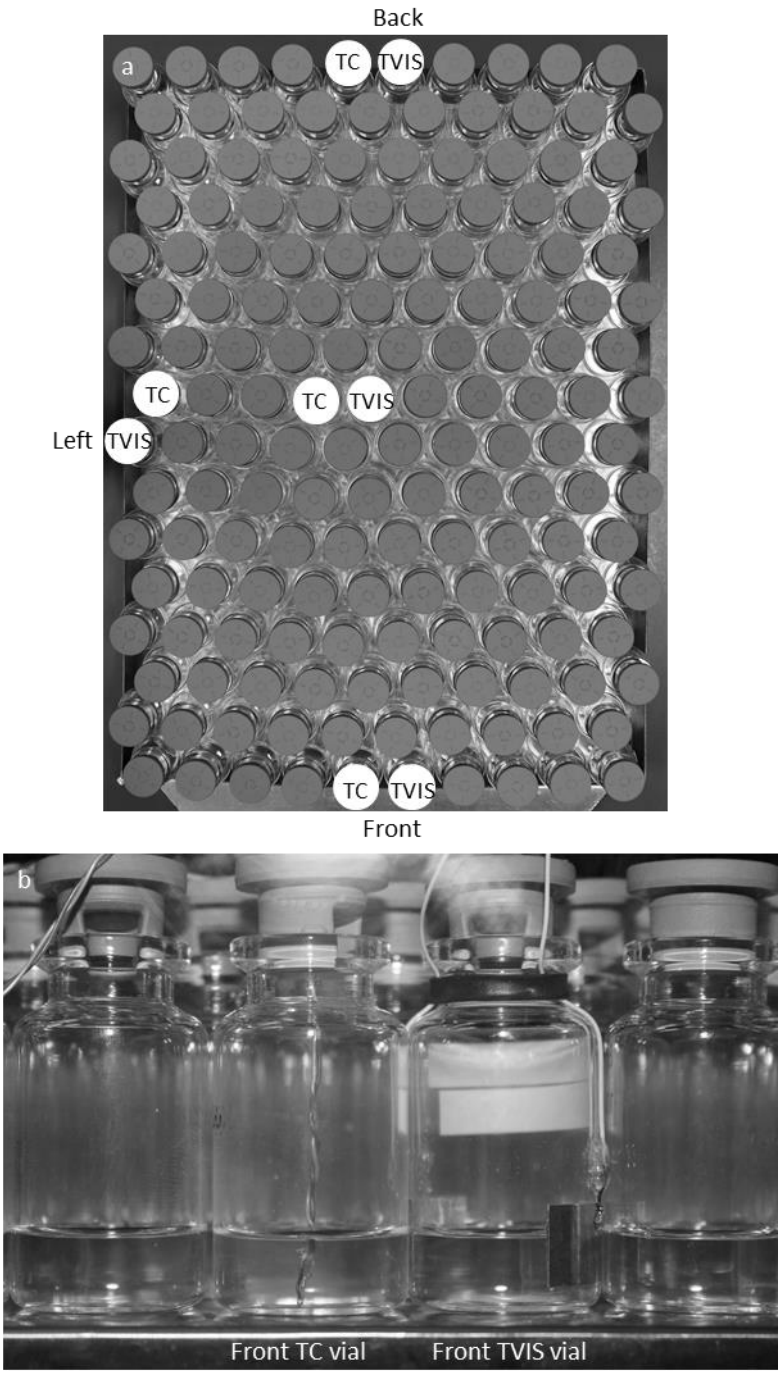

Figure 59: Freeze-drying of 3g of 5% sucrose solution in Ultrapure water in 160 x 10 mL Adelphi (VC010-20C) vials: (a) Top view of the vial batch showing the position of the measurement vials (b) A snapshot taken before starting freeze-drying of the front row of vials obtained from Canon 550D Digital Camera positioned on a tripod in front of the dryer. The TC vial next to the TVIS vial has a Type T thermocouple with its sensing tip at the bottom centre of the vial base.

Table 10: TVIS parameters and the details of the TVIS measurement for 5 % sucrose Solution

TVIS Parameters				
Frequency range	10 Hz to 1 MHz			
AC voltage	0.2 to 8 V			
Measurement/ Scan interval	2 min			
Channel	CH1	CH2	CH3	CH5
Vial Nomenclature	08JUN18-NG-01-10MM_3MMabB	08JUN18-NG-02-10MM_3MMabB	08JUN18-NG-03-10MM_3MMabB	08JUN18-NG-05-10MM_3MMabB
Vial position	Left edge	Back edge	Core	Front edge
Mass of Solution/ g	3.00	3.00	3.00	3.00
Thermocouple Number	TC1	TC3	TC2	TC4

Table 11: Freeze-drying protocol for 3 g of 5 % sucrose solution in 160 x 10 mL Adelphi (VC010-20C) vials

Step	Start Temperature (°C)	End Temperature (°C)	Ramp rate (°C/ min)	Duration (min)	Cumulative Time (h)	Set pressure (µbar)
Equilibrium phase	26.4 (RT)	20	-	30	0.5	-
Freezing	20	-40	0.5	120	2.50	-
Hold	-40	-40	-	180	5.50	-
Re-heating	-40	-10	0.5	60	6.50	-
Hold	-10	-10	-	180	9.50	-
Re-cooling	-10	-35	0.5	50	10.33	-
Hold	-35	-35	-	180	13.33	-
Primary drying	-35	-35	-	7387	136.5	400

6.3 Results

6.3.1 Monitoring the primary drying phase in the front TVIS vial

Figure 60(a) shows the spectra of the real part capacitance (plotted against log frequency) at various time-points during primary drying which demonstrate that the strength of the dielectric relaxation of ice 1 kHz decreases during primary drying. Further, the time dependency of $C'(100kHz)$ during the primary drying stage is presented in Figure 60(b) with the three distinct phases marked on its time-line, namely the linear drying phase A to B over the first 3 h of primary drying, the non-linear drying phase from B to G between 3 h and 20 h and the recovery phase from G to H between 20 h and 45 h. The key events labelled with boxed alphabets on the time-line have been mapped onto the photographs (i to ix) of the sample that are presented below the graphs.

The first photograph shows the ice cylinder in intimate contact with the glass wall at the beginning of the application of vacuum (0 h). The second photograph captured at 3 h shows that the ice sublimation front has advanced down the vial leaving behind a dry layer above the ice cylinder bounded by the electrodes, that reduces in height linearly over the first 3 h, hence a linear reduction in the magnitude of $C'(100kHz)$ from A to B. Thereafter, the impact of the additional heat contribution from the front door radiation is clearly visible in photographs iii to v (i.e. from 6.27 h to 9.1 h) which show the left side of the ice cylinder lags behind the right of the ice cylinder in reaching the bottom of the vial. This non-uniform reduction in the ice cylinder appears to manifest as a non-linear decrease in $C'(100kHz)$. Further, as discussed in the ice chapter, the measured capacitance is also impacted by a reduction in the interfacial capacitance at the glass-ice cylinder interface. In other words, a diminishing contribution of the interfacial capacitance with the decreasing area of contact between the ice cylinder and the glass wall is expected to result in a slower rate of decrease in $C'(100kHz)$. As evidenced by the visual examination of the pure ice in the previous ice chapter, the dip in $C'(100kHz)$ corresponds to the disappearance of the ice cylinder which leaves behind a significant volume of ice in the form an ice dome. A characteristic dip is also seen at 20 h as in Figure

60(b) which must mean that the ice dome is hidden behind the opaque dry sucrose matrix. Further, Figure 60(b) clearly shows a recovery phase that ends in plateau around 45 h, which suggests that the ice dome shrinks towards the centre of the vial until the last trace of ice is removed at the point which corresponds to the plateau. However, the visual examination fails to locate the visual endpoint because the ice is no longer visible by 11.27 h (photograph vi), which is several hours before $C'(100kHz)$ approaches the dip (20 h). Therefore, the TVIS methodology for the prediction of the primary drying endpoint that was described in the ice chapter has been applied to predict the TVIS endpoint for all the TVIS vials containing sucrose.

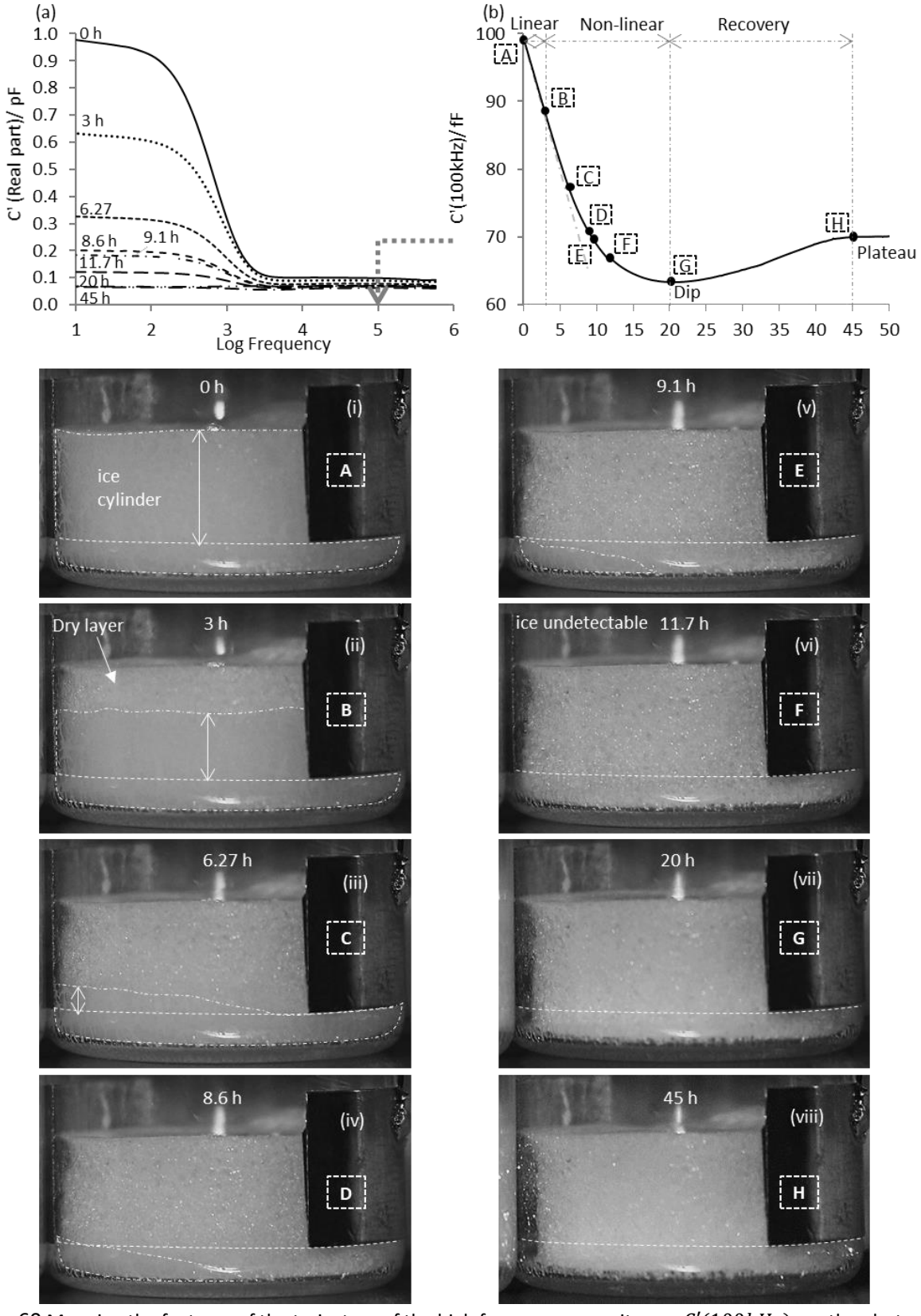

Figure 60 Mapping the features of the trajectory of the high frequency capacitance, $C'(100kHz)$, on the photographic images of the ice sublimation interface during the primary drying phase of a 5 % sucrose solution: (a) Spectra of the real part capacitance plotted against log frequency at various time-points; (b) primary drying time-line of $C'(100kHz)$ marked with key events: A to B: linear drying phase when the ice cylinder height decreases at a constant rate; B to G: non-linear drying phase, where at C: the right hand side of the ice cylinder has reached below the lower edge of the electrode; at D: no cylinder is left and the remaining ice mass in intimate contact with the front glass wall is at the lower edge of the left electrode; at E: the remaining ice mass has reached below the electrode; at F: there is no ice visible but an ice dome is expected to be present in the interior of the dry layer; at G: a characteristic dip in the time-line of $C'(100kHz)$ which is expected to correspond with the ice dome leaving the side walls; from G to H: $C'(100kHz)$ recovers to a plateau which is expected to correspond to the removal of the last trace of ice at H.

6.3.2 Prediction of the TVIS Endpoint

Figure 61(a) shows the time profiles of the shelf temperature and the chamber pressure during the primary phase, which lasts for 122 h 16 min. The time-lines of $C'(100kHz)$ for the 4 TVIS vials located at the front, the left, the back and the core are plotted on the primary Y-axes in Figure 61 (b) to (e) respectively. The methodology for predicting the TVIS endpoints for each vial has already been described in the previous chapter: (i) the values of the rolling average and the first derivative of the rolling average, $d(C'100kHz)/dt$, are determined retrospectively over every 10 datapoints (or every 20 min) going forward in time; (ii) the mean of the first derivative and three standard deviations from the mean are determined over the plateau region. Towards the end of the recovery phase, the point when the first derivative drops below the threshold as defined by each of the three standard deviations are taken as the three estimates for the predicted TVIS endpoint. Finally, in order to predict the endpoint in real time method the data is processed going backward in time, which effectively shifts the analysis period forward by 20 min with respect to retrospective method.

Once the limiting criteria have been established, the next stage is to explore their impact on the predicted TVIS endpoint for each TVIS vial and compare the relative position of the predicted TVIS endpoint with the point when $C'(100kHz)$ reaches a plateau because that corresponds to what is considered to be the visual endpoint as demonstrated for pure ice. In Figure 61 (b) to (e), on the primary Y-axes, the time-lines of the rolling average of $C'(100kHz)$, and on the secondary Y-axes, the time-lines of the first derivative, determined retrospectively, are shown for the front, left, back and core TVIS vials, respectively. The mean of the first derivative determined over the last ~12 h of primary drying is shown as a solid black line going through the scatter while the values of the first, second and third standard deviation are shown as a dotted line, short dashed line and long dashed line, respectively, over the same period as the that for the mean. Note the nomenclature for the three standard deviations in the case of each TVIS vial: 1st σ^{front}, 2nd σ^{front}, 3rd σ^{front} for the front TVIS vial; 1st σ^{left}, 2nd σ^{left}, 3rd σ^{left} for the left TVIS vial; 1st σ^{back}, 2nd σ^{back}, 3rd σ^{back} for the back TVIS vial; and 1st σ^{core}, 2nd σ^{core}, 3rd σ^{core} for the core TVIS vial.

The predicted endpoints determined retrospectively, are marked for each TVIS vial in Figure 61, while Table 12 includes the values of all the parameters determined retrospectively: the mean μ, the root mean square deviation (RMSD) and the three standard deviations from the mean (upper limits), and the corresponding predicted endpoints for each TVIS vial. Further, the predicted endpoints based on the real time analysis are given in the bottom half of the table. Finally, in the last column of the table in the right, the time-points at which $C'(100kHz)$ reaches a plateau for each case are included.

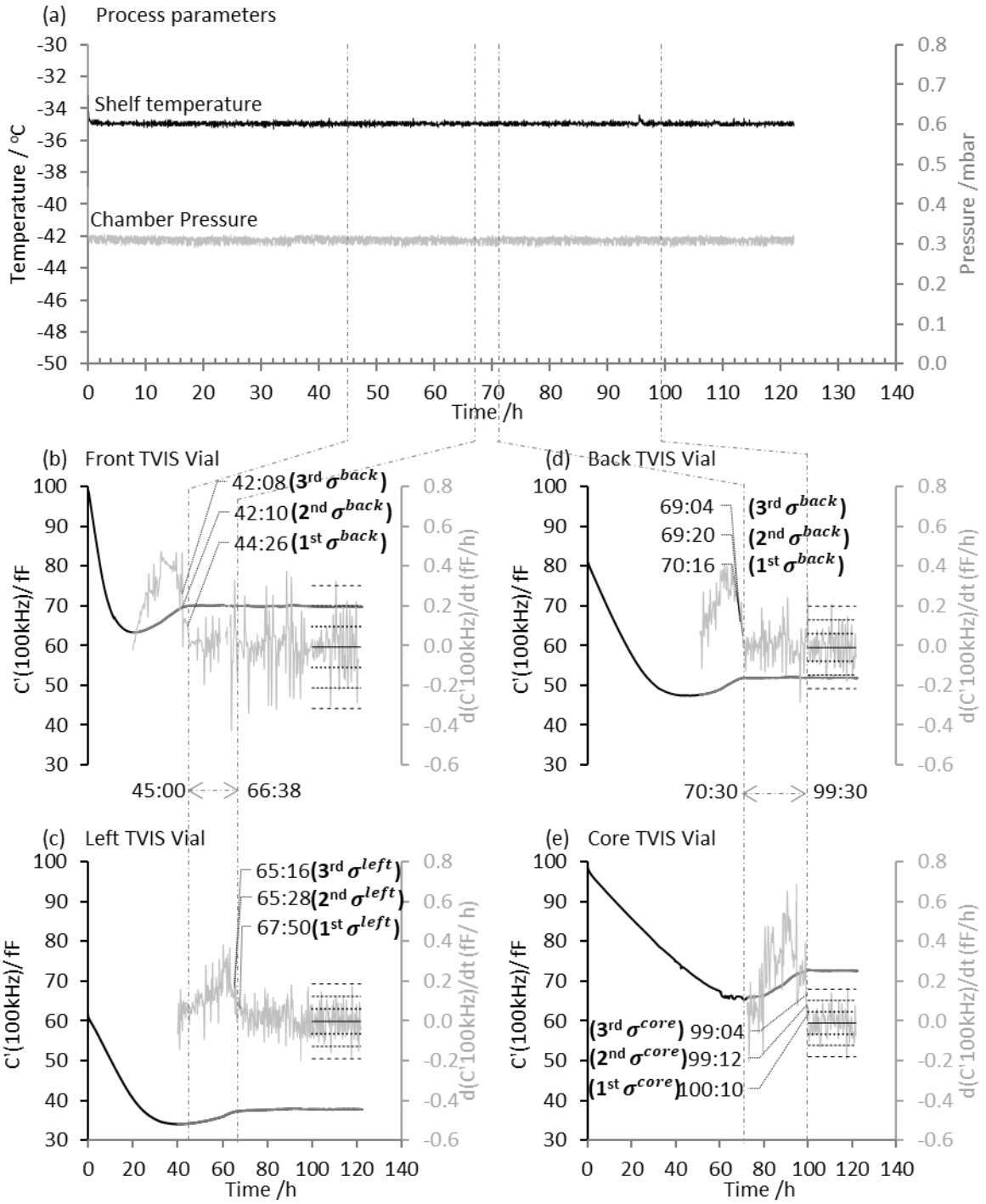

Figure 61: Prediction of the primary drying endpoint of ice for 5 % sucrose contained 4 TVIS vials located at the front, the left, the back and the core: (a) time-lines of the shelf temperature and the chamber pressure during the primary drying phase; On the primary Y-axes of (b) to (d): Primary drying time-lines of $C'(100kHz)$ for the front, the left, the back and the core TVIS vials respectively (solid black lines) with the rolling average of $C'(100kHz)$ determined retrospectively over every 20 min (10 datapoints) (solid grey lines); On the secondary Y-axes (b) to (e): primary drying time-lines of the 1st derivative of the rolling average, $d(C'100kHz)/dt$, also determined retrospectively over every 20 min. The values of $d(C'100kHz)/dt$ over the last ~12 h of primary drying have been averaged (solid black line going through the scatter). The upper and the lower limits of the three standard deviations from the mean are shown as dotted lines (1st σ), small dashed lines (2nd σ) and long dashed lines (3rd σ). The predicted TVIS endpoints based on the standard deviations are marked. The vertical time markers correspond to the point when $C'(100kHz)$ reaches a plateau in each case, which follows the rank order from the fastest to the slowest to reach the plateau: front (45:00), left (66:38), back (70:30) and core (99:30).

Table 12: TVIS endpoints predicted for 5 % sucrose in 4 TVIS vials based on the limiting criteria determined from three standard deviations from the mean of the first derivative in the plateau region. Also shown are the time-points which correspond to the beginning of the plateau in each case.

TVIS vial location on the shelf	Retrospective Methodology								
	Mean (μ) of $\frac{d(\mathrm{C}'(100\mathrm{kHz})}{dt}$	RMSD	1st σ	2nd σ	3rd σ	TVIS Endpoint (h:min)			Time at plateau (h:min)
						1st σ	2nd σ	3rd σ	
Front	-0.00687	0.010	0.096	0.20	0.30	44:26	42:10	42:08	45:00
Left	-0.00179	0.063	0.061	0.12	0.19	67:50	65:28	65:16	66:38
Back	-0.00920	0.069	0.060	0.13	0.20	70:16	69:20	69:04	70:30
Core	-0.00102	0.056	0.046	0.10	0.16	100:10	99:12	99:04	99:30
	Real Time Methodology								
Front	Addition of 20 min to the TVIS endpoints predicted from the retrospective method					44:46	42:30	42:28	45:00
Ledt						68:10	65:48	65:36	66:38
Back						70:36	69:40	69:24	70:30
Core						100:30	99:32	99:24	99:30

Two important inferences can be made from the results. First, ice sublimation appears to have been completed in the rank order: (1) front TVIS vial (45:00); (2) left TVIS vial (66:38); (3) back TVIS vial (70:30); (4) core TVIS vial (99:30). This clearly demonstrates the potential impact of one or a combination of these factors: (i) greater heat contribution via heat radiation and gas conduction to the vials located close to the periphery of the shelf (Pikal, et al. 1984; Rambhatla and Pikal 2003; Scutella, et al. 2017; Tchessalov 2017); (ii) heterogeneity in the ice nucleation temperatures, which has a direct impact on the ice crystal size and therefore the dry layer resistance, and hence the primary drying efficiency (Searles, et al. 2001); (iii) variability in the vial geometry, which can impact the vial heat transfer coefficient from the shelf to the product and therefore the product temperature (Scutella, et al. 2017) and ultimately the primary drying time; (iv) variability in the dry layer resistance can itself lead to a variability in the product temperature (Scutella, et al. 2018) and therefore the primary drying time. But, the range of primary drying times observed for the TVIS vials appear to have been impacted largely by vial location.

The second observation is that the retrospective method appears to underpredict the endpoint for all the TVIS vials except for the core TVIS vial. For example, in the case of the front TVIS vial, the TVIS endpoint from by 1st σ^{front} is underpredicted by 34 min in relation to the beginning of

the plateau (45:00) while 2nd σ^{front} and 3rd σ^{front} predict the endpoint even earlier, which suggests that lowering the value or the number of standard deviations allows for the predicted endpoint to be closer to the point of the beginning of the plateau. This result is, of course, contrary to the fact that previous study demonstrated, how by increasing the value or the number of standard deviations, it is possible to predict the endpoint closer to the visual endpoint. Nevertheless, under-prediction is not a problem because (1) the standard deviations can serve as an early warning for the operator in that they can provide sufficient time to the operator to switch to the secondary drying stage; (2) it presents opportunities to employ the real time method: the consequence of that is clear from predictions given in Table 12. In almost all the cases, the predicted endpoints lie after the beginning of the plateau except for that predicted for the front TVIS vial, which is slightly under-predicted. This exception may just be an anomaly and can be attributed to some noise in the signal which impacts the prediction. Nevertheless, it is more important to recognise the precision of the methodology for prediction.

6.3.3 Discussion

In this study, 4 TVIS vials containing 5% sucrose positioned at key shelf locations are freeze-dried until all the ice is removed by ~120 h of primary drying as demonstrated by the plateau region of $C'(100kHz)$ for the core TVIS vial. It is not possible to monitor the reduction in the ice mass in the front TVIS vial using the photographic method after the first ~11.5 h of primary drying, i.e. ~8.5 h before $C'(100kHz)$ reached a dip in its timeline: this is attributed to presence of the opaque dry layer. In such a scenario, the visual method serves no purpose. Nevertheless, having already established in the previous study that a significant amount of ice mass sublimates during the recovery phase of $C'(100kHz)$ and the visual endpoint corresponds to the beginning of the plateau, primary drying is continued well beyond the beginning of the plateau of $C'(100kHz)$ for each TVIS vial. Assuming that the beginning of the plateau for the sucrose containing TVIS vials corresponds to 100 % ice sublimation, then two inferences may be drawn. First, the vial which dries the fastest is the front TVIS vial and the one that dries the slowest is the core TVIS vial, while the left and the back TVIS vial have intermediate drying times. This reflects the heterogeneity in the heat transfer process which has a bearing on the vial location on the shelf. Secondly, the limit of detection of ice mass must be of the order of a few milligrams. The general rule of vitrification of an amorphous solute like sucrose is that nearly 20 % of the water is unfrozen and is trapped with the solute in the interstitial region of the ice crystals (Kasper, Winter, et al. 2013). In this study, the initial mass of the solution was 3 g, out of which 0.15 g (5 %) constituted sucrose. Thus, out of the 2.85 g of water, only 2.28 g formed ice (80 % of 2.85). Given that TVIS can detect up to ~1 mg of ice mass, then that gives a limit of detection of 0.04 % of the initial value (2.28 g) in the case of sucrose.

Once the time-points corresponding to the beginning of the plateau have been identified, it is a matter of using the retrospective and the real time methodologies for predicting the endpoint. The retrospective method appears to under-predict the TVIS endpoint even when one uses the first standard deviation. In order words, the TVIS endpoint predicted from all the three standard deviations

lie before the point that corresponds to the beginning of the plateau. This is in contrast to the results from the pure ice study described previous, wherein it was demonstrated that the higher the value of the number of standard deviations, the closer the predicted TVIS endpoint with respect to the beginning of the plateau. This does not appear to be a problem because the larger value of the standard deviations can provide the operator sufficient time to be prepared before switching to the secondary drying stage. Alternatively, the real time method proves to be more useful because it predicts the endpoint after the beginning of the plateau in most cases.

Coming back to the premise for detecting the visual endpoint and the endpoints predicted from the three standard deviations determined in real time, future work will involve qualifying these predictions. So far, it has been assumed that for the sucrose containing vials, the beginning of the plateau corresponds to 100 % ice sublimation based on the conclusion derived for pure ice. However, given that it is not possible to visually examine the progress of ice sublimation in the case of an opaque layer, a further study is warranted which can qualify this assumption. Moreover, if we are able to qualify that the beginning of the plateau for a sucrose containing TVIS vial corresponds to 100 % sublimation, then that invariably qualifies the endpoints predicted from the real time method. For this purpose, one possible protocol can involve a number of TVIS vials (e.g. 5), each placed in consecutive rows on the shelf starting from the front edge to the core region. During primary drying, these TVIS vials are expected to finish ice sublimation at different times depending on the relative contributions from the various heat sources, with the front edge TVIS vial being the fastest and the core TVIS vial being the last to reach the $C'(100kHz)$ plateau. The key point then, is one waits until $C'(100kHz)$ for one of the internal TVIS vials reaches the beginning of the plateau and then terminates primary drying in order to deliberately collapse the rest of the internal vials. It is important to recognise the principle difference between (i) terminating ice sublimation for a given test vial and investigate for melt-back during the secondary drying stage; and (ii) simply interrupting ice sublimation at the primary drying stage and then investigate for melt-back. If one does not switch to secondary drying (latter case), then even the vials that have dried completely will collapse due to the presence of unfrozen, amorphous

water associated with sucrose, which must be removed during secondary drying. During secondary drying, it is expected that the moisture content of the rubbery amorphous will reduce, which in turn will lead to an increase in the T_g value, and the phase will become glassy.

Let us consider the 2nd row vial is chosen as the test vial. Then, two cases can be investigated which are illustrated in Figure 62. In the first case, one can terminate primary drying at the beginning of the $C'(100kHz)$ plateau and immediately switch to the temperature ramp of secondary drying. If the point of the beginning of the plateau *is not the true endpoint*, then (i) the TVIS vial in the first row will be expected to be completely dry as $C'(100kHz)$ would have reached well beyond the beginning of the plateau; (ii) the product in the 2nd row vial will collapse due to melt-back from the small amount of ice present in the bottom interior of the vial; (ii) other internal vials that are still in the recovery phase of $C'(100kHz)$ will collapse due to a significant degree of melt-back. Alternatively, in the second case, let's assume one of standard deviations from the real time method predicts the TVIS endpoint 30 min later than the point that corresponds to the beginning of the plateau. Then, primary drying is continued until 30 min after $C'(100kHz)$ reaches the plateau. If no collapse is observed in the 2nd row TVIS vial, that would then qualify the prediction of the TVIS endpoint, and it would imply that the true endpoint lies somewhere between the beginning of the plateau and the point that corresponds to 30 min after the beginning of the plateau. It then follows that one should continue primary drying at for at least 30 min after the beginning of the plateau.

Finally, as discussed in the previous chapter, even though it is possible to be precise in terms of predicting the endpoint for a given TVIS vial, the fact remains that the predicted TVIS endpoint is more likely to be non-representative of the true batch endpoint, which is impacted by the variability in the vial geometry. It has already been established previously that the variability in the via geometry leads to a variability in the vial heat transfer coefficient which in turn results in the variability the product temperature (Scutella, et al. 2017). Moreover, one should also account for the variability in the mass transfer resistance (R_p) brought about by impact of method of ice nucleation on the dried

product layer. In one experimental study comprising sublimation experiments with either stochastic or controlled ice nucleation protocols, a product temperature variability of up to 4.4 °C during primary drying was reported, which was ascribed to the variability in R_p (Scutella, et al. 2018). In this study, mass transfer resistance was not determined; however; given that ice was allowed to form stochastically, there is likely to be a variability in the ice crystal structures across the batch, hence a variability in the mass transfer resistance during the primary drying stage. From the above discussion, the variability in both K_v and R_p combined, are going to have a significant bearing on the spread of endpoints across the core vial population. This may be partly addressed by batch monitoring techniques, which have been explored in the next chapter.

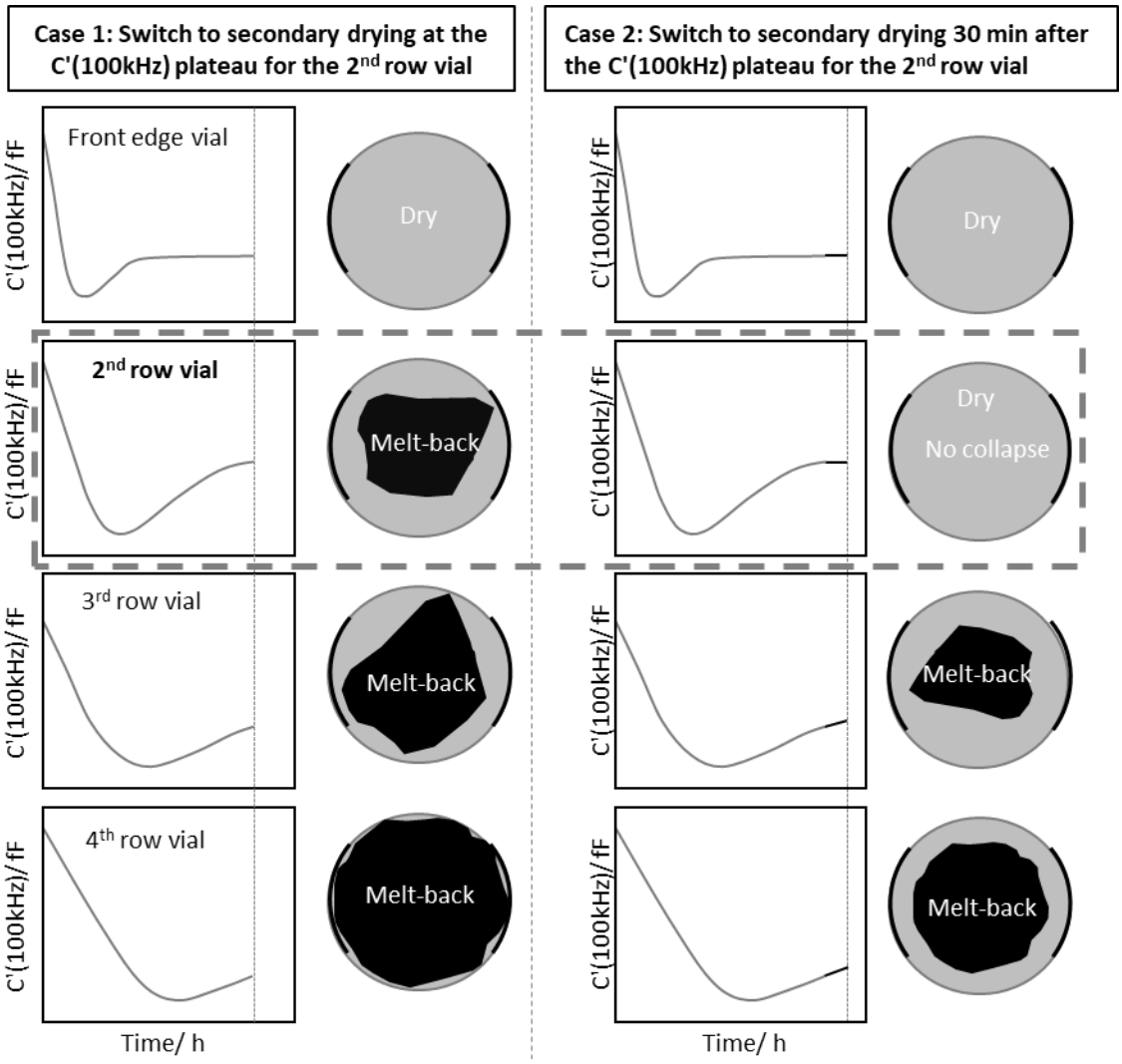

Figure 62: Illustration of the concept of the methodology for qualification of the primary drying endpoint: TVIS vials are placed in consecutive rows starting from the front edge of the shelf to the core region. The front edge vial will dry the fastest followed by the vials in the subsequent rows. Case 1 represents a situation where one terminates primary drying at a point which corresponds to the beginning of the $C'(100kHz)$ plateau in the 2nd row TVIS vial and investigates for melt-back during the temperature ramp of the secondary drying stage. The front row vial would have dried completely as one expects $C'(100kHz)$ to have reached a constant value. But the other internal vials will collapse due to melt-back from the remaining ice present in the bottom interior of the vial. If the second row vial collapses at the beginning of the plateau, it would imply that the beginning of the plateau is not the true endpoint for the 2nd row vial. Case 2 represents a situation where one qualifies the TVIS endpoint from a standard deviation value determined in real time which predicts an endpoint 30 min after the beginning of the plateau. For this purpose, the primary drying is terminated 30 min after C'100 kHz reaches a plateau and melt-back investigation is undertaken during secondary drying. If that point is the true primary drying endpoint, then the second row vial will be dry (no melt-back) while the rest of the internal vials will collapse. This would imply that the true endpoint for the 2nd row vial lies between the point at the beginning of the plateau and the point that lies 30 min after the beginning of the plateau.

6.4 Chapter Conclusion

It has been demonstated that TVIS provides opportunites to predict the primary drying endpoint for TVIS vials containing 5 %w/w sucrose solution using a retrospective and a real time methodology. The standard deviations determined from the real time method prove to be more useful in predicting endpoints, that lie after the point that correspond to the beginning of the plateau as opposed to when the data analysis is undertaken retrospectively. Nevertheless, the under-predicted time-point can serve as an early warning for ending the primary drying phase. Moreover, further work involves studies which warrant qualification of the beginning of the plateau as the true endpoint in situations where one cannot visually detect the removal of 100 % sublimation. Furthermore, it is also recognised that the predicted TVIS endpoint for the core TVIS vial is likely to be non-representative of the true endpoint of the batch because of possible variabilities in the vial heat trasnfer coefficient and the mass transfer resistances across the population.

7 Multiplexing Through Vial Impedance Spectroscopy with Comparative Pressure Measurement for the Determination of the Primary Drying Endpoint of Immunoglobulin G (IgG)

7.1 Objectives

The study has three objectives. The first objective is to extend the TVIS methodology for predicting the primary drying endpoint of ice using the TVIS parameter, $C'(100kHz)$ to a complex protein solution contained in TVIS vials positioned at the edge and the core. The second objective is to compare the predicted TVIS endpoints with the estimates obtained from the batch measurement PAT tools such as the comparative pressure measurement (Pirani/Capacitance Manometer) and the Pressure Rise Test (PRT). The third objective is to explore whether the high frequency capacitance can be used to monitor the secondary drying stage, in particular, the characterisation of the relative differences in the release of the unfrozen water from a predominantly amorphous formulation and the predominantly crystalline formulation during the secondary drying phase.

7.2 Materials and Methods

A batch of 308 x 5 mL vials (Adelphi VC005-20C) were filled with 3 g of 20 mM Histidine Buffer and 0.01% Tween 20 pH 6.5, containing either (i) 4 %w/v polyclonal IgG with 5 %w/v sucrose; (ii) 4 %w/v IgG with 5% of a 4:1 mannitol:sucrose mixture; or (iii) their placebo equivalents formulated in sterile water for injection (Baxter UKF7114). All materials were obtained at the National Institute of Biological Standards and Control (NIBSC), Potters Bar. Two vials from (i) and two vials from (ii) were modified with copper electrodes (19 mm by 10 mm; copper adhesive tape 1181 3M) attached externally to the glass wall at a distance of 3 mm from the vial baseline (Figure 63). One TVIS vial from each IgG containing formulation was placed in the middle of the first row of the edge vials facing the dryer door and the other two TVIS vials were placed in the core (Figure 64). Each TVIS vial was accompanied by two Type T thermocouples placed in the immediate neighbour vials with the sensing tip in contact with the bottom centre of the vial base.

Freeze drying was carried out in NIBSC's Telstar LyoBeta 15 dryer (Figure 65a) equipped with Pirani and Capacitance Manometer (Baratron®) pressure sensors and a 5-channel TVIS system (Sciospec, Germany) (Figure 65b). The TVIS vials were connected to the drive ports (channels 1 to 4) and the corresponding sensing cables (Figure 65d). The freeze dryer and the TVIS system were switched on simultaneously and a spectrum and the corresponding temperature and pressure values were obtained every 2 min throughout the process. The TVIS parameters and other details of the TVIS measurement are summarised in Table 13. The lyo-cycle (Table *14*) consisted of a freezing ramp from 20 °C to -50 °C at 0.2 °C/min, two annealing steps (to -15 °C and -28 °C), followed by a 73 h primary drying step at a shelf temperature of -25 °C and finally a secondary drying step at a shelf temperature of 30 °C for 12 h. The total cycle time for the recipe was approx. 113 h.

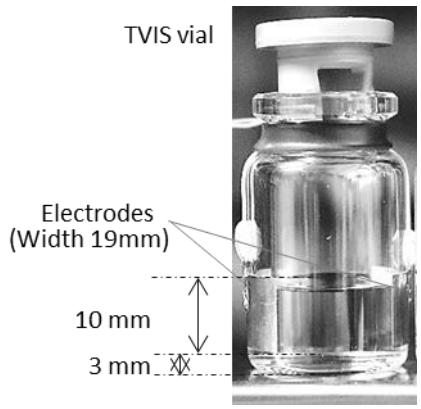

Figure 63: An Adelphi (VC005-20C) vial modified with a pair of copper electrodes (19 mm by 10 mm) attached externally to the glass wall at a distance of 3 mm from the vial base

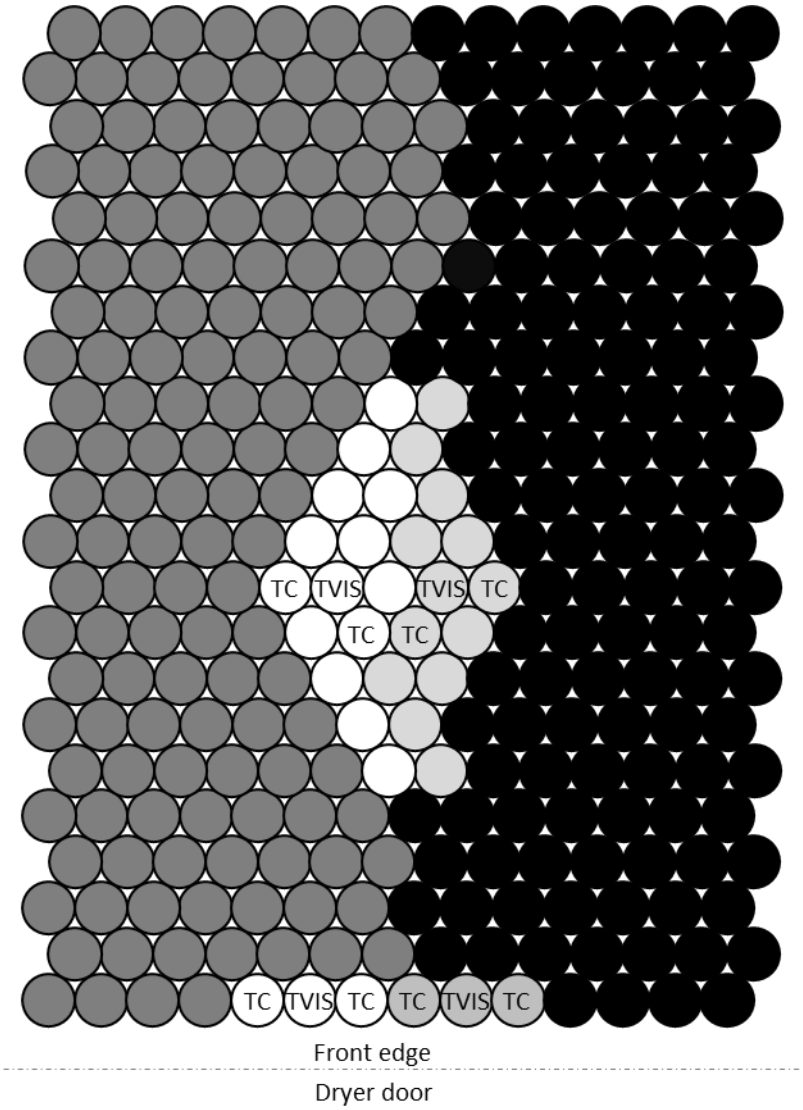

Figure 64: Layout of the 308 x 5 mL Adelphi (VC-005-20C) vials containing 3 g of 4 types of formulations. The colour scheme corresponds to 4 %w/v IgG 4:1 Mannitol: Sucrose in white, 4 % IgG-5 % sucrose in light grey, 5 % Sucrose placebo in dark grey and 4:1 Mannitol:Sucrose placebo in black. All solutions were prepared with 20 mM Histidine Buffer and 0.01% Tween 20 pH 6.5 in sterile water for injection. The measurement vials are labeled as "TVIS" and "TC.

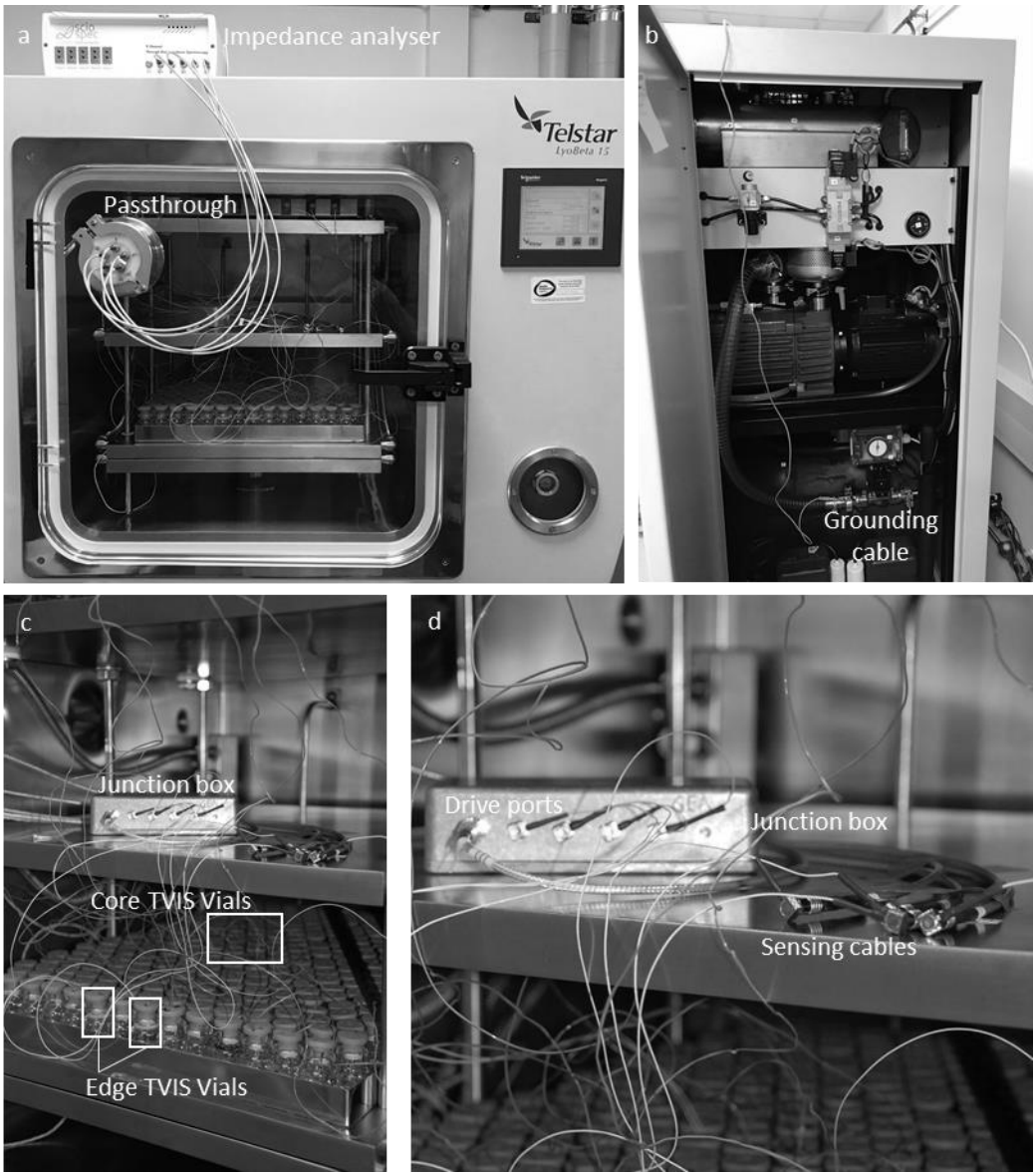

Figure 65: Freeze drying of 4% IgG in 308 x 5 mL Adelphi (VC005-20C) vials out of which 4 were modified with copper electrodes (19 mm by 10 mm; attached externally 3 mm from the vial base) each accompanied by 2 Type T thermocouples in immediate neighbour vials: (a) Two TVIS vials located at the front edge, one containing the 5% Sucrose formulation and the other containing 4:1 Mannitol:Sucrose formulation. The other two TVIS vials containing the same formulations were located in the core; (b) All TVIS vials were connected to the stimulating ports on the junction box and the corresponding sensing cables connected to a modified passthrough; (c) The passthrough was mounted on a Telstar LyoBeta 15 freeze dryer equipped with a 5-channel TVIS system (Sciospec, Germany).

Table 13: TVIS parameters and the details of the TVIS measurement for 4 % IgG containing formulations

TVIS Parameters				
Frequency range	10 Hz to 1 MHz			
AC voltage	0.2 to 8 V			
Measurement/ Scan interval	2 min			
Channel	CH1	CH2	CH3	CH4
Vial Nomenclature	TVIS 1	TVIS 2	TVIS 3	TVIS 4
Vial position	Edge	Core	Edge	Core
Formulation	4% IgG 4:1 Mannitol:Sucrose 20 mM Histidine buffer 0.01% Tween 20 pH 6.5		4% IgG 5% Sucrose 20 mM Histidine buffer and 0.01% Tween 20 pH 6.5	
Mass of Solution/ g	3.00			
Thermocouple Number	TC1 & TC2	TC3 & TC4	TC5 & TC6	TC7 & TC8

Table 14: Freeze-drying protocol for 3 g of 4 % IgG formulations in 308 x 5 mL Adelphi (VC005-20C) vials

Step	Start Temperature (°C)	End Temperature (°C)	Ramp rate (°C/ min)	Duration (min)	Cumulative Time (h)	Set pressure (mbar)
Equilibrium phase	24.6 (RT)	20	-	30	0.5	-
Freezing	20	-50	0.2	130	2.7	-
Hold	-50	-50	-	120	4.7	-
Re-heating	-50	-15	0.2	175	7.6	-
Hold	-15	-15	-	120	9.6	-
Re-cooling	-15	-50	0.5	70	10.8	-
Hold	-50	-50	-	120	12.8	-
Re-heating	-50	-28	0.2	90	14.3	-
Hold	-28	-28	-	120	16.3	-
Re-cooling	-28	-50	0.5	44	17	-
Hold	-50	-50	-	120	19	-
Primary drying	-50	-50	-	30	19	0.2
	-50	-25	0.8	30	20	0.2
	-25	-25	-	4320	92	0.2
Secondary drying	-25	30	0.15	360	98	0.2
	30	30	-	876	112.6	0.2

7.3 Results

7.3.1 Comparative pressure measurement and the Pressure Rise Test

Figure 66(a) shows the time-lines of the Pirani and the Capacitance Manometer (Baratron®) pressure sensors, the shelf temperature and the average product temperature at the bottom of the vials containing thermocouples at the edge and the core during the primary drying and the secondary drying phases. Note the pressure rise test involving repeated isolation (~30 s) of the chamber from the condenser results in the spikes in the pressure signals due to a rise in the chamber pressure (sensed by the capacitance manometer), which results from the rise in the water vapour pressure (sensed by the Pirani).

At the beginning of the primary drying phase, when the gas composition is essentially 100 % water vapour, the pressure detected by the Pirani increases sharply from ~0.244 mBar to a pseudo steady-state value (~0.333 mbar) over the first ~1 h of primary drying, which stays constant until the first 43 h; whereas the capacitance manometer continues to maintain the chamber pressure close to the setpoint (0.2 mbar). The free molecular flow thermal conductivity of water vapour is reported to be 6.34 x 10^{-3} cal. s^{-1} cm^{-2} $mmHg^{-1}$, which is about 60 % higher than that for Nitrogen gas or N_2 (3.98 x 10^{-3} cal. s^{-1} cm^{-2} $mmHg^{-1}$) (Amidon, et al. 1999).

Being a thermal conductivity type gauge, the Pirani senses this sharp increase in the thermal conductivity of water vapour in the chamber, which is in abundance over the first 43 h of primary drying. A large number of spikes in the pressure signals further confirm the presence of an abundance of water vapour escaping from the vials during the pressure rise test. Between 43:00 and ~61:00, the Pirani output decreases from 0.333 mBar to ~298 mBar due to a decrease in the partial pressure of water vapour relative to that of N_2. Note the presence of significantly fewer spikes in the Pirani signal, which implies the ice sublimation is nearly complete as most of the ice is removed over the first 43 h of primary drying. The Pirani pressure continues to decrease further after 61:00 and finally reaches a value of 0.236 mbar at 73:12. By this point, it is expected that the Pirani output stabilises either to a

pseudo steady value within 0.006-0.013 mBar with respect to the capacitance manometer reading or return to the CM value. However, neither of those features are observed in the Pirani profile, and yet it continues to remain active until 73:12.

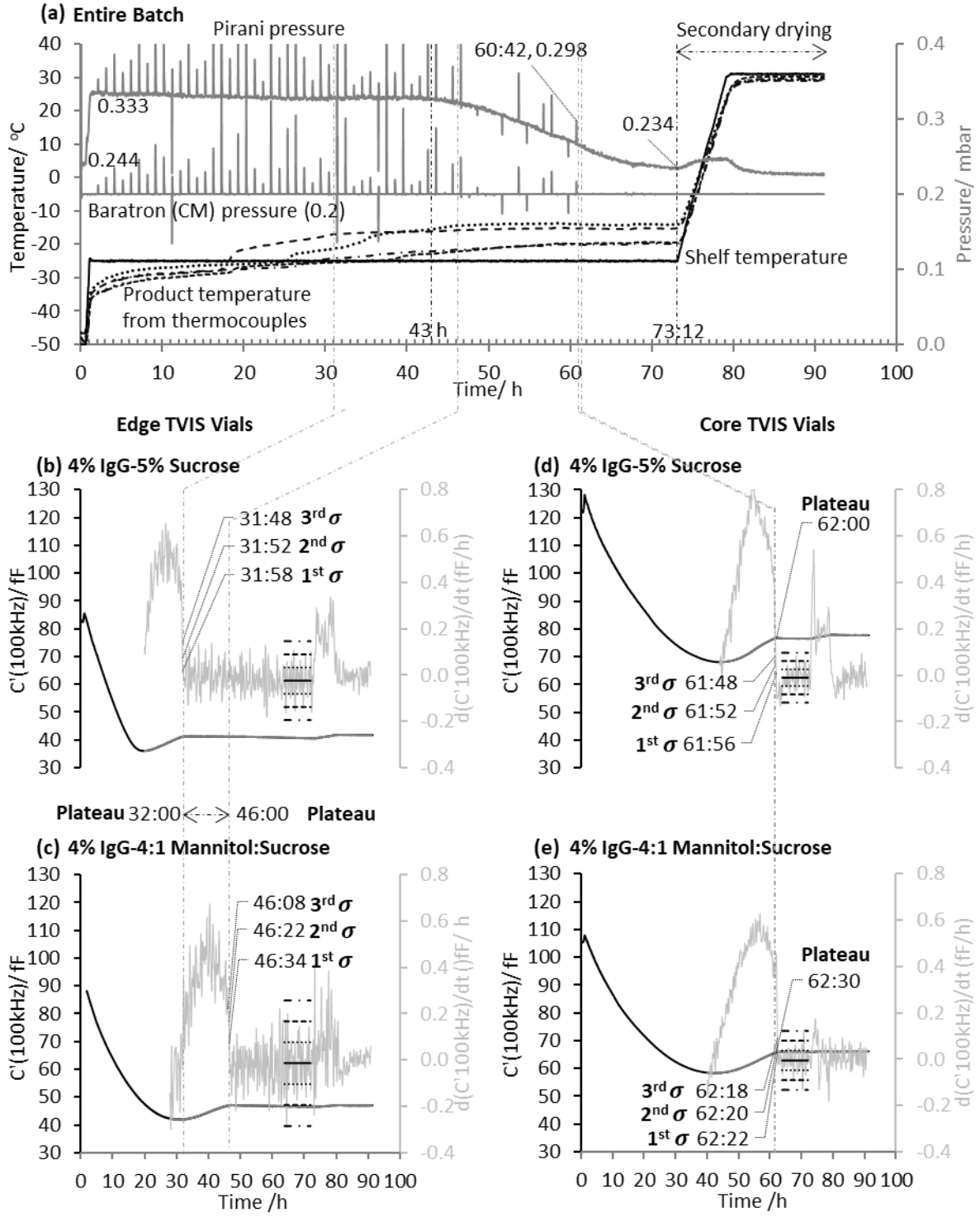

Figure 66: Comparison of the primary drying endpoint of the batch containing 4%IgG_5%sucrose and 4%IgG_4:1 mannitol:sucrose formulations and their placebo equivalents using the comparative pressure measurement against the prediction of the primary drying endpoint in the TVIS vials with the IgG_Sucrose and IgG_Mannitol:Sucrose containing formulations, each located at the edge and in the core: (a) Time-lines of the Pirani gauge pressure and the capacitance manometer pressure, the shelf temperature and the average product temperature from two thermocouples in the nearest neighbour vials; on the primary Y axes of b to e are the time-lines of $C'(100kHz)$ (solid black lines) and the rolling average of $C'(100kHz)$ (solid grey lines) determined retrospectively every 20 min; on the secondary Y axis of b to e are time-lines of the first derivative of the rolling average determined retrospectively over every 20 min. The mean of $d(C'100kHz)/dt$ (solid black lines passing through the scatter) and the values of the three standard deviations determined over the last ~8 h of primary drying are shown for each TVIS vial. The dashed vertical lines correspond to the beginning of the $C'(100kHz)$ plateau, which follows the rank order from the fastest to the slowest to reach the plateau: (1) Edge_IgG_Sucrose (32:00); (2) Edge_IgG_Mannitol:Sucrose (46:00); (3) Core_IgG_Sucrose (62:00); (4) Core_IgG_Mannitol:Sucrose (62:30).

7.3.2 Identification of the time-points that correspond to the beginning of $C'(100kHz)$ plateau

Figure 66 (b to e) show the time-lines of $C'(100kHz)$ on the primary Y-axis for the IgG_sucrose and the IgG_mannitol:sucrose formulations contained in the TVIS vials at the edge and the core. Assuming that the beginning of the plateau corresponds to 100 % ice sublimation, then the IgG sucrose and the IgG_mannitol:sucrose containing edge vials dry by 32:00 and 46:00, respectively; whereas the IgG_sucrose and IgG_mannitol:sucrose containing core vials dry by 62:00 and 62:30, respectively. These have been marked in Figure 66 using vertical dashed lines passing through the beginning of the plateau in each case.

7.3.3 Prediction of the primary drying endpoints in individual TVIS vials

The methodology for predicting the TVIS endpoints for each vial has already been demonstrated previously (Section 5.3.7.2) but it is briefly explained here: (i) the values of the rolling average and the first derivative of the rolling average, $d(C'100kHz)/dt$, are determined retrospectively over every 10 datapoints (or every 20 min) going forward in time; (ii) the mean of the first derivative and three standard deviations from the mean are determined over the plateau region. Towards the end of the recovery phase, the point when the first derivative drops below the threshold as defined by each of the three standard deviations are taken as the three estimates for the predicted TVIS endpoint. Finally, in order to predict the endpoint in real time method the data is processed going backward in time, which effectively shifts the analysis period forward by 20 min with respect to retrospective method.

Once the limiting criteria have been established, the next stage is to explore their impact on the predicted TVIS endpoint for each TVIS vial and compare the relative position of the predicted TVIS endpoint with the point when $C'(100kHz)$ reaches a plateau because that corresponds to what is considered to be the visual endpoint as demonstrated for pure ice. In Figure 66(b to e) on the primary Y-axes, the time-lines of the rolling average of $C'(100kHz)$, and on the secondary Y-axes, the time-lines of the first derivative, determined retrospectively, are shown for the front, left, back and core

TVIS vials, respectively. The mean of the first derivative determined over the last ~8 h of primary drying is shown as a solid black line going through the scatter while the values of the first, second and third standard deviation are shown as a dotted line, dashed line and dashed-dot line, respectively, over the same period as the that for the mean. The predicted endpoints determined retrospectively, are marked for each TVIS vial in Figure 66, while Table 12 includes the values of all the parameters determined retrospectively: the mean μ, the root mean square deviation (RMSD) and the three standard deviations from the mean (upper limits), and the corresponding predicted endpoints for each TVIS vial. Further, the predicted endpoints based on the real time analysis are given in the bottom half of the table. Finally, in the last column of the table in the right, the time-points at which $C'(100kHz)$ reaches a plateau for each case are included.

Clearly, the retrospective analysis results in the under-prediction of the TVIS endpoint in the majority of the cases (Figure 66). However, when the real time method is employed, it effective shifts the analysis period forward by 20 min. As a consequence, all the TVIS endpoints are over-predicted with respect to the beginning of the endpoint (Table 15). As with the sucrose endpoint study, where it was demonstrated that the real time method proves to be more practical than the retrospective method, the numbers in this study also suggest that the real time method is more practical. It follows that it is probably best to consider the real time method for comparison of the predicted TVIS endpoints with the endpoint indicated by the batch sensors.

Table 15: The TVIS endpoints predicted for the IgG_Sucrose and IgG_Mannitol:Sucrose containing formulations defined by the limiting criteria determined from three standard deviations from the mean of the first derivative in the plateau region. Also, shown are the time-points which correspond to the beginning of the plateau.

Retrospective Methodology										
Formulation	**TVIS vial location on the shelf**	**Mean (μ) of $\frac{d(C'(100kHz)}{dt}$**	**RMSD**	**1st σ**	**2nd σ**	**3rd σ**	**TVIS Endpoint (h:min)**			**Time at plateau (h:min)**
							1st σ	**2nd σ**	**3rd σ**	
4% IgG-5% Sucrose	Edge	-0.00242	0.057	0.032	0.089	0.15	31:58	31:52	31:48	32:00
4% IgG-4:1 Mannitol: Sucrose	Edge	-0.00137	0.090	0.077	0.170	0.26	46:34	46:22	46:08	46:00
4% IgG-5% Sucrose	Core	-0.00106	0.036	0.025	0.061	0.097	61:56	61:52	61:48	62:00
4% IgG-4:1 Mannitol: Sucrose	Core	-0.00493	0.042	0.038	0.080	0.12	62:22	62:20	62:18	62:30
Real Time Methodology										
4% IgG-5% Sucrose	Edge	Addition of 20 min to the TVIS endpoints predicted from the retrospective method					32:18	32:12	32:08	32:00
4% IgG-4:1 Mannitol: Sucrose	Edge						46:54	46:42	46:28	46:00
4% IgG-5% Sucrose	Core						62:16	62:12	62:08	62:00
4% IgG-4:1 Mannitol: Sucrose	Core						62:42	62:40	62:38	62:30

7.3.4 Comparison Among the Estimated Batch endpoint and the TVIS endpoints

The last spike in the Pirani reading occurs at 60:42 and the absence of any pressure rise between 61:00 h and 73:12 indicates either all the ice is removed by 60:42 or the test loses sensitivity to sublimation of the last traces of ice. However, the Pirani gauge still appears to be active until 73:12 (Figure 66a). Whether this is because not all the core vials finish drying, or it is the water vapour trapped in the chamber and/or the condenser that is sensed by the Pirani remains to be seen. This ambiguity was investigated using TVIS by predicting the primary drying endpoint in the edge and the core vials. For this purpose, the TVIS endpoints predicted from the 3rd standard deviation determined in real time have been considered because they lie after and very close to the beginning of the plateau, which has been assumed to be point of 100 % ice sublimation. Thus, the predicted TVIS endpoints are (Table 15): 32:08, 46:28, 62:08 and 62:38 for the IgG_sucrose edge, IgG_mannitol:sucrose edge, IgG_sucrose core and the IgG_mannitol:sucrose core vials, respectively

The IgG_sucrose containing edge TVIS vial is expected to have dried by 32:08, i.e. several hours before the onset of the reduction in the Pirani pressure (i.e. at 43:00) while the IgG_mannitol: sucrose edge TVIS vial is expected to have dried by 46:28, i.e. 3.5 h after the onset of the reduction in the pirani. This confirms that the comparative pressure measurement is more sensitive to core vials, which represent the majority of the batch.

The predicted TVIS endpoint for the IgG_sucrose and the IgG_mannitol:sucrose containing core TVIS vials were 62:08 and 62:38 respectively. It is worth recognising that (i) the variability in the vial geometry leads to a variability in the vial heat transfer coefficient (K_v) during primary drying (Scutella, et al. 2017); and (ii) during freezing, a heterogeneity in the ice crystal structures across the batch due to stochastic ice nucleation leads to a variability in the mass transfer resistance (R_p) during primary drying (Scutella, et al. 2018). As a consequence of both the factors, there can be a potential variability in the product temperature, hence the variability in the primary drying times across the batch. Assuming that this variability is 1 h, then it implies that both the core vials should have dried by

~64 h. Given that the pressure rise test indicates the ice sublimation is completed by 60:42 (as there is no pressure rise after 60:42) and the Pirani profile doesn't appear to have reached a pseudo steady value even by 73:12, it implies there might be a number of contributing factors: (i) other core vials are still drying (i.e. the variability in the batch endpoint is greater than 1 h), and/or (ii) the Pirani continues to sense water vapour in the chamber even when all the ice has sublimed; and/or (iii) batch sensors are insensitive to the sublimation of the last traces ice.

7.3.5 Monitoring of the Secondary Drying Phase

Figure 67 shows an enlarged plot of the secondary drying phase (73:12 to 91:06). It is clear from Figure 67(a) that a shelf temperature ramp from -25 °C to 30 °C at +0.15 °C/min results in an increase in the product temperature, which in turn results in an increase in the Pirani pressure from 0.236 mBar (at 73.2 h) to 0.247 mBar (at 73.9 h) which is characteristic of a "burst" release of the unfrozen water from the product (Fissore, et al. 2018; Nail, et al. 2017; Patel, et al. 2010). Over the next ∼12 h, at a constant shelf temperature (30 °C), the Pirani gauge output decreases to a new pseudo-steady value of ∼0.226 mBar. Further, very small spikes in the chamber pressure reaffirm that very little additional drying takes place at this shelf temperature.

Further, the plots in (b to e) have been enlarged to demonstrate that it is possible to follow the time-line of $C'(100kHz)$ to monitor the secondary drying phase. During the temperature ramp of the secondary drying stage, for the IgG_sucrose containing TVIS vials at the edge and the core, the magnitude of the rolling average of $C'(100kHz)$ increases from 40:36 to 41:48 fF (∼3 %) and from 76.5 fF to 77.9 fF (∼1.8 %) respectively, as demonstrated in Figure 67 (b) and (d). In contrast, a much smaller increase in $C'(100kHz)$ is observable in the case of the IgG_Mannitol:Sucrose containing formulations as in Figure 67 (c) and (e). This may be attributed to the release of the unfrozen water from sucrose, which is expected to attract more water than mannitol during vitrification, while mannitol crystallises out during the annealing stage. Moreover, the release of any bound water from the IgG is less likely to be the case, owing to the presence of the ionizable groups (NH3+ and COO-) in the IgG structure, which require a hydrophilic shell around them (Kindt, et al. 2007) and therefore, IgG does not give up the water that easily. Finally, towards the end of the secondary drying stage, it is interesting to note, when the Pirani reading attains an equilibrium (85:38), the time-profiles of $C'(100kHz)$ also attain a new pseudo steady state value.

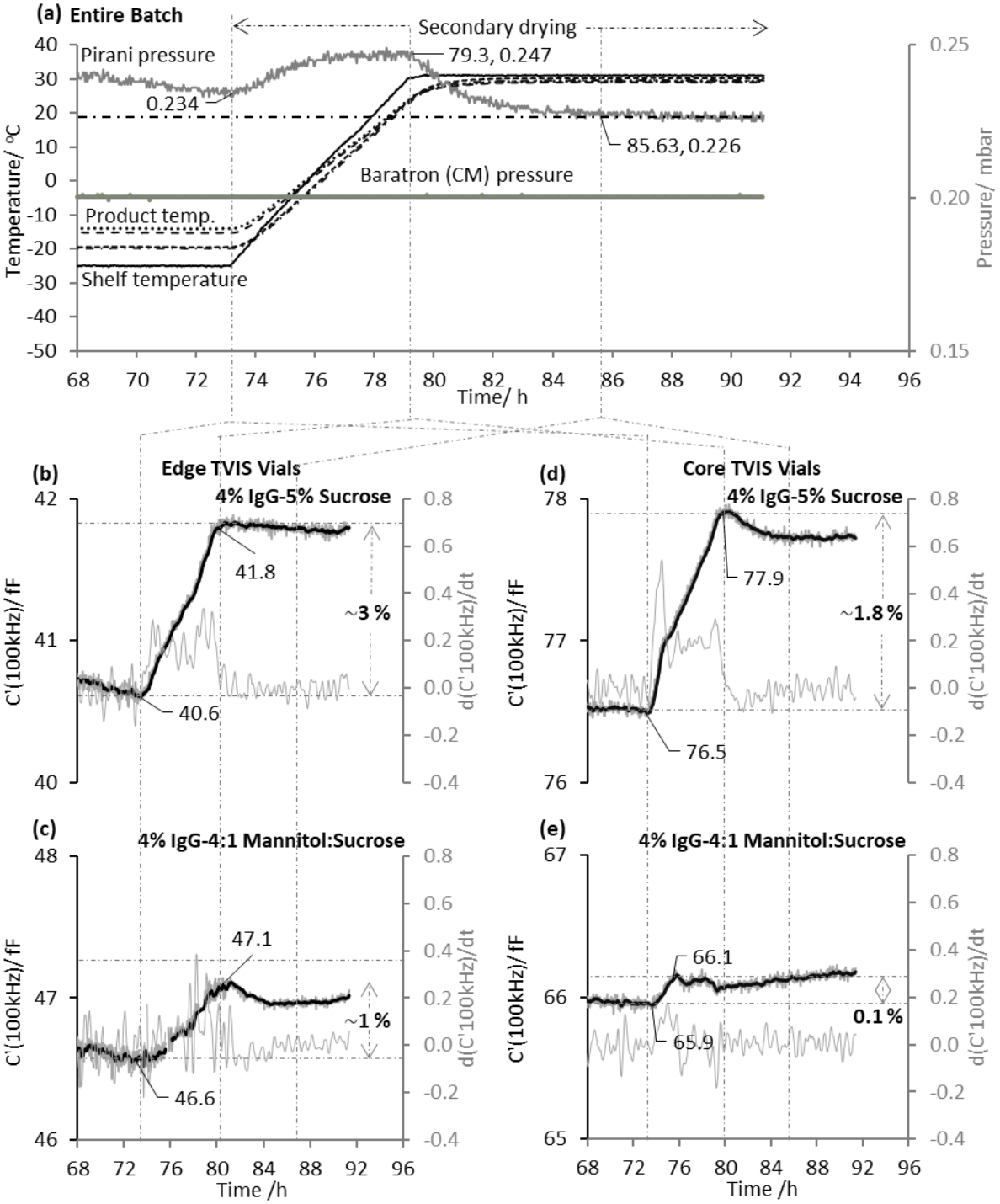

Figure 67: Monitoring of the secondary drying process using the comparative pressure measurement of the batch comprising the IgG_sucrose and the IgG_mannitol:sucrose formulations and their placebo equivalents, and using TVIS employing 4 TVIS vials containing the 2 IgG formulations, one of each at the edge and in the core: (a) a plot of the process parameters (enlarged for highlighting the secondary drying period), namely the Pirani and the capacitance manometer pressure outputs, the shelf temperature and the average thermocouple response in the immediate vicinity to the TVIS vials; on the primary Y axes of b to e: the time-lines of $C'(100kHz)$ (solid light grey lines) and the rolling average of $C'(100kHz)$ (solid black lines) taken every 20 min going back in time; on the secondary Y axis of b to e: time-lines of the gradient of the rolling average of $C'(100kHz)$ taken over every 20 min going back in time. The dashed vertical lines correspond to the specific time-points that illustrate the key events such as the increase in the Pirani pressure and in $C'(100kHz)$ during the temperature ramp from 73.2 h until 79.3 h, the decrease in the Pirani pressure and in $C'(100kHz)$ from 79.3 h until 85.63 h, and the equilibration phase for both the Pirani pressure and $C'(100kHz)$ from 85.63 h until the end of the process.

7.4 Discussion

It has been demonstrated in the previous study involving pure ice that the beginning of the $C'(100kHz)$ plateau corresponds to the visual endpoint. In this study, assuming that the beginning of the plateau corresponds to 100 % ice sublimation, then the IgG_sucrose and the IgG_mannitol:sucrose containing edge TVIS vials are expected to have dried by the first 46 h 30 min of primary drying. This time-point lies 3.5 h after the onset of the reduction in the pressure. Moreover, around the same time, the spikes in the vapour pressure continue to be observed from the pressure rise test. Thus, it can be stated that batch sensors are more sensitive to the core vials, which make up the majority of the batch.

Further, based on the limiting criteria of the 3rd standard deviation determined by the real time methodology, the core TVIS vials are expected to have dried by the first ~64 h of primary drying. Given that the pressure rise test shows very little to no spikes after 60:42 and the fact that the pirani gauge continues to be active until 73:12 (onset of secondary drying stage), it suggests that the other core vials of the batch are still drying and/or the Pirani pressure continues to sense the residual vapour in the chamber and/or the batch sensors, in general, are less sensitive to the last trace of ice. It follows that neither TVIS nor the batch methods appear to have found the true endpoint of the batch. Moreover, with the current TVIS set-up of 4 TVIS vials, it has not been possible to perturb the entire core vial population. Nevertheless, the study does demonstrate future opportunities for determining the TVIS endpoint at various shelf locations and therefore, obtain an estimate closer to that of true endpoint of a batch.

Finally, with TVIS, it has been potentially identify the differences in the cake morphologies between the IgG_Sucrose and the IgG_Mannitol:Sucrose containing formulations by studying the shape of the trajectory of the high frequency capacitance, $C'(100kHz)$, which is sensitive to subtle differences in the extent of release of the unfrozen water from the TVIS vials located at the edge and in the core during the temperature ramp of the secondary drying stage. The increase in $C'(100kHz)$ for the IgG_mannitol:sucrose containing TVIS vials has been found to be much smaller (up to 1 %)

relative to that for the IgG_Sucrose formulation (up to 3 %). As a general rule, for an amorphous material such as sucrose, nearly 20 % of the water remains unfrozen, trapped with the amorphous solute in the interstitial region of the ice crystals (Kasper and Friess 2011). In this study, about 0.15 g (5 %) of the initial weight of the sample (3 g) constituted sucrose in the case of the 4% IgG_5% sucrose containing formulation and therfore, the unfrozen water content is likely to be ~0.6 g (i.e. 20 % of 2.85 g), which is sensed by $C'(100kHz)$ as this unfrozen, amorphous water is released during the secondary drying stage. In constrast, the release of unfrozen water associated with the IgG_mannitol:sucrose is possibly inhibited by the crystallisation of mannitol during the annealing phase, hence a smaller increase in the magnitude of $C'(100kHz)$. Finally, the characterstic transition of the the Pirani profile at a constant shelf temperature of 30 °C towards a value of equilibrium is strikingly similar to that of $C'(100kHz)$ at the end of the secondary drying phase which suggests TVIS presentes opportunites for determining the secondary drying endpoint.

7.5 Chapter Conclusion

The study demonstrates an opportunity to multiplex single vial monitoring process analytical technologies such as the likes of TVIS with batch monitoring techniques for the determination of the primary drying endpoint. It has been demonstrated that while it is possible for TVIS to predict a more precise endpoint in individual vials in relation to the beginning of the plateau in the trajectory of the high frequency capacitance, $C'(100kHz)$, compared to that determined using conventional thermcouples, it has not been possible to ascertain whether the predicted TVIS endpoint is representative of the true endpoint of the batch owing to potential variabilitiies in the vial geomety and the heterogeneities in the ice crystal morphology formed during freezing. Finally, the study indicates that neither of the two batch monitoring techniques have been able to detect the true endpoint of the batch owing to a number of contributing factors. The pressure rise test appears to have indicated the end of primary drying before the core TVIS vials. Moreover, the pirani pressure continues to be active up to several hours after the core TVIS vials are expected to have dried. This

suggests that the batch sensors are either less sensitive to ice sublimation over the last few hours of primary drying and/or other core vials are still in the primary drying stage due to the variability in the batch endpoint or the batch sensors continue to sense some water vapour that is trapped in the drying chamber.

8 Study of the Dielectric Properties of the Glass Wall

8.1 Background

It has been demonstrated using equivalent circuit modelling that the low frequency end of the spectrum (10 Hz to 10 kHz) is impacted by the glass wall due to its frequency dependence, referred to as the anomalous low frequency dispersion (LFD), which is modelled by a constant phase element (CPE) (Smith and Polygalov 2019). The primary focus of this work is to study the dielectric behaviour of the glass wall at a range of frequencies and temperatures, with a goal to better understand the temperature dependence of the glass wall, particularly in the freeze drying temperature range of interest (-50 to 0 °C). Given that TVIS can only measure the impedance response in the low frequency end up to 10 Hz, the present work involves the use of broadband dielectric spectroscopy (BDS), which is a useful tool for investigating the dielectric behaviour of solids and liquids at various levels (e.g. macroscopic, mesoscopic, microscopic) over a broader frequency range (10^{-6} to 10^{12} Hz), hence the term broadband dielectric spectroscopy (Kremer and Schönhals 2003).

The Microstructure of the Glass Wall and the Percolation Paths for Molecular Motion

The Fiolax® glass used for the Adelphi VC010-20C vial (Figure 68a) used routinely for TVIS measurement, is a disordered porous material at the micro-scale which belongs to a broad class of complex systems (CS) that include polymers, biopolymers, colloidal systems (e.g. emulsions and micro-emulsions), liquid crystals, biological cells and other porous materials (e.g. porous glasses, sol-gels and porous silicon) (Feldman, et al. 2012) . With dielectric spectroscopy it has been possible to elucidate that the simple Debye law, which is applicable when all molecules of a material polarize and relax at the same time, referred to as a single time constant (i.e. $\tau = RC$) and Brownian diffusion (motion along a random path length) cannot adequately explain the relaxation phenomena and kinetics in such heterogeneous materials (Feldman, et al. 2012).

It is well known that in porous borosilicate glasses (such as the Adelphi freeze drying vial), two inter-connected phases exist: (i) an ordered insulating phase composed mainly of silica or silicon dioxide (SiO_2) and possibly other oxides (e.g. of Boron, Aluminium, Calcium etc.) in smaller proportions forming a rigid tetrahedral backbone of the microstructure, and (ii) a porous conducting phase where alkali ions (e.g. Sodium, Potassium, etc.) and water molecules reside (Feldman, Yuri, et al. 2006). Under the influence of an electric field, it is possible for protons and ions to traverse through continuous networks throughout the microstructure, referred to as a percolation channel (Essam 1980; Gutina, A., et al. 2003; Gutina, Anna, et al. 1998; Le Losq, et al. 2017; Nan, et al. 2010). Note that this phenomenon should not be confused with the classical crystal defect percolation (Popov, et al. 2017).

It follows that different percolation path lengths are possible for protons and ions which polarize the pores over various times scales depending on the applied frequency and temperature thus resulting in an overall distributed time constant (rather than a single time constant) (Feldman, et al. 2012). The various paths of percolation within a typical borosilicate glass microstructure such as that for the Adelphi VC010-20C vial (Figure 68a) have been visualized in Figure 68 (b to e) based on the understanding of the work on the dc and ac conductivity measurements performed by El-Egili et al. (1996) and the porous alkaline treated hydrated glasses by Feldman et al. (2006). Figure 68 (b) can be considered to be section of the glass vial with large irregular pores within a continuous phase of silica and other oxides (empty space) and the smaller structures within the larger pores termed “small pores” thought to be located near the surface of the glass. The small pores are interconnected with each other and so are the larger pores such that two levels of percolation are thought to be established, i.e. short range percolation and long range percolation (Figure 68d). Under the influence of an electric field, protons migrate from the water molecules and polarize a small pore when the applied frequency is lower than the time taken by protons to polarize the pore. In other words, the dielectric relaxation of protons within a pore has a certain time constant. A decrease in the applied frequency would then allow the percolation of protons from one small pore to the next small pore (shown as arrows within the small pores) hence the term **short range percolation**. As the frequency is lowered further, a **long**

range percolation path opens which allows ions to migrate from one large pore to the next large pore (shown as larger arrows pointing from one large pore to the next large pore). Thus, within the long range percolation path the dielectric relaxation of ions is thought to be associated with a different time constant. In other words, the long range percolation path won't open unless the applied frequency is lower than the time constant associated with it. A third type of percolation path, known as the **dc conduction path**, allows ions traverse through separate channels through the whole microstructure (Figure 68e) at elevated temperatures where the effect of thermal agitation is dominant, and the applied frequency has no influence (El-Egili 1996).

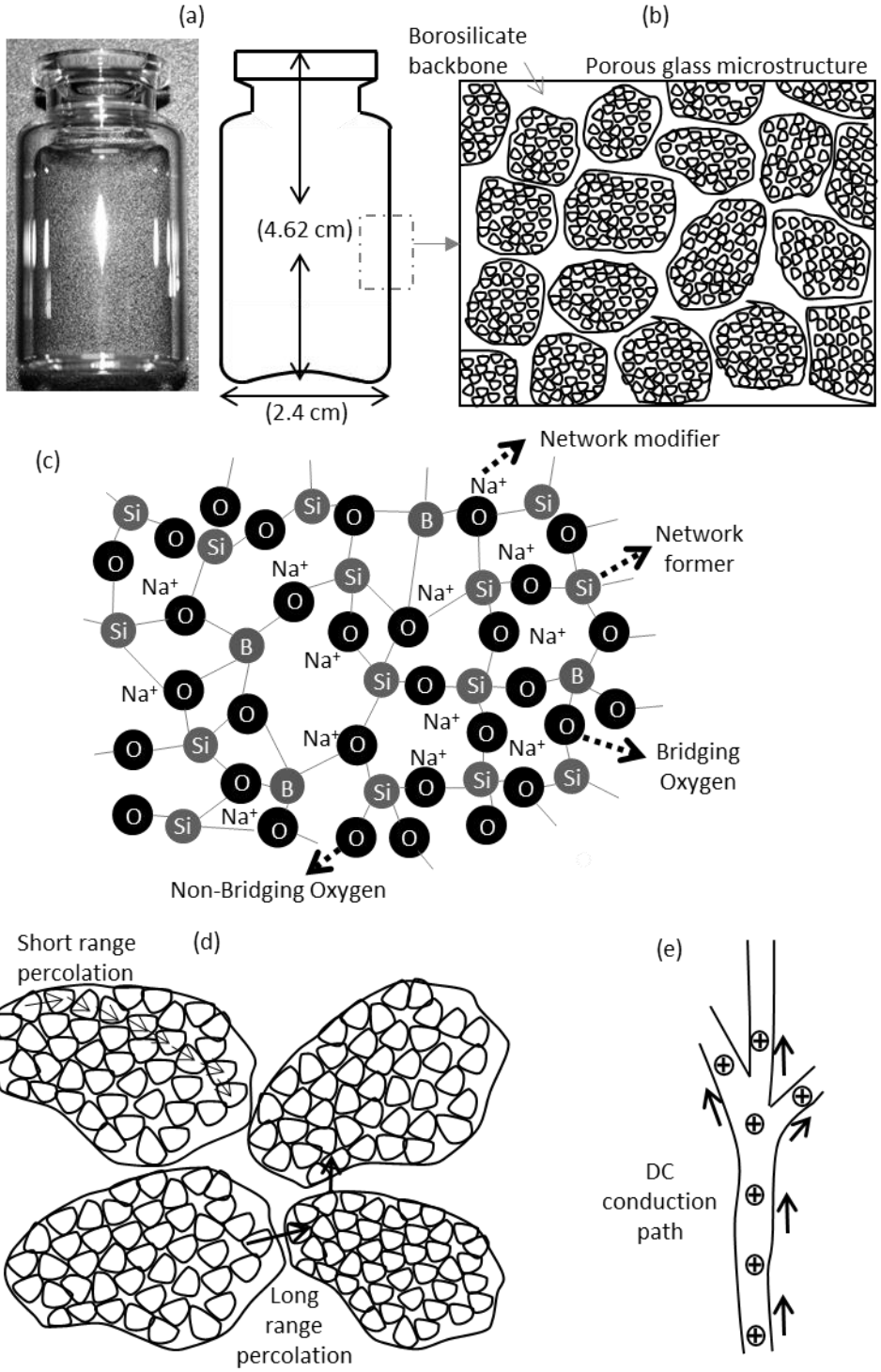

Figure 68: Paths for percolation taken by mobiles species within the microstructure of borosilicate glass (a) A photograph and a sketch of the Adelphi (VC010-20C) vial; (b) Porous glass microstructure with larger pores dispersed in an empty space composed of the rigid non conducting network of silica and the other oxides. The structures within the large pores are smaller pores; (c) Borosilicate network; (d) A close up of the large and the small pores. Short range percolation of protons occurs from one small pore to the next small pore over a certain frequency which is less than the time constant associated with this polarisation, whereas longer range percolation of ions occurs from one large pore to the next large pores as the frequency is lowered; (e) DC conduction path for ions that jump from one site to another and migrate through separate channels throughout the microstructure. This is realised only at elevated temperatures where the effect of thermal agitation is predominant, and the influence of the applied frequency is non-existent.

Simulation of the Dielectric Response of the Glass Wall

Having recognized the different frequency and temperature dependent percolation paths that the protons and ions use to migrate through the glass microstructure, it is now a matter of representing these behaviors in terms of the equivalent circuit elements and how a combination of one or more of such elements can yield an impedance response that can then be graphically represented to derive a direct understanding of the inter-relationship between the impedance response and the physics of the system.

The fundamentals of electricity and circuit modelling are described in Appendix I. In brief, while a good conductor of electricity is represented by a resistor, an insulator is represented by a capacitor. When placed in an alternating electric field, the impedance of the resistor is constant as it is independent of the applied frequency. However, the impedance of a capacitor decreases as the applied frequencies increases. In other words, the charging of a capacitor is associated with a single time constant and can be expressed as:

$$\tau = RC \qquad \text{Equation 17}$$

where τ corresponds to the relaxation time for the mobile species within an object, R and C are the resistance and the capacitance of the object respectively (Hazen 1990). If the applied frequency is higher than this time constant, the capacity of the object to accumulate charge will decreases as the frequency increases. It is important to recognise that most real objects have a combination of characteristics, for example, resistance and capacitance. When such objects are placed in an alternating electric field, they behave as a pure resistor at low frequencies and as a pure capacitor at high frequencies. Such objects are usually represented by a parallel combination of a resistor and a capacitor, i.e. a RC circuit (Smith and Polygalov 2019). A simulation of a parallel RC circuit is shown in

Figure 69 (a) and (b) where a Nyquist plot of the imaginary part impedance ($-Z^{"}$) is plotted against real part impedance (Z') and a Cole-Cole plot of imaginary part capacitance ($-C^{"}$) is plotted

against real part capacitance (C') respectively. Note the values of the resistor and the capacitor are 1 GΩ and 1 pF respectively, simulated over the frequency range 0.001 Hz to 1 MHz.

A Nyquist plot can be used to estimate the value of DC resistance (Macdonald, J.R., Johnson,W.B. 2005). Figure 69(a) shows a semicircle with its centre located on the Z'-axis. The low frequency part of the semicircle intercepts the Z'- axis to yield a value for the resistance (i.e. 1 GΩ). One can see how the low frequency part of the spectrum spans almost the entire spectrum and the high frequency end of the spectrum is confined to an extremely small region on the left side of the plot. This reiterates the fact that a resistor dominates at low frequencies. Likewise, on a Cole-Cole plot (Figure 69b) a vertical straight line indicates that a resistor dominates the spectrum at low frequencies and a dc conduction path is open for ion migration. In order to estimate the value of capacitance one would then need to zoom into the Cole-Cole plot at the high frequency end of the spectrum. This is highlighted in Figure 70(a). Note how the scale has been adjusted in order to pinpoint the location of a black dot that corresponds to the simulated value of the capacitance (i.e. 1 pF).

As discussed previously, complex systems such as porous glasses have a distributed time constant due to the molecular motion that occurs at several levels depending on the applied frequency and temperature (Feldman, et al. 2012). In the impedance community, this type of behaviour, where the object's character is intermediate between purely capacitive and purely resistive, may be modelled by a constant phase element (CPE). It is known that time constant dispersion is a more complicated frequency response compared to a simple "undistributed" RC time constant process (Figure 70a) and is frequently modelled by a CPE (Orazem and Tribollet 2008). A theoretical account on the use of CPEs is given in Appendix II. Briefly, there are two essential parameters of a CPE, the Q value which corresponds to a CPE's magnitude (e.g 1 pF) and the p value which ranges from 1 to 0. A pure capacitor has a p value of 1 and on a Cole-Cole plot it is observed as a straight line that contributes completely to the real part capacitance (zero phase angle with respect to the C'-axis). When the p value is equal

to 0, then the object is purely resistive and, on a Cole-Cole plot it will be seen as a vertical line perpendicular to the C'-axis (phase angle 90°).

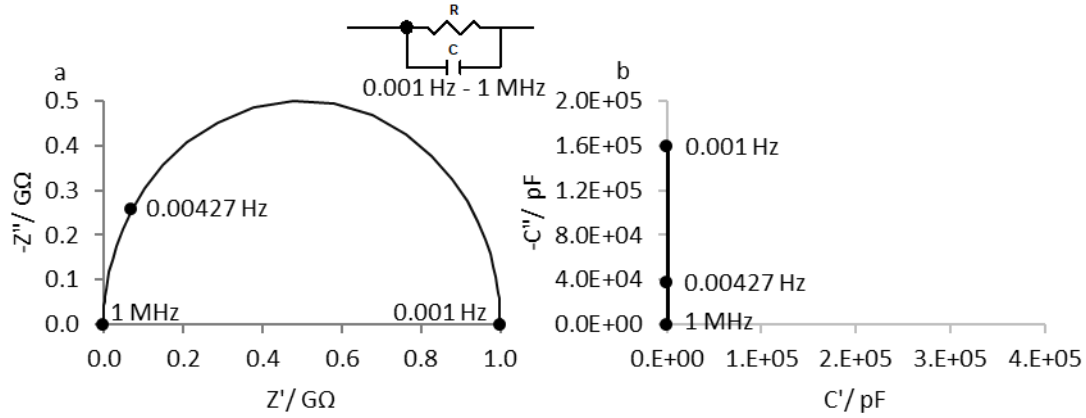

Figure 69: Simulation of parallel RC circuit over the frequency range 0.001 Hz to 1 MHz with values of 1 GΩ and 1 pF for the resistor and the capacitor respectively: (a) Nyquist plot of imaginary part impedance v/s real part impedance showing a semi-circular shape of the impedance spectrum with its centre located on the x-axis. The observed response is dominated by the low frequency part of the spectrum which indicates that a resistor dominates at low frequencies and the intercept on the right side of the semicircle can be used to estimate a value of DC resistance; (b) Cole-Cole plot of imaginary capacitance v/s real part capacitance showing a vertical line perpendicular to the x-axis which is characteristic of a resistor in the model dominating at low frequencies. The value of the capacitor appears to be zero but when the scale is readjusted to highlight the high frequency part of the spectrum, the plot reads a value of 1 pF. This is clarified in Figure 70(a).

A simulation of the different percolation pathways over the frequency range 0.001 Hz to 1 MHz has been depicted in Figure 70(b) to (d) in terms of equivalent circuit models where the high frequency end of the spectrum has been highlighted. Starting from the highest frequency, i.e. 1 MHz, consider that an object's capacitance is equal to 1 pF at 1 MHz (black dot on the C'-axis). As the frequency is lowered and provided this frequency is lower than the time constant associated with proton hopping, a short-range percolation path is going to open where protons will begin to polarise the small pores over short path lengths. One can see how that behaviour may manifest itself on a Cole-Cole plot where a CPE of 1 pF with p value equal 0.9 has been simulated in parallel with a 1 pF capacitor (solid black line). Note the dc conduction path represented by a parallel RC circuit is also shown (solid grey line) for comparison. One can see how the dielectric response for short-range percolation as modelled by the CPE-0.9 is contributing more to the real part capacitance than the resistance. Note

that without the capacitor, this CPE would start from the origin (black dotted line). As the frequency approaches 0.001 Hz, the short-range percolation path also approaches its end.

In Figure 70(c) a more complicated dielectric response for 2 CPEs in parallel with a capacitor is presented (solid black line). This response may be attributed to a situation where the object contains a few ions along with protons such that as the frequency is lowered, the proton hopping occurs via the short-range percolation path as modelled by the largely capacitive CPE (p = 0.9), but at some frequency a separate path opens which allows ions to pass through the object over longer distances. In other words, at low enough frequencies these ions will jump to another path which is quite different from the former. This is likely to be something that is akin to long-range percolation in a porous glass where the smaller pores have to get polarised before one begins to see a longer-range migration of ions from one large pore to next large pore. This migration will not take place until the frequency is lowered further and such a dielectric response may be modelled by a second CPE with more resistive characteristics, hence a p value of 0.5. Note how the inclusion of a second CPE with p value equal to 0.5 (black dotted line) to the pre-existing model (solid grey line) changes the angle of the impedance spectrum with respect to the C'-axis such that overall response contributes more towards resistance (solid black line).

Another complicated response is shown in in Figure 70(d) which is usually for an object that contains a relatively larger number of ions. As the frequency is lowered, a dc conduction path opens for ion migration over much longer distances than what could be modelled by a CPE. Therefore, a resistor has to be included in the model that already has two CPEs and a capacitor (solid grey line). Note the response manifests as a nearly vertical line when a resistor is included.

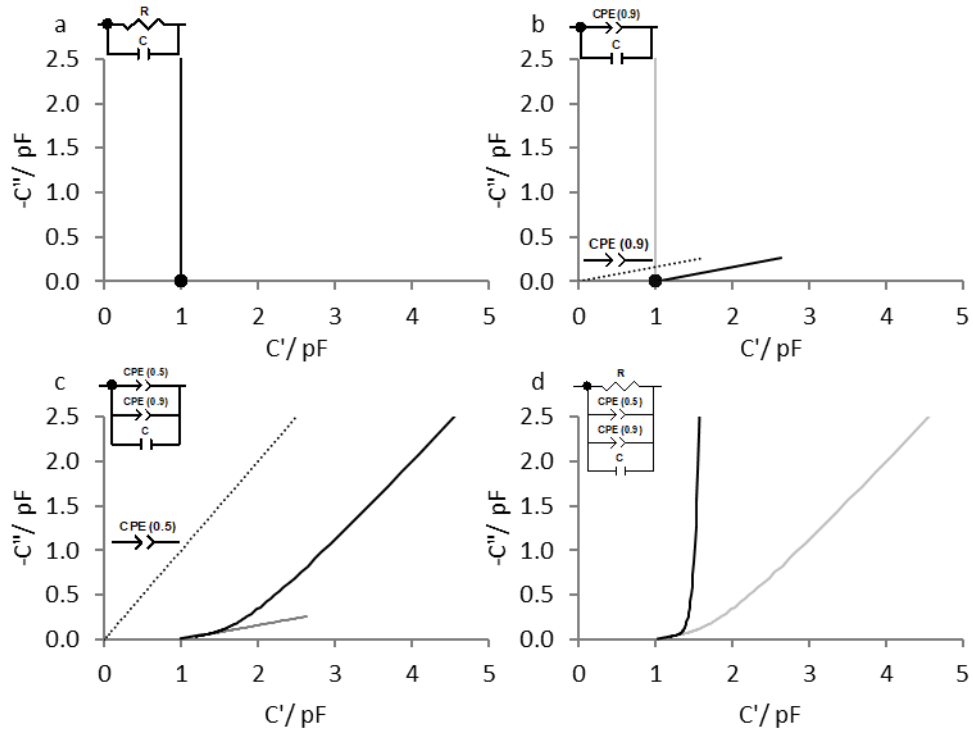

Figure 70: Simulation of the various pathways represented by different circuits for mobile species within an object to traverse from high frequency (1 MHz) towards lower frequencies: (A) towards (B) on the grey dashed line can be modelled by an equally resistive and capacitive CPE (1 pF) with p= 0.5; (A) towards (C) on the long dashed line can be modelled by a largely capacitive CPE (1 pF) with p= 0.5; (A) to (D) along the x-axis of the real part capacitance if the object is a pure capacitor; (D) towards (E) on the black solid line if the object has a capacitance of 1 pF but its characteristics are partially distributed as the frequency is lowered, hence modelled by a pure capacitor in parallel with a largely capacitive CPE (1 pF, p= 0.5); (D) towards (F) on the black dashed line when a second CPE (1 pF) with equally resistive and capacitive behavior is included to model an object that goes from a pure capacitor to a largely capacitive behavior towards a more resistive behavior as the frequency is lowered; (D) towards (G) on the black dot dashed line when the object goes from a purely capacitive behavior to a largely capacitive behavior to an equally capacitive and resistive behavior to a purely resistive behavior; (D) towards (H) on the grey solid line when the object goes from a purely capacitive behavior directly to a purely resistive behavior, i.e. in the absence of any distributed characteristics.

Dielectric Permittivity of Porous Glasses

The dielectric permittivity or the dielectric constant is a measure of the extent to which a material holds electric charge or a measure of its ability to allow charge migration under the influence of an electric field. It follows that its magnitude would then have a bearing on the composition of the material. Previous studies demonstrate that the dielectric properties of porous glasses are strongly impacted by the silica content and the concentration of alkali ions especially Sodium ions (Na^+) (Ehrt and Keding 2009; El-Egili 1996; Grandjean, et al. 2006; Hirayama and Berg 1960) Therefore, it is expected that the value of the dielectric constant falls as the silica content increases as demonstrated in Figure 71. However, with an increase in the concentration of Na^+ the dielectric constant increases. In other words, a higher dielectric constant can be equated with a more conducting glass. The values of the dielectric constant for various glasses as a function of the silica and Na^+ content are given in Table 16. The relative permittivity or the dielectric constant (ε_g) of the Adelphi VC010-20C vial has been reported by the manufacturer (Schott) to be 5.7 at 1 MHz (25 °C), which has been highlighted in Figure 71 (as a black dot) among the values for other glasses. As expected, the value is positioned higher than the value for Quartz which has no ions. Whether the relative permittivity of the vial represents the instantaneous relative permittivity of the vial has been investigated in this study.

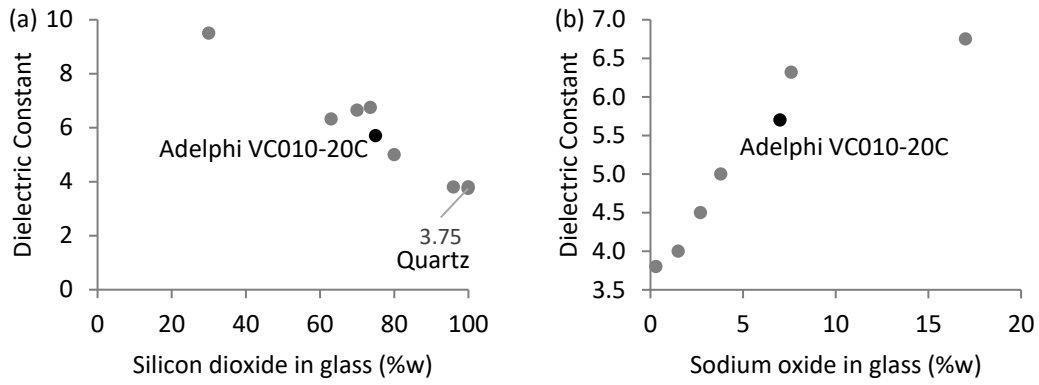

Figure 71:Dielectric constant measured at 100 MHz (20 °C) as a function of the content (%w) of (a) Silicon dioxide and (b) Sodium oxide. Values obtained from various sources.

Table 16: Dielectric constant of various glass types measured at 100 MHz (20 °C) as a function of Silicon dioxide content and Sodium oxide content.

Glass Type	**Dielectric Constant***	**Silicon dioxide (%w)**
Silica	3.81	100.0
Quartz (Fused)	3.75[a]	99.9 (Dulski and Dulski 1996)
Vycor (7911, 7910, 7900)	3.80	96.0 (Espe 2013)
Pyrex 7740 (Borosilicate)	5.00	80.0 (Espe 2013)
Fiolax® (Adelphi VC010-20C)	5.70[b]	75.0 (Espe 2013)
Corning 0080 (Lamp bulbs)	6.75	73.6 (Espe 2013)
Corning 0120 (Soda lime lead)	6.65	70.0 (Espe 2013)
Corning 0010 (Soft glass)	6.32	63.0 (Espe 2013)
Corning 8870 (Potash Lead)	9.50	30.0 (Liu, C., et al. 1997)
Glass Type	**Dielectric Constant**	**Sodium oxide (%w)**
Corning 0080 (lamp bulbs)	6.75	17.0 (Conn 1999)
Corning 0010 (Soft glass)	6.32	7.60 (Conn 1999)
Fiolax® (Adelphi VC010-20C)	5.70[b]	7.00 (Conn 1999)
Pyrex 7740 (Borosilicate)	5.00	3.80 (Conn 1999)
Pyrex 7760	4.50	2.70 (Espe 2013)
Pyrex 7070	4.00	1.50 (Conn 1999)
Vycor (7911, 7910, 7900)	3.80	0.30 (Conn 1999)

[a]At 1 MHz, [b]At 1 MHz (25 °C)*source:(Rumble 2019)

8.2 Objectives

The objectives of the experimental work include:

- To extract glass segments from the Adelphi (VC010-20C) glass vial for the manufacture of different electrode systems
- To manufacture an effective electrode system for the dielectric measurement of the glass segments
- To develop a method of determining the instantaneous relative permittivity of the glass wall at room temperature
- To develop an equivalent circuit model for the glass segment at a range of frequencies and temperatures

8.3 Materials and Methods

Given that all TVIS freeze drying studies are routinely performed with an Adelphi (VC010-20C) modified with a stick-on copper electrode system placed in a Virtis Advantage Plus freeze dryer equipped with a five channel TVIS System, preliminary studies involved placing glass wall segments with copper electrodes on the stainless-steel shelf. However, there were too many variables that impacted the spectra which have been described in Appendix III.

All dielectric measurements carried out in this study involved the use of a Broadband Dielectric (BDS) System (Figure 72) comprising a Concept-80 dielectric spectrometer (Novocontrol, Germany) with automatic temperature control by Quatro Cryosystem (precision of 0.5 °C). The main parts of the BDS system include the cryostat BDS 1100, gas heating module BDS 1310, pressurizer module BDS 1320, vacuum system with BDS 1350, liquid nitrogen dewar, Quatro controller BDS 1330 and power supply BDS 1340. It can perform dielectric measurements from 10^{-5} Hz to 3×10^{9} Hz from a temperature of -160 °C to as high as 400 °C. The BDS system communicates with a Windows operating system via the WinDETA software (v 5.81).

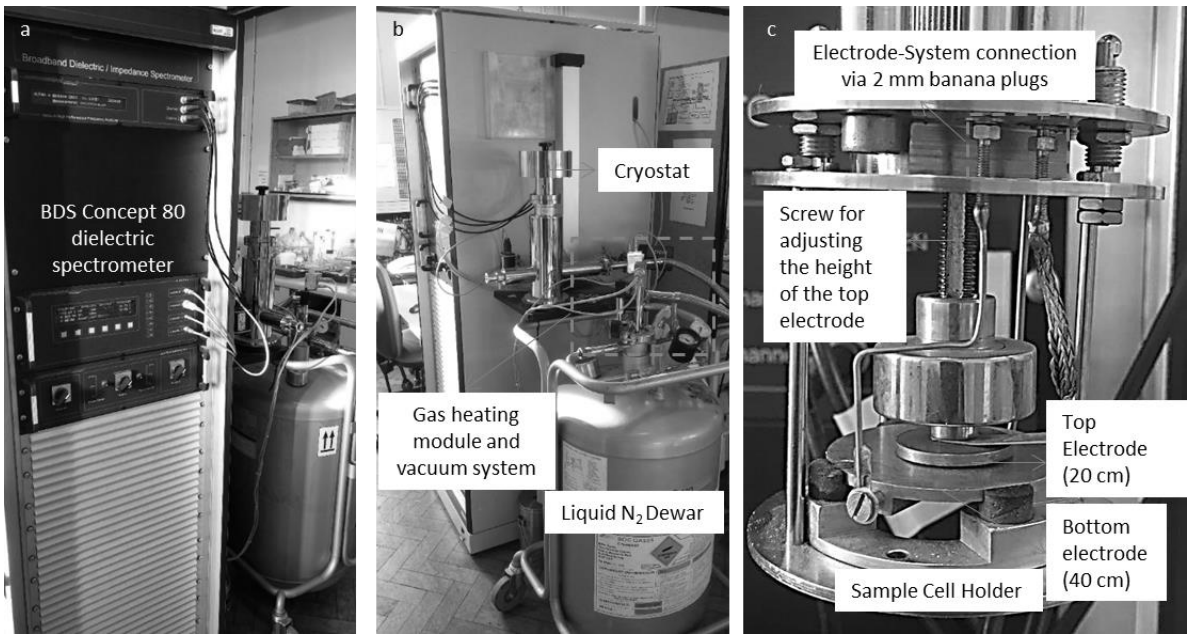

Figure 72: Broadband Dielectric Spectroscopy (BDS) System: (a) Spectrometer; (b) temperature control; (c) Conventional BDS sample hold with a pair of top and bottom electrodes wired to the system via a pair of Banana plugs

8.3.1 Determination of Relative Permittivity at Room Temperature

The classic equation for a parallel plate capacitor (Hewis 2017) is expressed as

$$\mathrm{C} = \varepsilon_0 \varepsilon_g \frac{A}{\mathrm{d}} \qquad \text{Equation 18}$$

where ε_0 is the permittivity of free space (8.854 pF m^{-1}), ε_g is the relative permittivity or the dielectric constant of the dielectric material, A is the area of the electrode (equal to the width and height of the electrode) and d is the separation between the electrodes or the thickness of the dielectric material. The significance of Equation 18 is that for a given material the values for ε_0, ε_g and d are constant, such that the capacitance is directly proportional to the area of the electrode, i.e.

$$\mathrm{C} \propto \mathrm{A} \qquad \text{Equation 19}$$

Therefore, for given material with different electrode areas, a linear relationship between the area and the corresponding value of the capacitance can be established. Equation 18 can then be rewritten as

$$\mathrm{C} = \mathrm{m}.\mathrm{A} \qquad \text{Equation 20}$$

where the gradient of the line, m, can be expressed as

$$\mathrm{m} = \frac{\varepsilon_g \varepsilon_0}{d} \qquad \text{Equation 21}$$

The proportionality (Equation 19) was applied in this study to determine the dielectric constant of the Adelphi (VC010-20C) vial. For this purpose, six glass segments were extracted from a few Adelphi (VC010-20C) vials using a handheld PROXXON 28440 saw with a diamond blade attachment. These segments were semi-circular or smaller parts of the curved wall of the glass vials. Electrodes of different areas were deposited by Gold sputter-coating. A method for gold sputter-coating is described in Section 8.3.2.

Two different methods of determining the dielectric constant were explored to find the best approach that yields a value closest to the one reported by Schott, i.e. 5.7 at 1 MHz (25 °C). The method

varied depending on the type of connection. In the **first method**, 3 out of the 6 glass segments were placed on a hemi-cylindrical saddle manufactured from Brass, hereafter simply referred to as the Brass saddle. This Brass saddle method has been described in Section 8.3.3.1 and the segments measured with this method have been referred to as S-1, S-2 and S-3. In the **second method**, the 3 segments were hard-wired before gold sputter-coating. This method is described in Section 8.3.3.2 and the segments measured with this method are called S-4, S-5 and S-6. The details of the methods are summarised in Table 17.

Table 17: Glass Segments from the Adelphi (VC010-20C) vial with different configurations

Glass Segment Nomenclature	Type of Electrode Material	Method for Attaching Electrodes on Glass	Type of Connection
S-1	Gold	Gold sputter-coating	Brass saddle (no hard-wiring)
S-2	Gold	Gold sputter-coating	Brass saddle (no hard-wiring)
S-3	Gold	Gold sputter-coating	Brass saddle (no hard-wiring)
S-4	Gold	Gold sputter-coating	Hard-wired with UV Curing glue before Gold sputtering
S-5	Gold	Gold sputter-coating	Hard-wired with UV Curing glue before Gold sputtering
S-6	Gold	Gold sputter-coating	Hard-wired with UV Curing glue before Gold sputtering

8.3.2 Gold Sputter-Coating (Gold Sputtered Electrodes)

Gold sputtering was carried out in a Q150RS sputter coater (Quorum Technologies UK). The procedure is presented for one of the segments in Figure 73. Briefly, a glass segment was cleaned with Ethanol to remove any fingerprints and then taped suitably around the edges of the concave and the convex surfaces to expose the desired areas for gold sputtering such that the electrodes formed after sputtering overlapped one another. It was not possible to ascertain the height and the width of the electrodes at the time of masking the curved surfaces of the glass segments but they were estimated by a method described in Appendix I. A glass segment is then placed on the sample platform located a few centimetres below a gold target (Purity 99.99%, 57mm diameter and 0.1 mm thickness) inside the sputter coater. The chamber is evacuated at 0.1 mbar and a gold film of a desired thickness (usually

between 15-30 nm) is sputtered on both surfaces of the segment. After completion, the tape is removed carefully to obtain the glass segment sputtered with gold electrodes. In this manner described above, a batch of three segments, S-1, S-2 and S-3, with different areas of the sputtered electrodes were sputter-coated as shown in Figure 74.

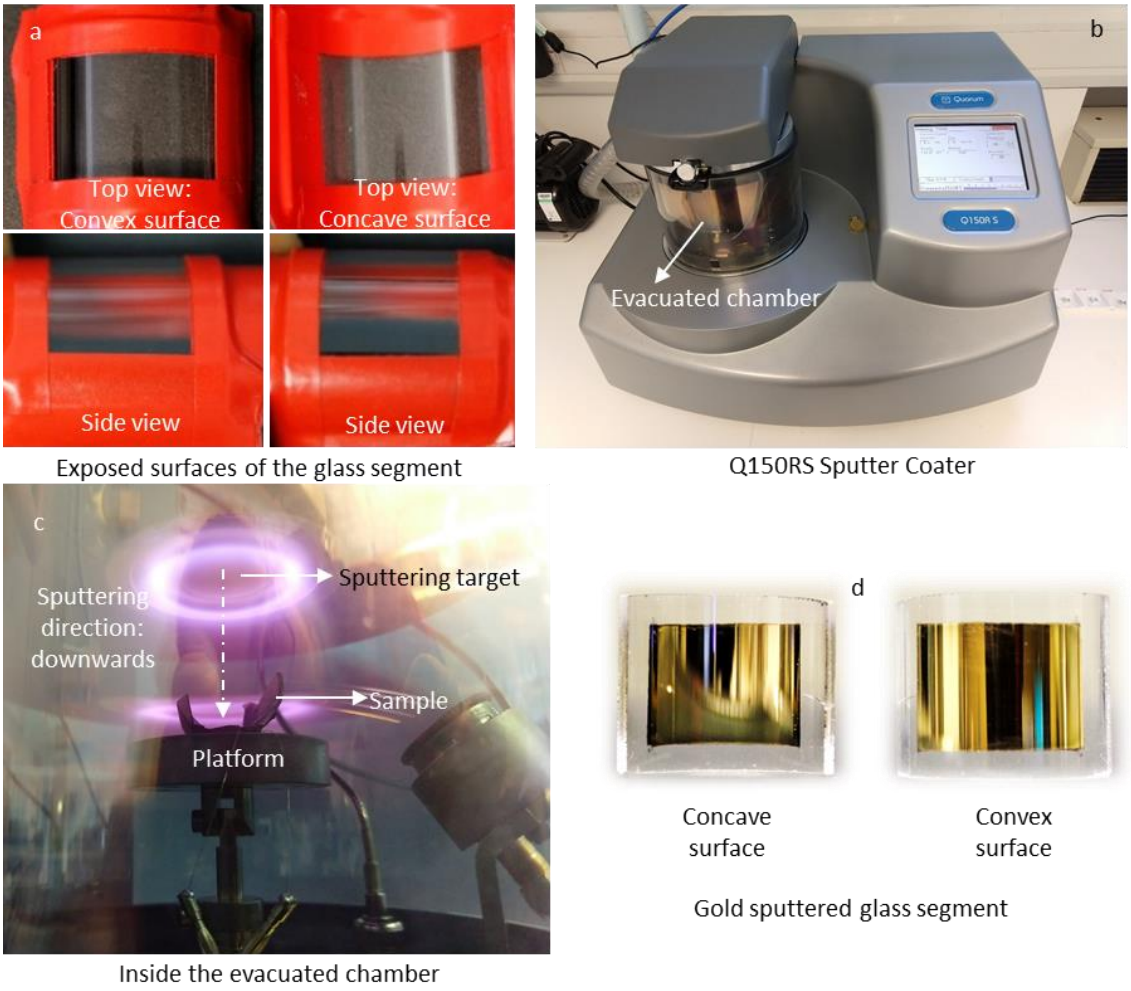

Figure 73: Method for sputtering gold on the semi-circular glass segment (a) Using tape to expose the desired surfaces of the glass segment on both the concave and convex sides; (b) Q150RS sputter coater used for sputter coating; (c) Gold sputtering in progress inside the evacuated chamber (0.1 mbar); (d) The areas on the concave and convex sides of the glass segment that were exposed are now sputtered with a gold film.

Figure 74: Gold electrodes of different surface areas sputtered onto the glass segments from the Adelphi (VC010-20C) glass vials. The samples have been referred to as S-1, S-2 and S-3.

8.3.3 Types of Connection for Measurement

In practice, solid samples are usually flat in shape with a given thickness such that they can be sandwiched between a pair of circular electrodes located within a factory-made BDS sample cell holder. Given that the glass segments were curved it was not possible to apply the conventional method of measurement. Therefore, two different types of connection between the glass segment and the BDS system were fabricated.

8.3.3.1 The Hemicylindrical Brass Saddle Method

For the first type of connection, a brass saddle (Figure 75a) was manufactured. Note that the diameter of the convex surface of the brass saddle was equivalent to the internal diameter (22 mm) of the Adelphi (VC010-20C) vial and the length of the brass saddle was equal to 30 cm such that it could easily be accommodated within the circumference of the lower electrode of diameter 40 cm as shown in Figure 75b). A gold sputtered glass segment was then placed over the brass saddle as in Figure 76, and the top electrode (diameter 20 cm) of the sample holder was then carefully lowered to make contact with the sputtered electrode on the convex surface of the glass segment without scratching the sputtered layer whilst fixing the position of the top electrode. In this manner the three gold sputtered glass segments, S-1, S-2 and S-3, were measured one after another.

Figure 75: (a) A hemi-cylindrical brass saddle of diameter 22 mm, equivalent to the internal diameter of a standard Adelphi (VC010-20C) vial

Figure 76: Method of placing a gold sputtered glass segment from the Adelphi (VC010-20C) vial on the brass saddle (a) and (b): Side and front view of the arrangement where the concave surface of the glass segment is in intimate contact with the convex surface of the brass saddle and the convex surface of the glass segment is in intimate contact with top electrode of the BDS sample cell holder. In turn, the planar bottom of the saddle makes intimate contact with the bottom electrode of the sample cell holder; (c) to (e): A close up of the three segments, S-1, S-2 and S-3 that were measured in this configuration.

8.3.3.2 Hard-Wiring of Glass Segments

For the second type of connection, the glass segments, S-4, S-5 and S-6 and S-7 were hard-wired before Gold sputtering. That then allowed for a direct connection to be made between the glass segment and the BDS system (rather than having a brass saddle within a conventional sample holder). The procedure involved: (i) taking 6 naked wires (i.e. without the outer plastic sheath) 3 cm in length and soldering one end of each of the 6 wires with a Banana plug (2 mm Gold Connector Banana Plug Male); (ii) masking a glass segments to expose the desired surface areas; (iii) creating a tiny depression on the concave surface of the glass segments close to the curved edge using a rotatory grinding drill with a spherical head attachment; (iv) taking one of the etched glass segments and filling the etched surface with a tiny drop of UV-curing glue; (v) placing a wire (the side which is not soldered to the Banana plug) carefully on this glue and curing the glue with UV light thus fixing the wire in its desired place; (vi) repeating step v to fix a wire on the other side of the segment. The steps (iv) to (vi) were repeated for wiring the other two glass segments. The finished segments are shown in Figure 77. These segments were placed one after another in a separate sample cell holder (manufactured from stainless steel) to provide a direct connection to the system via the Banana plugs. Figure 78 shows an example of how one of the hard-wired gold sputtered segments was connected. Note that this sample holder does not have the original top and bottom electrode configuration as used in the case of the glass segments measured with the brass saddle method (Figure 76).

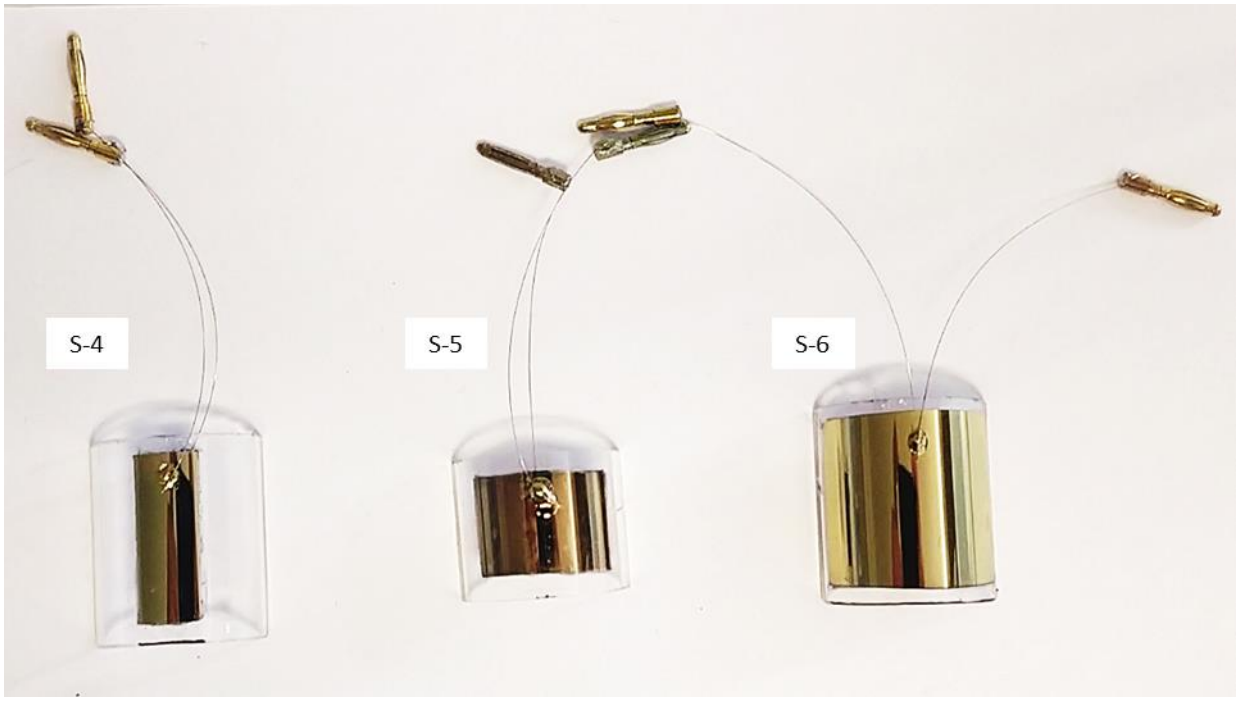

Figure 77: Hard-wired gold sputtered segments, S-4, S-5 and S-6, extracted from the Adelphi (VC010-20C) glass vials

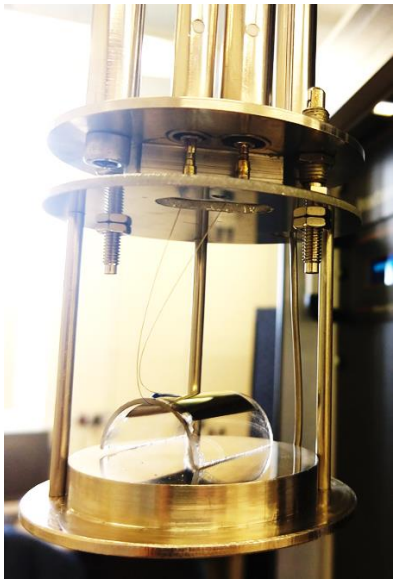

Figure 78: A bespoke sample cell holder that serves as a base for a hard-wired segment comprising a pair of gold electrodes sputtered on either side of a glass segment extracted from an Adelphi (VC010-20C) vial.

8.3.4 Method for the Determination of the Glass Wall Properties as a Function of Temperature

In addition to the six glass segments measured for the determination of the relative permittivity of the glass wall, the top and the base of an Adelphi (VC010-20C) were removed to obtain a cylindrical segment which was employed to gain an understanding of how the glass wall behaves over a wide range of temperatures, particularly in the temperature range (e.g. -20 °C to -50 °C) routinely encountered in freeze drying.

The method for constructing the electrode system for measuring this segment involved attaching a pair of “stick-on” copper electrodes (copper adhesive tape 3M 1181) on the either side of the glass segment such that they overlapped one another and then hard-wiring the electrodes using thicker wires by soldering. A right balance of the durability and malleability of the wires allowed the segment to be connected without the need for a sample holder. This glass segment has been referred to as S-7 and is shown in Figure 79 .

The procedure for attaching the electrodes involved: (i) cutting a segment of the copper foil tape of dimensions 19 mm by 10 mm and attaching that to the outer surface (i.e. convex face) of the glass segment, (ii) cutting another segment of the tape of dimensions 17 mm by 10 mm and attaching that to the inner surface of the glass segment across the area that was occupied by the outer electrode. Given that the glass segment on which the electrode is attached is curved rather than planar, the width of the inner arc electrode has to be a few millimetres shorter than the width of the outer electrode to allow them to overlap one another. The effective width that would contribute to the measured capacitance is more likely to be closer to the average of the width of the external electrode (19 mm) and the inner electrode (17 mm), i.e. 18 mm. This method of estimating the width of the electrodes has been described for the standard TVIS vial previously (Smith and Polygalov 2019).

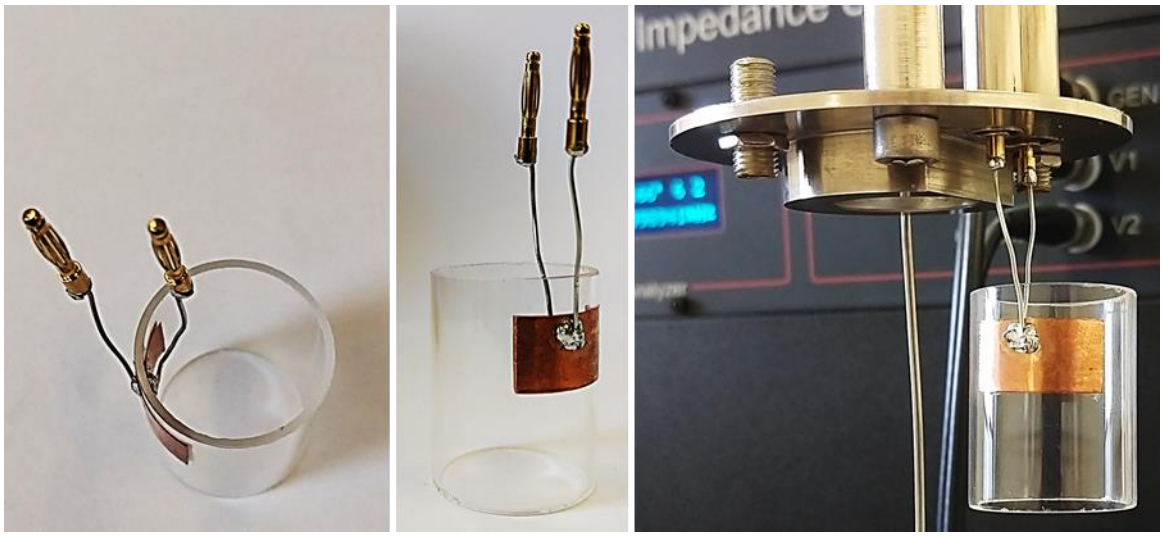

Figure 79: A glass cylinder extracted from an Adelphi (VC010-10C) vial with a pair of copper electrodes attached on the either side of glass hard-wired to the BDS system. Dimensions of the outer and the inner electrodes are 19 mm by 10 mm and 17 mm by 10 mm respectively.

8.3.5 BDS Parameters

All gold sputter-coated glass segments (S-1 to S-6) were measured within the cryostat at room temperature (~22 °C) in the frequency range 0.01 Hz- 1 MHz using the single sweep option of the WinDETA software. The copper electrode segment, S-7 was also placed within the cryostat and then subjected to a controlled temperature regime where it was heated from ambient temperature to 40°C and then cooled from 40°C and -90 °C. Dielectric spectra were obtained for various temperatures during cooling over the frequency range 0.01 Hz- 10 MHz. The BDS parameters used for all measurements are given in Table 18.

Table 18: BDS Parameters for all dielectric measurements

Parameter	
Frequency Factor	1.467799269
Points per decade	6
Analyser	ALPHA-BETA
Integration time	0.5 seconds
Voltage	1.5 mV
Type of Calibration	Low impedance load short calibration
Type of Correction	Low loss correction

8.4 Results

8.4.1 Dielectric Spectra of Gold Sputter-Coated Segments

Figure 80 shows the Cole-Cole plots (where the imaginary part capacitance $-\mathrm{C}''$ is plotted against real part capacitance, C') that highlight the high frequency end of the spectra for the gold sputter-coated glass segments measured at room temperature (~22 °C) with the saddle method (Figure 80a to c) and those that were hard-wired (Figure 80d to f).

It is clear from the Cole-Cole plots that none of the spectra in the high frequency region intercept the C'-axis which suggests that there was some stray capacitance associated with these measurements. Further, the shape of the spectra obtained for the hard-wired segments appear to have a second process which grows larger as the area of the electrode increases. Whether this process had any relevance to the estimation of the relative permittivity of the glass wall was realised after the values of the real part capacitance at 1 MHz, $\mathrm{C}'(1MHz)$, were plotted against the area of the electrode in each case.

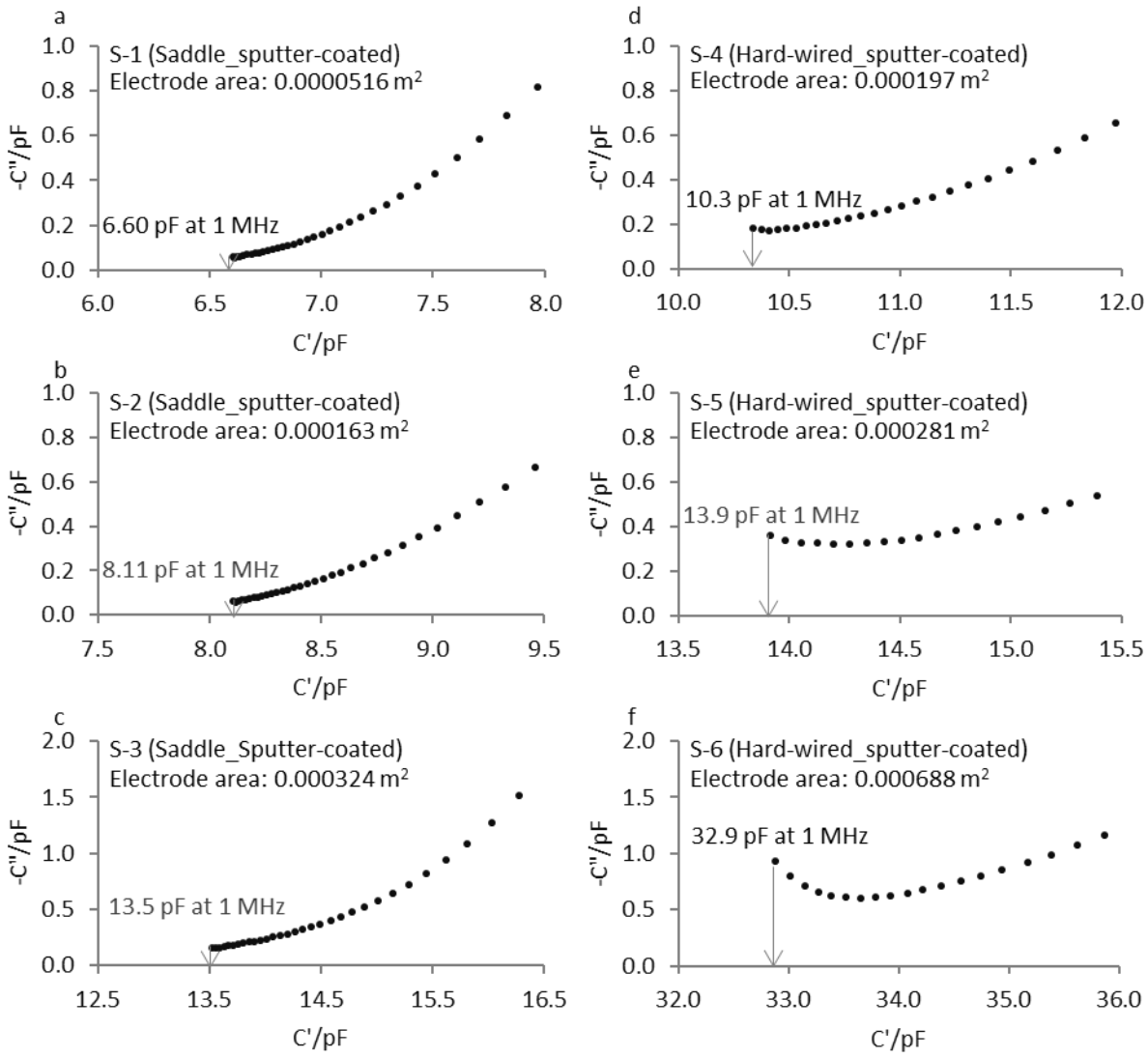

Figure 80: Cole-Cole plots of imaginary part capacitance ($-C^{"}$) plotted against real part capacitance (C') highlighting the high frequency end of the spectra obtained for the gold sputter-coated glass segments from the Adelphi (VC010-20C) vials: (a) The glass segments that were placed on the saddle (S1, S-2 and S-3); (b) The glass segments that were hard-wired. The values of C' at 1 MHz have been shown, which were used to estimate the relative permittivity of the glass vial.

The values are given in Table 19 and the plot of $\mathrm{C}'(1MHz)$ as a function of area is shown in Figure 81. The relative permittivity of the glass wall, ε_g, was calculated by substituting the values for the gradient of the line, the permittivity of the free space, ε_0, (8.854 pF m^{-1}), the glass wall thickness (0.0011 m as reported by Schott) in Equation 21. The value for ε_g from the sputter-coated hard-wired glass segments (S-4 to S-6) was found to be 5.73, which coincidently was in very good agreement with the value reported by Schott (5.7 at 1 MHz at 25°C). In contrast, a much lower value for ε_g (3.22) was

obtained from the brass saddle method which can be attributed to the impact of stray capacitance (~5 pF) associated with the saddle method as shown in Figure 81, where the lines have been extrapolated to the Y-intercept. Clearly, despite the fact a second process was not observed at the high frequency end of the spectra obtained with the saddle method, the magnitude of the stray capacitance associated with the saddle method was greater than the empty cell capacitance (2.3 pF) that was measured separately by simply leaving a small air gap between the saddle and the top electrode of the sample cell holder. In contrast, despite there being a second process present in the spectra for the hard-wired segments, the value of the stray capacitance was close to zero. Furthermore, as previously shown in Figure 71, the magnitude of the dielectric constant increases as the concentration of Na^+ ions increases in porous glasses. Quartz is largely silica with no alkali ions present, hence a low value for its dielectric constant, i.e. 3.75 at 1 MHz (Table 16). However, the Na^+ ion content in an Adelphi (VC010-20C) has been reported by Schott to be 7 % of the total composition, which must mean that the value for its dielectric constant cannot be lower than 3.75. Thus, it can be concluded that the glass segments should be hard-hired rather than measuring them on the brass saddle.

The presence of second process in the spectra for the sputter-coated hard-wired segments does not appear to impact the estimation of the dielectric constant. However, given that the conventional TVIS measurements for freeze drying are performed with stick-on copper electrodes rather than sputter-coated electrodes, a qualitative analysis of the spectra from the “stick-on” copper electrodes and the sputter-coated hard-wired segment of a similar electrode area is discussed in the next section.

Table 19: Values of the real part capacitance measured at 1 MHz, C′(1MHz), at 22 °C, as a function of area of the electrode for the gold sputter coated glass segments from the Adelphi (VC-010-20C) vials, placed on a saddle (S-1 to S-3) and those that were hard-wired (S-4 to S-6).

Sample Nomenclature	Type of Connection	Width/ Height (m)	Area/ m^2	Measured Capacitance at 1 MHz (23 °C)/ pF
S-1	Saddle	0.0138/0.0370	0.0000516	6.60
S-2	Saddle	0.0156/0.0105	0.000163	8.11
S-3	Saddle	0.0203/0.0160	0.000324	13.5
S-4	Hard-wired	0.0874/0.0225	0.000197	10.3
S-5	Hard-wired	0.0208/0.0135	0.000281	13.9
S-6	Hard-wired	0.0299/0.0230	0.000688	32.9

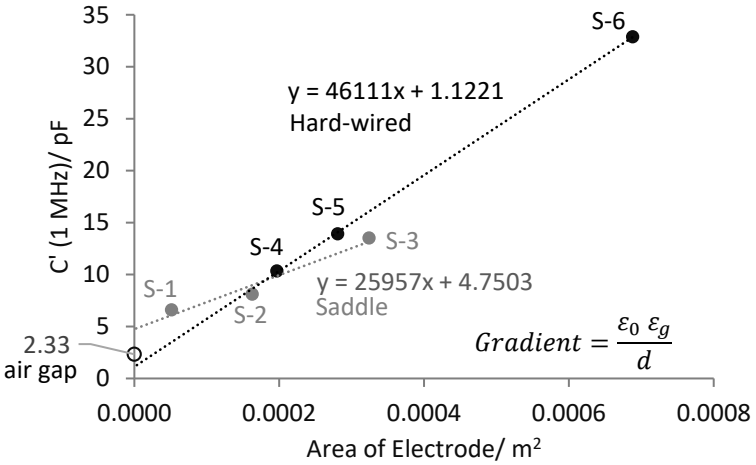

Figure 81: Capacitance of the gold sputter-coated glass segments (on saddle and hard-wired) measured at room temperature (~22 °C) at 1 MHz as a function of the area of the electrode. The gradient of each line can be used to determine the relative permittivity of the Adelphi (VC010-20C) vial. The stray capacitance was found to be 2.3 pF, obtained by removing the glass segment from the sample holder and leaving a small air gap between the brass saddle and the top electrode of the BDS sample cell holder.

8.4.2 A Qualitative Assessment of the Spectra for Gold-Sputtered Electrode Hard-Wired Segment (S-4) and the Stick-On Copper Electrode Hard-Wired Segment Measured at Room Temperature

Figure 82 shows the various representations of the spectrum for the sputter-coated hard-wired segment (S-4) with electrode area 0.000197 m^2 (plots a to d) and for the stick-on copper electrode hard-wired segment (S-7) (plots e to h) with electrode area 0.000170 m^2 measured at ambient cryostat temperature on two different days with similar lab temperatures. Further, the spectra have been fitted with two CPEs in parallel with a capacitor. One can see how well this model appears to fit the spectra. However, this model has been developed further for a range of temperatures in the next section. In this section, a qualitative analysis of the data has been presented.

In general, the dielectric response was very similar amongst the segments at the low frequency end as observed on the Nyquist impedance plots in Figure 82(a) & (e). The shape of the spectra is in the form semi-circular arcs, typically seen in porous glasses (Yadav, et al. 2017). However, the semi-circular arc for S-4 is clearly larger than the one for S-7 which may be attributed to the fact that these were single sweep measurements performed at ambient temperature within the cryostat which can have an effect on the conductivity of the glass and therefore, on the observed dielectric response. It was not possible to ascertain that both measurements were performed at identical temperatures which is only possible when one measures in a controlled environment where the liquid Nitrogen temperature is controlled by the system. It is important to recognise that the temperature value displayed for the cryostat at the time of measurement may be misleading when one performs single sweep measurements. The Bode plots of the log of impedance magnitude v/s log frequencies, the Cole-Cole plots of $-C''$ v/s C' and the Bode plots of $-C''$ and C' v/s log frequency also demonstrate similar dielectric behaviour at low frequencies between the two electrode systems.

One important difference in the spectra, however, comes to light as one observes the shape of the spectra at the high frequency end as shown in Figure 82(c) & (g). While the high frequency response

for the sputter-coated segment is characterised by a small process which becomes more prominent as the electrode area increases (previously shown in *Figure 80*), the spectra for the copper electrode segment (which had a similar electrode area) did not have such a process. This difference in the high frequency response between the two electrode systems may be associated with the type of contact between the electrode and the glass surface.

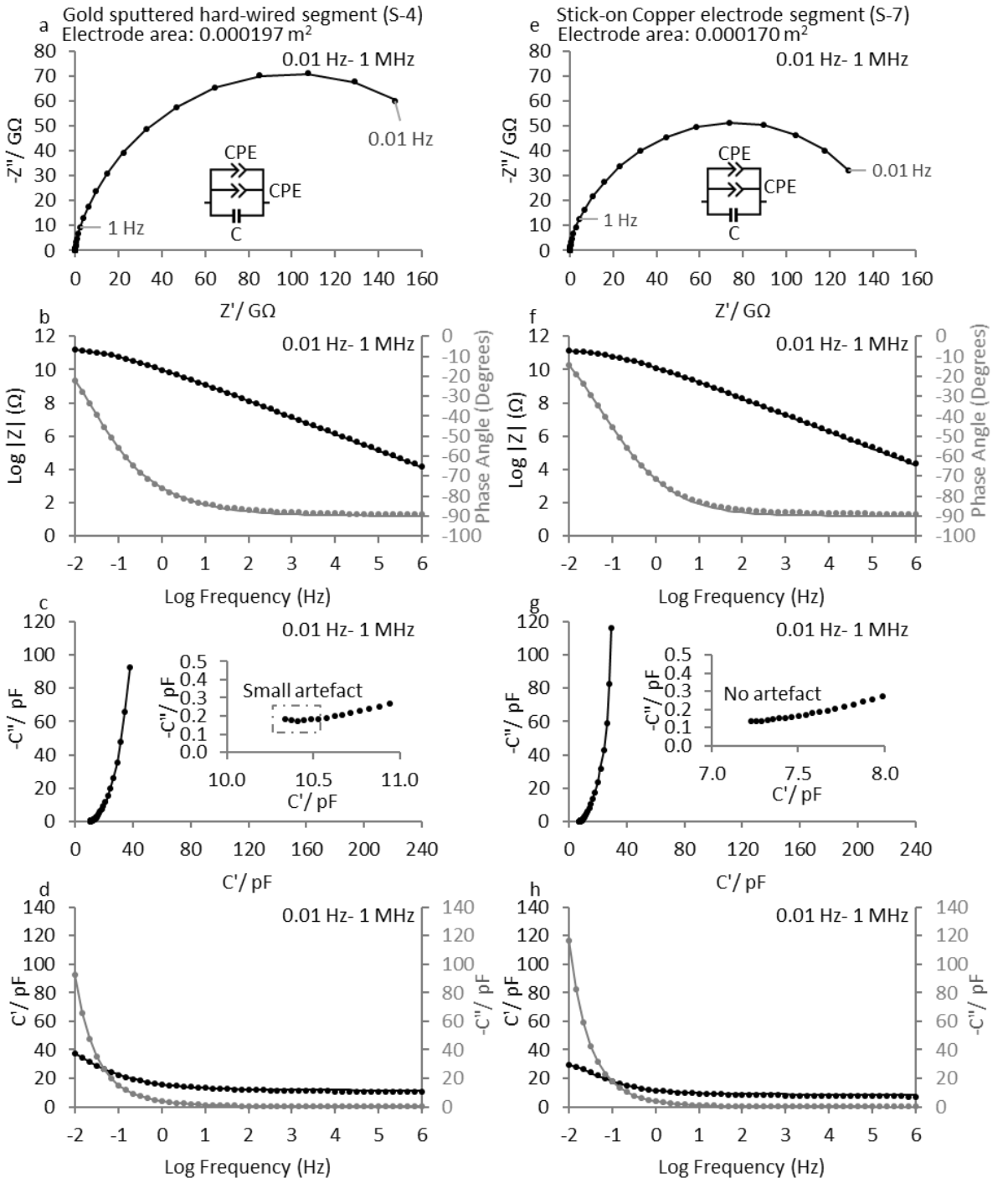

Figure 82: Representations of the spectra for the Gold-sputtered and the stick-on Copper electrode hard-wired segments (S-4 and S-7 respectively) measured at room temperature in the frequency range 0.01 Hz- 1MHz: Left side plots correspond to S-4, i.e. (a) to (d) Nyquist plot of imaginary part impedance v/s real part impedance, Bode plot of log of impedance magnitude v/s log frequency, Cole-Cole plot of imaginary part capacitance v/s real part capacitance also showing the shape of the spectra at the high frequency end, Bode plot of real (primary Y-axis) and imaginary capacitance (secondary Y-axis) v/s log frequency. Right Side plots (e) to (h) correspond to S-7.

A fundamental difference between the two interfaces is that with the copper electrode system, there is an additional 0.026 mm thin layer of conductive adhesive layer present between the electrode and the glass surface (Smith and Polygalov 2019). In contrast, Gold coating of the order 15-30 nm is expected to conform to the topography of the glass surface which might have nano-sized air gaps in the microstructure as one might find on performing a typical Atomic Fluorescence Microscopy (AFM) study of the glass surface. This is illustrated in Figure 83. It is possible that this intimate contact is allowed for an additional process across the glass surface resulting in a short-scale exchange or diffusion phenomena at high frequencies. The pathways operating across this conforming metalized glass surface are likely to be different from those that are associated with a conductive adhesive layer which is merely glued to the surface with no intimate contact.

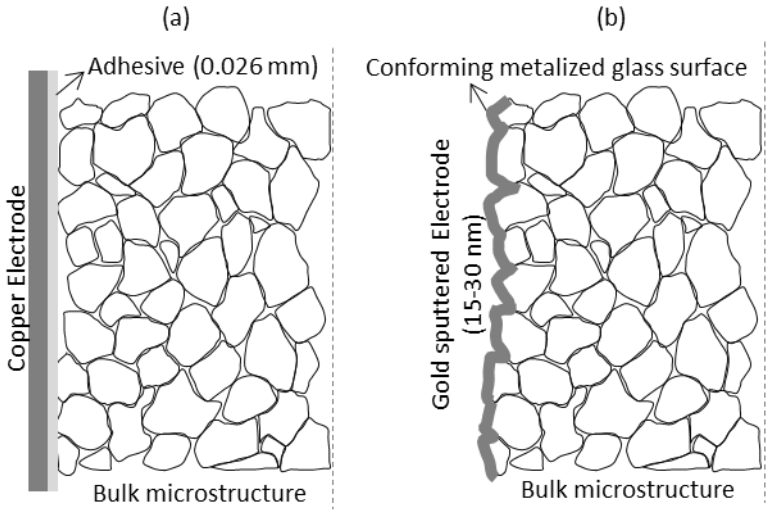

Figure 83:Difference in the electrode-glass contact between the stick-on copper electrode glass segment and the gold sputtered-coated glass segment: (a) Stick-on copper electrode has a 0.026 mm conductive adhesive layer that does not intimate conform to the glass surface; (b) Gold coating conforms to the glass surface

8.4.3 Development of a Model for the Glass Wall with the Copper Electrode System

It has been established that the wiring method is most suited to determining the dielectric constant for the sputter-coated glass segment. In addition, its low frequency response is similar to that for the stick-on copper electrode segment as demonstrated through fitting a basic circuit model. The next part of the study addresses the final objective, which is to use the copper electrode segment with an electrode area comparable to that for the TVIS vial to further one's understanding of behaviour of the glass wall across a range of temperatures.

8.4.3.1 Features of the Dielectric Spectra Across a Range of Temperatures

The dielectric spectra for temperatures from 40 °C to -90 °C are shown in various representations in Figure 84, from which various features of the glass behaviour as a function of temperature and the applied frequency can be identified. The spectra were noisy in the high frequency region between 464 kHz and 10 MHz. Therefore, any data shown henceforth has been limited to 464 kHz. Figure 84(a) & (b) show the Nyquist plot where the imaginary part impedance is plotted against real part impedance for the spectra at all the temperatures. A closer look at the spectra for temperatures from 40 °C to 10 °C in Figure 84(b) reveals the shape of the low frequency data, i.e. depressed semi-circular arcs with their centres lying below the Z'-axis. As the temperature is increased, the diameter of the semi-circular arcs decreases indicating a bulk resistance phenomenon (Yadav, et al. 2017) i.e. the resistance offered by the glass microstructure to the mobile species. In studies where glass has been heated to very high temperatures (Ehrt and Keding 2009; Yadav, et al. 2017) ionic migration makes it possible to estimate resistance from the intercept of the semicircle on the Z'-axis.

Alternatively, resistance can be determined from the low frequency part of the spectrum where the impedance of a resistor is invariant with frequency on a bode plot of impedance magnitude, $|Z|$, plotted against the log frequency as shown in Figure 84(c) & (d). However, in the present study, the glass segment was cooled from 40 °C to -90 °C and therefore, as the temperature decreases the

sample becomes increasingly resistive (Figure 84d). As a result, the part of the spectrum which is independent of the applied frequency continues to shift to frequencies lower than the low frequency limit (i.e. 0.01 Hz) of the measured frequency range.

Other interesting features of the glass segment are demonstrated in Figure 84(e) & (f), where the frequency dependence (as a function of temperature) of the log of real part capacitance, $\log C'$, and the log of imaginary part capacitance, $\log(-C")$ respectively, is shown. It is clearly visible that at any given temperature, the values of the real and imaginary part capacitance decrease as the frequency increases and finally attain a constant minimum value at higher frequencies. The mechanism behind these frequency dependent variations can be attributed to the conduction of ionic species and other orientation sources within the porous microstructure of the glass. The glass sample has stuck-on copper electrodes attached on the either side of the glass and is hard wired to the measurement system. At low frequencies, a bulk polarisation phenomenon (or space charge polarisation) occurs owing to the presence of the blocking electrodes which prevent charge transfer through the external circuit (Orazem and Tribollet 2008). Consequently, all the charge gets accumulated at the electrode-glass interface that leads to bulk polarisation. As a result, the values of the real and imaginary capacitance increase at higher rates as the frequency is lowered. However, as the frequency is increased, the contribution from the mobile species continues to decrease as the polarity of the electric field is switched rapidly, i.e. much faster than the time taken for the dipoles to reorient themselves. Ultimately, at high frequencies, accumulation of charge is not possible owing to the inertia of the charge carriers. In addition, it is important to recognise the characteristics of the high frequency end of the spectra.

The instantaneous glass wall capacitance may be estimated from the high frequency intercept on the C'-axis of a Cole-Cole plot of the imaginary part capacitance and the real part capacitance as shown in Figure 84(g). Although the spectra appear to meet at the x-intercept (where imaginary part capacitance is zero), a closer look at the high frequency part of the spectra in Figure 84(f) reveals that

as the temperature is decreased a second process emerges which is revealed fully at low enough temperatures. This is clear from Figure 85 which shows an enlarged view of the high frequency part of spectra in the temperature range 20 °C to -90 °C. One can see there is a “kink” in the data around 10 °C which then evolves into a second process as the temperature is lowered.

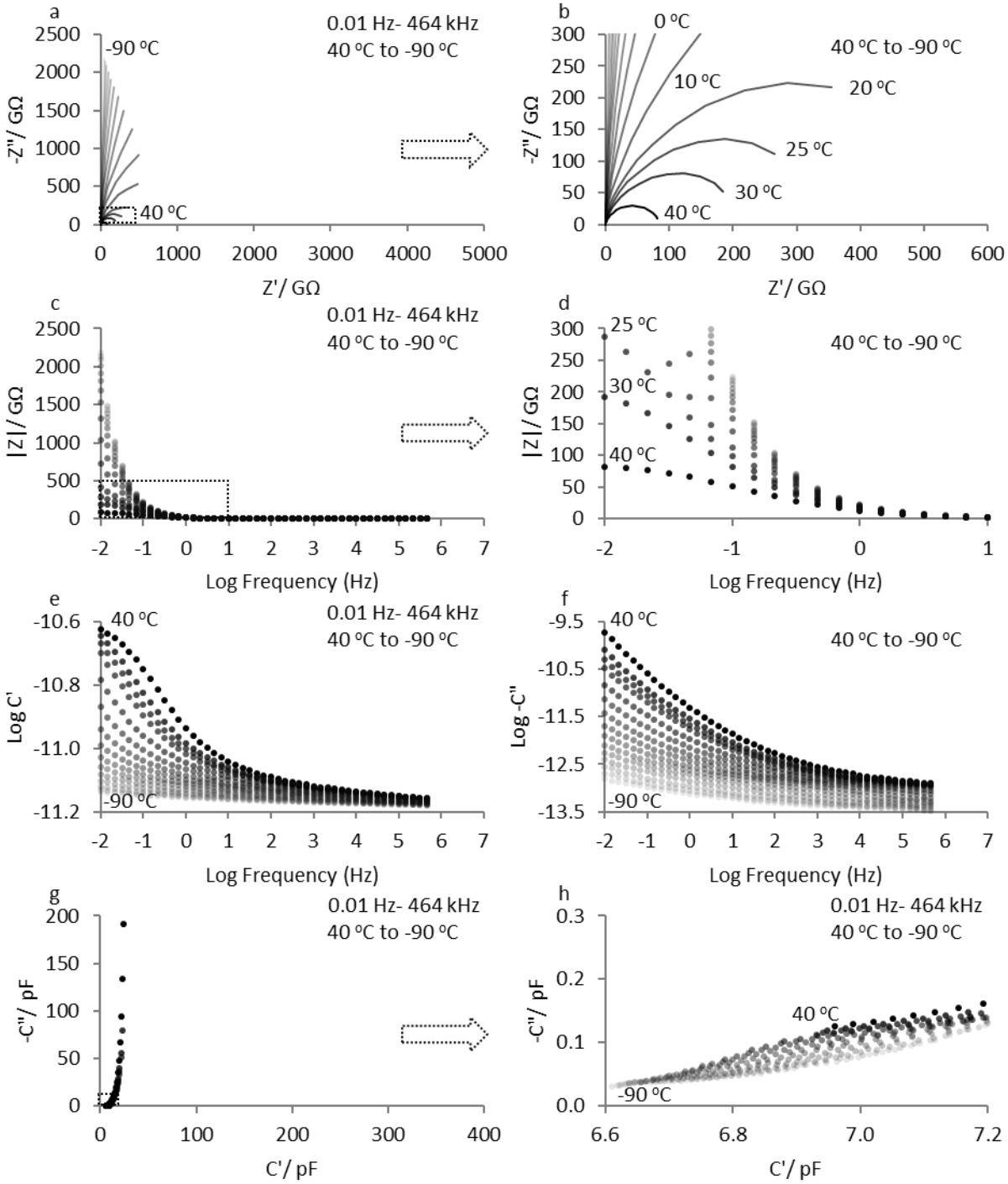

Figure 84: Dielectric spectra of the glass segment from the Adelphi (VC010-20C) vial, with copper electrodes attached on either side of the glass wall, measured during a cooling protocol from 40 °C to -90 °C: (a) & (b) Nyquist plots of imaginary part impedance v/s real part impedance; (c) & (d): Bode plots of the log of impedance magnitude v/s log frequency; (e) log of negative of imaginary part capacitance v/s log frequency; (f) log of real part capacitance v/s log frequency; (g) Cole-Cole plot of the imaginary part capacitance v/s real part capacitance; (h) The high frequency part of the spectra on a Cole-Cole plot.

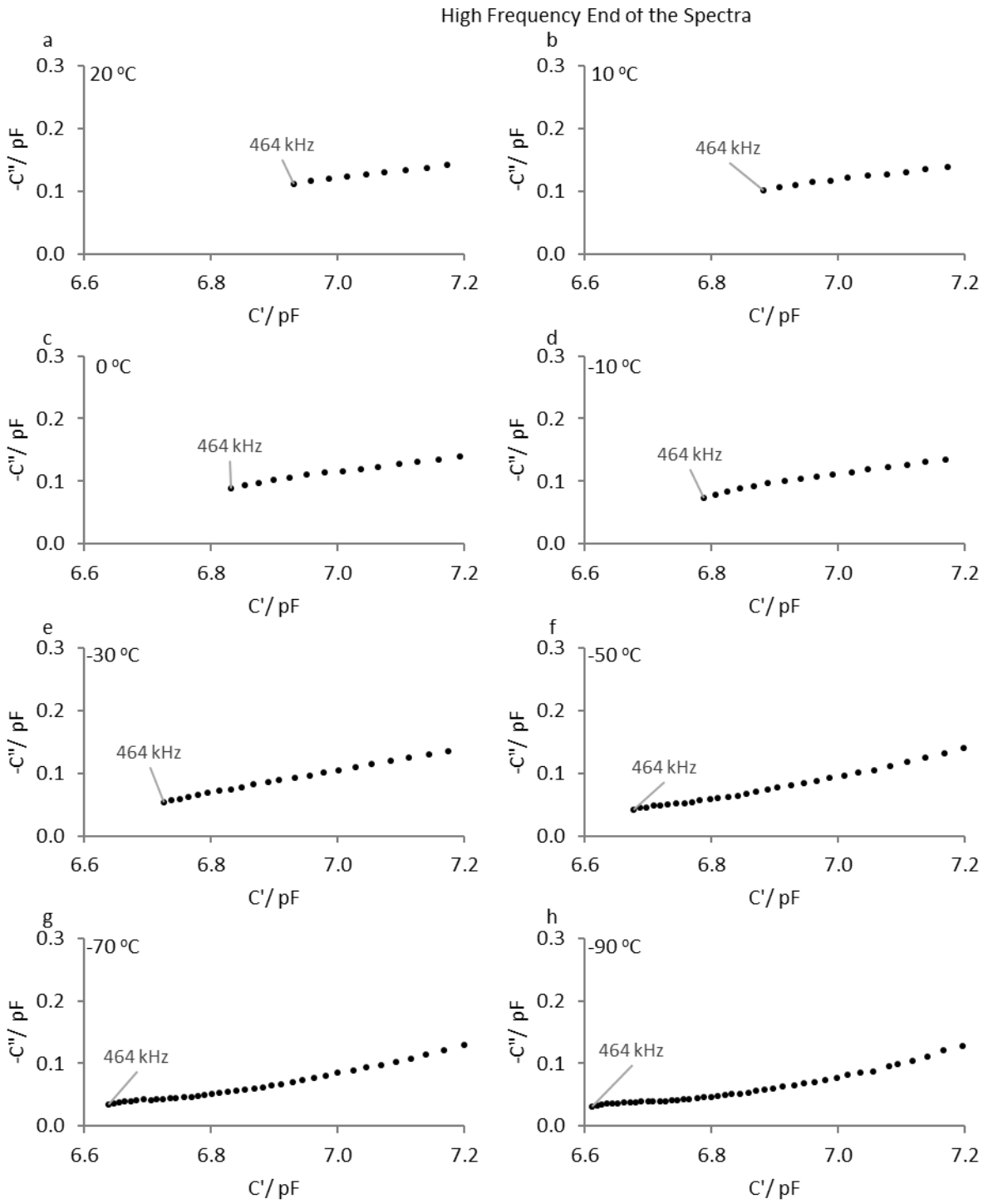

Figure 85: Dielectric spectra of the glass segment from the Adelphi (VC010-20C) vial, with copper electrodes attached on either side of the glass wall, measured during a cooling protocol from 40 °C to -90 °C: (a) & (b) Nyquist plots of imaginary part impedance v/s real part impedance; (c) & (d): Bode plots of the log of impedance magnitude v/s log frequency; (e) log of negative of imaginary part capacitance v/s log frequency; (f) log of real part capacitance v/s log frequency; (g) Cole-Cole plot of the imaginary part capacitance v/s real part capacitance; (h) The high frequency part of the spectra on a Cole-Cole plot.

Further, it is evident that as the temperature is increased, the extent of conduction within the glass increases which manifests as an ever increasingly contribution to the low frequency part of the spectra. In impedance community this low frequency response is frequently referred to as the low frequency dispersion (Smith and Polygalov 2019). It is evident that the real part capacitance, which changes only within half a decade in the temperature range of 40 °C to -90 °C, is much less sensitive to temperature compared to the imaginary part capacitance, which changes over several decades over that temperature range. This is clear from Figure 86, where the values of the real part capacitance and the imaginary part capacitance measured at 100 Hz have been plotted as a function of temperature on the primary Y- axis and the secondary Y-axis, respectively in the temperature range -50 °C to 20 °C. Moreover, Table 20, shows the temperature coefficient of the real part capacitance changes by only ∼12 % from -50 °C to 20 °C, when all the values are normalised to -50 °C.

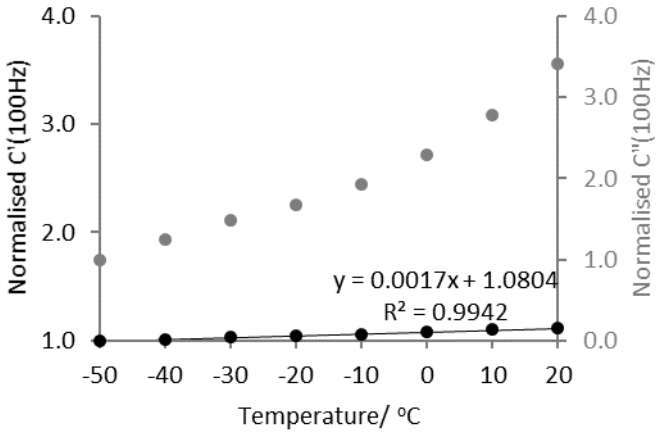

Figure 86: Temperature dependency of the real part capacitance (primary Y-axis) and the imaginary part capacitance measured (secondary Y-axis) at 100 Hz in the temperature range -50 °C to 20 °C.

Table 20: Percentage change in the temperature coefficient of the real part capacitance measured at 100 Hz in the temperature range -50 °C to 20 °C.

C'(100Hz)/pF	Normalised C'(100Hz)/pF	% change from -50 °C	Temperature/ °C
7.01	1.00	0.0	-50
7.11	1.01	1.4	-40
7.21	1.03	2.8	-30
7.32	1.04	4.4	-20
7.43	1.06	6.0	-10
7.56	1.08	7.8	0
7.70	1.10	9.8	10
7.84	1.12	11.9	20

8.4.3.2 Fitting of the Spectrum at 40 °C

Having recognised the various features of the dielectric spectra of the glass sample as a function of temperature and frequency, an empirical circuit model comprising different circuit elements has been described in this section. In Figure 87 a step-wise breakdown of the contribution of different elements to the observed dielectric response of the glass segment at 40 °C is shown on Cole-Cole plots of $-C^{"}$ v/s C' as the frequency is decreased from 464 kHz to 0.01 Hz. Note that in Figure 87(a) to (d), the dataset within the frequency range that was used in model construction is shown as filled circles and the dataset which wasn't part of the model is represented by empty circles. Further, note the use of symbols "±" and "x" adjacent to the model parameters, where the former corresponds to a "free" or a "floating" parameter and the latter is referred to as a "fixed" parameter whose value from the previous step has been brought into the next step unchanged, and fixed before fitting is performed.

It is evident that the second process was not visible at 40 °C at the high frequency end of the spectrum. Therefore, in the absence of the second process, the dataset in the frequency range 464- and 21.5 kHz was assumed to be a straight line with a shallow gradient with respect to the C'-axis on the Cole-Cole plot. Such a response could therefore be approximated to a largely capacitive CPE. Also, this CPE was offset from the C'-axis with respect to the origin which suggests a capacitor must be involved. Therefore, the **first** step was to fit the dataset between 464 kHz and 21.5 kHz with an

empirical model comprising a floating capacitor and a floating CPE in parallel, hereafter simply referred to as the $\mathrm{C}(\pm) = \mathrm{CPE}(\pm)$ model. In Figure 87(b) one can see that the fit (solid black line) passing through this dataset is linear. The fitting resulted in minimum errors in the values of the fitting parameters (Table 21) which strongly suggests the dataset in this frequency range could be modelled with a capacitor in parallel with a CPE. The p value of the CPE was equal to 0.902 which suggests that behaviour of the sample in this frequency range was largely capacitive.

Table 21: Parameters of the $C(\pm) = CPE(\pm)$ Model for the spectrum at 40 °C in the frequency range 464-21.5 kHz

Parameter/ Unit	Free (±) or Fixed (x)	Value	Absolute Error	% Error
C/ pF	±	6.16	0.0436	0.707
CPE Q/ pF	±	3.43	0.0530	1.54
CPE p	±	0.902	0.0457	0.506

However, a limitation of this approximation comes to light when the fit line from the $\mathrm{C}(\pm) = \mathrm{CPE}(\pm)$ model is simulated to the X-intercept (zero pF imaginary part capacitance) in order derive the instantaneous glass wall capacitance. It is clear from Figure 87(c) one would need to extrapolate the line to an extremely high frequency of $1 \times 10^{55}\ Hz$ in order to approach the X-intercept. Herein lies a paradox that the model fits the linear part in the frequency range 464-21.5 kHz, but it yields an unrealistic estimate of the instantaneous glass wall capacitance. Nevertheless, it is also true that this high frequency dataset is part of a second process which emerges at low enough temperatures. This resolves the conundrum why the CPE was indicating a capacitance at the infinite frequency. In other words, this estimate is not the true instantaneous glass wall capacitance. Nevertheless, the focus was then shifted to fulfilling the broader objective of developing a model for the whole spectrum.

When the $\mathrm{C}(\pm) = \mathrm{CPE}(\pm)$ model is simulated towards lower frequencies (i.e. from 21.5 kHz to 0.01 Hz) as shown in Figure 87(c), it starts to deviate from the data at 21.5 kHz as the shape of the spectrum curves or transitions into a more resistive behaviour. It has already been demonstrated how a second line representing a CPE with a relatively steeper gradient (i.e. p value less than 0.9) in parallel

with a largely capacitive CPE can model such a transition in a spectrum. Therefore, in the **second** step, the frequency range was extended to 3.16 Hz and the $\mathrm{C}(\pm) = \mathrm{CPE}(\pm)$ model was modified to a $\mathrm{C(X)} = \mathrm{CPE1(X)} = \mathrm{CPE2}(\pm)$ model, where the first CPE and second CPE are referred to as $\mathrm{CPE1}$ and $\mathrm{CPE2}$ respectively. Note the use of "X" next to C and $\mathrm{CPE1}$ and "$\pm$" next to $\mathrm{CPE2}$ which signify that after having the original fit values of the C and $\mathrm{CPE1}$ parameters from the $\mathrm{C}(\pm) = \mathrm{CPE}(\pm)$ model inserted into $\mathrm{C(X)} = \mathrm{CPE1(X)} = \mathrm{CPE2}(\pm)$ model, they were fixed whilst the $\mathrm{CPE2}$ parameters (Q and p) were floated before fitting was performed. The fit from this model is shown in Figure 87(d) and the values of the parameters are given in Table 22.

Table 22: Parameters of the $C(\pm) = CPE1(\pm) = CPE2(X)$ model for the spectrum at 40 °C in the frequency range 464 kHz-3.16 Hz

Parameter/ Unit	Free (±) or Fixed (x)	Value	Absolute Error	% Error
C/ pF	x	6.16	0.000	0.000
CPE Q1/ pF	x	3.43	0.000	0.000
CPE $p1$	x	0.902	0.000	0.000
CPE Q2/ pF	±	16.6	0.117	0.707
CPE $p2$	±	0.369	0.00117	0.465

The p value of $\mathrm{CPE2}$ amounts to 0.369 for the dataset that was fitted in the frequency range 464 kHz-3.16 Hz which is representative of a largely resistive behaviour. The minimum errors in the values of the fit parameters as generated by the software suggest that the model fits the dataset in the frequency range 464 kHz- 3.16 Hz well and it is indeed indicating that the sample goes from a capacitive behaviour to a relatively resistive behaviour as the frequency is lowered from 464 kHz to 3.16 Hz. However, the capacitor and the two $\mathrm{CPE}s$ could not sufficiently account for a highly conductive response that the sample presented in the frequency range 3.16- 0.01 Hz (Figure 87d) which suggests that the sample behaves like a resistor at very low frequencies. Thus, the **third** step was to include a resistor in the model (referred to as the $\mathrm{C(X)} = \mathrm{CPE1(X)} = \mathrm{CPE2(X)} = \mathrm{R}(\pm)$ model) and fit the entire data set from 464 kHz to 0.01 Hz, where the values of C, $\mathrm{CPE1}$ and $\mathrm{CPE2}$ from the previous step were copied into the modified model and fixed whilst the resistor was left free before a fit was performed. However, this did not result in an acceptable fit (Figure 87e) which suggests that these

circuit elements must be working together to compensate each other to model the characteristics of the spectrum. Therefore, the **fourth** step was to float all the parameters and perform the fit again. The values of the fitting parameters from the $\mathrm{C}(\pm) = \mathrm{CPE1}(\pm) = \mathrm{CPE2}(\pm) = \mathrm{R}(\pm)$ model are given in Table 23. When all parameters were allowed to float, while large errors in the values estimated for C and $\mathrm{CPE\ Q1}$ parameters were found, the % error in the estimation of the $\mathrm{CPE2}$ parameters had also increased when compared to previous model where they were kept fixed (Table 22). Further, Figure 87(g) & (h) show how the quality of the fit in the high frequency part of the spectrum became worse after floating the capacitance-associated parameters. Note how the simulated fit line in Figure 87(h) erroneously indicates a capacitance towards infinity when the capacitance- associated parameters are floated. That in turn disturbs part of the fit that is modelled by $\mathrm{CPE2}$. Nevertheless, a negligible error was found in the estimate for resistance and therefore, the $C(\pm) = CPE1(\pm) = CPE2(\pm) = R(\pm)$ model was extended to other temperatures to investigate the quality of fit.

Table 23: Parameters of the $C(\pm) = CPE1(\pm) = CPE2(\pm) = R(\pm)$ model for the spectrum at 40 °C in the frequency range 464 kHz- 0.01 Hz

Parameter/ Unit	Free (±) or Fixed (x)	Value	Absolute Error	% Error
C/ pF	±	0.00100	57.5	>100
CPE Q1/ pF	±	8.00	57.1	>100
CPE $p1$	±	0.991	0.0756	7.6
CPE Q2/ pF	±	10.1	0.379	3.7
CPE $p2$	±	0.586	0.0188	3.2
R/ GΩ	±	90.7	1.24	1.36

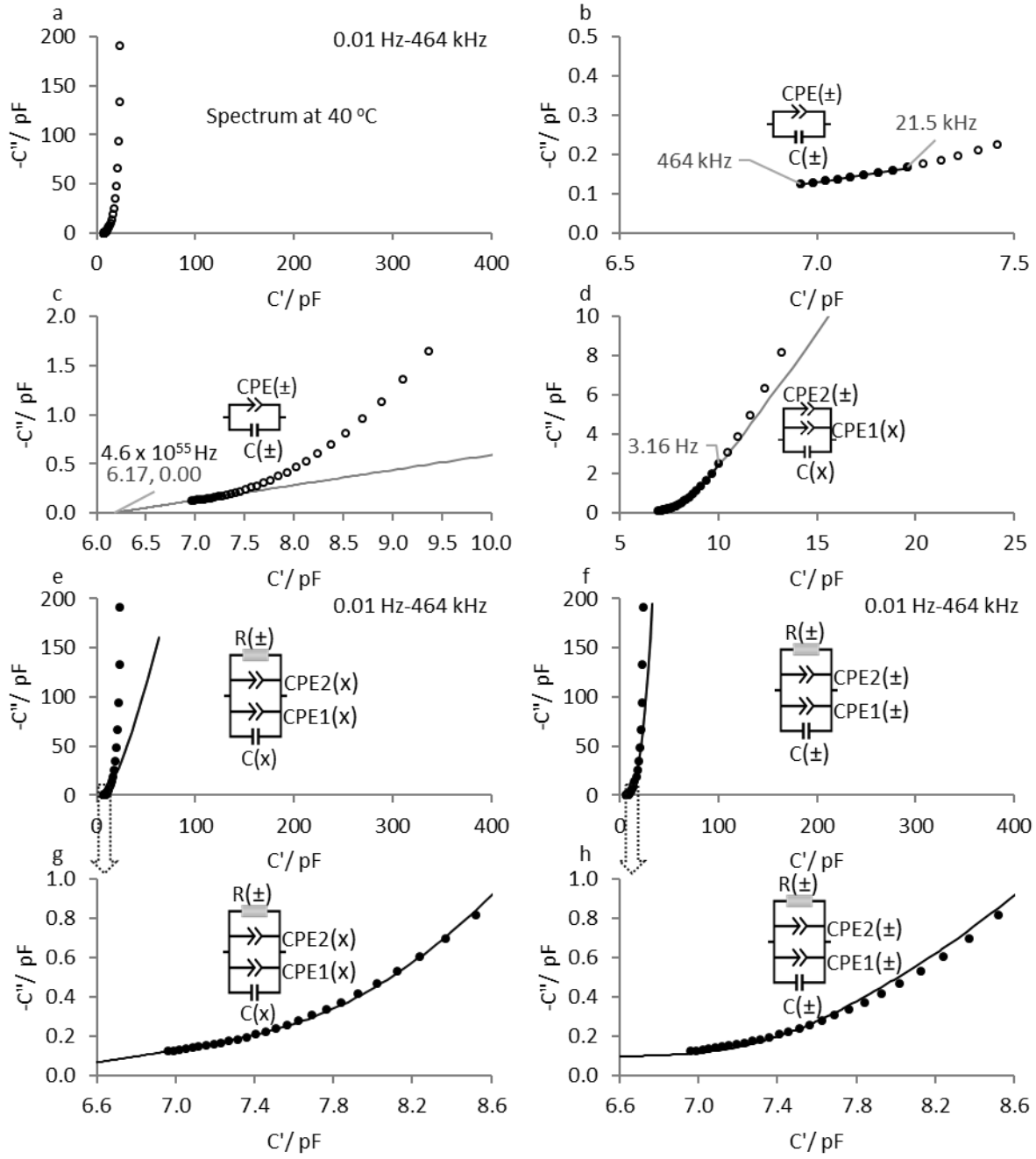

Figure 87: Construction of the $C(\pm) = CPE1(\pm) = CPE2(\pm) = R(\pm)$ model for the spectrum at 40 °C in various steps shown on Cole-Cole plots of the imaginary part capacitance and the real part capacitance: (a) Spectrum acquired over 464 kHz to 0.01 Hz; (b) First step is model the high frequency end of the spectrum between 464 kHz and 21.5 kHz with a capacitor in parallel with a CPE; (b) Determination of the instantaneous glass wall capacitance requires one to simulate the C=CPE model to the x-intercept but that corresponds to an unrealistic frequency of $1 \times 10^{55}\ Hz$ but simulation of the C=CPE model below 21.5 kHz suggests a second CPE is required to model the spectrum below 21.5 kHz; (d) Inclusion of a second CPE allows one to model the spectrum up to 3.16 Hz; (e) A resistor is included and the model is fitted over the entire frequency range whilst the other parameters in the model are fixed with their values brought into the model from the previous steps. However, that does not result in a good fit; (f) All parameters are floated or freed and the resultant fit agrees closely with the low frequency end of the spectrum; (g) High frequency part fitted fairly well when the capacitive parameters are fixed; (h) Quality of fit in the high frequency end of the spectrum is poor when all parameters are allowed to float which causes the simulated line to erroneously indicate a capacitance in the direction of towards infinity.

8.4.4 Extension of the $\boldsymbol{C}(\pm) = \boldsymbol{CPE1}(\pm) = \boldsymbol{C}\mathbf{PE2}(\pm) = \mathbf{R}(\pm)$ Model to all the Temperatures

The values of the fit parameters for the spectrum at 40 °C were used as starting values to batch fit the spectra for the rest of the temperatures. Note that the fit results for some representative temperatures are shown in Figure 88 where the smaller Cole-Cole plots correspond to the high frequency end of the spectra. These plots are enclosed within the larger Cole-Cole plots that show the entire frequency range. For all the temperatures between 40 °C and -90 °C, these values with their corresponding absolute errors as error bars have been plotted against temperature as shown in Figure 89 and also given in Table 24. It is clear that the large errors found in the values of C (Figure 89a), $\mathrm{CPE1\ Q}$ (Figure 89b), $\mathrm{CPE1\ p}$ (Figure 89c) that model the high frequency part of the spectra in the temperature range 40 °C to 20 °C suggests that this model with floating parameters did not work particularly well at higher temperatures. This can be attributed to the earlier assumption that the high frequency part of the spectrum is a CPE, except that it isn't one, rather a portion of an incomplete second process that emerges at low enough temperatures.

It appears that the high frequency part of the spectra at those higher temperatures is not enough to capture this second process which at the microstructure level is characterised by a localised shot range order of percolation of mobile species within the fused silica beads of the glass segment. Therefore, in order to capture this behaviour a CPE was used as the next available option. Nevertheless, the observation of this "low temperature high frequency process" is quite useful, but it does mean that in the temperature range -20 °C to -70 °C that is routinely encountered in freeze drying, the second process was ignored, and a capacitor was used instead but it doesn't have any physical relevance. Further, since there isn't enough data to model the second process at temperatures above -10 °C, the high frequency dataset being modelled by a CPE seems acceptable (Figure 87b) but that does mean the values of C and $\mathrm{CPE1}$ parameters cannot be allowed to float as that would then lead to a CPE that extrapolates to infinite frequency resulting in a poor quality of the fit at high frequencies.

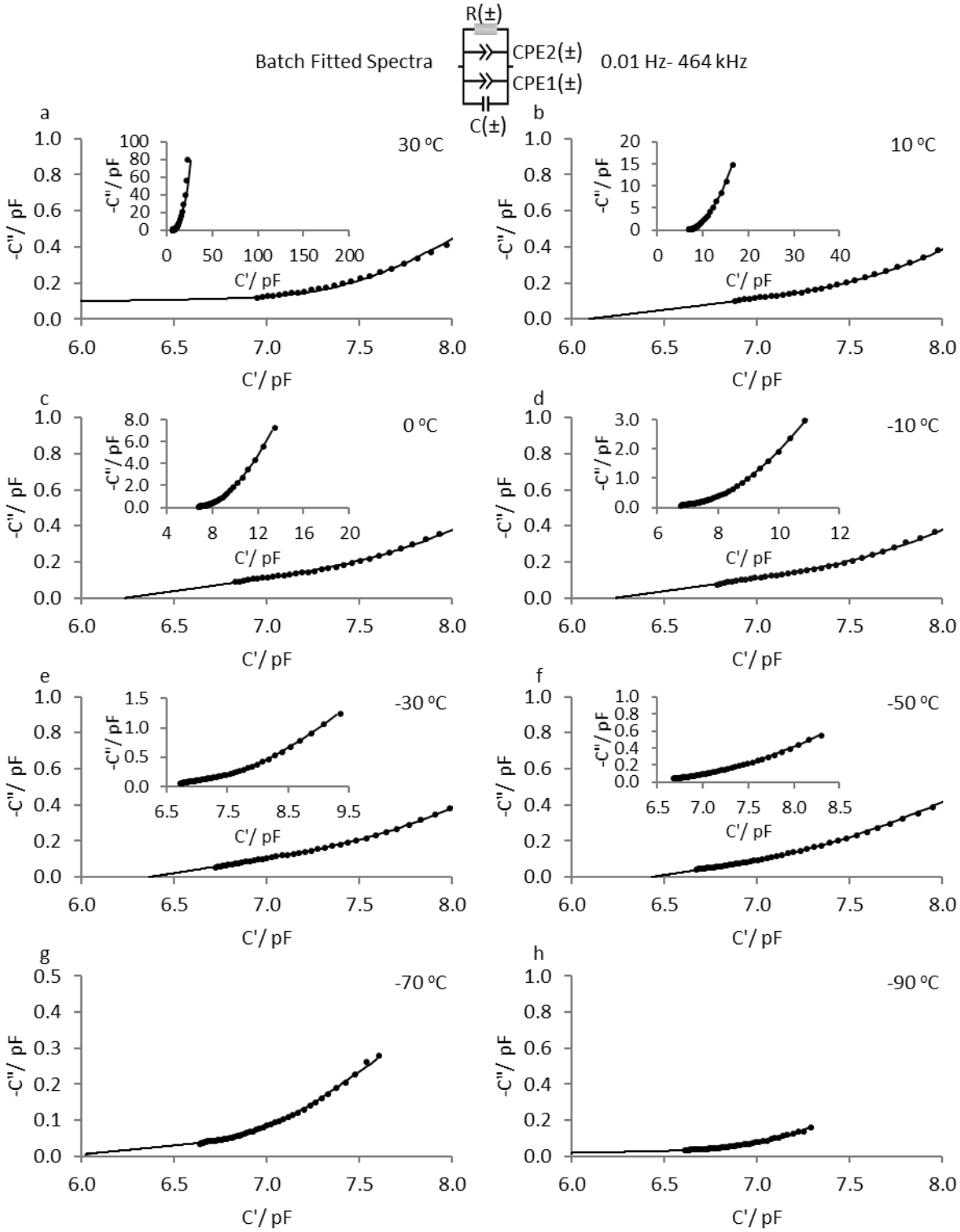

Figure 88: Cole-Cole plots of the imaginary part capacitance v/s real part capacitance for the spectra and their fit results from the $C(\pm) = CPE1(\pm) = CPE2(\pm) = R(\pm)$ model at temperatures between 30 °C and -90 °C in the frequency range 0.01 Hz- 464 kHz. The values of the fit parameters obtained at 40 °C were used to batch fit the spectra at the rest of the temperatures. The smaller Cole-Cole plots contain the full spectral data while the larger plots highlight the quality of the fit result at the high frequency end of the spectra.

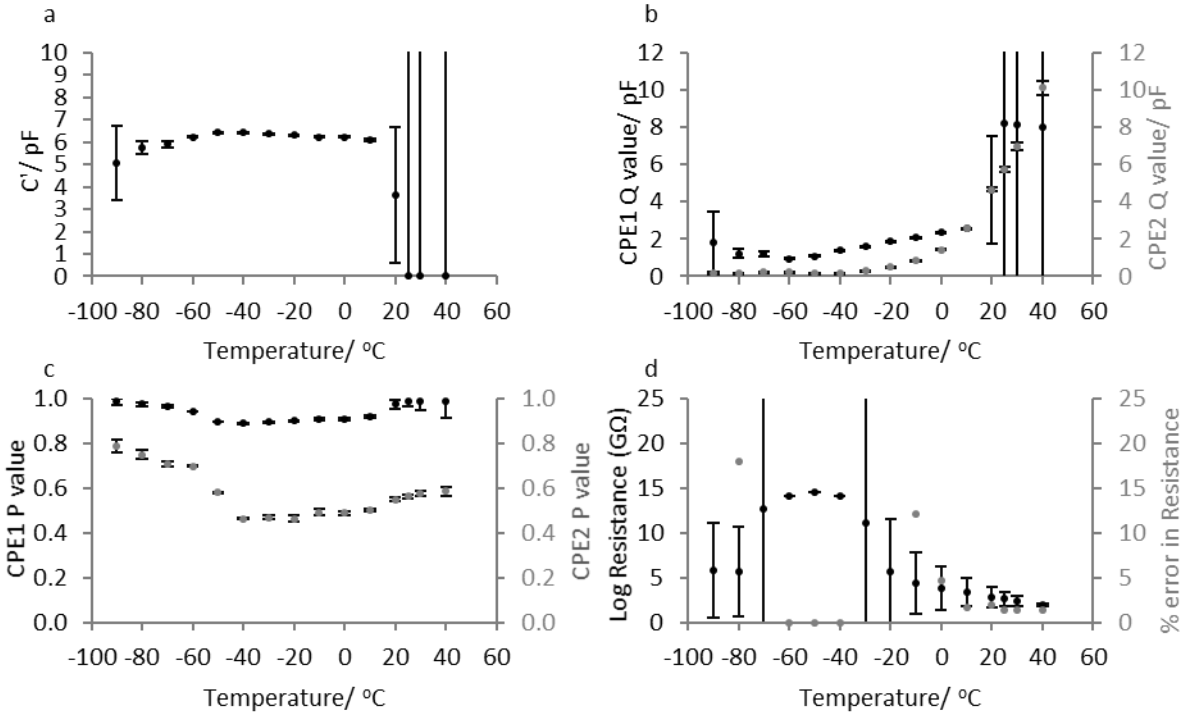

Figure 89: Values of fit parameters and their associated errors as error bars from the $C(\pm) = CPE1(\pm) = CPE2(\pm) = R(\pm)$ model plotted as a function of temperature for the spectra obtained in the temperature range 40 °C to -90 °C and in the frequency range 0.01 Hz- 464 kHz: (a) log of resistance on the primary Y-axis with absolute errors as error bars and % error on the secondary Y-axis; (b) Magnitude of the largely capacitive CPE1 (CPE Q1) on the primary Y-axis and the largely resistive CPE2 (CPE Q2) on the secondary Y-axis; (c) Magnitude of the p values of the largely capacitive CPE1 on the primary Y-axis and the largely resistive CPE2 on the secondary Y-axis; (d) Values of the capacitance in the real part.

Table 24: Resistances between 40 °C to -10 °C estimated from the $C(\pm) = CPE1(\pm) = CPE2(\pm) = R(\pm)$ model

Temperature/ °C	Resistance/ GΩ	Absolute Error/ GΩ	% Error
40	90.7	1.24	1.36
30	248	3.32	1.34
25	423	5.72	1.35
20	730	14.0	1.91
10	2252	37.0	1.64
0	6681	313	4.68
-10	22385	2724	12.2

Further, in regard to the spectra at the low frequency end, one can see how the sample starts to behave more like a resistor between 40 °C and -10 °C which is demonstrated by the low percentage of errors in the estimates of CPE2 parameters (Figure 89b &c) and resistance (Figure 89d). The estimates of resistance between 40 °C and -10 °C (Table 24) were also plotted on Arrhenius coordinates (i.e. Ln R

v/x 1000/T) to quality whether they correlate with temperature. It is evident from Figure 90 that a linear increase in the resistance with a decrease in temperature correlates well with Arrhenius behaviour observed in borosilicate glasses (Ehrt and Keding 2009) below the glass transition temperature, T_g, which has been reported by Schott to be 565 °C for the Adelphi (VC010-20C) vial.

The temperatures coefficients are given in Table 25 terms of resistance, which is an inverse function of conductivity, the relationship can be expressed as

$$ln(R) = \ln(A) - \frac{E_a}{R}\left(\frac{1}{T}\right) \qquad \text{Equation 22}$$

where A is the pre-exponential factor, E_a is the activation energy in kJ/ mol, R is the universal gas constant (8.314) and T is the absolute temperature in Kelvin. When resistance is plotted in the manner described above, the value of the Y-intercept (i.e. $x = \frac{1}{T} = 0$) will be equal to $ln(A)$ and the gradient of the line will be equal to $-\frac{E_a}{R}$. In this manner the activation energy (~75 kJ/mol) was thus calculated. In borosilicate glasses such as the glass segment used in this study, electrical conduction is based on the transport of sodium (Na^+) ions through the glass microstructure which are otherwise strongly bonded to BO_4^- groups with one bridging oxygen atom. As the temperature of the glass increases, the electrical mobility of Na^+ increases (Ehrt and Keding 2009).

In the context of this study, this gives a clear indication that as the temperature of the glass segment is increased and the frequency is decreased, the localised motion of mobile species percolates through a longer-range order which is captured by have a second CPE of p value around 0.5 in the $\mathrm{C}(\pm) = \mathrm{CPE1}(\pm) = \mathrm{CPE2}(\pm) = \mathrm{R}(\pm)$ model. At high enough temperatures and very low frequencies this percolation path reshapes into a dc conductive path. That then allows the mobile species to traverse through the porous microstructure of the glass segment and this behaviour is captured by having a resistor in the $\mathrm{C}(\pm) = \mathrm{CPE1}(\pm) = \mathrm{CPE2}(\pm) = \mathrm{R}(\pm)$ model.

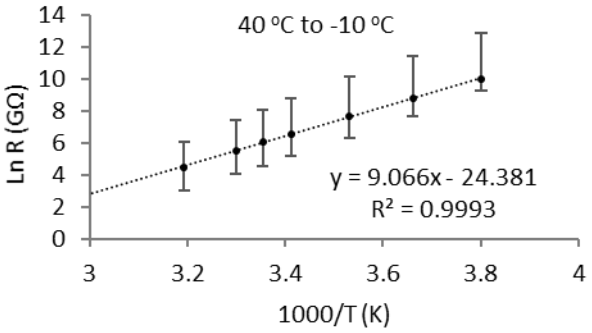

Figure 90: Arrhenius plot of the natural log of resistance for temperatures 40 °C to -10 °C

Table 25: Temperature coefficients for the resistance for temperatures 40 °C to -10 °C on Arrhenius coordinates

Order	**1**	**0**
Temperature Coefficients	9.07	-24.4

It is also true that there were large errors in the estimates of resistance below -10 °C which can be attributed to the fact that as the temperature decreased, the bulk resistance offered by the sample increased, such that it was not possible to predict it accurately from the spectra. In this study, this was manifest in a continuous shift in the spectra to much lower frequencies and beyond the lower limit (i.e. 0.01 Hz) of the measured frequency range, when viewed on the bode plot of impedance magnitude v/s log frequency as shown previously (Figure 84c & d). Alternatively, on the Nyquist plots in Figure 84(b), one can realise the difficulty in estimating the intercept as the temperature is lowered. One would need to go towards much lower frequencies in order to obtain the intercept on Z' axis. However, it can be argued whether a resistor features in the spectra at temperatures below -10 °C. Afterall, a resistor is used to model a dc conduction path for ion migration which is open only when there is enough energy in the system (i.e. at higher temperatures). In other words, as the frequency is decreased and provided there is enough energy in the system, a full dc conduction path can open for the ions to migrate through the glass microstructure. When the energy is reduced by lowering the temperature the conduction path is lost. Therefore, it was not surprising to find large errors in the estimates of resistance below -10 °C in this study. Since, a dc conduction path does not feature at low

temperatures, the resistor appears to be largely irrelevant in the model. It is possible that by having the resistor removed from the model for temperatures below -10 °C, the values of $\mathrm{CPE\ p2}$ could show a trend. Nevertheless, other than resistance, the model is in very good agreement with the data for the temperatures between -10 °C and -70 °C which is a temperature range of interest in the field of freeze drying.

Having recognised that the $\mathrm{C}(\pm) = \mathrm{CPE1}(\pm) = \mathrm{CPE2}(\pm) = \mathrm{R}(\pm)$ model cannot be used to fit the spectra across the whole temperature range, therefore, two models, one representing the behaviour of glass at temperatures between 40 °C and -10 °C, and the other model representing the characteristics of the sample below -10 °C have been proposed in the next two sections.

8.4.5 Circuit Model with a Resistor for Temperatures 40 °C to -10 °C

The $\mathrm{C}(\pm) = \mathrm{CPE1}(\pm) = \mathrm{CPE2}(\pm) = \mathrm{R}(\pm)$ which had floating parameters was modified for temperatures between 40 °C and -10 °C which has been described in a number of steps. As shown previously, a resistor is an essential feature of the observed spectra at temperatures between 40 °C and -10 °C at the low frequency end. Thus, in the **first step**, the resistance estimates (Table 24) for these temperatures from the previous $\mathrm{C}(\pm) = \mathrm{CPE1}(\pm) = \mathrm{CPE2}(\pm) = \mathrm{R}(\pm)$ model were retained and fixed. Having said that, it is also true that floating C and $\mathrm{CPE\ 1}$ had invariably resulted in unreasonable errors in the temperature range 40 °C to 20 °C.

Therefore, in the **second step**, the high frequency part of the spectrum (464 kHz-21.5 kHz) at 40 °C, 30 °C, 25 °C and 20 °C was fitted with the $\mathrm{C}(\pm) = \mathrm{CPE1}(\pm)$ model as per the first step described for the spectrum at 40 °C (Figure 87b) to obtain the fit values for C and $\mathrm{CPE\ 1}$ for each temperature which are given in Table 26. Here, it is important to recognise that the values of C and $\mathrm{CPE\ 1}$ had negligible errors for temperatures 10 °C, 0 °C and -10 °C when the spectra were fitted with the $\mathrm{C}(\pm) = \mathrm{CPE1}(\pm) = \mathrm{CPE2}(\pm) = \mathrm{R}(\pm)$ model as shown in Figure 89(b) & (c). Therefore, there was no need to fix them. In other words, the high frequency part of the spectra for temperatures 40 °C to 20 °C were

fitted separately to obtain the estimates for C and $\mathrm{CPE}\ 1$ which were then fixed in the revised model. On the other hand, the values of C and $\mathrm{CPE1}$ for temperatures 10 °C to -10 °C were kept free.

In the **third** step, for all temperatures between 40 °C and -10 °C, the $\mathrm{CPE2}$ parameters Q and p were allowed to float. The revised model for temperatures 40 °C to 20 °C was thus referred to as the $\mathrm{C(x) = CPE1(x) = CPE2(\pm) = R(x)}$ model. Note the use of "x" next to C and $\mathrm{CPE}\ 1$ and R. And, for temperatures 20 °C to -10 °C, where all parameters were floated except for the resistor, the revised model has been referred to as the $\mathrm{C(\pm) = CPE1(\pm) = CPE2(\pm) = R(x)}$. Note the use of "x" next to R.

Table 26: Estimates for C and CPE 1 after fitting the high frequency part of the spectrum (464 kHz-21.5 kHz) for temperatures 40 °C to 20 °C

Temperature/ °C	Free (±) or Fixed (x)	C value (pF)/ Error (pF)	CPE1 Q (pF)/ Error
40	±	6.16/ 0.0436	3.43/ 0.0530
30	±	6.06/ 0.0423	3.11/ 0.0185
25	±	6.02/ 0.0393	3.00/ 0.00958
20	±	6.00/ 0.0319	2.91/ 0.00583

Figure 91 highlights the part of the spectra that was modelled by the capacitor and the two CPEs. One can see that for temperatures 40 °C to 20 °C, the model does not fit quite well with the spectra in the frequency range annotated on the plots for 40 °C, 30 °C and 20 °C. Nevertheless, the model works very well in the temperature 10 °C to -10 °C. The values of the fit parameters obtained for temperatures 40 °C to -10 °C have been plotted (as a function of temperature) in Figure 92. Note that only those errors have been shown as error bars where the parameters were floated, and the software generated the corresponding errors. For obvious reasons, the software does not generate errors for those parameters which are fixed. As expected, although the capacitor does not have any physical relevance as discussed before, it is constant around ~6 pF which demonstrates that its contribution to the high frequency part of the spectra did not change as the temperature was decreased. The magnitude of CPE1 Q changed only slightly over this temperature range and the fact the CPE1 p parameter is almost constant around 0.9 demonstrates that it modelled the high frequency part of the spectrum reasonably

well across the temperature range shown. However, as already known, this CPE is simply an approximation for the second process that appears at low enough temperatures. The magnitude of $\mathrm{CPE2\ Q}$ decreases as the temperature is decreased which suggests the resistance has increased considering $\mathrm{CPE\ Q}$ is equal to the inverse of impedance. The $\mathrm{CPE2\ p}$ values are constant around 0.5 which appears to be the intra-cluster and inter-resistance modelling the percolation path which reshapes into a full-fledged dc conductive path as the temperature is increased.

Figure 93(a) to (g) show the Nyquist plots of the imaginary part impedance v/s real part impedance and the corresponding fit results (black line) obtained after carrying out the aforementioned changes to the fitting approach for temperature 40 °C to -10 °C. The software generated fit has been simulated to estimate the resistances which is shown as a grey line that continues immediately from the point where the fit line terminates. This was included in order to demonstrate that the fit had to be simulated to frequencies as low as 1×10^{-9} Hz in order to estimate the resistance at the x-intercept. Furthermore, one can see how at higher temperatures, it is the low frequency end of the spectrum that occupies most of the space whilst the high frequency is squashed within a small region. For example, in Figure 93(a), the asymmetrical arc is largely made up of the data in the frequency 0.01 Hz-1.47 Hz whilst the rest of the data in the frequency range 1.47 Hz- 464 kHz is confined within a small region on the plot. As the temperature decreases, the arcs become smaller such at after a point the resistor does not feature in the spectra. Therefore, for temperature below -10 °C, a separate model without a resistor has been proposed which is described in the next section. In addition, Figure 93(h) shows the Arrhenius plot of the resistance estimates that were estimated from the Nyquist plots to reiterate the fact that these estimates follow Arrhenius behaviour in the temperature range 40 °C to -10 °C.

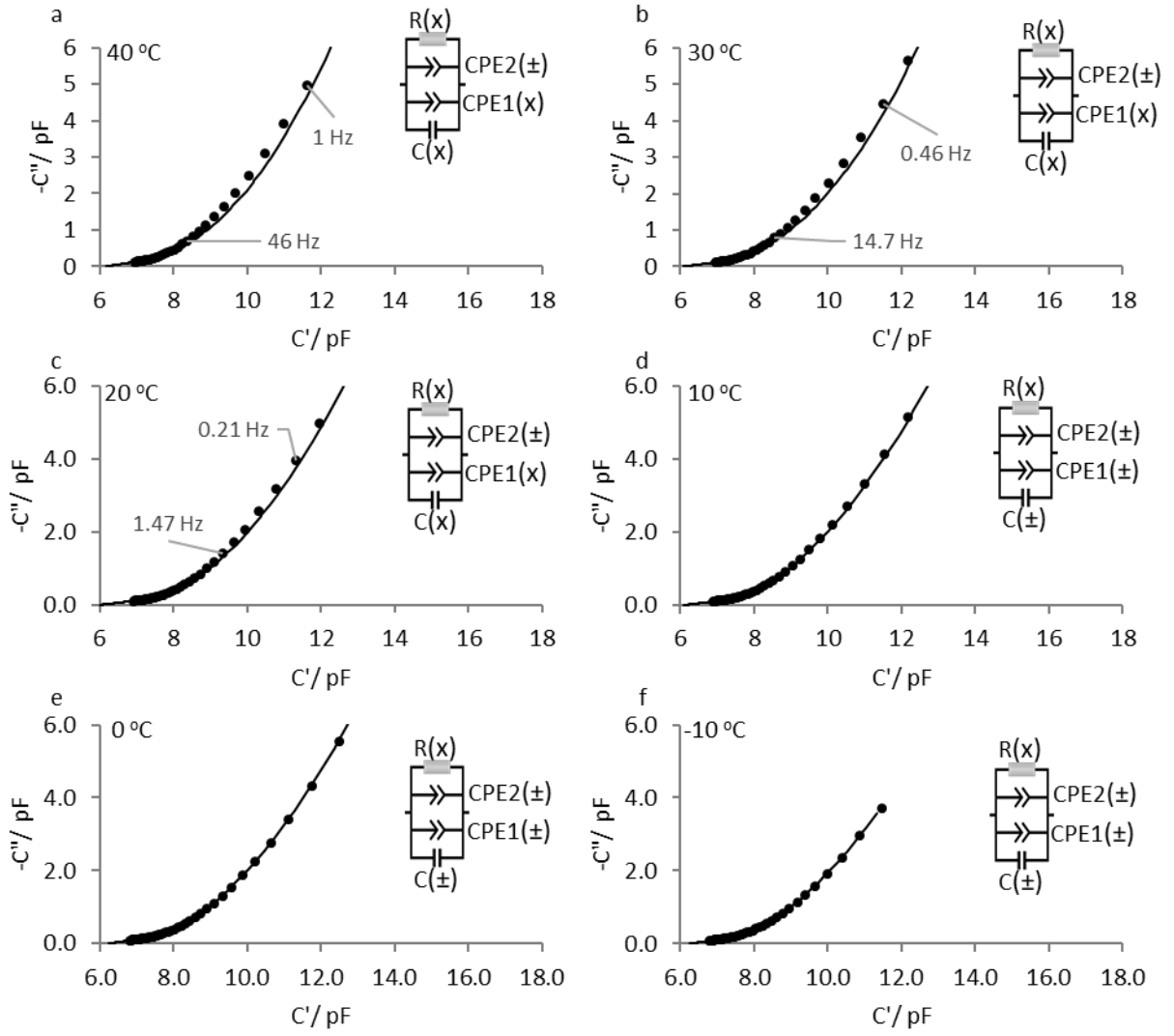

Figure 91: Cole-Cole plots of the imaginary part capacitance v/s real part capacitance for the spectra and their fit results from the model comprising a capacitor in parallel with two CPEs and a resistor for the temperatures between 40 °C and -10 °C in the frequency range 0.01 Hz- 464 kHz. For temperatures 40 °C, 30 °C and 20 °C, the values of C and $CPE1$ are the same as those given in Table 26 and the value for R is the same as given in Table 24. For temperatures below 20 °C, C and $CPE1$ parameters (Q and p) were floated and the value of R was the same as given in Table 24. For all temperatures, the $CPE2$ parameters (Q and p) were floated.

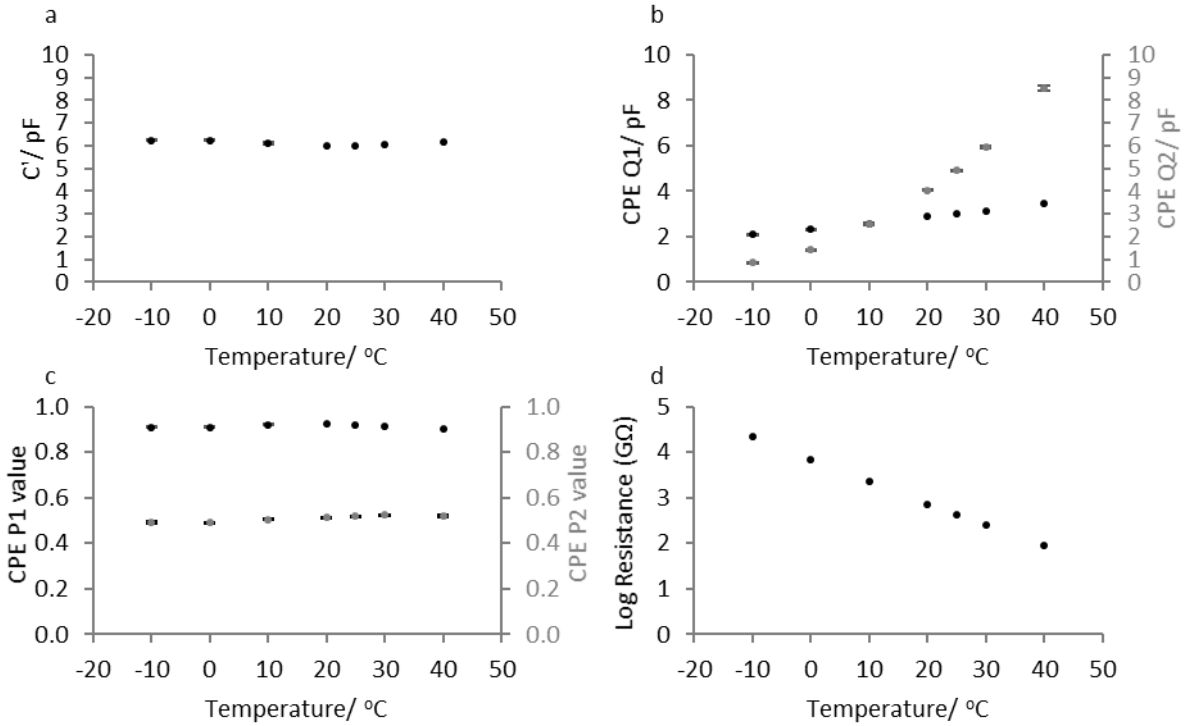

Figure 92: Values of fit parameters (as a function of temperature) from the $C(x) = CPE1(x) = CPE2(\pm) = R(x)$ model for temperatures 40 °C to 20 °C and from the $C(\pm) = CPE1(\pm) = CPE2(\pm) = R(x)$ model for temperatures 20 °C to -10 °C, fitted in the frequency range 0.01 Hz- 464 kHz: (a) Values of the high frequency capacitance in the real part; (b) the Q values for CPE1 and CPE2 on the primary Y-axis and the secondary Y-axis respectively; (c) The p values of CPE1 and CPE2 on the primary Y-axis and the secondary Y-axis respectively; (d) log of resistance on the primary Y-axis. The error bars have been plotted for only those parameters which were floated before fitting.

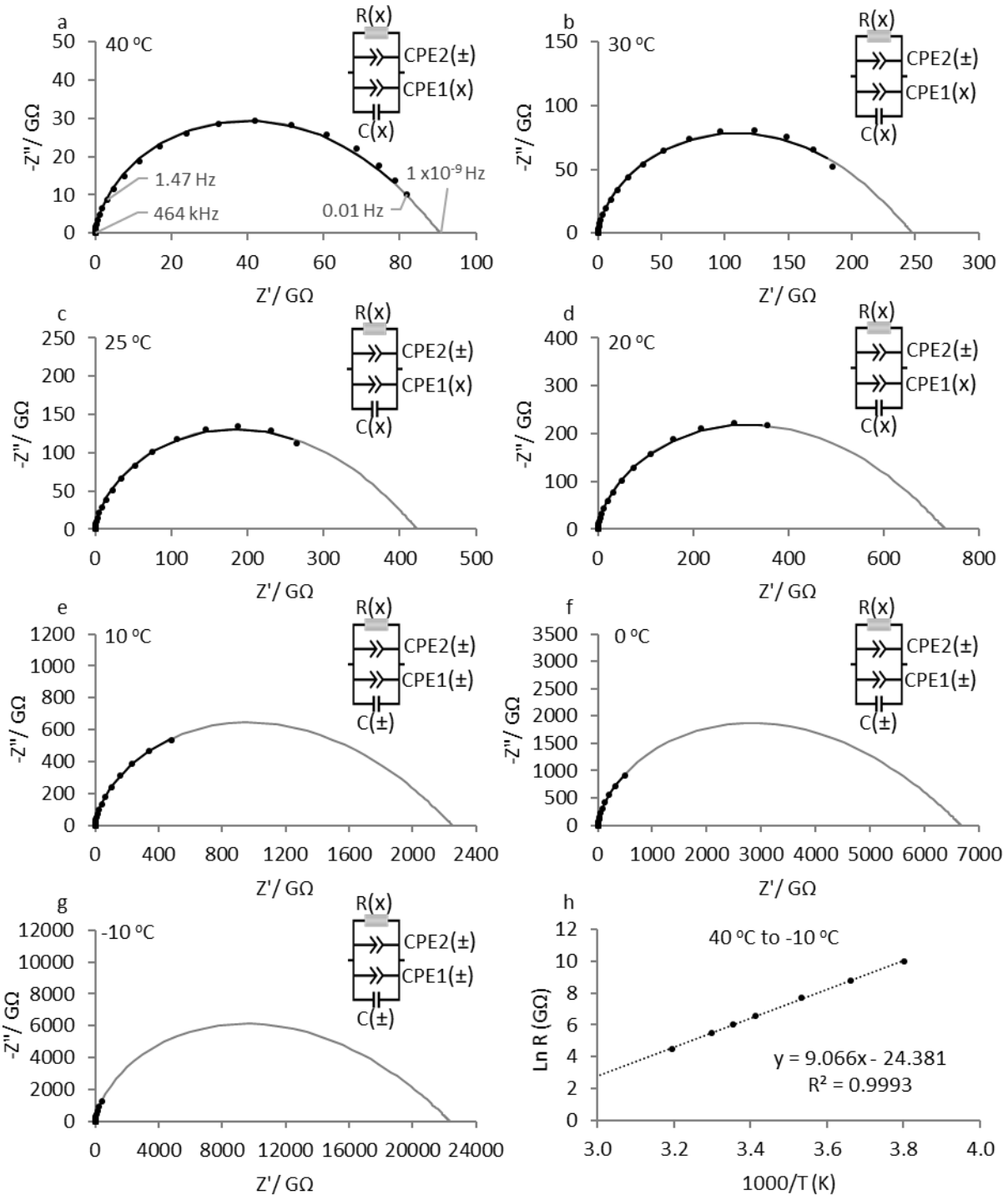

Figure 93: Nyquist plots of the imaginary part impedance v/s real part impedance for the spectra and their fit results from the model comprising a capacitor in parallel with two CPEs and a resistor for the temperatures between 40 °C and -10 °C in the frequency range 0.01 Hz- 464 kHz. For temperatures 40 °C, 30 °C and 20 °C, the values of C and $CPE1$ are the same as those given in Table 26 and the value for R is the same as given in Table 24. For temperatures below 20 °C, C and $CPE1$ parameters (Q and p) were floated and the value of R was the same as given in Table 24. For all temperatures, the $CPE2$ parameters (Q and p) were floated. An arrehenius plot for the values of Resistance estimates from the intercept have been plotted against the temperatures 40 °C to -10 °C for reference.

8.4.6 Circuit Model Without the Resistor for Temperatures -10 °C to -90 °C

Figure 94 shows the Cole-Cole plots of the spectra and the fit results (0.01 Hz-464 kHz) from the $C(\pm) = CPE(\pm) = CPE2(\pm)$ model for temperatures -10 °C to -90 °C. The values of the fit parameters have been plotted as a function temperature in Figure 95. It is clear that the $C(\pm) = CPE(\pm) = CPE2(\pm)$ model works very well in this temperature range. Resistance clearly does not feature in the spectra at low temperatures which confirms that there was no dc conductivity present in the sample. It has already been shown how the second process emerges as the temperature is decreases and therefore, the significance a capacitor and a CPE with p value equal to 0.9 is only limited to the fact that their presence allows the model to fit the spectra in the high frequency region. The only parameter that is likely to have a real meaning is the second CPE with its p value increasing from 0.5 at -10 °C to 0.7 at -90 °C. This supports the idea of charge percolation through short-scale pathways that are interconnected with long-range percolation pathways within the fused silica network which allow mobile species to traverse through the microstructure at a small scale that gradually grows into a larger scale as the frequency is lowered. It is known that a CPE behaviour of close to 0.5 is frequently observed for porous materials at the interface of blocking electrodes and diffusion pathways (Ben Amor, et al. 2014; Orazem and Tribollet 2017).

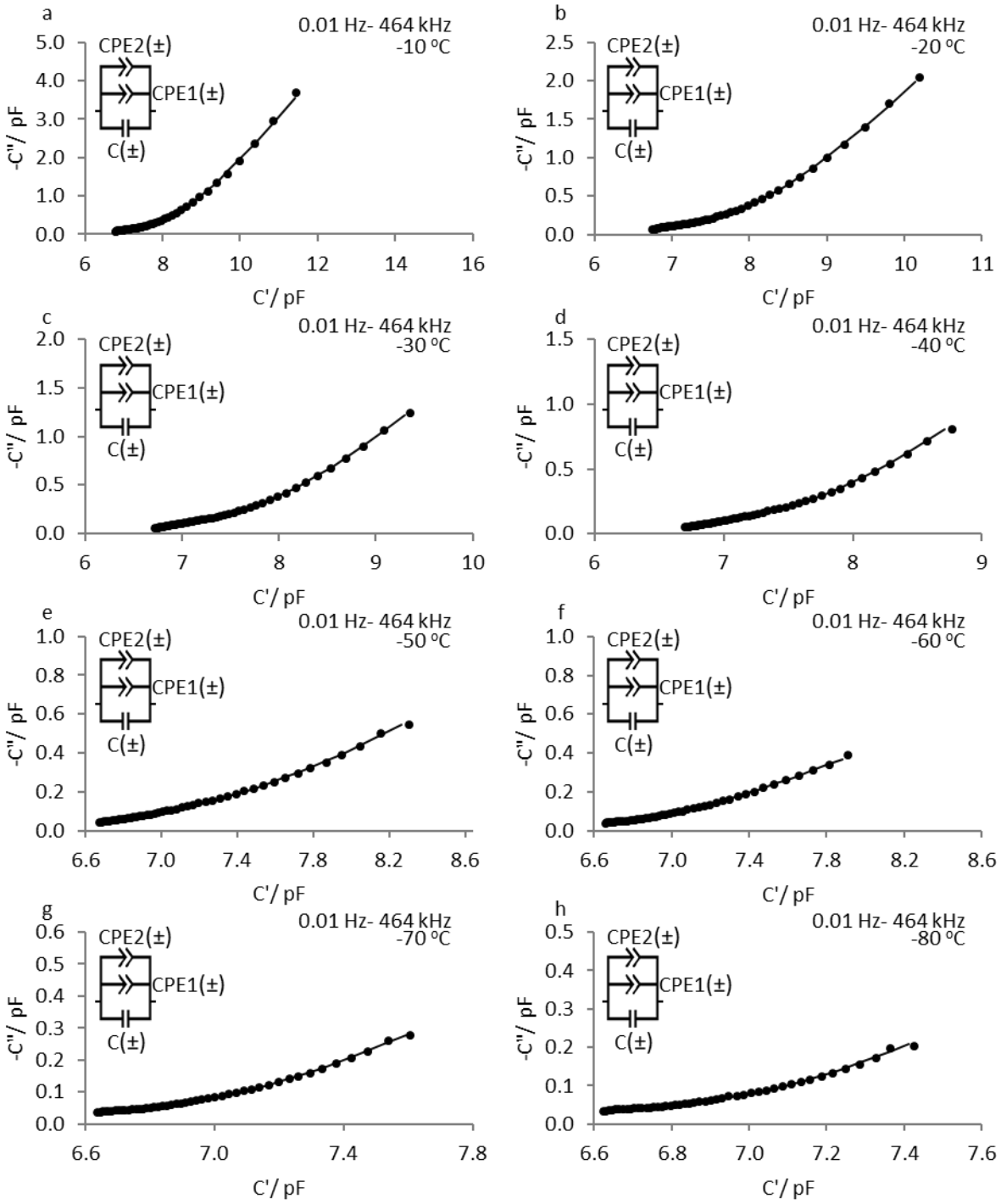

Figure 94: Cole-Cole plots of the imaginary part capacitance v/s real part capacitance for the spectra and their fit results from the $C(\pm) = CPE1(\pm) = CPE2(\pm)$ model at temperatures between -10 °C and -90 °C in the frequency range 0.01 Hz- 464 kHz.

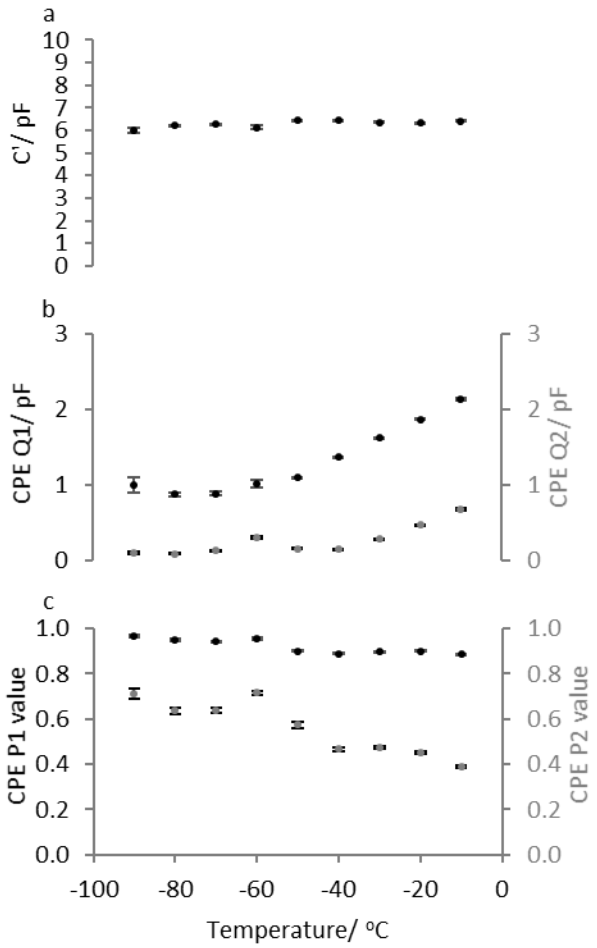

Figure 95: Values of fit parameters (as a function of temperature) from the $C(\pm) = CPE1(\pm) = CPE2(\pm)$ model for temperatures -10 °C to -90 °C in the frequency range 0.01 Hz- 464 kHz: (a) Values of the high frequency capacitance in the real part; (b) the Q values for CPE1 and CPE2 on the primary Y-axis and the secondary Y-axis respectively; (c) The p values of CPE1 and CPE2 on the primary Y-axis and the secondary Y-axis respectively.

8.5 Discussion

There were two parts of the present study. In the first part, the value of the relative permittivity of the standard Adelphi (VC010-20C) vial was determined by two methods. In the first method, gold sputtered electrode segments were measured without hard wiring, i.e. by placing the sputter coated segments directly on a conductive hemi-cylindrical brass saddle. In the second method, the sputter coated segments were hard-wired to allow for a direct connection between the glass segment and the BDS system. A value of ε_g of 5.73 was obtained from the measurement of the hard-wired glass segments. This was in excellent agreement with that reported by Schott (5.7).

Further, hard-wired glass segments and the hard-wired segments with stick-on copper electrodes (of areas similar to that of the hard-wired sputter coated segments) were compared at room temperature. It was shown that both types had a similar dielectric behaviour over most of the frequency range. The only difference was the appearance of a second process which was more prominent in the case of the sputter coated segment as the area of the electrode increased. This difference in the high frequency response between the two electrode systems may be ascribed to the type of contact between the electrode and the glass surface. However, it is important to recognise that this high frequency process associated with the sputter-coated electrode-glass interface might not be relevant to the bulk measurement of the TVIS vial, where the electrodes are present on the either side of vial containing a liquid or a frozen solid, because it is likely to be smaller compared to a Maxwell-Wagner polarisation in the liquid state or a dielectric relaxation of ice. Nevertheless, the observation of this process associated with sputter-coated electrodes is interesting and its knowledge might be useful if sputter-coated electrode systems are used in the future. Having said that, TVIS measurements are mostly performed with vials with stick-on copper electrodes and therefore, the similarities in the low frequency response between the sputtered coated and the stick-on copper electrode glass segments are most interesting because it is the low frequency end of the TVIS spectrum that is impacted by the glass wall (Smith and Polygalov 2019).

Given that the hard-wiring method was more suitable for determining the dielectric constant, the next part of the study involved employing the copper electrode segment with an electrode area comparable to that for the TVIS vial to understand the dielectric behaviour of the glass wall across a range of temperatures. It was demonstrated that the real part capacitance was less sensitive to temperature than imaginary part capacitance in the temperature range of 40 °C to -90 °C. For example, when the values of the real part capacitance measured at 100 Hz were normalised to 50 °C, % change in the temperature coefficient was only up to 12 % in the temperature range -50 °C to 20 °C.

Furthermore, a more definitive circuit model was developed to understand the underlying mechanisms of the charge percolation in the microstructure of the glass wall. It was recognised the model should include a resistor and two CPEs in the temperature range 40 °C to -10 °C, wherein the estimates of the resistance followed the Arrhenius behaviour, which was consistent with the studies that have involved the measurement of porous glasses at very high temperatures. Finally, it was demonstrated that the resistor does not features at temperatures below -10 °C which suggested the absence of a DC conduction path for ion migration.

The next phase of the dielectric measurements of the glass wall will involve the development of a methodology for calibrating the glass wall capacitance for temperature, with the objective to predict the product temperature in a real freeze-drying scenario. This will warrant the manufacture of a special electrode system such as the likes of microfine interdigitated electrodes which allow for the restriction of the field lines within the glass wall, as opposed to conventional copper electrodes, wherein the field lines are likely to pass into the sample (Allen 1998).

8.6 Chapter Conclusion

Broadband dielectric spectroscopy has proved to be useful tool for studying the dielectric properties of the glass wall, in particular, the determination of the dielectric constant of the Adelphi (VC010-20C vial). Moreover, a definitive model for the glass across a range of temperatures has been developed for the first time, which serves as a foundation for the future work that will involve the development of a methodology for the prediction of the product temperature using the temperature dependency of the glass wall.

9 General Conclusions

9.1 Characterisation of the Freezing Stage

It has been demonstrated that the TVIS parameters, the peak frequency of the dielectric loss peak (F_{PEAK}) and the real part capacitance measured at a characteristic frequency of 0.2 MHz or $C'(0.2MHz)$ can be employed to monitor the entire freezing stage, particularly, the transition from a Maxwell-Wagner (MW) polarization of the liquid at the glass-liquid interface to the dielectric relaxation of ice in the frozen state. While F_{PEAK} can be used to predict the ice nucleation temperature, $C'(0.2MHz)$ can be used to determine the ice growth time. When employed together, it is possible to demonstrate a lower nucleation temperature translates to a shorter ice growth time and vice versa. Further, it has been demonstrated that the peak imaginary amplitude, C''_{PEAK}, is uniquely sensitive to the subtle changes in the stability of the ice microstructure, which results from the way ice is initially formed (either stochastically or by controlled nucleation). Thus, the prospect of multiplexing TVIS with an advanced controlled nucleation technique is interesting, as it can serve as a useful tool for monitoring the impact of the thermal history of the sample (before primary drying) on the subsequent stages of the freeze drying process.

9.2 Prediction of the Primary Drying Endpoint

It has been demonstrated that the unique sensitivity of the high frequency real part capacitance measured at 100 kHz or $\mathrm{C}'(100\mathrm{kHz})$ to the changes in the shape of the ice sublimation interface and the amount of ice in the vial can be exploited to determine the primary drying endpoint. The characteristic dip in the time-line of $\mathrm{C}'(100\mathrm{kHz})$ corresponds to the point when the ice cylinder (initially in intimate contact with the glass wall) transforms into an ice dome with its sides touching the point where the glass wall and the vial base meet. As the ice dome continues to retract and shrink towards the centre of the vial base, $\mathrm{C}'(100\mathrm{kHz})$ also continues to recover towards a pseudo-steady state plateau. The point when $\mathrm{C}'(100\mathrm{kHz})$ reaches the plateau corresponds to the disappearance of the last ice crystal as shown by the photographic evidence.

It should be recognised that the above method cannot be used to determine the endpoint in internal vials or for solutions (which develop an opaque dry layer). Therefore, a methodology based on retrospective and real time analysis has been proposed which allows for the prediction of the endpoint in a TVIS vial positioned at any location and for any solution. In the particular case, a simple sugar solution (5% w/w sucrose) and a more complicated protein solution (IgG containing formulations) have been used to demonstrate the applicability of the methodology.

It has been demonstrated that by applying suitable limiting criteria to the magnitude of the first derivative of the rolling average of $\mathrm{C}'(100\mathrm{kHz})$, it is possible to predict the endpoint very close to the point when $\mathrm{C}'(100\mathrm{kHz})$ reaches a plateau. In some cases, the limiting criteria can also serve as an early warning for the operator to switch to secondary drying stage without the need to introduce an unnecessarily long soak period, which is often the case with thermocouples. Moreover, the probability of the predicted TVIS endpoint being the true endpoint of the batch is low given that one should account for the variability in the primary drying times across the core vial population due to the variability in the vial heat transfer coefficient and the mass transfer resistance. Both factors impact the product temperature and therefore the rate of sublimation.

Furthermore, the endpoints predicted from TVIS at the edge and at the core were compared with the endpoints estimated by the batch monitoring sensors (Pirani/Capacitance Manometer and Pressure Rise Test). It has been demonstrated that none of the techniques can determine the true endpoint of the batch, i.e. the point when the last vestiges of ice disappear. It follows that a soak period should still be added in any case. Moving forward, TVIS can be used to perturb several locations of the shelf simultaneously in order to obtain an estimate for the endpoint which is potentially close to the true batch endpoint provided an instrument with several channels is manufactured.

9.3 Dielectric Properties of the Glass Wall

It is well known that product temperature is one of the most critical process parameters in a freeze drying process. One of the methods for monitoring the product temperature is to monitor the temperature of the glass wall, given its close proximity to the product. In the published domain, a number of authors have used infrared thermography coupled with a mathematical model to monitor the evolution of the temperature of the glass wall and therefore the product temperature. With TVIS, the measured impedance response is a combination of the contribution from the glass vial and that from the contents of the vial. And it has been shown that the glass vial is perturbing to the TVIS spectrum. It therefore seemed prudent to understand the dielectric properties of the glass wall per se as a function of frequency over a broad range of temperatures, some of which are of relevance to the freeze drying process. The ultimate objective then is to exploit the temperature dependency of the glass wall in order to predict the product temperature. The present work completes only a part of the whole picture. It involved preliminary studies on the impact of the applied frequency and temperature on the migration of mobile species within the porous glass microstructure. In effect, two equivalent circuit models have been developed, one which is applicable at low temperatures (-90 to -10 °C) with a capacitor and two constant phase elements (CPEs); and the other which is applicable at high temperatures (capacitor, two CPEs and a resistor). The individual components of the circuit model represent the various migratory paths that the mobiles species use to traverse through the microstructure depending on the applied frequency and temperature. This information is useful in understanding of the temperature dependency of the glass wall as a whole when studied through the lens of impedance spectroscopy. In future, these circuit models will potentially serve as a foundation for establishing the temperature dependency of the glass wall. In addition, more advanced electrode systems will also be used to further develop the circuit model for the glass wall.

Final Remarks

It is worth noting that the experimental studies described previously have been centred on the use of the “process understanding” part of QbD, in particular, the use of TVIS as a PAT tool for freeze drying process monitoring. By identifying a number of TVIS parameters, it has been possible to characterize the different stages of the freeze drying process. Once TVIS becomes a well-established technique, it may then be employed for application studies: these will involve establishing risks associated with exceeding the maximum allowable product temperature and equipment capacity. That would then enable the construction of a design space reflective of a controlled freeze drying process for a given formulation. The ultimate aim then would be to identify an optimal sublimation rate whilst still working within the confines of the design space or the edge of failure.

10 Appendices

10.1 Appendix I: Determination of the Dimensions of Sputter-Coated Electrodes

In the case of a parallel plate capacitor comprising two planar electrodes of equal size placed in close proximity to one another relative to their surface area, the instantaneous glass wall capacitance (C_g) is given by (Smith and Polygalov 2019)

$$C_g = \varepsilon_0 \varepsilon_g k_g \qquad \text{Equation 23}$$

where ε_0 is the permittivity of free space ($8.854 \times 10^{-12} F.m^{-1}$), ε_g is the dielectric constant of the Fiolax® glass used for the Adelphi VC010-20C vial reported to be 5.7 at 1 MHz at 25 °C. The cell constant, k_g, would be defined by A/d, where A is the area of an electrode (product of the width and the height of the electrode) and d is the separation between the electrode pair reported to be 1.1 mm for the Adelphi VC010-20C vial.

In this study (Section 8), the electrodes are sputtered over a curved surface rather than a planer one and the fact that a tape was used to manually create a border around the surface area exposed for gold sputtering, it is more difficult to define the area of the electrode pair using a simple measuring device such as a ruler. Hence, a more accurate estimation of the height (13.5 mm) and the width of the electrodes (20.9 mm) can be derived from an alternative methodology.

Estimation of the Height of the Electrodes

The height of the electrodes (13.5 mm) on both the sides of the glass segment has been estimated using the procedure given in Table 27 and Figure 96.

Table 27: Procedure for the estimation of height of the gold sputtered electrodes

Step #	Description
1	Hold a ruler parallel to the height of the electrodes on side 1 of the segment and take a photograph (Figure 96a) and repeat for side 2 of the segment (Figure 96b)
2	Paste the pictures in PowerPoint or Word
3	Choose a reference distance on the ruler. In this case, 13 mm has been chosen for both Side 1 and 2.
4	For Side 1, draw a line from point A to B and record the image length (i.e. 26.7 mm). Thus, the image length of 26.7 mm is equivalent to a reference distance of 13 mm on the ruler
5	Draw another line that spans the height of the electrode on the image, i.e. from C to B and record the image length.
6	For side 2, the image lengths have been recorded accordingly as Figure 96b
7	Calculate the actual height of the electrodes on both the sides using the equation below $Height\ of\ Electrode = \frac{Reference\ distance\ on\ the\ ruler}{Image\ distance\ on\ the\ ruler} \times Image\ height\ of\ the\ electrode$
8	$Height\ of\ Electrode\ on\ Side\ 1 = \frac{13}{26.7} \times 27.9 = 13.6\ mm$ $Height\ of\ Electrode\ on\ Side\ 2 = \frac{13}{27.9} \times 28.8 = 13.4\ mm$ Average height of the electrode pair = 13.5 mm

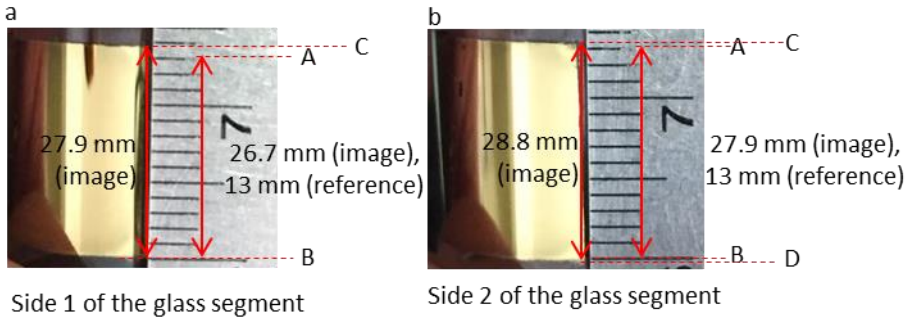

Figure 96: Procedure for the estimation of the height of the electrodes for both the sides of the glass segment using the images: (a) Side 1 of the electrode pair, where the reference length on the ruler is 13 mm and its corresponding image length is 26.7 mm. The image height of the electrode is 27.9 mm. Using these three values, the actual height of the electrode on side 1 can be calculated (13.6 mm). Likewise, the actual height of the electrode on Side 2 can be calculated (13.4 mm). Thus, for the calculation of area, an average height of 13.5 mm is used.

Estimation of the Width of the Electrodes

Given that the electrodes are sputtered over a curved glass segment, the effective width of the electrode is more likely to be the closer to the average of the length of the external arc (21.9 mm) and the internal arc (19.9 mm) of the electrode, i.e. $w = 20.9$ mm. The procedure for calculating these lengths involves shading the area enclosed by the external and the internal arcs and positioning the glass segment over the brass saddle such that their edges are aligned as shown in Figure 97. That then allows for the determination of the angle subtended by the arcs which is used for estimating their length by employing the Pythagoras theorem ($\sin\theta = perpendicular/hypotenuse$). The steps are detailed in Table 28.

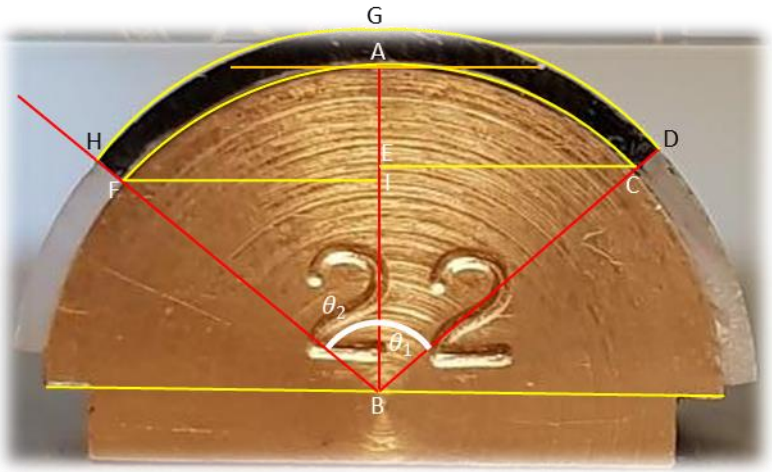

Figure 97: Estimation of the width of the electrode. The curved segment is aligned with the edge of the brass saddle. The area enclosed by the outer arc (HGD) and the inner arc (FAC) of the sputtered electrode pair is shaded in black. The angle, θ subtended by the length of the arcs is equal to the sum of the angle subtended by the arc FA (θ_1) and arc CA (θ_2).

Table 28: Procedure for the estimation of the width of the gold sputtered electrodes

Step #	Description	Value	Unit
1	Radius of the brass saddle AB, BC and BF	11.0	mm
2	Radius of the inner arc FAC	11.0	mm
3	Thickness of glass segment	1.10	mm
4	Radius of the outer arc HGD	12.1	mm
5	Image Length of AB in Figure 97	42.8	mm
6	Image Length of Chord EC in Figure 97	34.0	mm
7	Actual length of chord EC	8.74	mm
8	Image Length of Chord IF in Figure 97	33.3	mm
9	Actual length of chord IF	8.56	mm
10	Sin $\theta_1 = EC/BC$	0.794	
11	$\theta_1 = Sin^{-1}\left(\frac{EC}{BC}\right) = Sin^{-1}\left(\frac{8.74}{11}\right)$	0.918	rad
12	Sin $\theta_2 = IF/BF$	0.778	
13	$\theta_2 = Sin^{-1}\left(\frac{IF}{BF}\right) = Sin^{-1}\left(\frac{8.56}{11}\right)$	0.892	rad
14	Total angle subtended by the arcs ($\theta = \theta_1 + \theta_2$)	1.81	rad
15	Length of inner arc FAC (Inner radius x θ)	19.9	mm
16	Length of outer arc HGD (Outer radius x θ)	21.9	mm
17	Average width of the electrode (Average length of the arcs)	20.9	mm

10.2 Appendix II: Impedance Theory

When direct current flows through a closed circuit under the influence of an applied voltage (V), the circuit (including the circuit element e.g. resistor, capacitor, etc.) presents an opposition to this flow. This opposition or restriction to the flow of electric current (I) is measured in terms of Electrical Impedance (Z). In quantitative terms, impedance is the ratio of the magnitude of voltage to the current magnitude and is equal to Resistance (R) in case of a DC-circuit given by Ohm's Law (Equation 24). Resistance works against voltage to control current flow. If voltage is increased more current will flow. If resistance is increased less current will flow (Morris and Senior 1991).

$$Z = R = \frac{V}{I} \qquad \text{Equation 24}$$

The concept of Impedance extends beyond resistance to Alternating Current (AC) circuits. An AC is that electric current which switches direction periodically in the elements through which it flows (Figure 98). In other words, an AC is a periodic waveform (Hazen 1990).

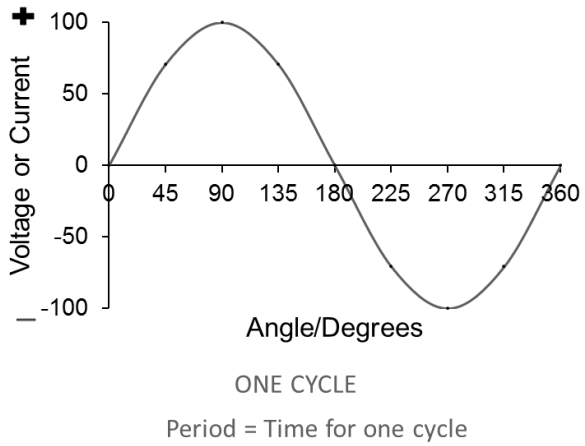

Figure 98: Alternating Current- A Periodic Waveform

The switching of the direction or polarity is measured in terms of frequency or the number of cycles repeated every second, given by

$$f = \frac{1}{T} \qquad \text{Equation 25}$$

where f is the frequency expressed in Hertz (Hz) and T is time in seconds.

One cycle of an AC waveform is a trigonometric sine function (Figure 99) given by

$$\text{SIN}\ \theta = e_i/E_p \qquad \text{Equation 26}$$

where E_p is the peak voltage or the peak current and can be calculated from the instantaneous voltage or instantaneous current, e_i, which can also be expressed in terms of angular velocity (ω) which defines the number of degrees per second or radians per second. Hence,

$$e_i = E_p\ \text{SIN}\ (\omega.t + \theta) \qquad \text{Equation 27}$$

where $\omega = 2\pi f$ and θ is the offset angle in radians (Hazen 1990).

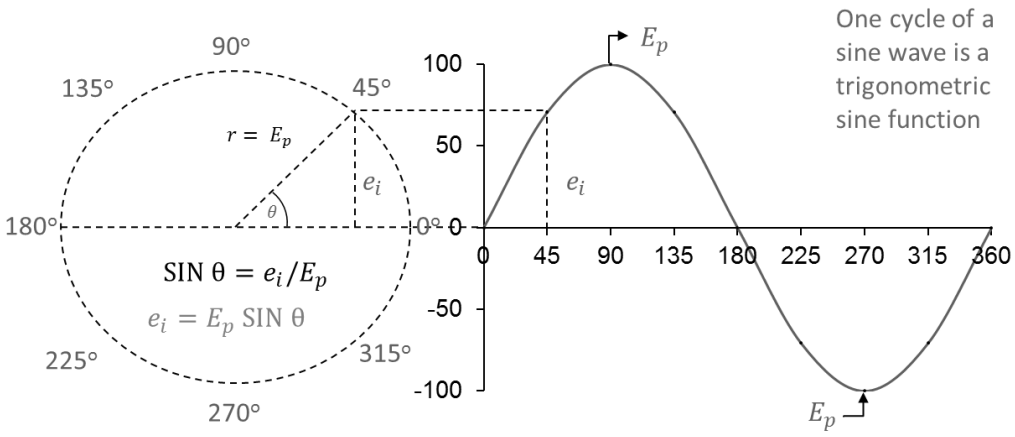

Figure 99: Alternating Current- A Trigonometric Sine Function

In complex terms, Impedance is a complex number comprising a real component and an imaginary component (Figure 100). The real components of the elements in series combination are added together and the vice versa (Wang 2010).

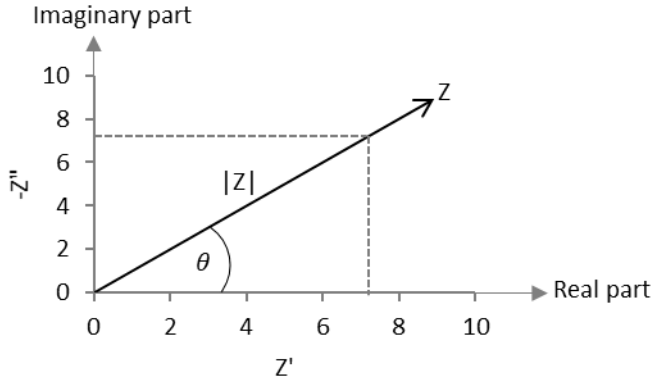

Figure 100: Real and Imaginary Components of Impedance

Capacitive Reactance

It is important to extend the concept of impedance to AC circuits because there are two impeding mechanisms in addition to the normal resistance in DC circuits: inductance and capacitance. While inductance is a property of a conductors, wherein a voltage is self-induced by the magnetic fields of currents, capacitance is the ability of a body to store charges induced by voltages between conductors. The contributions arising from these two effects are collectively termed reactance. While the capacitive reactance and the inductive reactance form the imaginary part of the complex impedance, the real part of the complex impedance is formed by resistance (Hazen 1990).

The capacitive reactance (X_C) is expressed as,

$$X_C = \frac{-i}{2\pi f C} \qquad \text{Equation 28}$$

where f is the frequency of the electrical signal passing through a capacitor and C is the capacitance.

The resistance and the reactance cannot be added simply to give the resultant impedance, rather a vector sum of the resistance and reactance at 90 degrees to the former (Figure 101) yields an effective representation of total impedance (Equation 29) (Macdonald, J.R., Johnson,W.B. 2005).

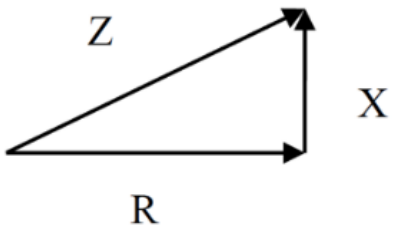

Figure 101: Direction of Impedance parameters

$$Z = \sqrt{R^2 + X^2} \qquad \text{Equation 29}$$

Total Impedance in Series and Parallel Combination

For circuit elements in series,

$$Z_{total} = Z_1 + Z_2 \qquad \text{Equation 30}$$

Here, the total impedance is dominated by the component with the largest impedance. For example, if $Z_1 << Z_2$, then

$$Z_{total} \cong Z_2 \qquad \text{Equation 31}$$

For circuit elements in parallel, the admittance values (inverse of impedance) are added to obtain the total obstruction in the current flow,

$$\frac{1}{Z_{total}} = \frac{1}{Z_1} + \frac{1}{Z_2} \qquad \text{Equation 32}$$

Here, the total impedance is dominated by the component with the smallest impedance. For example, if $Z_1 << Z_2$, then

$$Z_{total} = \frac{Z_1 \times Z_2}{Z_1 + Z_2} = \frac{Z_1 \times Z_2}{Z_2} \cong Z_1 \qquad \text{Equation 33}$$

Capacitance

Capacitance, another determinant of dielectric responses of the materials, is a measure of the amount of charge (Q) stored onto a pair of capacitor plates over an applied voltage (V) and is expressed (Equation 34) by the coulombs law.

$$C = \frac{Q}{V} \qquad \text{Equation 34}$$

The charge storage capacity in turn depends on the geometric configuration of the capacitor, viz. the area (A) of the plates that directly overlap and the distance (d) between the plates. This relationship between the capacitance and the geometric dimensions is given by

$$C = \varepsilon \frac{A}{d} \qquad \text{Equation 35}$$

where ε is the absolute permittivity of the dielectric material, given by

$$\varepsilon = \varepsilon_r \times \varepsilon_0 \; or \; \kappa \times \varepsilon_0 \qquad \text{Equation 36}$$

where ε_r is the relative permittivity of dielectric material or Dielectric constant (κ) and ε_0 is the permittivity of free space or air (8.85 x 10^{-12} F/m).

For a parallel plate capacitor filled with air and another dielectric material, the capacitance is given by (Craig 1995),

$$C = \varepsilon_r . \varepsilon_0 . \frac{A}{d} \text{ or } C = \kappa . \varepsilon_0 . \frac{A}{d} \qquad \text{Equation 37}$$

Charging of a Capacitor

When a capacitor is connected to a DC voltage source (Figure 102) the free electrons are conducted to one of the plates. As these electrons accumulate on that plate, the opposite plate becomes positively charged by electrostatic induction. The presence of negative charge on one plate repels negative charges on the neighbouring plate and thus the opposite plate receives an equal and opposite positive charge or holes. These negative charges or electrons which are repelled from the negatively charged plate appear to flow through the dielectric. And so, two things occur at once when the capacitor is connected. First, a large quantity of current flows in the circuit. The induced charge on the positive plate caused by repulsion of electrons away from the plate gives an appearance of current flow through the insulator. And second, as electrons accumulate on one plate and a positive charge is induced on the other, a difference in potential (voltage) is developed on the capacitor on the plate. The capacitor voltage increases as positive and negative charges continue to accumulate. As the capacitor charges, the rate of charge steadily decreases to zero, at which point the capacitor is fully charged. The charge current ceases because the capacitor voltage matches the source voltage. The capacitor acts as a voltage source itself, countering the applied voltage (Hazen 1990).

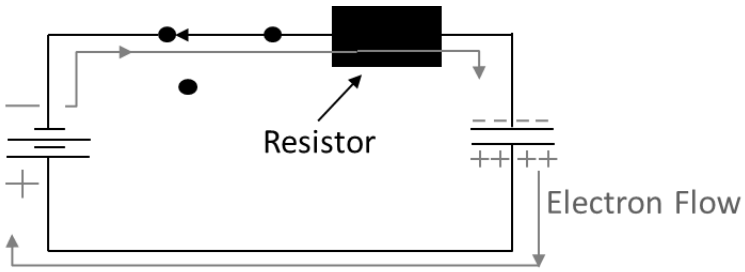

Figure 102: Charging of a Capacitor connected to a DC Voltage Source

The voltage across the capacitor does not jump instantly to a maximum value (equal to the applied voltage. This is so because when a capacitor is fully charged, there is a large quantity of electrons on one plate. Those electrons first arrive at the plate through circuit resistance and we know that resistance limits the amount of current flow through the circuit. Thus, the total capacitor charge arrives a little at a time over a period. And secondly as the charge increases on the plate the capacitor voltage increases in polarity that opposes the applied source voltage. As a result, the charge current is delivered at an ever-decreasing rate through any circuit resistance. And we know that the amount of current at any instant of time is the rate of charge at that instant of time. So, by the time the capacitor is fully charged the charge current will have dropped to zero. Therefore, current only flows during the time the capacitor is charging or discharging (Hazen 1990) .

The charging current (I) is determined by voltage across the resistor (Vs-Vc)

$$I = \frac{(V_S - V_C)}{R} \qquad \text{Equation 38}$$

The value of Vc follows the course; $V_C = 0 \rightarrow V_S$.

The rate of charging of the capacitor is measured in terms of time constant or Tau (τ) (Hewis 2017):

$$Time\ Constant\ (\tau) = R\ \times\ C \qquad \text{Equation 39}$$

where τ is time constant in seconds, R is resistance in ohm and C is capacitance in Farads. A large time constant reflects slow charging of the capacitor.

The time constant is the time taken for the charging (or discharging) current (I) to fall to 1/e of its initial value (I_0).

$$Time\ Constant\ (\tau) = I_0 e^{-1} \qquad \text{Equation 40}$$

where 'e' is the base of natural logarithms, e = 2.71828.

After each time constant, the current falls by 1/e (about 1/3). After 5 time constants (5RC) the current has fallen to less than 1% of its initial value (Hewis 2017) (Figure 103).

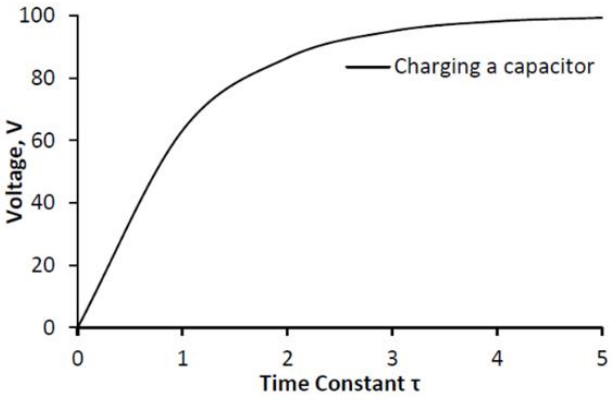

Figure 103: Static time constant for charging of a capacitor (Hewis 2017)

When an alternating voltage is applied to the plates of the capacitor, the capacitor is forced to follow repeated cycles of charge and discharge. As the AC voltage increases, decreases and changes polarity, the quantity of charge on the capacitor's plates also increases, decreases and changes polarity. Therefore, the alternating capacitor current at any instant in time depends on the rate of change of charge at that instant in time. It is the changing difference in potential that causes a change in the rate of charge which is what current is at that instant in time (Hazen 1990).

Total Capacitance in Series and Parallel

For capacitors in series, the inverse of individual capacitance values are added to obtain the total capacitance of the circuit,

$$\frac{1}{C_{total}} = \frac{1}{C_1} + \frac{1}{C_2}$$ Equation 41

For capacitors in parallel, the total capacitance is the sum of individual capacitances added together,

$$C_{total} = C_1 + C_2$$ Equation 42

Equivalent Circuit Models

Equivalent circuit models help one to derive a more direct understanding of the relationships between the impedance response and the physicality of the system being studied (Smith and Polygalov 2019). A model can comprise different circuit elements such as resistors, capacitors, sometimes inductances and possibly various distributed elements. In such a circuit, a resistor represents a conductive path and accounts for the bulk conductivity of the material. Capacitors and inductors generally account for the space charge polarisation at the electrode (Macdonald, J.R., Johnson,W.B. 2005).

Resistor and Capacitor

It is important to recognise that most real objects have a combination of characteristics, for example, resistance and capacitance (Smith and Polygalov 2019). When such objects are placed in an alternating electric field, they behave as a pure resistor at low frequencies and become increasingly capacitive as the frequency of the applied field increases. This is due to the fact that the impedance of a resistor is independent of the frequency (Figure 104a); whereas the impedance of a capacitor or capacitive reactance is frequency dependent. In terms of the impedance magnitude and the phase angle, an impedance spectrum of a capacitor, as shown in Figure 104(b) displays a characteristic negative slope of -1 in the plot of log impedance magnitude v/s log frequency. This is because the impedance of a capacitor is an inverse function of the capacitor and the applied frequency as previously expressed in Equation 28 for capacitive reactance. In other words, a capacitor has enough time to get charged at low frequency. This build-up of charge results in a very high impedance to the flow of current through the circuit.

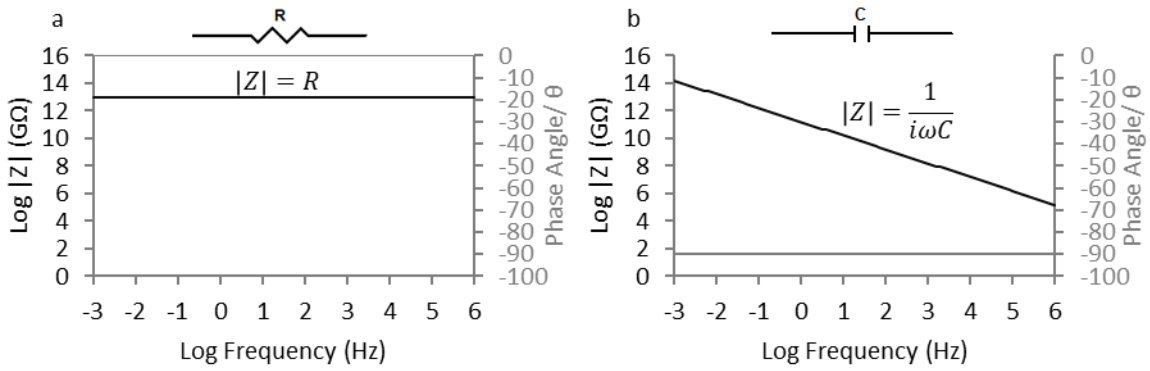

Figure 104: Bode Plots (impedance magnitude (|Z|) and phase angle (θ) for the impedances of a resistor (a) and a capacitor (b)

Resistor and Capacitor in Series and Parallel

The impedance of a composite object that has some resistance and capacitance would then depend on whether these elements are in series or in parallel and how the frequency of the applied field defines the relative magnitude of the impedance of the capacitance and the resistance (Smith and Polygalov 2019).

Series R=C Circuit

In Figure 105(a) to (d) the bode plot of the impedance spectrum (where $Z'\text{and } -Z^{"}$ are plotted against the log frequency) and the bode plot of the log of impedance magnitude ($|Z|$) and the phase angle (θ) have been plotted against the log frequency. At low frequency, the capacitor dominates the spectrum because the time taken by the charge build up on the capacitor plates is less than the time constant of the capacitor (Smith and Polygalov 2019). In other words, the capacitor has sufficient time to get charged which results in a very high impedance (in the imaginary part) to the flow of current through the circuit. Effectively, the capacitor controls the flow of current through the circuit at low frequency. However, as the frequency is increased, the time taken by the charge build up approaches the time constant which increasingly reduces the ability of the capacitor to hold the charge. The frequency at which the capacitor can no longer become charged (or when the resistor begins to dominate) is the point where the capacitance in the imaginary part reaches a peak in its profile as in

Figure 105(b) or when the phase angle is 45° as in Figure 105(c). It follows that at high frequency, the resistor dominates the circuit as the current now flows through the resistor (rather than the capacitor). Further, on a Nyquist plot (where $-Z^{"}$ is plotted against Z'), a straight vertical line is observed (Figure 105e). On the other hand, on a Cole Cole plot ($-C^{"}$ is plotted against C'), as in Figure 105f a semicircle is observed with most of the contribution arising from the low frequency response.

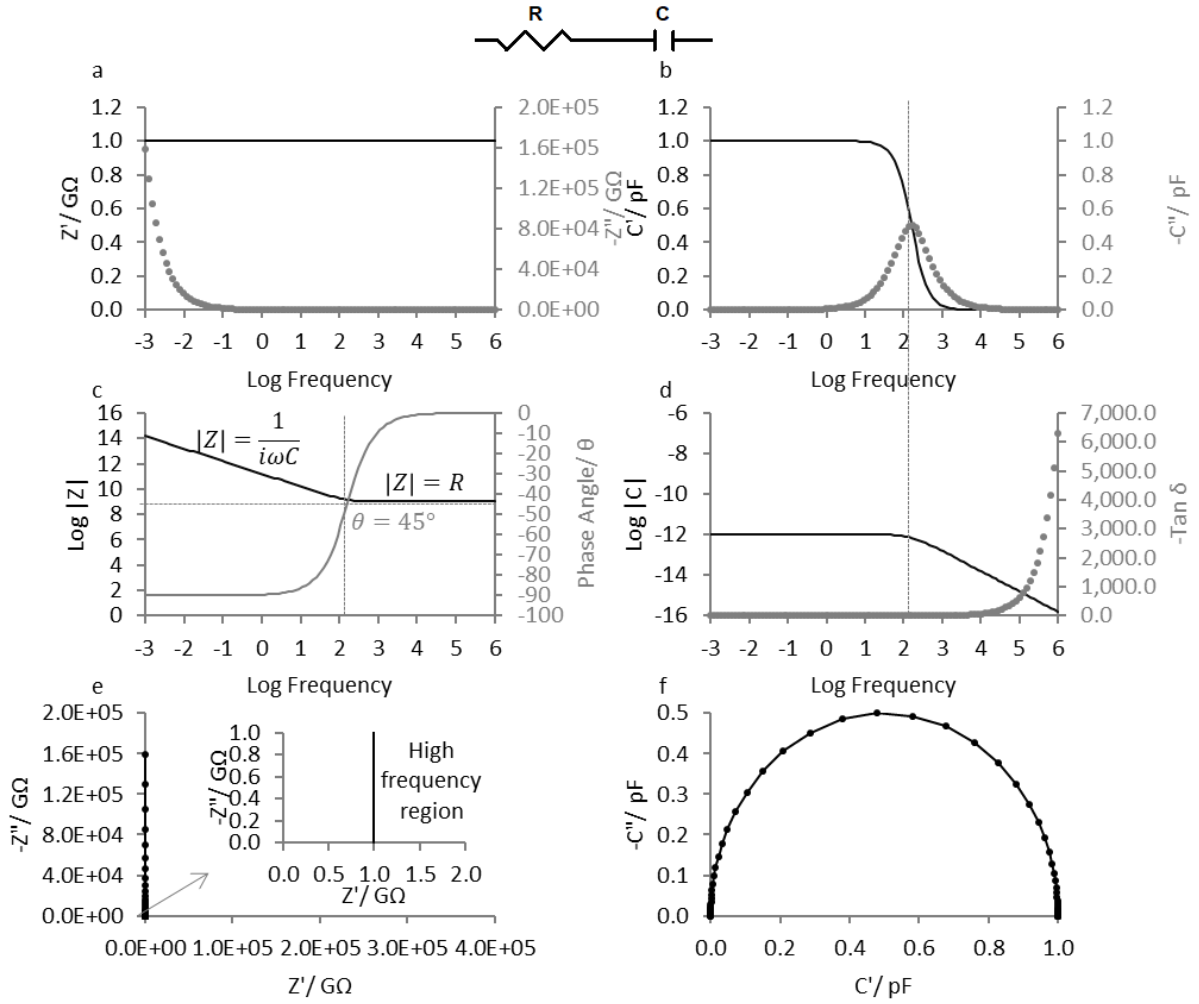

Figure 105: Resistor in series with a capacitor (a) Bode plot of the impedance spectrum v/s log frequency; (b) Bode plot of the capacitance spectrum v/s log frequency; (c) Bode plot of the impedance magnitude and phase angle (θ) v/s log frequency; (d) Bode plot of the capacitance magnitude and the dielectric loss tangent (Tan δ) v/s log frequency; (e) Nyquist plot of the impedance spectrum; (f) Cole -Cole plot of the capacitance spectrum

Parallel R=C Circuit

Different representations of a classical RC circuit are shown in Figure 106. The main plots to identify a typical response from a resistor in parallel with a capacitor are the Nyquist plot of the impedance spectrum (Figure 106a) and the Bode plot of the impedance magnitude and the phase angle against log frequency (Figure 106c). On the Bode plot, at low frequency, the resistor dominates the spectrum because the impedance of the capacitor is so high that all the current flows through the resistor. At high frequency, the capacitor dominates the spectrum because the impedance of the capacitor is now lower than then the impedance of the resistor such that all the current now flows through the capacitor**. T**he Nyquist plot shows a semicircle with the center on the x-axis.

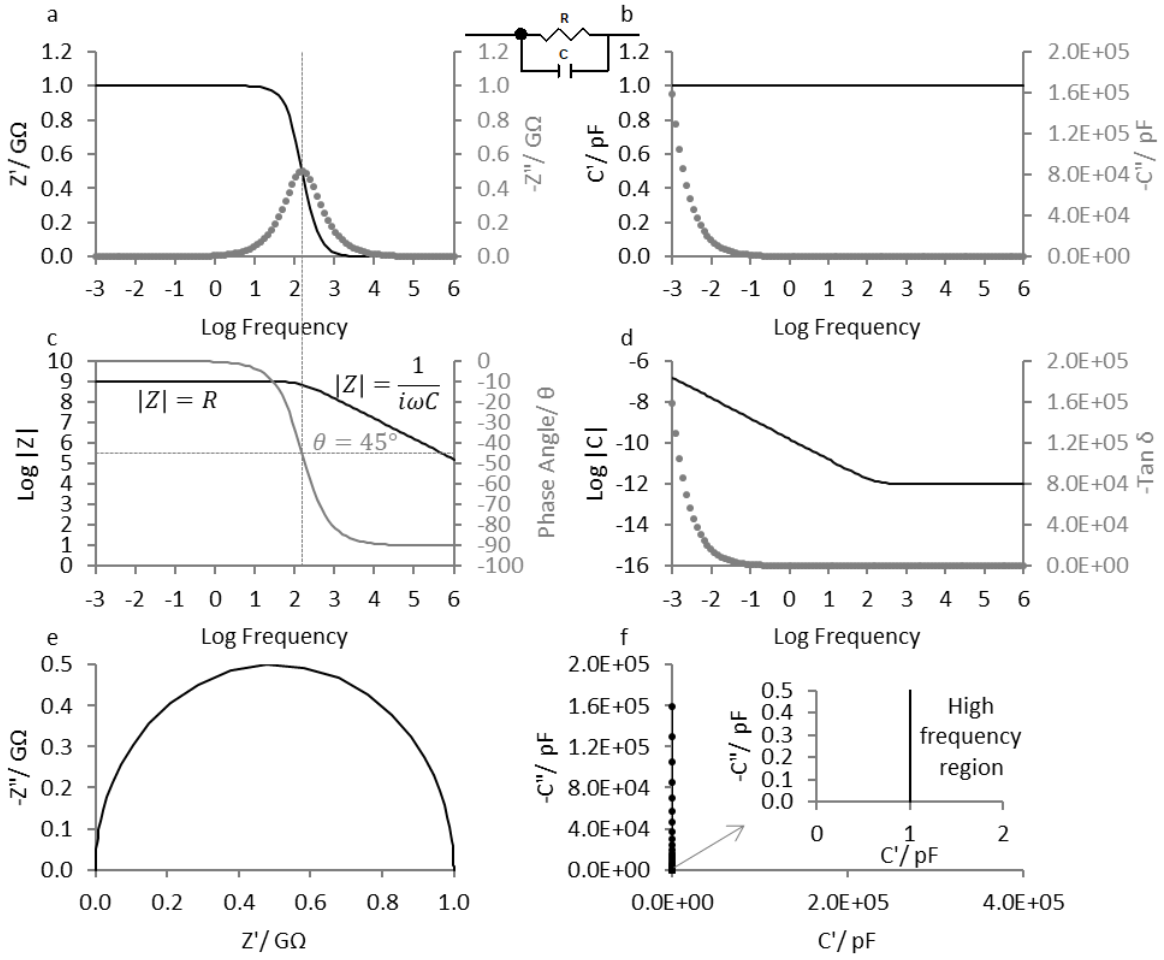

Figure 106: Resistor in parallel with a capacitor (a) Bode plot of the impedance spectrum v/s log frequency; (b) Bode plot of the capacitance spectrum v/s log frequency; (c) Bode plot of the impedance magnitude and phase angle (θ) v/s log frequency; (d) Bode plot of the capacitance magnitude and the dielectric loss tangent (Tan δ) v/s log frequency; (e) Nyquist plot of the impedance spectrum; (f) Cole -Cole plot of the capacitance spectrum.

Constant Phase Element (CPE)

A constant phase element (CPE) is a type of distributed equivalent circuit element that is essentially used to model those semicircles that are depressed, with their centres lying below Z'-axis on the Nyquist plot (Macdonald, J.R., Johnson,W.B. 2005). A depressed semicircle arises because some property of the system being studied is non-homogeneous or the value of the property of the material is dispersed owing to a rough or porous electrode-object interface (Orazem and Tribollet 2008). In the case of glass, a CPE can model proton percolation (space charge polarisation) within the porous hydrated silica. The extent of migration (i.e. number of charges and the length of percolation path) is dependent on temperature and the frequency of the applied field (Smith and Polygalov 2019). For example, when a given time constant associated with an interface or a bulk process is thermally activated with a distribution of activation energies, the material then passes from a simple resistor and a capacitor in series or parallel to a system with distributed material properties that can be represented by a constant phase element. Such a system exhibits a more complicated frequency response compared to a simple "undistributed" RC time constant process (Orazem and Tribollet 2008).

The admittance (Υ) and hence impedance (Z) of a CPE is given by

$$\Upsilon_{CPE} = \frac{1}{\Upsilon_{CPE}} = Q_o(i\omega)^p \qquad \text{Equation 43}$$

where Q_o has the numerical value of admittance at the angular frequency of $\omega = 1$ rad s^{-1}, and units of $F.s^{(p-1)}$ or $S.s^p$ (where F is farad, S is Siemens and s is second) (Macdonald, J.R., Johnson,W.B. 2005). The parameter p defines the impedance phase angle (ϑ) according to the expression $\vartheta = -(90 \times p)$ degrees. If the object behaves more like a capacitor then p tends to 1, (for a pure capacitor, $p = 1$ hence $\frac{1}{\mathrm{Z}_C} = \Upsilon_C = Q_o(i\omega)^1 = i\omega C$ and $\theta = -90°$), whereas if the object behaves more like a resistor then p tends to 0 (for a pure resistor, $p = 0$ hence $\frac{1}{\mathrm{Z}_R} = \Upsilon_R = Q_o(i\omega)^0 = \frac{1}{R}$ and $\theta = 0°$).

These values can be represented on both the Nyqusit plot of impedance and the Cole-Cole plot of capacitance as shown in Figure 107. On the Nyquist plot (Figure 107a) the negative of the imaginary impedance $-Z^{"}$ toward the low frequency is directly proportional to the increase in the impedance in the real part, Z' for a given value of p . In other words, the phase angle between the impedance phasor and the x-axis for the real part impedance is invariant with frequency, hence the name constant phase element (Macdonald, J.R., Johnson,W.B. 2005). The phase angle of the impedance phasor can be determined from the slope of the impedance phasor according to

$$\theta = \alpha \tan\ (slope) \qquad \text{Equation 44}$$

On the Cole-Cole plot (Figure 107b) the angle (α) between the capacitance scalar and the axis of the real part capacitance (C') serves as an alternative for determining the impedance phase angle (where $\alpha = 90 - \theta$).

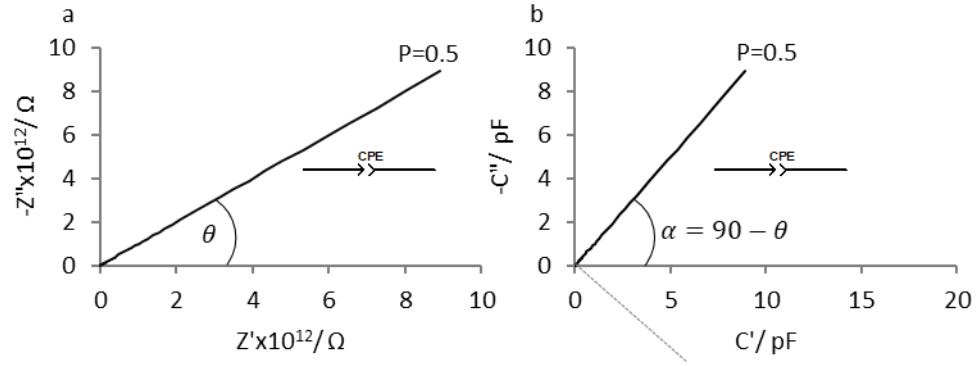

Figure 107: Representation of a CPE (1 pF) with p value of 0.5: (a) Nyquist plot of imaginary part impedance v/s real part impedance with the phase angle θ between the impedance phasor and the x-axis of the real part impedance; (b) Cole-Cole plot of imaginary part capacitance v/s real part capacitance with the angle α between the capacitance scalar and the x-axis of the real part capacitance.

In Figure 108, a simulation of CPE (1 pF) with p value from 0 to 1 over a frequency range 0.001 Hz-1MHz is presented. One can see when p is equal to 1 (i.e. pure capacitor) on the Nyquist plot of $-Z^{"}$v/s Z', the impedance phasor lies on the Y-axis. And as the CPE behaves more and more like a resistor, the impedance phase angle with the x-axis decreases such that the contribution from the real part impedance increases until p becomes equal to 0 (i.e. pure resistor). In contrast, the behavior of the CPE element is opposite, i.e. the CPE is a pure resistor when the capacitance scalar is perpendicular to the x-axis of the real part capacitance on the Cole-Cole plot. Further, as all the CPEs have been simulated over the same frequency range, one can see how each CPE represents a "finite" path length for the mobile species to traverse within the microstructure of the material being investigated.

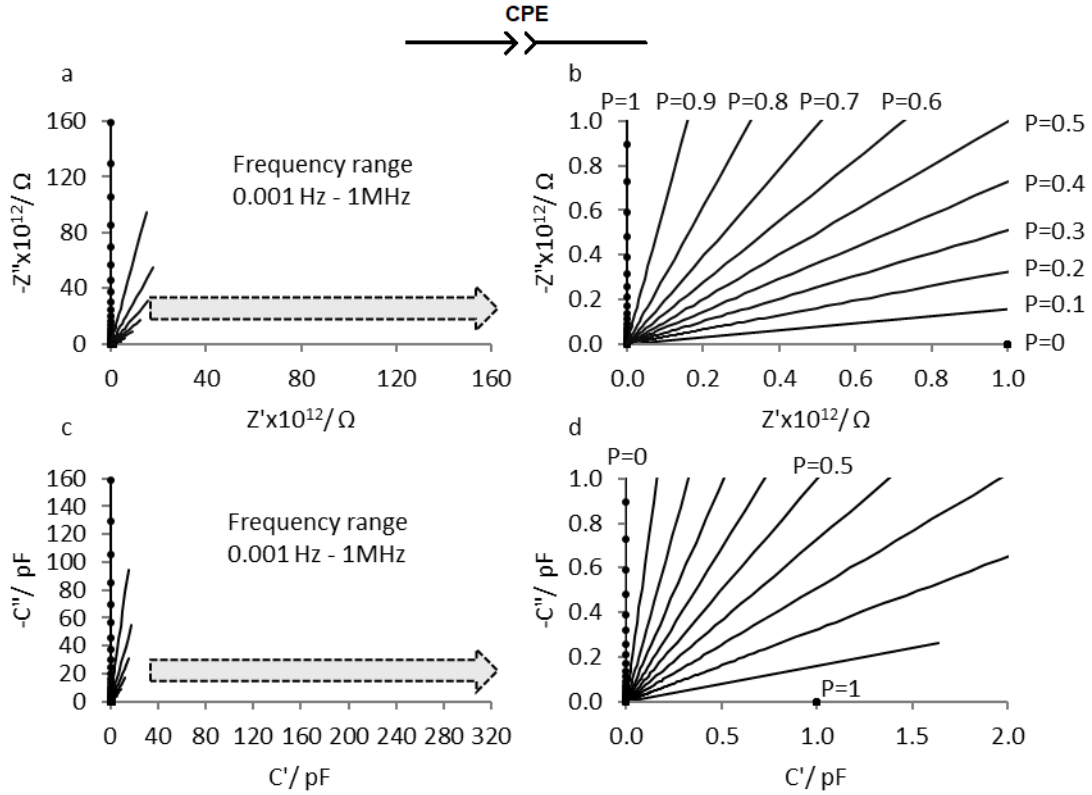

Figure 108: Simulation of various CPEs (1 pF) with p values ranging from 0 to 1, i.e. expressing a purely resistive behavior to a purely capacitive behaviour over a frequency range 0.001 Hz- 1 MHz: (a) Nyquist plot of imaginary part impedance v/s real part impedance; (b) The scale of the Nyquist Plot has been enlarged to show the impedance phasor making different angles with the x-axis depending on the p value; (c) Cole-Cole plot of imaginary part capacitance v/s real part capacitance; (d) The scale of the Cole-Cole plot has been enlarged to show the different slopes of the capacitance scalar can be simulated depending on the p value.

CPE in Parallel with a Capacitor

Having a CPE in parallel with a capacitor shift the value of the instantaneous capacitance over a distance corresponding to the magnitude of the capacitor as shown in Figure 109.

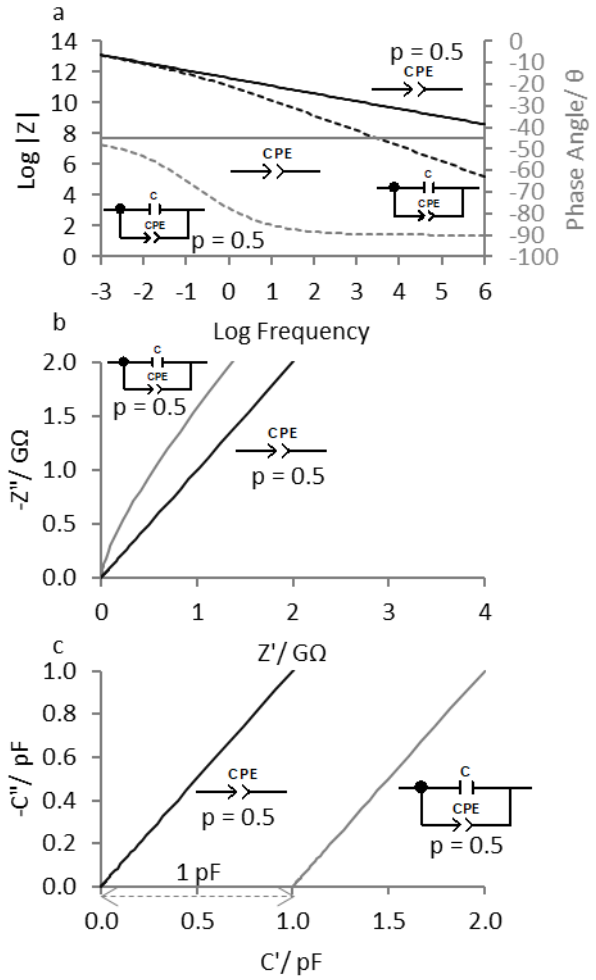

Figure 109: Simulation of a CPE (1 pF, p= 0.5) alone v/s a capacitor (1 pF) in parallel with a CPE (1 pF, p=0.5) over a frequency range 0.001 Hz- 1MHz: (a) Bode plot of the impedance magnitude v/s log frequency (black solid line represents CPE and black dashed line represents the parallel combination) and phase angle (Grey solid line represents CPE alone and grey dashed line represents the parallel combination); (b) Nyquist plot of imaginary part impedance v/s real part impedance (Black line represents CPE alone and grey represents the parallel combination); (c) Cole-Cole plot of imaginary part capacitance v/s real part capacitance (Black line represents CPE alone and grey line represents the parallel combination).

CPE in Parallel with a Resistor

The difference response can be seen when a CPE is in parallel with a resistor as shown in Figure 110 and Figure 111.

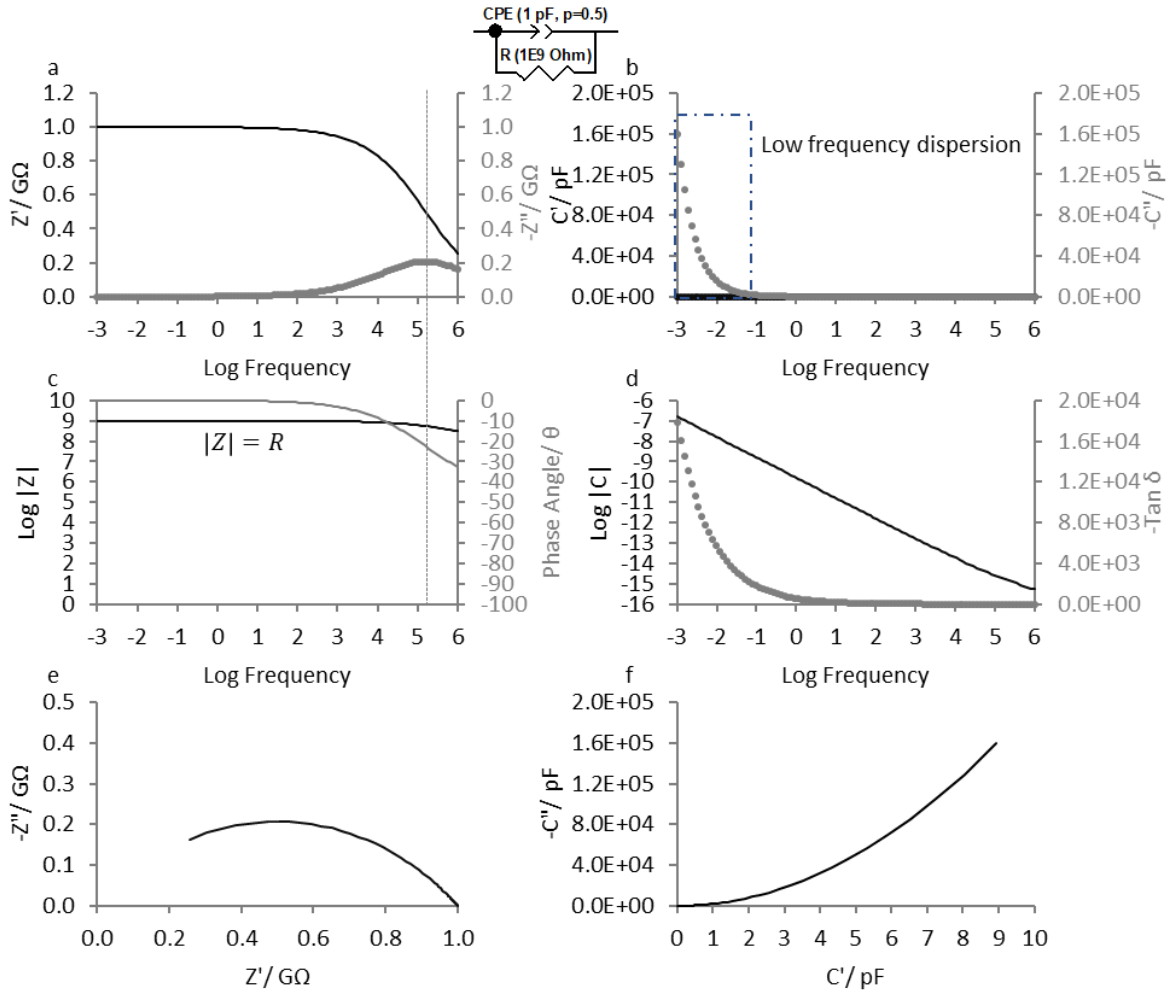

Figure 110: Simulation of a CPE (1 pF, p= 0.5) in parallel with a resistor (1 GΩ) over a frequency range 0.001 Hz-1MHz: (a) Bode plot of real and imaginary part impedance v/s log frequency with a characteristic peak in the imaginary part at a frequency of around 100 kHz; (b) Bode plot of real and imaginary capacitance v/s log frequency with a characteristic low frequency dispersion in the imaginary part; (c) Bode plot of impedance magnitude and phase angle v/s log frequency; (d) Bode plot of capacitance magnitude and dielectric loss tangent v/s frequency; (e) Nyquist plot of imaginary part impedance v/s real part impedance; (f) Cole-Cole plot of imaginary capacitance v/s real part capacitance showing a curvature which is a net result of having a resistor in parallel to a CPE which equally resistive and capacitive.

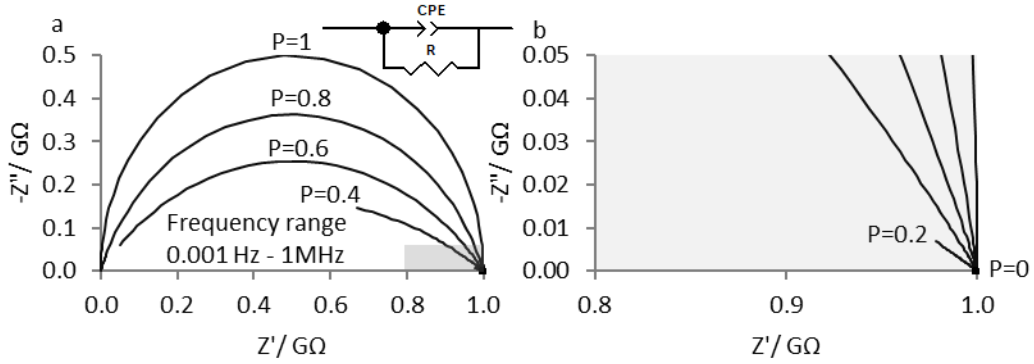

Figure 111: Simulation of a CPE (1 pF) at different p values in parallel with a resistor (1 GΩ) over the frequency range 0.001 Hz- 1 MHz: (a) Nyquist plot of imaginary part impedance v/s real part impedance showing an increase in the arc length of the semicircle as p value approaches 1 (i.e. pure capacitor); (b) Nyquist plot a is enlarged to highlight the response when p value is equal to 0 (pure resistor) and 2 (some capacitance with largely a resistive response).

When two CPEs in parallel, it can result in a curved type of response. For example, when a CPE with p value equal to 0.5 (typically common among with diffusion processes in porous materials) is in parallel with a largely capacitive CPE (p value = 0.9), the observed spectrum is shown in Figure 112.

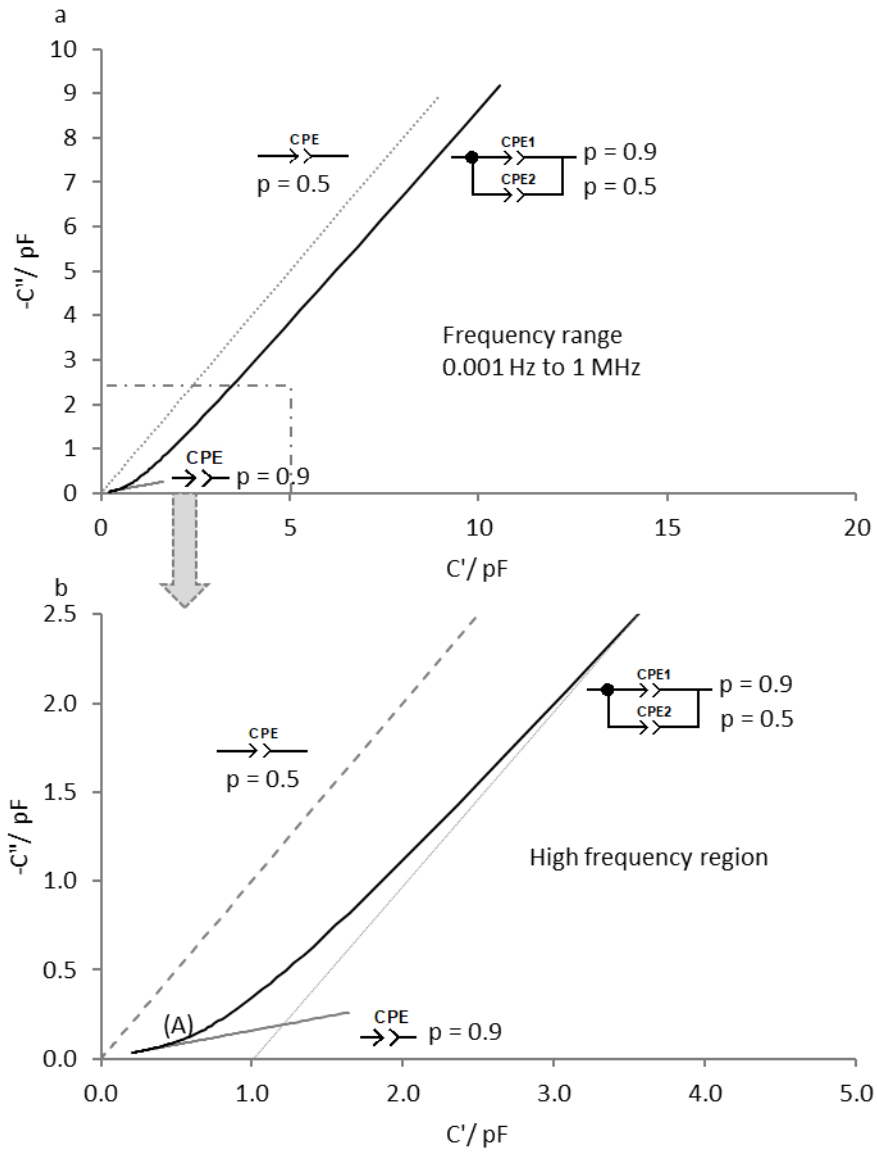

Figure 112: Simulation of 2 different CPEs separately v/s 2 CPEs in parallel over the frequency range 0.001 Hz-1MHz: (a) Cole-Cole plot of imaginary part capacitance v/s real part capacitance wherein a CPE (1 pF) with p value equal to 0.5 (grey dashed line), a CPE (1 pF) with p value 0.9 (solid grey line) are shown seprately to compare them with a parallel combination of the two CPEs of the same values (solid black line); (b) The high frequency region of the Cole-Cole plot is shown to highlight the characteristics of the observed response. Inclusion of a more resistive CPE2 (p =0.5) in parallel with a largely capacitive CPE1 (p =0.9) results in curved profile after point A. As one goes towards the low frequencies from point A, one can see how CPE1 increasingly contributes to the overall dielectric response. Effectively, the behaviour of the parallel combination lies in between the largely resistive CPE1 and the largely capacitive CPE2.

CPE within a Parallel RC Circuit

Similarities and Dissimilarities in the dielectric response among RC, R=CPE=C and R=CPE=CPE=C are shown in Figure 113.

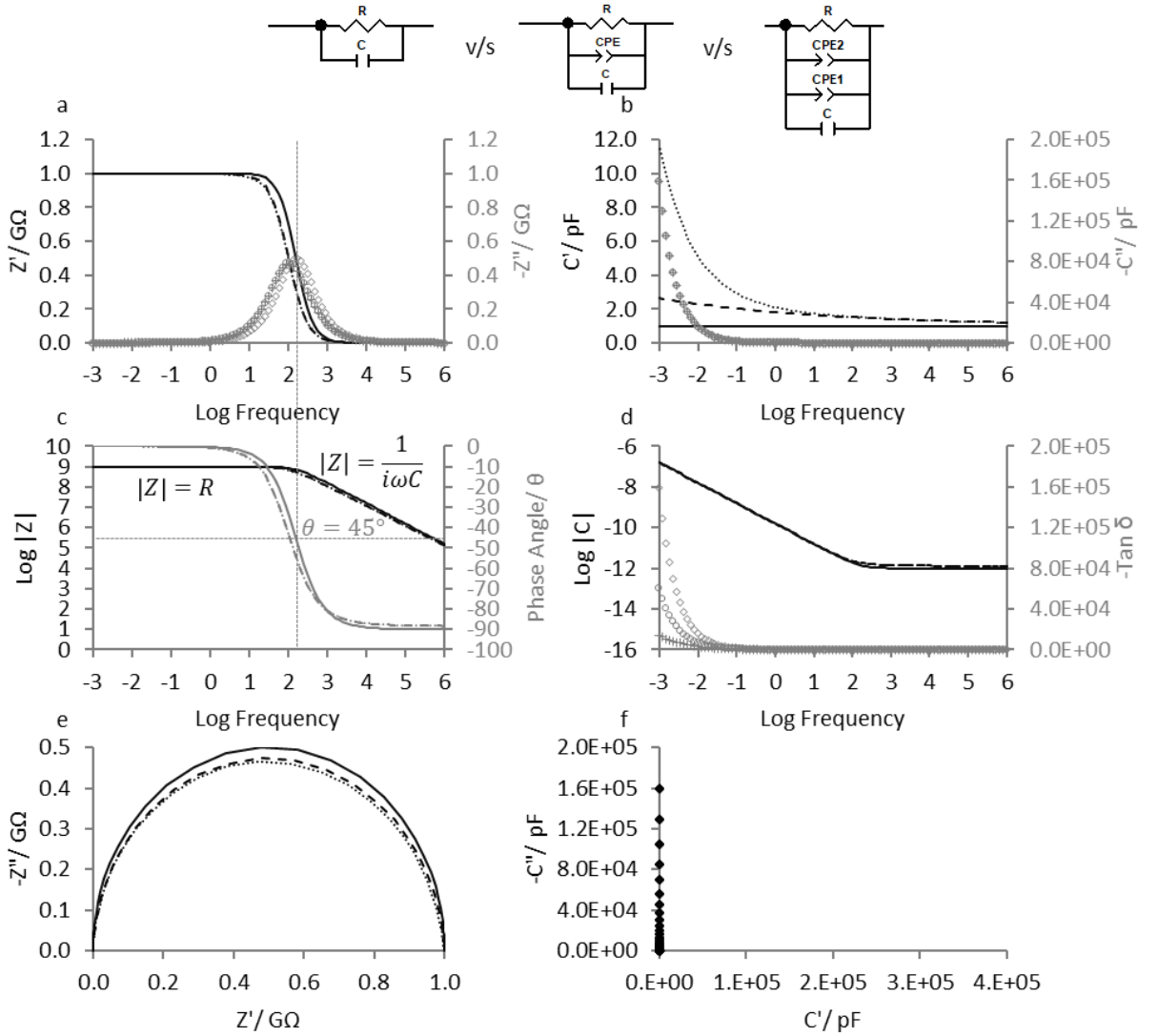

Figure 113: Simulation of a parallel RC circuit v/s a parallel RC circuit with a largely capacitive CPE v/s a parallel RC circuit with two CPEs of different behaviour over the frequency range 0.001 Hz- 1 MHz; simulated data in black solid line and grey diamonds represents the R=C circuit, in black dashed line and grey circles represents the R=CPE1=C circuit, and in black dotted line and grey plusses represents the R=CPE2=CPE1=C circuit, where R is equal to 1 GΩ, CPE2 has a value of 1 pF with p= 0.5, CPE1 has a value of 1 pF with p= 0.9 and C is equal to 1 pF: (a) Bode plot of real and imaginary part impedance v/s log frequency; (b) Bode plot of real and imaginary capacitance v/s log frequency with a larger extent of low frequency dispersion and dc conductivity behaviours observed for the model containing two CPEs owing to a more resistive CPE2; (c) Bode plot of impedance magnitude and phase angle v/s log frequency; (d) Bode plot of capacitance magnitude and dielectric loss tangent v/s frequency; (e) Nyquist plot of imaginary part impedance v/s real part impedance; (f) Cole-Cole plot of imaginary capacitance v/s real part capacitance.

10.3 Appendix III: Studies Involving Copper Electrode Systems Measured with the DMU TVIS System

10.3.1 TVIS Measurement of Cropped Vial as a Function of Temperature

Aim: To measure the dielectric properties of the glass vial

Objective: To develop a model for the Adelphi (VC010-20C) glass wall using the DMU five-channel TVIS system and build it into the model for the TVIS vial containing a liquid or a frozen solid

Material and Methods

- **Equipment and Sample Set-up**

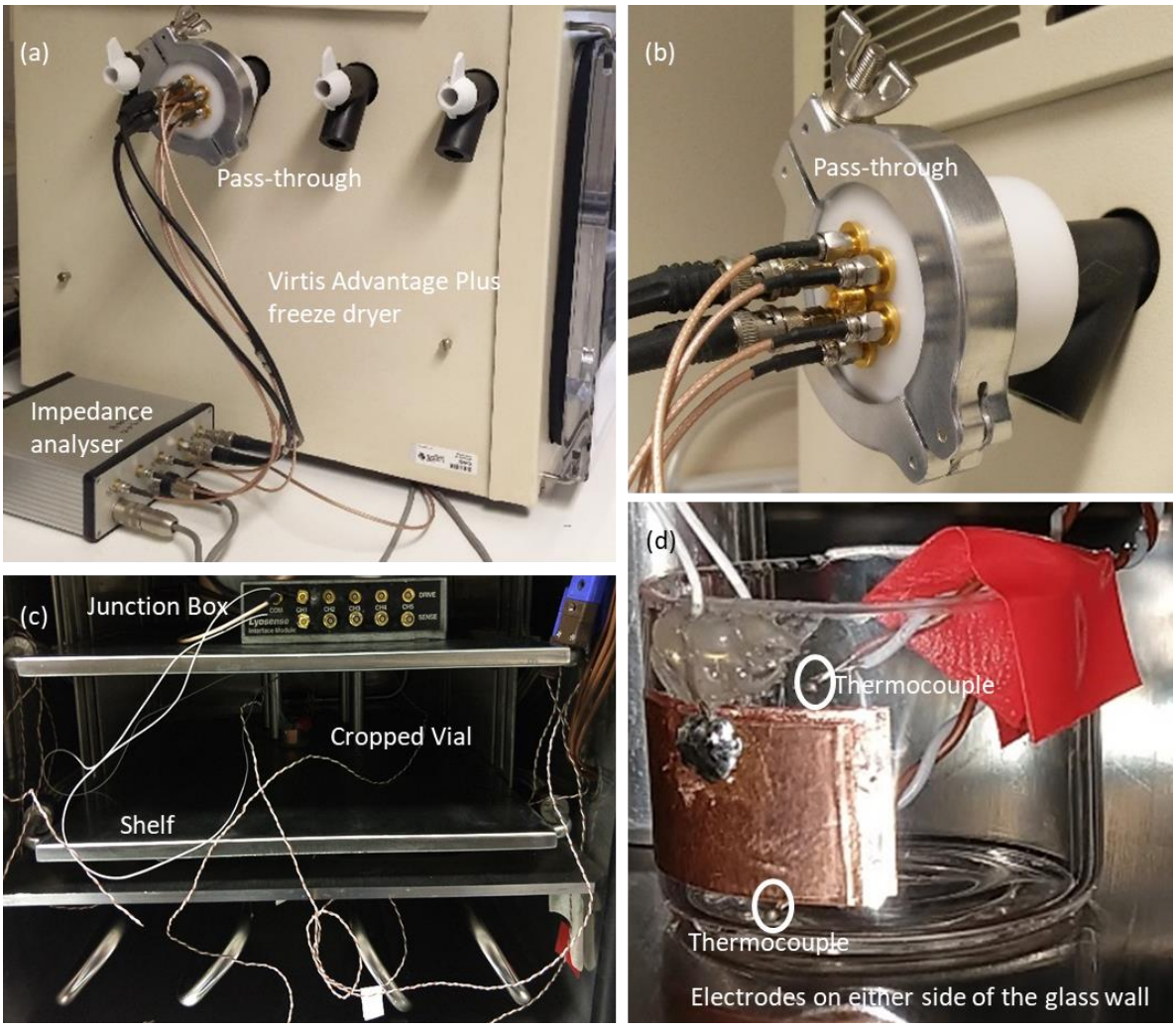

Figure 114: Equipment and sample set up for the TVIS measurement of an empty cropped Adelphi (VC010-20C) vial with copper electrodes (19 mm by 10 mm) attached on either side of the glass wall: (a) Virtis Advantage Plus freeze dryer equipped with DMU five-channel TVIS system; (b) modified passthrough; (c) cropped vial placed in the centre of the bottom stain-less steel shelf; (d) Positions where the two thermocouples were placed in contact with the glass wall.

- **Temperature protocol**

The shelf temperature was equilibrated to 25 °C and then heated to 50 °C at 1 °C/min and then held at 50 °C for 60 min before cooling to -45 °C at 0.5 °C/min. Temperature was recorded every 2 min.

- **TVIS Parameters**

Table 29: TVIS Parameters for the measurement of the cropped Adelphi (VC010-20C glass vial

Frequency range	**10 Hz to 1 MHz**
AC Voltage	0.2 to 8 V
Measurement time or Scan Interval	1 spectrum every 4 min
Electrode Design	No Guard Electrode_3mm above the vial base
Electrode Dimensions	Approx. 10 mm x 19 mm (3 mm from base to top)
TVIS System	LyoDEA

- **Method for Fitting C=CPE=DE Model**

A spectrum for the empty glass vial was obtained at room temperature. A model comprising C in parallel with a CPE and Distributed Element (DE) was developed as follows:

Step 1: Inclusion of a capacitor

A capacitor was added, and its value was estimated from the low frequency intercept (6.531×10^{-12} pF) on a Cole-Cole plot using the Circle line fit option in Zview™ . The model was then simulated, and the result is shown below:

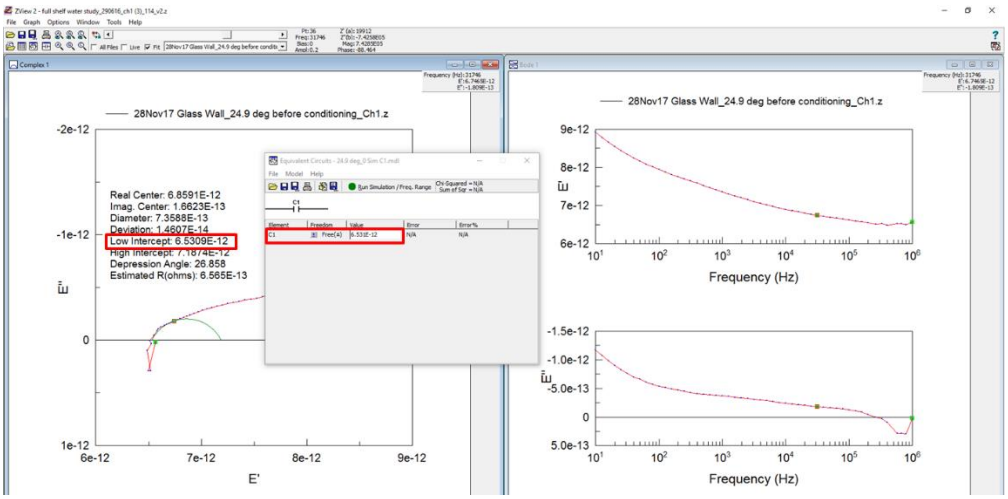

Step 2: Inclusion of a distributed element

A distributed element (DE) was added. A DE has three parameters, DE-R, DE-T, DE-P, DE-U.

DE-R corresponds to the height of the relaxation process. In other words, it is the difference between the magnitude of the capacitance at the peak frequency (i.e. 7.931 x 10^{-12} F at 100 Hz in this case) and the magnitude of the low frequency capacitance (i.e. 6.531 x 10^{-12} F) that was determined in Step 2. The resulting value was 1.4 x 10 -12 F which was inserted in the box designated for DE-R and was left free.

DE-T corresponds to the relaxation time which expressed as $\tau = 1/2\pi f$, where f is the peak frequency. In this case the peak frequency was equal to 1996 Hz. Therefore, the value for DE-T was equal to 8 x 10^{5} seconds which inserted in the box and was left free.

DE-P is referred to as the peak broadening parameter, where a p value equal to 1 is corresponds to a Debye process, i.e. the dielectric relaxation is considered to have a single time constant. In this case DE-P was fixed at 1. DE-U corresponds to resistance. A value of 0.6 was used as a starting value for DE-U.

The model was then simulated, and result is shown below:

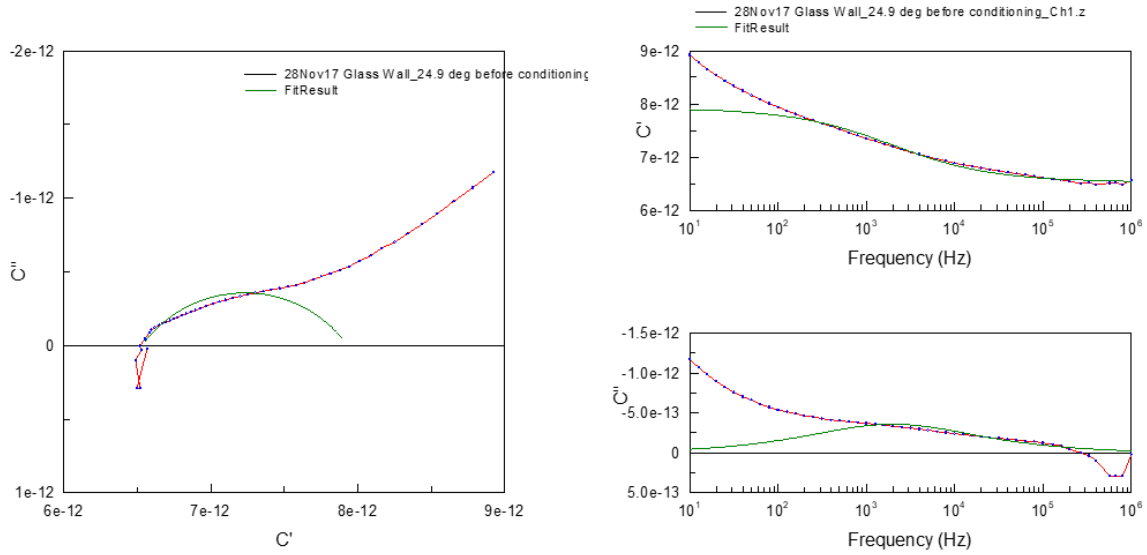

Step 3: Inclusion a Constant Phase Element (CPE)

A CPE has two parameters, CPE-T and CPE-P. CPE-T corresponds to the magnitude of the CPE and CPE-P corresponds to the phase angle with respect to the C′-axis on a Cole-Cole plot of imaginary part capacitance v/s real part capacitance. For CPE-T, the value is read off for the capacitance at the lowest frequency of the measured frequency range. In this case that value was at 10 Hz, i.e. 8.932 x 10^{-12} F which inserted into the box designated for CPE-T and was left free. The starting value for CPE-P was 0.5 which was left free. Frequently, a CPE behaviour of 0.5 relates to a diffusion process within a porous materials (Ben Amor, et al. 2014; Orazem and Tribollet 2017). Since glass is a porous structure, a CPE-P of 0.5 was used as a starting value. A simulation was then performed and resulting fit is shown below:

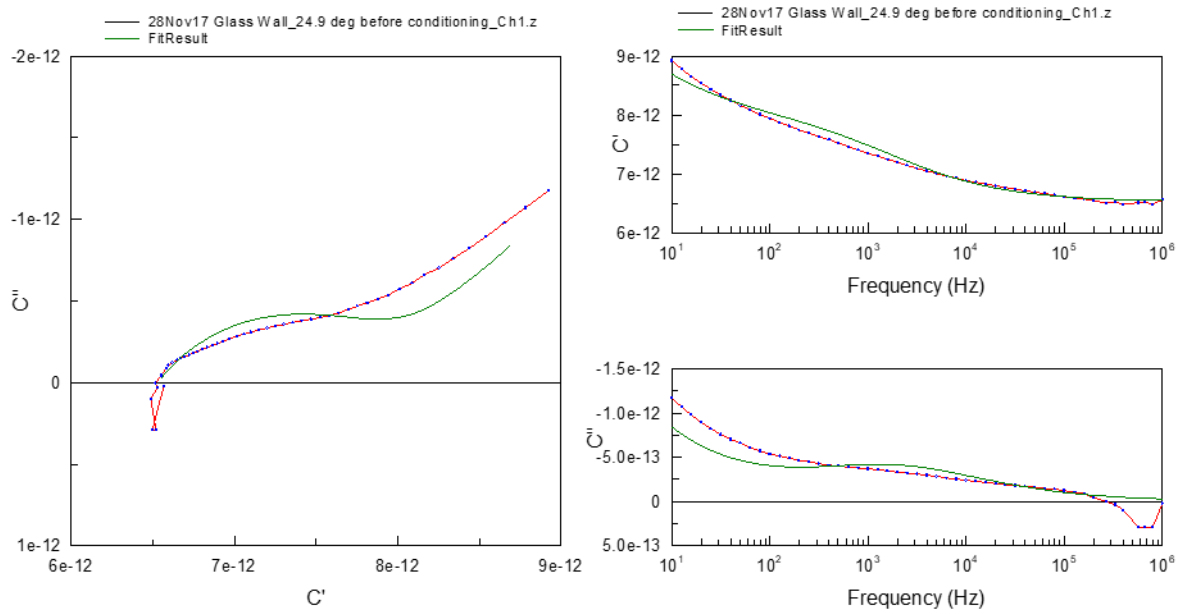

Step 4: Fitting of the C=CPE=DE Model

The last step was fit the model after fixing the value for the capacitor and floating all the other parameters. The fit is shown below:

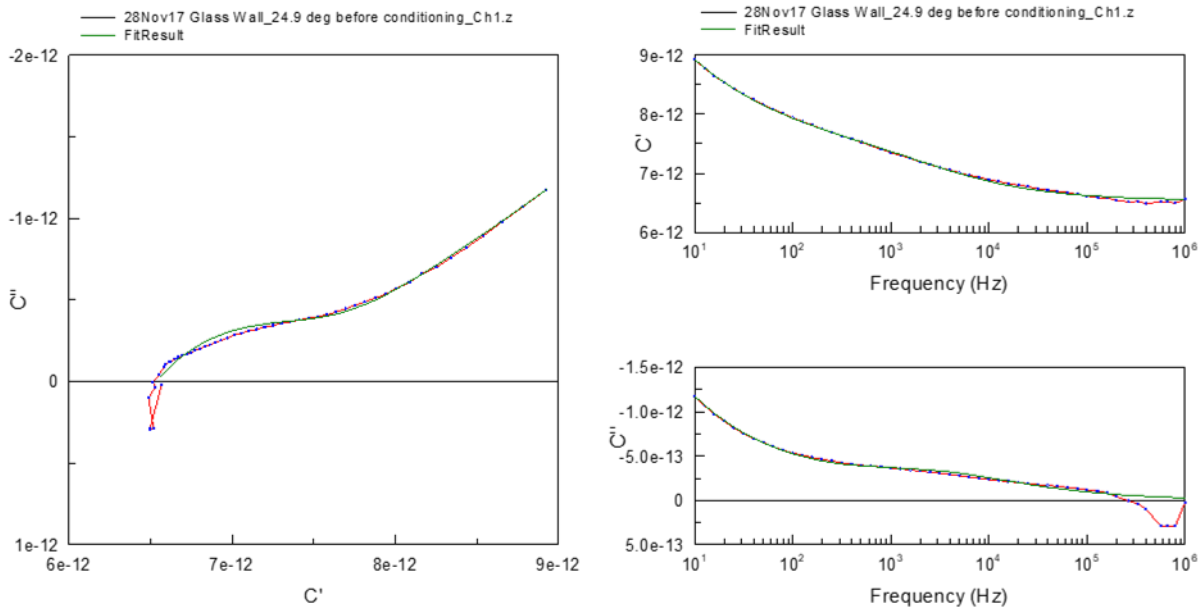

After removing the high frequency noise, the final fit result is shown below:

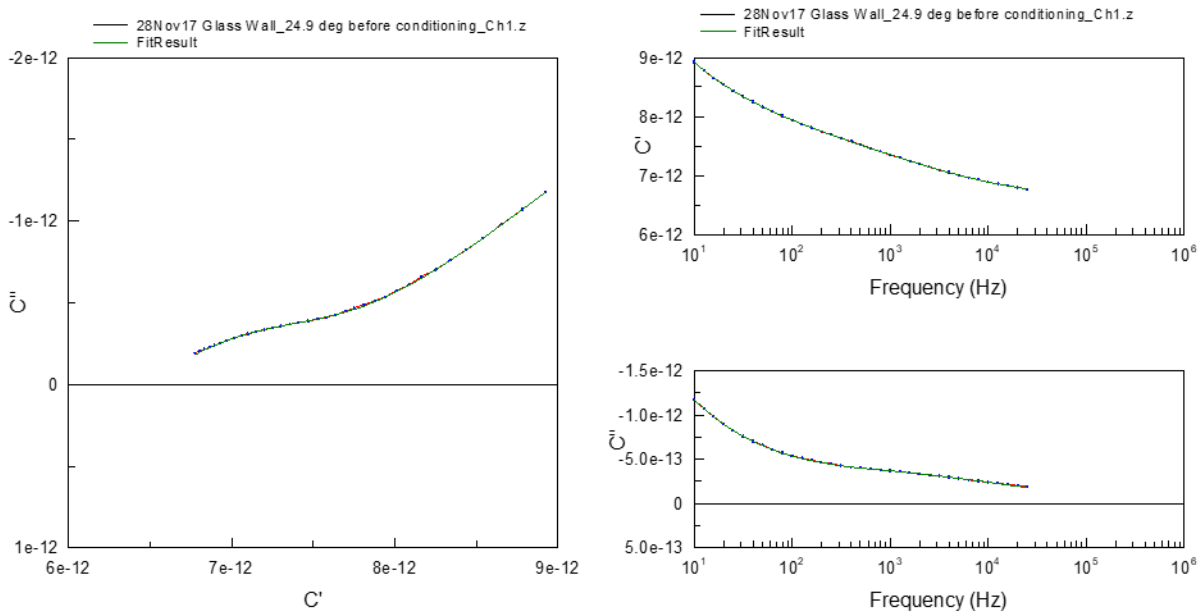

Results and Discussion

Figure 115 shows the time-line of the shelf temperature and the average temperature recorded by the 2 thermocouples (Figure 115a). Also shown are the Bode plots of real part capacitance (Figure 115b) and the imaginary part capacitance (Figure 115c) plotted against log frequency. Note that most of the spectra at the high frequency end (between 100 kHz and 1 MHz) were noisy and will therefore, it might not be possible to determine the instantaneous glass wall capacitance. Other observations include the low frequency dispersion in the spectra as the temperature increases. It would be interesting to find how this manifests below 10 Hz. Moreover, a second process which looked a small Cole-Cole relaxation process with a step in the real part and a peak in the imaginary part kHz appeared around 1 kHz as the temperature was decreased. A circuit model comprising a capacitor in parallel with a CPE (used for modelling low frequency dispersion) and a distributed element (for modelling dielectric relaxation) was developed using a fitting software, ZView^{TM}. The noise in the high frequency end was first removed and the spectrum for each temperature was fitted individually as per the method described previously and over the frequency range shown in Figure 116 for each spectrum. It is clear that the model is an

approximate fit at both the low and the high frequency end and therefore, warrants further work. Moreover, the source of this second process also requires further investigation.

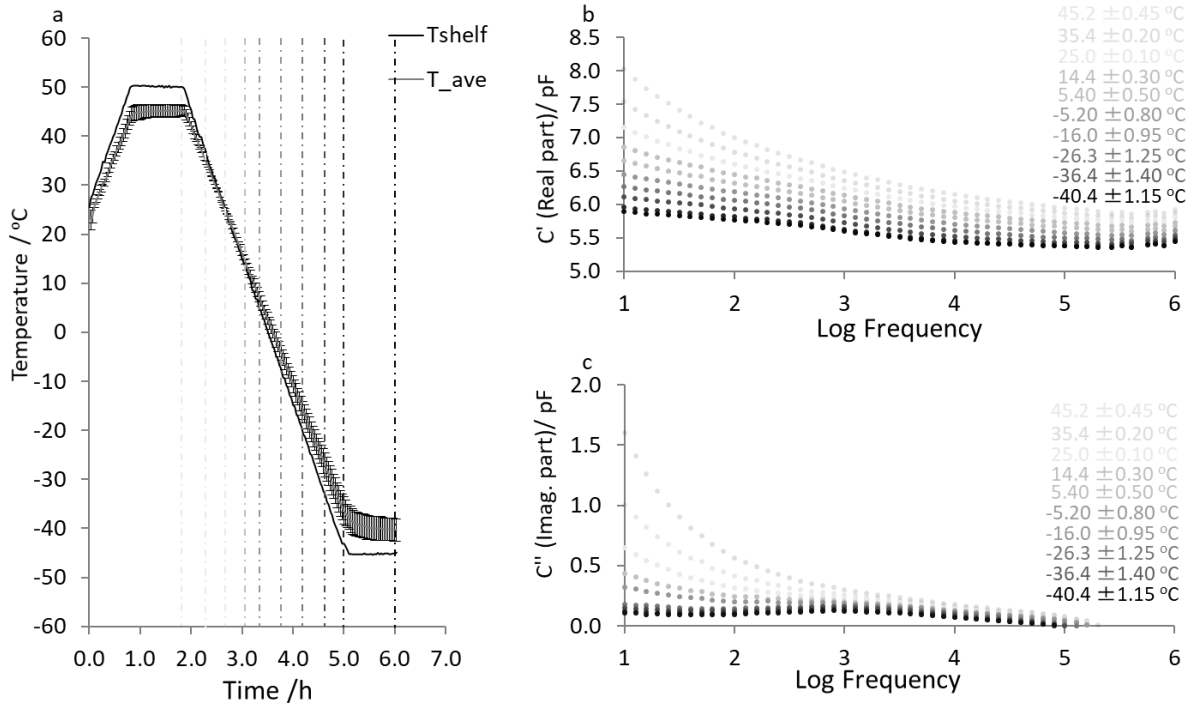

Figure 115: TVIS Spectra for an empty cropped Adelphi (VC010-20C) glass vial with copper electrodes (19 mm by 10 mm) attached on either side of the glass wall measured at various temperatures recorded by two thermocouples from the Virtis Advantage Plus freeze dryer equipped with the DMU five-channel TVIS system.

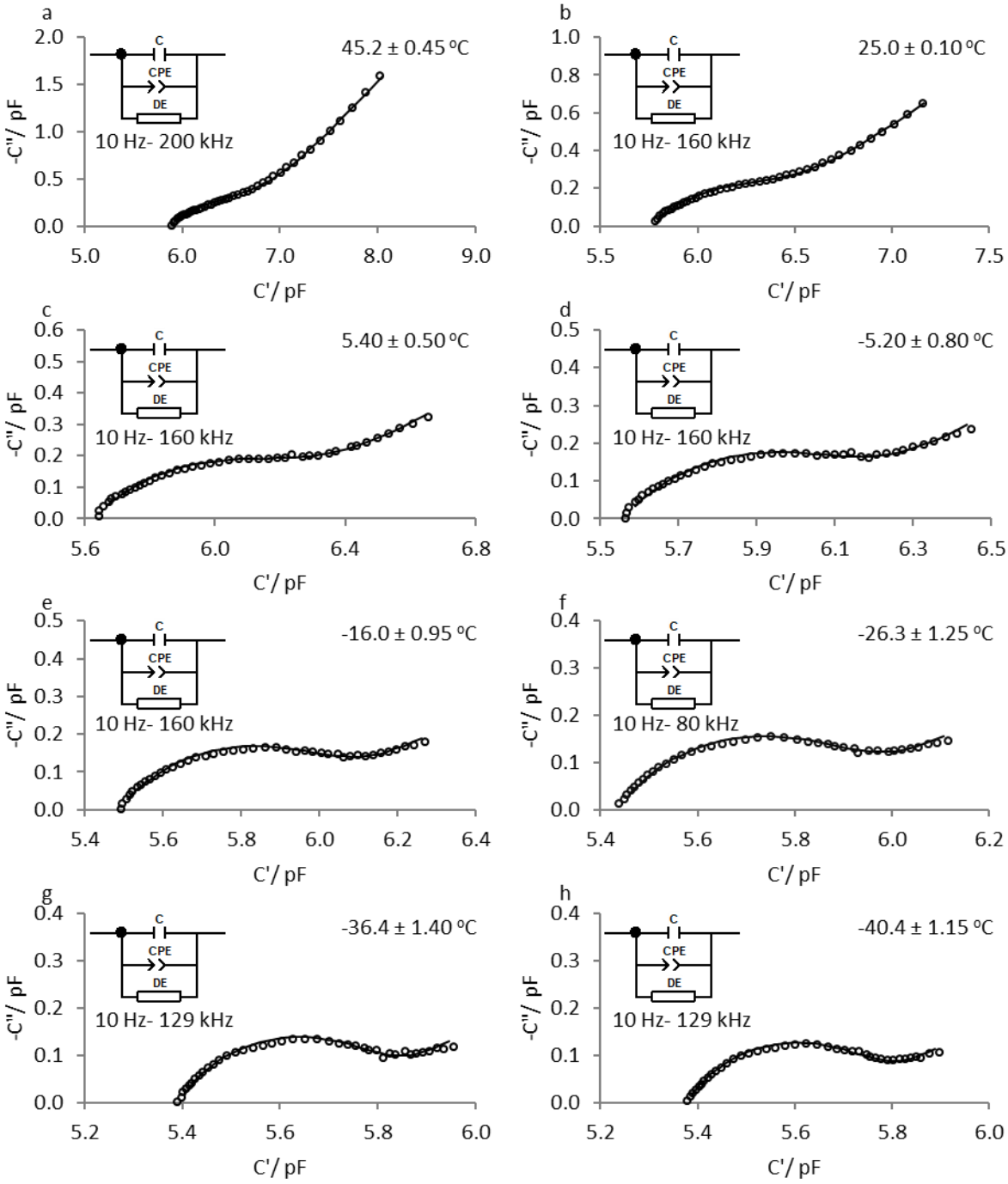

Figure 116: Cole Cole plots of imaginary part capacitance v/s real part capacitance for the spectra for an empty cropped Adelphi (VC010-20C) glass vial with copper electrodes (19 mm by 10 mm) attached on the either side of the glass wall placed measured at representative temperatures from two thermocouples from the Virtis Advantage plus freeze dryer equipped with the DMU five-channel TVIS system. Spectra have been fitting with a C=CPE=DE model.

Conclusions

Two conclusions may be drawn from this study: (i) Although the DE element of the C=CPE=DE model approximately fits the second process observed at intermediate frequencies it may not represent the physicality of the system, i.e. a Cole-Cole relaxation. A further investigation is required to determine the nature of the second process; (ii) with TVIS it is not possible to measure below 10 Hz and the spectra at the high frequency end are noisy. Therefore, an alternative dielectric spectroscopic technique might be required to extend the measurable frequency range both at the low frequency end of the spectrum in order understand the low frequency dispersion behaviour and at the high frequency end to determine the instantaneous glass wall capacitance.

10.3.2 Investigation of the 1 kHz Process in the TVIS Spectra for the Cropped Adelphi (VC010-20C) Vial with a Copper Electrode System

Aim: To measure the dielectric properties of the glass vial

Objective: To investigate the characteristics of the second process that was observed in the spectra in the middle part of the TVIS frequency range (i.e. around 1 kHz) for the Adelphi (VC010-20C) glass vial attached with copper electrodes on the either side of the glass wall

Three studies were undertaken to investigate the nature of the second process, and their objectives have been listed below:

- **First study:** to investigate the impact of drying the vial, shelf conditions and changing the channel of the TVIS System on the second process
- **Second study:** to investigate the impact of varying the width of the outer electrode on the second process
- **Third study:** Impact of the Adhesive side and the non-adhesive side of the copper electrodes on the second process

Materials and methods for the first study: impact of drying the vial, the shelf conditions and changing the channel of the TVIS system on the second process

A cropped vial was dried in an oven for 15 minutes at 90 °C before attaching a pair of copper electrodes (copper adhesive tape 1181 3M) and its spectrum was compared with that for a normal cropped vial (not pre-dried) using Ch1 of the TVIS system. A single spectrum (10 Hz- 1 MHz) for each vial was obtained at room temperature by first placing vials directly on the bottom shelf of the Virtis Advantage Plus freeze drier as shown in as shown in Figure 117 and the measuring them again after placing a 5 mm thick PTFE slab in between the vial base and the shelf. Thereafter, the normal cropped vial was measured with all the 5 channels of the TVIS system whilst it was placed on the PTFE slab.

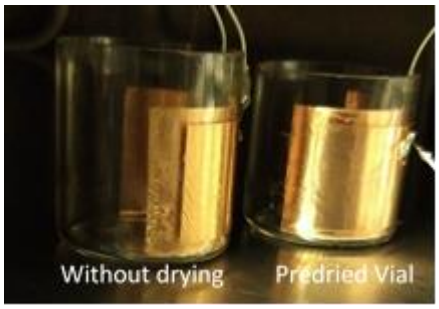

Figure 117: Cropped Adelphi (VC010-20C) vials with copper electrodes attached on the either side of the glass wall measured with DMU five-channel TVIS system. The dimensions of the inner electrode were 38 mm by 19 mm and dimensions of the outer electrode were 34 mm by 15 mm such that 2 mm border was left at the top and the bottom of the outer electrode and a 4 mm border was left on the sides of the outer electrode. These vials were first measured on the shelf and then on a PTFE slab. Channel 1 of the junction box was used to connect the vials to the TVIS system.

Materials and methods for the second study: Impact of varying the outer electrode width on the second process

A copper electrode of dimensions 38 mm by 19 mm was attached along the inner wall of a normal cropped vial (no pre-drying) and another electrode of dimensions 34 mm by 15 mm was attached on the outer surface leaving a 2 mm border with respect to the top and the bottom edges of the inner electrode and a 4 mm border on the either side as shown in the first photograph in Figure 118 where the both the sides of the vial have been shown. It was then placed on the 5 mm thick PTFE slab positioned in the centre of the bottom shelf and a spectrum at room temperature was obtained after connecting the vial to Ch1 of the junction box as shown in Figure 118. Thereafter, the vial was disconnected and a small segment of the electrode of width equal to 2 mm was removed from the either side of the outer electrode and the vial was measured again. This procedure was repeated until one obtained a spectrum for each of the widths labelled in Figure 118.

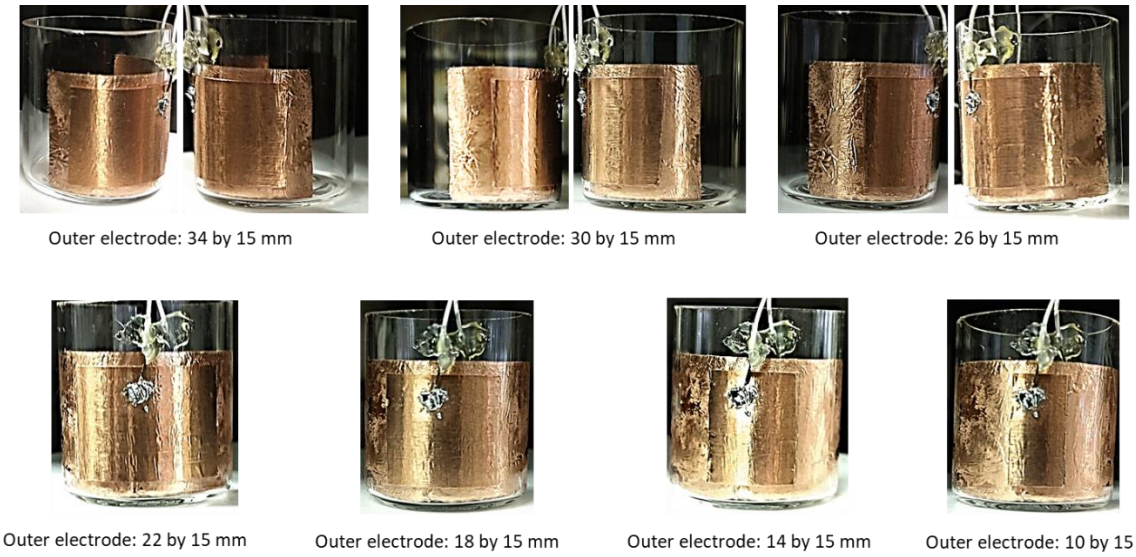

Figure 118: Varying the outer electrode width of a normal cropped Adelphi (VC010-20C) to assess its impact on the second process.

Figure 119: An example of a how a cropped Adelphi (VC010-20C) vial placed on a 5 mm thick PTFE slab positioned at the centre of the Virtis Advantage Plus freeze dryer shelf and connected to CH1 of the junction box which is part of the DMU five-channel TVIS system.

Materials and methods for the third study: Impact of the adhesive side and the non-adhesive side of the copper electrodes on the second process

The Copper foil tape (3M 1181) that is routinely used for the measurement of the TVIS vial has a 0.026 mm conductive adhesive layer that allows the electrode to stick to the glass wall. A sketch is shown in Figure 120. To investigate whether the second process was due to this conductive adhesive, two types of the electrode attachment on a semi-circular glass segment (Figure 121a) were compared. In the first case, a copper electrode (31 mm by 16.5 mm) was attached along the inner wall and another copper electrode (34 mm by 16.5 mm) was attached on the outer surface of the glass segment which was then placed on a 5 mm thick PTFE slab positioned in the centre of the shelf of the Virtis Advantage Plus freeze dryer. A spectrum was obtained from CH1 of the TVIS system at room temperature. Thereafter, the copper electrodes were removed. Another pair of copper electrodes with the same dimensions were sliced out from the copper tape and their non-adhesive sides were attached using an insulating tape to the same glass segment (Figure 121a) after removing the adhesive residue from it using Ethanol. The finished sample ready for measurement is shown in Figure 121(c). A spectrum was obtained at room temperature from CH1 of the TVIS system. Both the spectra (for the adhesive side and the non-adhesive side) were compared qualitatively to investigate whether a second process was observed for the glass segment with the electrodes without the adhesive.

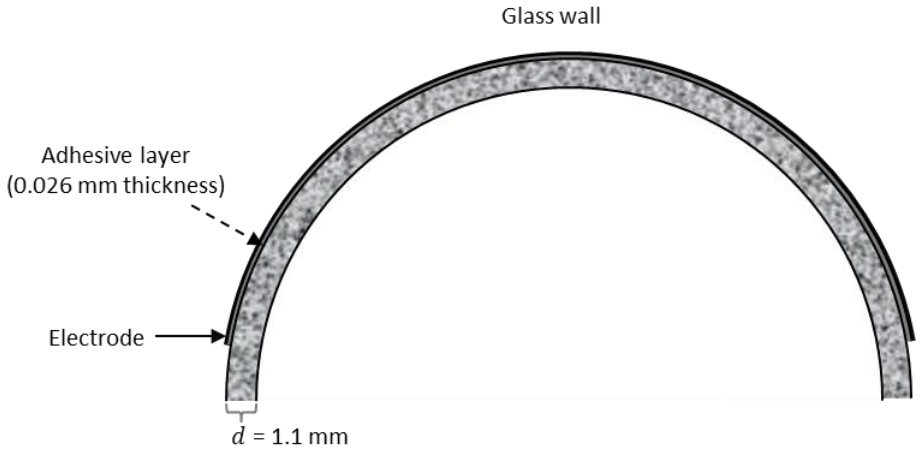

Figure 120: A sketch of the glass wall with the adhesive side of the copper electrode (copper foil tape 3M 1181).

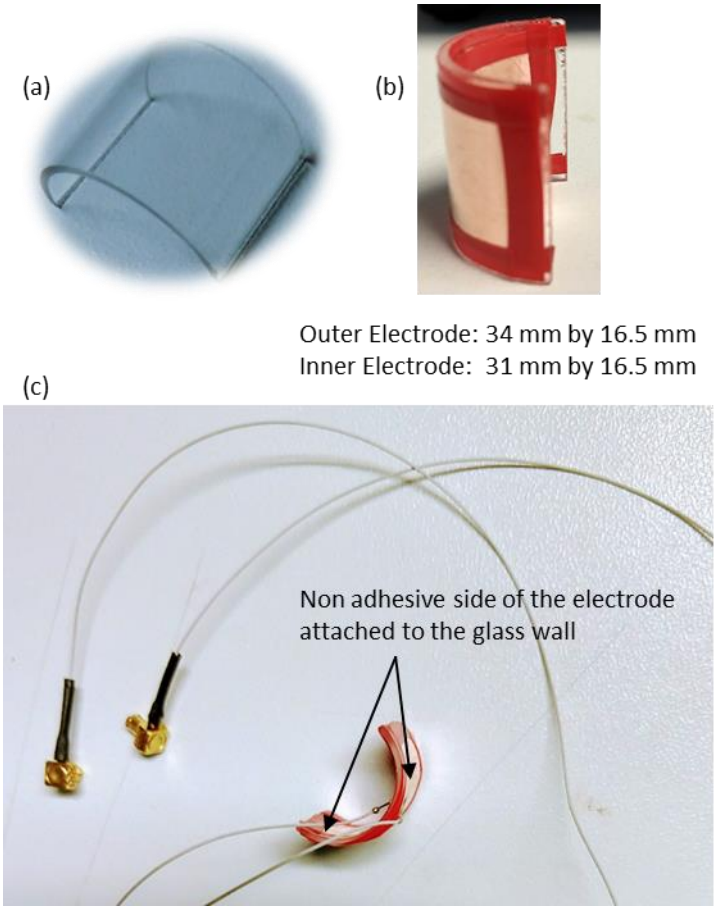

Figure 121: The glass segment with the non-adhesive side of the copper electrodes attached using an insulating tape: (a) the semi-circular glass segment measured; (b) The non-adhesive sides of the copper electrodes (outer electrode 34 mm by 16.5 mm and inner electrode 31 mm by 16.5 mm); (c) the finished sample ready for measurement.

Results for the first study: Measurement of a normal cropped vial and a pre-dried cropped vial

Figure 122(a to c) shows the bode and the Cole-Cole plots of capacitance for the CH1 spectra obtained from the 2 cropped vials out of which one of them was dried before attaching the electrodes. It is clear that the second process did not disappear on drying the vial which suggests that it was not due any component within the glass microstructure. Further, the spectra marginally changed when the vials were placed on a PTFE slab as shown in Figure 122(d to f) which suggests it was not an issue of current leakage through the grounded shelf. However, the spectra were noisy in the high frequency end (i.e. between 100 kHz and 1 MHz) in all cases. Further, Figure 123 demonstrates how the shape of the second process differs among the 5 channels of the TVIS system.

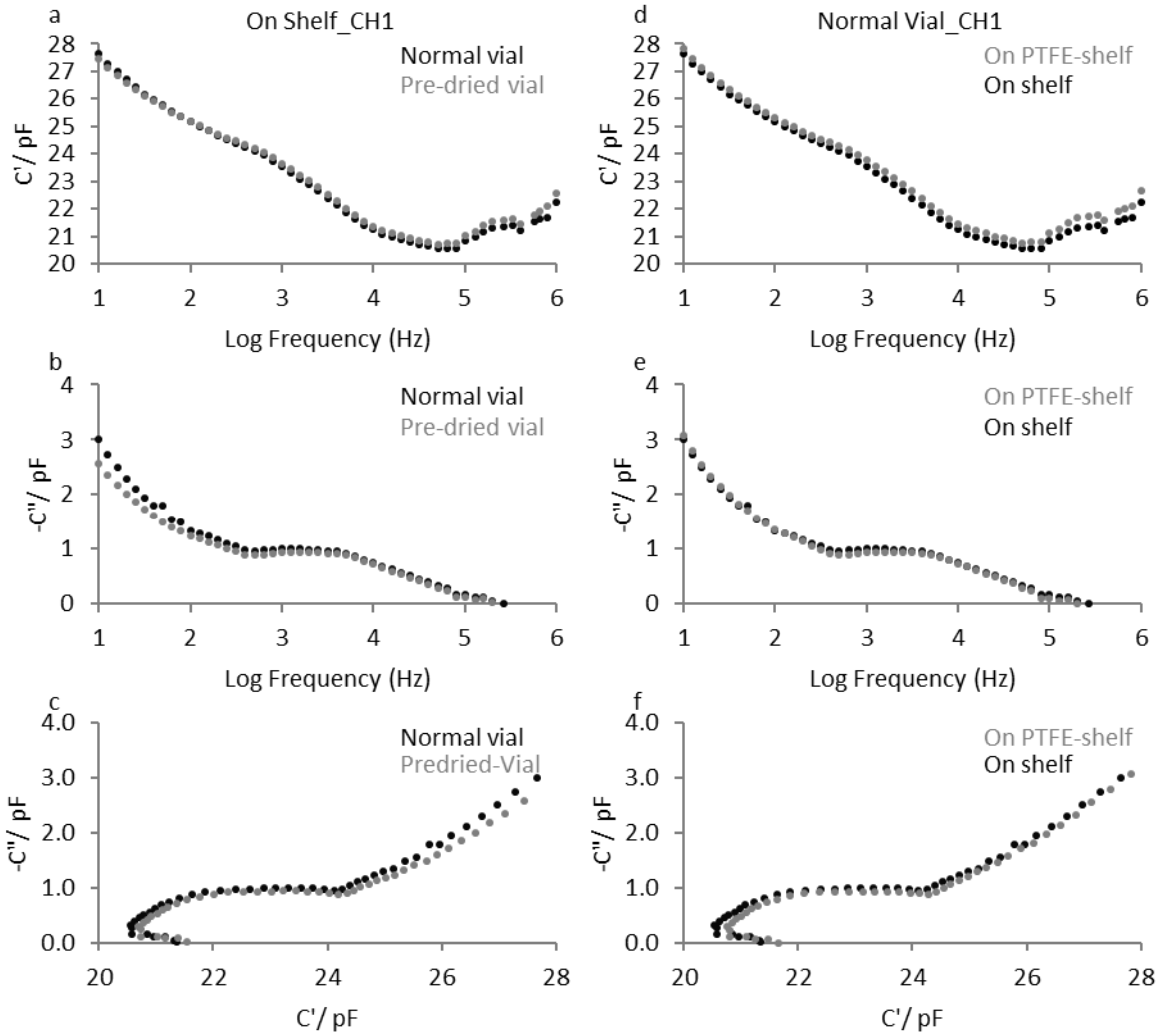

Figure 122: Various representations of the spectra obtained for the cropped Adelphi (VC010-20C) vials with copper electrodes (inner 38 mm by 19 mm; outer 34 mm by 15 mm): (a) Bode plot of real part capacitance v/s log frequency for the two cropped vials out of which one was dried before attaching the electrodes; (b) Bode plot of imaginary part capacitance v/s log frequency for the two cropped vials out of which one was dried before attaching the electrodes; (c) Cole-Cole plot of imaginary part capacitance v/s real part capacitance for the two cropped vials out of which one was dried before attaching the electrodes; (d) to (f) same representations but the comparison is between having vials placed on a PTFE slab and when placed directly on the shelf for the normal cropped vial.

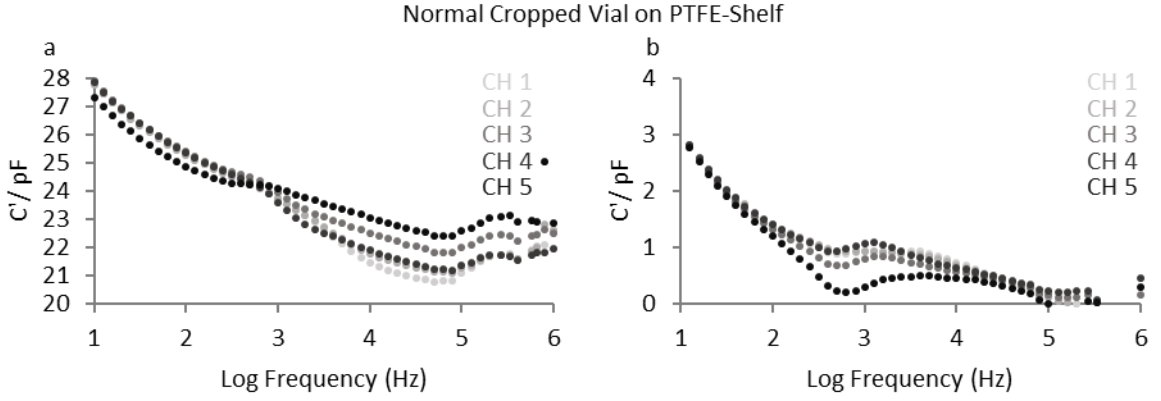

Figure 123: Bode plots of real and imaginary capacitance showing the differences in the appearance of the second process at intermediate frequencies among the 5 channels of the TVIS system

Results for the second study: Impact of varying the outer electrode width on the second process

Figure 124 shows the Cole-Cole plots of the CH1 spectra for the cropped glass vial where the outer electrode width was decreased from 34 mm to 10 mm. It is clear that the second process gets stretched out towards lower frequencies as the width of the outer electrode increases which suggests the second process is either a property of the electrode coverage along the curved glass wall or simply an artefact. Moreover, note the data points in grey solid circles at the high frequency end of the spectra appear to be some noise. The effective electrode areas corresponding to the spectra shown in Figure 124(e) & (f) are 270 mm^2 (18 mm by 15 mm) and 150 mm^2 (10 mm by 15 mm), which are comparable to the area of the electrodes (i.e. 19 mm by 10 mm =190 mm^2) that are attached on either side of a standard TVIS vial. For these spectra in particular, there seems to be a signal overload which might have caused the values of the imaginary part capacitance to drop after 129 kHz. This must mean that for the spectra corresponding to larger widths, at least those data points that are shown in grey solid circles might be part of some artefact.

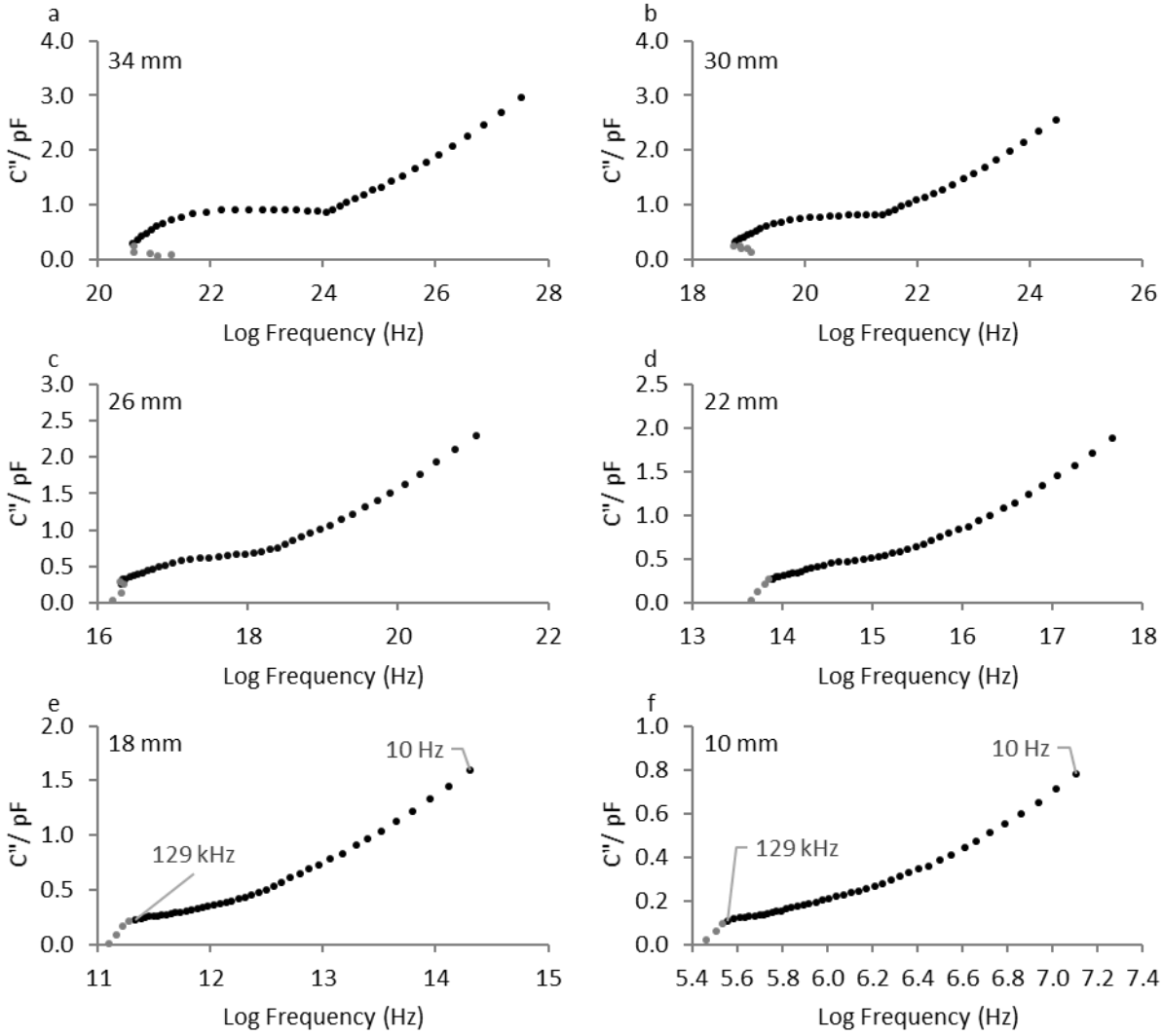

Figure 124: Cole-Cole plots of imaginary part capacitance v/s real part capacitance of the spectrum obtained from varying the width of the outer electrode (height 15 mm) from 34 mm to 10 mm whilst keeping the inner electrode dimensions (38 mm by 19 mm) the same for the cropped Adelphi (VC010-20C) vial connected to Ch1 of the DMU five-channel TVIS system. The second process gets stretched out as the width of the outer electrode increases which suggests that this is an artefact rather than dielectric relaxation. The data points in grey solid circles do not seem to be showing a real process.

Results for the third study: Impact of the adhesive side and the non-adhesive side of the copper electrodes on the second process

Figure 125 shows a qualitative comparison of the spectra for the glass segment with the adhesive sides and the non-adhesive sides of the copper electrode. The second process is clearly not present in the case of the non-adhesive electrode-glass segment which suggests the conductive adhesive layer might have a role to play in the appearance of the second process.

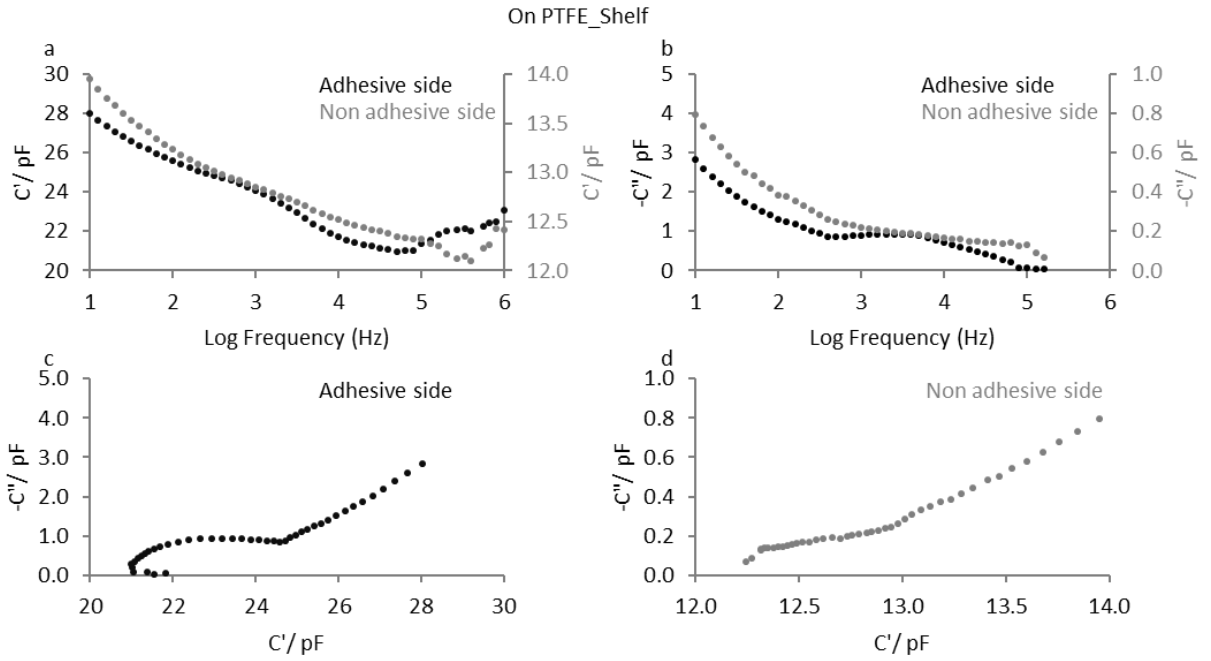

Figure 125: Comparison of the spectra for the glass vial segment with the adhesive side and the non-adhesive sides of the copper electrodes (outer electrode 34 mm by 16.5 mm and inner electrode 31 mm by 16.5 mm) measured on a 5 mm thick PTFE slab in the centre of the shelf at room temperature from CH1 of the TVIS system; (a) Bode plot of real part capacitance v/s log frequency; (b) Bode plot of imaginary part capacitance v/s log frequency; (c) Cole-Cole plot of imaginary part capacitance and real part capacitance for the glass segment with the adhesive sides of the electrodes; (d) Cole-Cole plot of imaginary part capacitance and real part capacitance for the glass segment with the non-adhesive sides of the electrodes.

Summary and Conclusions for the Three Studies for Understanding the Nature of the Second Process

The first study involving a normal cropped vial and a cropped vial that was dried before attaching copper electrodes demonstrated that the second process at the intermediate frequencies was not impacted by either drying the vial or placing it on a PTFE slab for CH1. The next part of the first study involved measuring the normal cropped vial (not dried) with rest of the channels of the TVIS system where it was observed that the shape of the second process differed significantly among all the 5 channels. The subsequent studies were therefore performed with CH1 only. In the second study, it was shown that an increase in the width of the outer electrode of the cropped vial lead to a stretching of the second process which suggested that this might be a property associated with electrode coverage along the curved glass wall. However, the second process was not present in the case where the outer electrode width was below 18 mm which is comparable to that for the electrodes attached on the either side of a TVIS vial. The final study, where the adhesive side and the non-adhesive sides of the copper electrodes were studied, demonstrated that the second process was not present in the case of the non-adhesive sample. In general, the results seem ambiguous. It has not been possible to discern whether the second process is due to dielectric relaxation or an artefact of the TVIS system. Moreover, it was not possible to see how this second process manifests at the high frequency end because in most cases the data gets noisy after 100 kHz. For further studies, both the measurement technique and the type of electrode-glass contact may be assessed. Broadband Dielectric Spectroscopy and Gold sputter-coated electrodes may be used to further understand the dielectric properties of the glass wall.

11 References

Allen, S.A.B., 1998. Interdigitated ElectrodesIn: Brown, M.E. (Ed.), Handbook of Thermal Analysis and Calorimetry: Principles and Practice Handbook of Thermal Analysis and Calorimetry V. 1, Elsevier Science, NL, pp. 419.

Amidon, G.L., Lee, P.I., Topp, E.M., 1999. Heat and Mass Transfer in Low Pressure Gases: Applications to Freeze DryingIn: Anonymous Transport Processes in Pharmaceutical Systems, Vol. 102, CRC Press, New York, pp. 611-686.

Angell, C.A., 2002. Liquid Fragility and the Glass Transition in Water and Aqueous Solutions. Chem. Rev., 102, 2627-2650. doi: 10.1021/cr000689q.

Arshad, M.S., Smith, G., Polygalov, E., Ermolina, I., 2014. Through-vial impedance spectroscopy of critical events during the freezing stage of the lyophilization cycle: The example of the impact of sucrose on the crystallization of mannitol. European Journal of Pharmaceutics and Biopharmaceutics, 87, 598-605. doi: 10.1016/j.ejpb.2014.05.005.

Arsiccio, A., Sparavigna, A.C., Pisano, R., Barresi, A.A., 2018. Measuring and predicting pore size distribution of freeze-dried solutions. Drying Technol, 1-13. doi: 10.1080/07373937.2018.1430042.

Arsiccio, A., Pisano, R., 2018. Application of the Quality by Design Approach to the Freezing Step of Freeze-Drying: Building the Design Space. J. Pharm. Sci., 107, 1586-1596. doi: 10.1016/j.xphs.2018.02.003.

Assegehegn, G., Brito-de la Fuente, E., Franco, J.M., Gallegos, C., 2019. The Importance of Understanding the Freezing Step and Its Impact on Freeze-Drying Process Performance. J. Pharm. Sci., 108, 1378-1395. doi: 10.1016/j.xphs.2018.11.039.

Awotwe−Otoo, D., Agarabi, C., Khan, M.A., 2014. An Integrated Process Analytical Technology (PAT) Approach to Monitoring the Effect of Supercooling on Lyophilization Product and Process Parameters of Model Monoclonal Antibody Formulations. J. Pharm. Sci., 103, 2042-2052. doi: 10.1002/jps.24005.

Awotwe-Otoo, D., Agarabi, C., Read, E.K., Lute, S., Brorson, K.A., Khan, M.A., Shah, R.B., 2013. Impact of controlled ice nucleation on process performance and quality attributes of a lyophilized monoclonal antibody. Int. J. Pharm., 450, 70-78. doi: 10.1016/j.ijpharm.2013.04.041.

Azzarella, J., Mudhivarthi, V.K., Wexler, E., Ganguly, A., 2016. Increasing vial-to-vial homogeneity: An analysis of using Veriseq nucleation on production-scale freeze dryers. BioPharm International, 29, 55.

Bardat, A., Biguet, J., Chatenet, E., Courteille, F., 1993. Moisture measurement: A new method for monitoring freeze-drying cycles. Journal of Parenteral Science and Technology, 47, 293-299.

Barker, S., Antonijevic, M.D., 2011. Solid State Characterization of PharmaceuticalsIn: Storey, R.A., Ymén, I. (Eds.), Solid State Characterization of Pharmaceuticals, 1st Ed., Wiley-Blackwell, Hoboken, pp. 187-206.

Barresi, A.A., Pisano, R., Fissore, D., Rasetto, V., Velardi, S.A., Vallan, A., Parvis, M., Galan, M., 2009a. Monitoring of the primary drying of a lyophilization process in vials. Chemical Engineering & Processing: Process Intensification, 48, 408-423. doi: 10.1016/j.cep.2008.05.004.

Barresi, A.A., Pisano, R., Fissore, D., Rasetto, V., Velardi, S.A., Vallan, A., Parvis, M., Galan, M., 2009b. Monitoring of the primary drying of a lyophilization process in vials. Chemical Engineering & Processing: Process Intensification, 48, 408-423. doi: 10.1016/j.cep.2008.05.004.

Barresi, A.A., Pisano, R., Rasetto, V., Fissore, D., Marchisio, D.L., 2010. Model-Based Monitoring and Control of Industrial Freeze-Drying Processes: Effect of Batch Nonuniformity. Drying Technol, 28, 577-590. doi: 10.1080/07373931003787934.

Ben Amor, Y., Sutter, E.M.M., Takenouti, H., Orazem, M.E., Tribollet, B., 2014. Interpretation of electrochemical impedance for corrosion of a coated silver film in terms of a pore-in-pore model. J. Electrochem. Soc., 161, C573-C579. doi: 10.1149/2.1151412jes.

Bhardwaj, S.P., Suryanarayanan, R., 2012. Use of Dielectric Spectroscopy To Monitor Molecular Mobility in Glassy and Supercooled Trehalose. The Journal of Physical Chemistry B, 116, 11728-11736. doi: 10.1021/jp303317p.

Bhardwaj, S.P., Suryanarayanan, R., 2011. Subtraction of DC Conductivity and Annealing: Approaches To Identify Johari–Goldstein Relaxation in Amorphous Trehalose. Molecular Pharmaceutics, 8, 1416-1422. doi: 10.1021/mp2000154.

Bhatnagar, B.S., Bogner, R.H., Pikal, M.J., 2007. Protein Stability During Freezing: Separation of Stresses and Mechanisms of Protein Stabilization. Pharm. Dev. Technol., 12, 505-523. doi: 10.1080/10837450701481157.

Blackburn, T.D., Mazzuchi, T.A., Sarkani, S., 2011. Overcoming Inherent Limits to Pharmaceutical Manufacturing Quality Performance with QbD (Quality by Design). Journal of Pharmaceutical Innovation, 6, 69-76. doi: 10.1007/s12247-011-9102-x.

Bosca, S., Barresi, A.A., Fissore, D., 2014. Use of soft sensors to monitor a pharmaceutical freeze-drying process in vials. Pharm. Dev. Technol., 19, 148-159. doi: 10.3109/10837450.2012.757786.

Bosca, S., Barresi, A.A., Fissore, D., 2013. Use of a soft sensor for the fast estimation of dried cake resistance during a freeze-drying cycle. Int. J. Pharm., 451, 23-33. doi: 10.1016/j.ijpharm.2013.04.046.

Bosca, S., Corbellini, S., Barresi, A.A., Fissore, D., 2013. Freeze-Drying Monitoring Using a New Process Analytical Technology: Toward a "Zero Defect" Process. Drying Technol, 31, 1744-1755. doi: 10.1080/07373937.2013.807431.

Breen, E.D., Curley, J.G., Overcashier, D.E., Hsu, C.C., Shire, S.J., 2001. Effect of Moisture on the Stability of a Lyophilized Humanized Monoclonal Antibody Formulation. Pharm. Res., 18, 1345-1353. doi: 10.1023/A:1013054431517.

Breen, E., Curley, J., Overcashier, D., Hsu, C., Shire, S., 2001. Effect of Moisture on the Stability of a Lyophilized Humanized Monoclonal Antibody Formulation. Pharm Res, 18, 1345-1353. doi: 1013054431517.

Brülls, M., Folestad, S., Sparén, A., Rasmuson, A., 2003. In-Situ Near-Infrared Spectroscopy Monitoring of the Lyophilization Process. Pharm. Res., 20, 494-499. doi: 10.1023/A:1022680810474.

Bursac, R., Sever, R., Hunek, B., 2009. A practical method for resolving the nucleation problem in lyophilization. BioProcess International, 7, 66-72.

Cameron, P., Butler, L.D., 1997. Good Pharmaceutical Freeze-Drying Practice, Interpharm Press, Buffalo Grove, Il.

Carpenter, J.F., Pikal, M.J., Chang, B.S., Randolph, T.W., 1997. Rational design of stable lyophilized protein formulations: Some practical advice. Pharm. Res., 14, 969-975. doi: 1012180707283.

Carullo, A., Vallan, A., 2012. Measurement uncertainty issues in freeze-drying processes. Measurement, 45, 1706-1712. doi: 10.1016/j.measurement.2012.04.017.

Chakravarty, P., Lee, R., Demarco, F., Renzi, E., 2012. Ice fog as a means to induce uniform ice nucleation during lyophilization. BioPharm International, 25, 38.

Chen, R., Slater, N., Gatlin, L., Kramer, T., Shalaev, E., 2008. Comparative Rates of Freeze-Drying for Lactose and Sucrose Solutions as Measured by Photographic Recording, Product Temperature, and Heat Flux Transducer. Pharm. Dev. Technol., 13, 367-374. doi: 10.1080/10837450802244744.

Colucci, D., Maniaci, R., Fissore, D., 2019. Monitoring of the freezing stage in a freeze-drying process using IR thermography. Int. J. Pharm., 566, 488-499. doi: 10.1016/j.ijpharm.2019.06.005.

Conn, P.M., 1999. Ion Channels, Academic, London; San Diego.

Connelly, J.P., Welch, J.V., 1993. Monitor lyophilization with mass spectrometer gas analysis. Journal of Parenteral Science and Technology, 47, 70-75.

Constantino, H.R., Pikal, M.J., 2004. Lyophilisation of Biopharmaceuticals, Illustrated Ed., American Association of Pharmaceutical Scientists, U.S.A.

Corbellini, S., Parvis, M., Vallan, A., 2010. In-Process Temperature Mapping System for Industrial Freeze Dryers. IEEE Transactions on Instrumentation and Measurement, 59, 1134-1140. doi: 10.1109/TIM.2010.2040909.

Craig, D., 1995. Pharmaceutical Sciences: Dielectric Analysis of Pharmaceutical Systems (1), CRC Press.

Cutnell, J.D., Johnson, K.W., 2012. Electric Forces and Electric FieldsIn: Johnson, S. (Ed.), Physics, John Wiley and Sons Inc., USA, pp. 529-558.

Dawson, P.J., Hockley, D.J., 1992. Scanning electron microscopy of freeze-dried preparations: relationship of morphology to freeze-drying parameters. Dev. Biol. Stand., 74, 185-192.

De Beer, T., Allesø, M., Goethals, F., Coppens, A., Vander Heyden, Y., Lopez De Diego, H., Rantanen, J., Verpoort, F., Vervaet, C., Remon, J.P., Baeyens, W.R.G., 2007. Implementation of a Process Analytical Technology System in a Freeze-Drying Process Using Raman Spectroscopy for In-Line Process Monitoring. Anal. Chem., 79, 7992-8003. doi: 10.1021/ac070549h.

De Beer, T., Burggraeve, A., Fonteyne, M., Saerens, L., Remon, J.P., Vervaet, C., 2011. Near infrared and Raman spectroscopy for the in-process monitoring of pharmaceutical production processes. Int. J. Pharm., 417, 32-47. doi: 10.1016/j.ijpharm.2010.12.012.

De Beer, T., Wiggenhorn, M., Hawe, A., Kasper, J.C., Almeida, A., Quinten, T., Friess, W., Winter, G., Vervaet, C., Remon, J.P., 2011. Optimization of a pharmaceutical freeze-dried product and its process

using an experimental design approach and innovative process analyzers. Talanta, 83, 1623-1633. doi: 10.1016/j.talanta.2010.11.051.

De Beer, T., Wiggenhorn, M., Veillon, R., Debacq, C., Mayeresse, Y., Moreau, B., Burggraeve, A., Quinten, T., Friess, W., Winter, G., Vervaet, C., Remon, J.P., Baeyens, W.R.G., 2009. Importance of Using Complementary Process Analyzers for the Process Monitoring, Analysis, and Understanding of Freeze Drying. Anal. Chem., 81, 7639-7649. doi: 10.1021/ac9010414.

Douglas, S.F., Thompson, S.R., Taylor, N., 1990. Positioning device for temperature sensor in freeze drying. U.S. Patent 4966469 A.

Douglas, S.F., Thompson, T.M., 1995. Positioning device for temperature sensor in freeze drying 6th U.S. Patent 5447374 A.

Duddu, S.P., Dal Monte, P.R., 1997. Effect of Glass Transition Temperature on the Stability of Lyophilized Formulations Containing a Chimeric Therapeutic Monoclonal Antibody. Pharm. Res., 14, 591-595. doi: 10.1023/A:1012144810067.

Duddu, S.P., Zhang, G., Dal Monte, P.R., 1997. The Relationship Between Protein Aggregation and Molecular Mobility Below the Glass Transition Temperature of Lyophilized Formulations Containing a Monoclonal Antibody. Pharm. Res., 14, 596-600. doi: 10.1023/A:1012196826905.

Dulski, T.R., Dulski, T.R., 1996. A Manual for the Chemical Analysis of Metals, ASTM International.

Ehrt, D., Keding, R., 2009. Electrical conductivity and viscosity of borosilicate glasses and melts. PHYSICS AND CHEMISTRY OF GLASSES-EUROPEAN JOURNAL OF GLASS SCIENCE AND TECHNOLOGY PART B, 50, 165-171.

El-Egili, K., 1996. AC conductivity of some alkali borosilicate glasses. Journal of Physics: Condensed Matter, 8, 3419-3426. doi: 10.1088/0953-8984/8/19/017.

Emteborg, H., Zeleny, R., Charoud-Got, J., Martos, G., Lüddeke, J., Schellin, H., Teipel, K., 2014. Infrared Thermography for Monitoring of Freeze-Drying Processes: Instrumental Developments and Preliminary Results. J. Pharm. Sci., 103, 2088-2097. doi: 10.1002/jps.24017.

Ermolina, I., Polygalov, E., Bland, C., Smith, G., 2007a. Dielectric spectroscopy of low-loss sugar lyophiles: I. A methodical approach to measurement in the frequency domain 10−1–106 Hz. J. Phys. D, 40, 36-44. doi: 10.1088/0022-3727/40/1/S07.

Ermolina, I., Polygalov, E., Bland, C., Smith, G., 2007b. Dielectric spectroscopy of low-loss sugar lyophiles: II. Relaxation mechanisms in freeze-dried lactose and lactose monohydrate. J. Non Cryst. Solids, 353, 4485-4491. doi: 10.1016/j.jnoncrysol.2007.02.078.

Ermolina, I., Smith, G., 2010. Dielectric spectroscopy of low-losses sugar lyophiles: III. The influence of moisture on the dielectric response of freeze-dried lactose.

Esfandiary, R., Gattu, S.K., Stewart, J.M., Patel, S.M., 2016. Effect of Freezing on Lyophilization Process Performance and Drug Product Cake Appearance. J. Pharm. Sci., 105, 1427-1433. doi: 10.1016/j.xphs.2016.02.003.

Espe, W., 2013. Silicates : Materials of High Vacuum Technology, Elsevier Science & Technology, Kent.

Essam, J.W., 1980. Percolation theory. Reports on Progress in Physics, 43, 833-912. doi: 10.1088/0034-4885/43/7/001.

FDA, 2014. Inspection guides-lyophilization of parenteral. , 2018.

FDA, 2004. PAT — A Framework for Innovative Pharmaceutical Development, Manufacturing, and Quality Assurance.

Feldman, Y., Gusev, Y.A., Vasilyeva, M.A., 2012. Dielectric relaxation phenomena in complex systems.

Feldman, Y., Puzenko, A., Ryabov, Y., 2006. Dielectric Relaxation Phenomena in Complex MaterialsIn: Anonymous , Vol. 133, John Wiley & Sons, Inc, Hoboken, NJ, USA, pp. 1-125.

FirstWord, 2018. Charting the Global Biosimilar Pipeline. FirstWord Publishing.

Fissore, D., Pisano, R., Barresi, A., 2015. Using Mathematical Modeling and Prior Knowledge for QbD in Freeze-Drying ProcessesIn: Jameel, F. (Ed.), Search Results Quality by Design for Biopharmaceutical Drug Product Development, Vol. 18, Springer, pp. 565-593.

Fissore, D., Pisano, R., Barresi, A.A., 2018. Process analytical technology for monitoring pharmaceuticals freeze-drying - A comprehensive review. Drying Technol, 36, 1839-1865. doi: 10.1080/07373937.2018.1440590.

Fissore, D., Pisano, R., Barresi, A.A., 2011. On the Methods Based on the Pressure Rise Test for Monitoring a Freeze-Drying Process. Drying Technol, 29, 73-90. doi: 10.1080/07373937.2010.482715.

Fissore, D., Velardi, S.A., Barresi, A.A., 2008. In-Line Control of a Freeze-Drying Process in Vials. Drying Technol, 26, 685-694. doi: 10.1080/07373930802046161.

Franks, F., 2007. Freeze-Drying of Pharmaceuticals and Biopharmaceuticals, The Royal Society of Chemistry, Cambridge.

Franks, F., 1998. Freeze-drying of bioproducts: putting principles into practice. European Journal of Pharmaceutics and Biopharmaceutics, 45, 221-229. doi: 10.1016/S0939-6411(98)00004-6.

Ganguly, A., Stewart, J., Rhoden, A., Volny, M., Saad, N., 2018. Mass spectrometry in freeze-drying: Motivations for using a bespoke PAT for laboratory and production environment. European Journal of Pharmaceutics and Biopharmaceutics, 127, 298-308. doi: 10.1016/j.ejpb.2018.02.036.

Ganguly, A., Nail, S.L., Alexeenko, A., 2013. Experimental Determination of the Key Heat Transfer Mechanisms in Pharmaceutical Freeze-Drying. J. Pharm. Sci., 102, 1610-1625. doi: 10.1002/jps.23514.

Gasteyer, T.H., Sever, R.R., Hunek, B., Grinter, N., Verdone, M.L., 2007. Lyophilization system and method US20070186437A1, May.

Geidobler, R., Winter, G., 2013. Controlled ice nucleation in the field of freeze-drying: Fundamentals and technology review. European Journal of Pharmaceutics and Biopharmaceutics, 85, 214-222. doi: //dx.doi.org/10.1016/j.ejpb.2013.04.014.

Geidobler, R., Mannschedel, S., Winter, G., 2012. A New Approach to Achieve Controlled Ice Nucleation of Supercooled Solutions During the Freezing Step in Freeze-Drying. J. Pharm. Sci., 101, 4409-4413. doi: 10.1002/jps.23308.

Genin, N., Rene, F., Corrieu, G., 1996. A method for on-line determination of residual water content and sublimation end-point during freeze-drying. Chemical Engineering & Processing: Process Intensification, 35, 255-263. doi: 10.1016/0255-2701(95)04131-1.

Gieseler, H., Kessler, W.J., Finson, M., Davis, S.J., Mulhall, P.A., Bons, V., Debo, D.J., Pikal, M.J., 2007. Evaluation of tunable diode laser absorption spectroscopy for in-process water vapor mass flux measurements during freeze drying. J. Pharm. Sci., 96, 1776-1793. doi: 10.1002/jps.20827.

Gieseler, H., Kramer, T., Pikal, M.J., 2007. Use of manometric temperature measurement (MTM) and SMART™ freeze dryer technology for development of an optimized freeze-drying cycle. J. Pharm. Sci., 96, 3402-3418. doi: //doi.org/10.1002/jps.20982.

Giordano, S., 2003. Effective medium theory for dispersions of dielectric ellipsoids. J. Electrostatics, 58, 59-76. doi: 10.1016/S0304-3886(02)00199-7.

Grandjean, A., Malki, M., Simonnet, C., 2006. Effect of composition on ionic transport in SiO2–B2O3–Na2O glasses. J. Non Cryst. Solids, 352, 2731-2736. doi: 10.1016/j.jnoncrysol.2006.03.058.

Grassini, S., Parvis, M., Barresi, A.A., 2013. Inert Thermocouple With Nanometric Thickness for Lyophilization Monitoring. IEEE Transactions on Instrumentation and Measurement, 62, 1276-1283. doi: 10.1109/TIM.2012.2223312.

Grassini, S., Pisano, R., Barresi, A.A., Angelini, E., Parvis, M., 2016. Frequency domain image analysis for the characterization of porous products. Measurement, 94, 515-522. doi: 10.1016/j.measurement.2016.08.031.

Grassini, S., Fulginiti, D., Pisano, R., Oddone, I., Parvis, M., 2014. , pp. 1-5.

Grohganz, H., Fonteyne, M., Skibsted, E., Falck, T., Palmqvist, B., Rantanen, J., 2009. Role of excipients in the quantification of water in lyophilised mixtures using NIR spectroscopy. J. Pharm. Biomed. Anal., 49, 901-907. doi: 10.1016/j.jpba.2009.01.021.

Gutina, A., Antropova, T., Rysiakiewicz-Pasek, E., Virnik, K., Feldman, Y., 2003. Dielectric relaxation in porous glasses. Microporous and Mesoporous Materials, 58, 237-254. doi: 10.1016/S1387-1811(02)00651-0.

Gutina, A., Axelrod, E., Puzenko, A., Rysiakiewicz-Pasek, E., Kozlovich, N., Feldman, Y., 1998. Dielectric relaxation of porous glasses. J. Non Cryst. Solids, 235, 302-307. doi: 10.1016/S0022-3093(98)00562-6.

Hawe, A., Friess, W., 2006. Physicohemical characterization of the freezing behavior of mannitol-human serum albumin formulations. AAPS PharmSciTech, 7, E85-E94. doi: 10.1208/pt070494.

Hazen, M.E., 1990. Fundamentals of DC and AC Circuits, Saunders College Pub, Philadelphia.

Heller, M.C., Carpenter, J.F., Randolph, T.W., 1999. Protein formulation and lyophilization cycle design: Prevention of damage due to freeze-concentration induced phase separation. Biotechnol. Bioeng., 63, 166-174.

Her, L.M., Nail, S.L., 1994. Measurement of glass transition temperatures of freeze-concentrated solutes by differential scanning calorimetry. Pharm. Res., 11, 54.

Hewis, J., 2017. Capacitance and Uses of Capacitors. , 2017.

Hirayama, C., Berg, D., 1960. , pp. 163-167.

Hottot, A., Andrieu, J., Hoang, V., Shalaev, E.Y., Gatlin, L.A., Ricketts, S., 2009. Experimental Study and Modeling of Freeze-Drying in Syringe Configuration. Part II: Mass and Heat Transfer Parameters and Sublimation End-Points. Drying Technol, 27, 49-58. doi: 10.1080/07373930802565814.

Hottot, A., Andrieu, J., Vessot, S., Shalaev, E., Gatlin, L.A., Ricketts, S., 2009. Experimental Study and Modeling of Freeze-Drying in Syringe Configuration. Part I: Freezing Step. Drying Technol, 27, 40-48. doi: 10.1080/07373930802565806.

Hottot, A., Peczalski, R., Vessot, S., Andrieu, J., 2006. Freeze-Drying of Pharmaceutical Proteins in Vials: Modeling of Freezing and Sublimation Steps. Drying Technol, 24, 561-570. doi: 10.1080/07373930600626388.

Hottot, A., Vessot, S., Andrieu, J., 2007. Freeze drying of pharmaceuticals in vials: Influence of freezing protocol and sample configuration on ice morphology and freeze-dried cake texture. Chemical Engineering and Processing: Process Intensification, 46, 666-674. doi: //dx.doi.org/10.1016/j.cep.2006.09.003.

ICH, 2009. International Conference on Harmonisation of Technical Requirements for Registration of Pharmaceuticals for Human Use, Topic Q8(R2): Pharmaceutical Development.

Jennings, T.A., Duan, H., 1995. Calorimetric monitoring of lyophilization. PDA journal of pharmaceutical science and technology, 49, 272.

Jennings, T.A., 1980. Residual gas analysis and vacuum freeze drying. J. Parenter. Drug Assoc., 34, 62-69.

Jennings, T.A., 1999. Lyophilization: Introduction and Basic Principles, CRC Press, Baton Rouge.

Johari, G.P., 1976. The dielectric properties of H2O and D2O ice Ih at MHz frequencies. J. Chem. Phys., 64, 3998-4005. doi: 10.1063/1.432033.

Johari, G.P., Whalley, E., 1981. The dielectric properties of ice Ih in the range 272-133 K. J. Chem. Phys., 75, 1333-1340. doi: 10.1063/1.442139.

Johnson, R.E., Oldroyd, M.E., Ahmed, S.S., Gieseler, H., Lewis, L.M., 2010a. Use of Manometric Temperature Measurements (MTM) to Characterize the Freeze-Drying Behavior of Amorphous Protein Formulations. J. Pharm. Sci., 99, 2863-2873. doi: 10.1002/jps.22031.

Johnson, R.E., Oldroyd, M.E., Ahmed, S.S., Gieseler, H., Lewis, L.M., 2010b. Use of Manometric Temperature Measurements (MTM) to Characterize the Freeze-Drying Behavior of Amorphous Protein Formulations. J. Pharm. Sci., 99, 2863-2873. doi: 10.1002/jps.22031.

Johnson, R.E., Teagarden, D.L., Lewis, L.M., Gieseler, H., 2009. Analytical accessories for formulation and process development in freeze-drying. American Pharmaceutical Review, 12, 60.

Kasper, J.C., Friess, W., 2011. The freezing step in lyophilization: Physico-chemical fundamentals, freezing methods and consequences on process performance and quality attributes of biopharmaceuticals. European Journal of Pharmaceutics and Biopharmaceutics, 78, 248-263. doi: 10.1016/j.ejpb.2011.03.010.

Kasper, J.C., Wiggenhorn, M., Resch, M., Friess, W., 2013. Implementation and evaluation of an optical fiber system as novel process monitoring tool during lyophilization. European Journal of Pharmaceutics and Biopharmaceutics, 83, 449-459. doi: 10.1016/j.ejpb.2012.10.009.

Kasper, J.C., Winter, G., Friess, W., 2013. Recent advances and further challenges in lyophilization. European Journal of Pharmaceutics and Biopharmaceutics, 85, 162-169. doi: //dx.doi.org/10.1016/j.ejpb.2013.05.019.

Kauppinen, A., 2015. Raman and Near-Infrared Spectroscopic Methods for In-Line Monitoring of Freeze-Drying Process. Ph.D. Thesis. , University of Eastern Finland.

Kilmartin, P.A., Reid, D.S., Samson, I., 2000. The measurement of the glass transition temperature of sucrose and maltose solutions with added NaCl. J. Sci. Food Agric., 80, 2196-2202. doi: 10.1002/1097-0010(200012)80:153.0.CO;2-C.

Kindt, T.J., Goldsby, R.A., Osborne, B.A., Kuby, J., 2007. Kuby Immunology, 6th Ed., W.H. Freeman, Basingstoke; New York, N.Y.

Konstantinidis, A.K., Kuu, W., Otten, L., Nail, S.L., Sever, R.R., 2011. Controlled Nucleation in Freeze-drying: Effects on Pore Size in the Dried Product Layer, Mass Transfer Resistance, and Primary Drying Rate. J. Pharm. Sci., 100, 3453-3470. doi: 10.1002/jps.22561.

Kremer, F., 2002. Dielectric spectroscopy – yesterday, today and tomorrow. J. Non Cryst. Solids, 305, 1-9. doi: 10.1016/S0022-3093(02)01083-9.

Kremer, F., Schönhals, A., 2003. Broadband Dielectric Spectroscopy, Springer, London; Berlin.

Kuu, W.Y., Hardwick, L.M., Akers, M.J., 2006. Rapid determination of dry layer mass transfer resistance for various pharmaceutical formulations during primary drying using product temperature profiles. Int. J. Pharm., 313, 99-113. doi: 10.1016/j.ijpharm.2006.01.036.

Kuu, W.Y., Hardwick, L.M., Akers, M.J., 2005. Correlation of laboratory and production freeze drying cycles. Int. J. Pharm., 302, 56-67. doi: 10.1016/j.ijpharm.2005.06.022.

Kuu, W.Y., O'Bryan, K.R., Hardwick, L.M., Paul, T.W., 2011. Product mass transfer resistance directly determined during freeze-drying cycle runs using tunable diode laser absorption spectroscopy (TDLAS) and pore diffusion model. Pharm. Dev. Technol., 16, 343-357. doi: 10.3109/10837451003739263.

Lawrence, S., Lahteenmaki, R., 2014. Public biotech 2013-the numbers. Nat. Biotechnol., 32, 626-632. doi: 10.1038/nbt.2949.

Le Losq, C., Neuville, D.R., Chen, W., Florian, P., Massiot, D., Zhou, Z., Greaves, G.N., 2017. Percolation channels: A universal idea to describe the atomic structure and dynamics of glasses and melts. Scientific Reports, 7, 16490-12. doi: 10.1038/s41598-017-16741-3.

Lesker, K.J., 1996. Pressure Measurement Technical Notes. , 2019.

Lietta, E., Colucci, D., Distefano, G., Fissore, D., 2019. On the Use of Infrared Thermography for Monitoring a Vial Freeze-Drying Process. J. Pharm. Sci., 108, 391-398. doi: 10.1016/j.xphs.2018.07.025.

Ling, W., 2015. Using surface heat flux measurement to monitor and control a freeze drying process U.S. Patent 9121637 B2.

Liptak, B.J., 2003. Vacuum SensorsIn: Anonymous Instrument Engineers' Handbook, Volume One: Process Measurement and Analysis, CRC Press, pp. 795-806.

Liu, C., Snyder, S.R., Bard, A.J., 1997. Electrochemistry in Near-Critical and Supercritical Fluids. 9. Improved Apparatus for Water Systems (23−385 °C). The Oxidation of Hydroquinone and Iodide. The Journal of Physical Chemistry B, 101, 1180-1185. doi: 10.1021/jp9627741.

Liu, J., 2006. Physical Characterization of Pharmaceutical Formulations in Frozen and Freeze-Dried Solid States: Techniques and Applications in Freeze-Drying Development. Pharm. Dev. Technol., 11, 3-28. doi: 10.1080/10837450500463729.

Lu, X.F., Pikal, M.J., 2004. Freeze-drying of mannitol-trehalose-sodium chloride-based formulations: The impact of annealing on dry layer resistance to mass transfer and cake structure. Pharm. Dev. Technol., 9, 85-95. doi: 10.1081/PDT-120027421.

Lueckel, B., Bodmer, D., Helk, B., Leuenberger, H., 1998. Formulations of Sugars with Amino Acids or Mannitol-Influence of Concentration Ratio on the Properties of the Freeze-Concentrate and the Lyophilizate. Pharm. Dev. Technol., 3, 325-336. doi: 10.3109/10837459809009860.

Macdonald, J.R., Johnson,W.B., 2005. Fundamentals of Impedance SpectroscopyIn: Barsoukov, E., Macdonald, J.R. (Eds.), Impedance Spectroscopy: Theory, Experiment, and Applications, 2nd; 2 Ed., Wiley-Interscience, Chichester; New York, pp. 1-26.

MacKenzie, A.P., Derbyshire, W., Reid, D.S., 1977. Non-Equilibrium Freezing Behaviour of Aqueous Systems [and Discussion]. Philosophical Transactions of the Royal Society of London.B, Biological Sciences, 278, 167-189. doi: 10.1098/rstb.1977.0036.

May, J.C., 2004. Regulatory Control of Freeze-Dried Products: Importance and Evaluation of Residual MoistureIn: Rey, L., May, J.C. (Eds.), Freeze-Drying/Lyophilization of Pharmaceutical and Biological Products, Informa Healthcare, pp. 288-316.

Mayeresse, Y., Veillon, R., Sibille, P.H., Nomine, C., 2007. Freeze-drying process monitoring using a cold plasma ionization device. PDA J. Pharm. Sci. Technol., 61, 160.

Meissner, U., Stahl, H., Steinkellner, D., 2011. Detection of silicone oil leakages in freeze dryers. PDA journal of pharmaceutical science and technology, 65, 481-485. doi: 10.5731/pdajpst.2011.00748.

Meister, E., Gieseler, H., 2009. Freeze-dry microscopy of protein/sugar mixtures: Drying behavior, interpretation of collapse temperatures and a comparison to corresponding glass transition data. J. Pharm. Sci., 98, 3072-3087. doi: 10.1002/jps.21586.

Millman, M.J., Liapis, A.I., Marchello, J.M., 1985. An analysis of the lyophilization process using a sorption-sublimation model and various operational policies. AIChE J., 31, 1594-1604. doi: 10.1002/aic.690311003.

Milton, N., Pikal, M.J., Roy, M.L., Nail, S.L., 1997. Evaluation of manometric temperature measurement as a method of monitoring product temperature during lyophilization. PDA J. Pharm. Sci. Technol., 51, 7.

Moore, E.B., Molinero, V., 2011. Structural transformation in supercooled water controls the crystallization rate of ice. Nature, 479, 506-508. doi: 10.1038/nature10586.

Morris, N.M., Senior, F.W., 1991. Electric Circuits, Macmillan Education, Basingstoke.

Mousavi, R., Miri, T., Cox, P.W., Fryer, P.J., 2005. A Novel Technique for Ice Crystal Visualization in Frozen Solids Using X-Ray Micro-Computed Tomography. J. Food Sci., 70, e437-e442. doi: 10.1111/j.1365-2621.2005.tb11473.x.

Nail, S.L., Johnson, W., 1992. Methodology for in-process determination of residual water in freeze-dried products. Dev. Biol. Stand., 74, 137.

Nail, S.L., Searles, J.A., 2008. Elements of quality by design in development and scale-up of freeze-dried parenterals. BioPharm International, 21, 44-52.

Nail, S., Tchessalov, S., Shalaev, E., Ganguly, A., Renzi, E., Dimarco, F., Wegiel, L., Ferris, S., Kessler, W., Pikal, M., Sacha, G., Alexeenko, A., Thompson, T.N., Reiter, C., Searles, J., Coiteux, P., 2017. Recommended Best Practices for Process Monitoring Instrumentation in Pharmaceutical Freeze Drying—2017. AAPS PharmSciTech, 18, 2379-2393. doi: 10.1208/s12249-017-0733-1.

Nan, C.-., Shen, Y., Ma, J., 2010. Physical Properties of Composites Near Percolation. Annual Review of Materials Research, 40, 131-151. doi: 10.1146/annurev-matsci-070909-104529.

Neumann, K.H., 1961. Freeze drying apparatus US Patent 2994132 A.

Oddone, I., Fulginiti, D., Barresi, A.A., Grassini, S., Pisano, R., 2015. Non-Invasive Temperature Monitoring in Freeze Drying: Control of Freezing as a Case Study. Drying Technol, 33, 1621-1630. doi: 10.1080/07373937.2015.1040026.

Oetjen, G., 1999. Freeze-Drying, Wiley-VCH, Chichester; Weinheim.

Orazem, M.E., Tribollet, B., 2017. Time-Constant Dispersion.In: Orazem, M.E., Tribollet, B. (Eds.), Electrochemical Impedance Spectroscopy, 2nd Ed., John Wiley & Sons, Incorporated, New York, pp. 382-394.

Orazem, M.E., Tribollet, B., 2008. Constant Phase ElementsIn: Anonymous Electrochemical Impedance Spectroscopy, Wiley, New Jersey, pp. 237.

Parker, A., Rigby-Singleton, S., Perkins, M., Bates, D., Le Roux, D., Roberts, C.J., Madden-Smith, C., Lewis, L., Teagarden, D.L., Johnson, R.E., Ahmed, S.S., 2010. Determination of the Influence of Primary Drying Rates on the Microscale Structural Attributes and Physicochemical Properties of Protein Containing Lyophilized Products. J. Pharm. Sci., 99, 4616-4629. doi: 10.1002/jps.22185.

Parvis, M., Grassini, S., Barresi, A., 2012. , pp. 1994-1998.

Parvis, M., Grassini, S., Fulginiti, D., Pisano, R., Barresi, A.A., 2014. , pp. 1465.

Patel, S.M., Lobo, B., Shah, A., 2013. Practical considerations for freeze-drying process design, development and scale-up. American Pharmaceutical Review, 16.

Patel, S.M., Nail, S.L., Pikal, M.J., Geidobler, R., Winter, G., Hawe, A., Davagnino, J., Rambhatla Gupta, S., 2017. Lyophilized Drug Product Cake Appearance: What Is Acceptable? J. Pharm. Sci., 106, 1706-1721. doi: 10.1016/j.xphs.2017.03.014.

Patel, S.M., Pikal, M.J., 2009. Process Analytical Technologies (PAT) in freeze-drying of parenteral products. Pharm. Dev. Technol., 14, 567-587. doi: 10.3109/10837450903295116.

Patel, S.M., Bhugra, C., Pikal, M.J., 2009. Reduced Pressure Ice Fog Technique for Controlled Ice Nucleation during Freeze-Drying. AAPS PharmSciTech, 10, 1406-1411. doi: 10.1208/s12249-009-9338-7.

Patel, S.M., Doen, T., Pikal, M.J., 2010. Determination of End Point of Primary Drying in Freeze-Drying Process Control. AAPS PharmSciTech, 11, 73-84. doi: 10.1208/s12249-009-9362-7.

Pearson, D.S., Smith, G., 1998. Dielectric analysis as a tool for investigating the lyophilization of proteins. Pharmaceutical Science and Technology Today, 1, 108-117. doi: 10.1016/S1461-5347(98)00030-3.

Petzold, G., Aguilera, J.M., 2009. Ice Morphology: Fundamentals and Technological Applications in Foods. Food Biophysics, 4, 378-396. doi: 10.1007/s11483-009-9136-5.

Pieters, S., De Beer, T., Kasper, J.C., Boulpaep, D., Waszkiewicz, O., Goodarzi, M., Tistaert, C., Friess, W., Remon, J., Vervaet, C., Vander Heyden, Y., 2012. Near-Infrared Spectroscopy for In-Line Monitoring of Protein Unfolding and Its Interactions with Lyoprotectants during Freeze-Drying. Anal. Chem., 84, 947-955. doi: 10.1021/ac2022184.

Pieters, S., De Beer, T., Vander Heyden, Y., 2012. Near-infrared and Raman spectroscopy: Potential tools for monitoring of protein conformational instability during freeze-drying processes. American Pharmaceutical Review, 15.

Pikal, M.J., 1985. Use of laboratory data in freeze drying process design: heat and mass transfer coefficients and the computer simulation of freeze drying. Journal of parenteral science and technology : a publication of the Parenteral Drug Association, 39, 115.

Pikal, M.J., Shah, S., 1997. Intravial distribution of moisture during the secondary drying stage of freeze drying. PDA journal of pharmaceutical science and technology, 51, 17.

Pikal, M.J., Pikal, M.J., Dellerman, K.M., Dellerman, K.M., Roy, M.L., Roy, M.L., Riggin, R.M., Riggin, R.M., 1991. The effects of formulation variables on the stability of freeze-dried human growth hormone. Pharm. Res., 8, 427-436. doi: 10.1023/A:1015834724528.

Pikal, M.J., Roy, M.L., Shah, S., 1984. Mass and Heat-Transfer in Vial Freeze-Drying of Pharmaceuticals - Role of the Vial. J. Pharm. Sci., 73, 1224-1237. doi: 10.1002/jps.2600730910.

Pikal, M.J., Shah, S., Roy, M.L., Putman, R., 1990. The secondary drying stage of freeze drying: drying kinetics as a function of temperature and chamber pressure. Int. J. Pharm., 60, 203-207. doi: 10.1016/0378-5173(90)90074-E.

Pikal, M.J., Shah, S., Senior, D., Lang, J.E., 1983. Physical Chemistry of Freeze-drying: Measurement of Sublimation Rates for Frozen Aqueous Solutions by a Microbalance Technique. J. Pharm. Sci., 72, 635-650. doi: 10.1002/jps.2600720614.

Pikal, M.J., 1990. Freeze-drying of proteins. Part I: Process design. BioPharm, 3, 18-27.

Pikal, M.J., Rambhatla, S., Ramot, R., 2002. The impact of the freezing stage in lyophilization: Effects of the ice nucleation temperature on process design and product quality. American Pharmaceutical Review, 5, 48-52.

Pisano, R., Barresi, A.A., Barresi, A.A., Capozzi, L.C., Novajra, G., Oddone, I., Vitale-Brovarone, C., 2017. Characterization of the mass transfer of lyophilized products based on X-ray micro-computed tomography images. Drying Technol, 35, 933-938. doi: 10.1080/07373937.2016.1222540.

Pisano, R., Barresi, A.A., Fissore, D., 2011. Innovation in Monitoring Food Freeze Drying. Drying Technol, 29, 1920-1931. doi: 10.1080/07373937.2011.596299.

Pisano, R., Fissore, D., Barresi, A.A., 2011. Heat Transfer in Freeze-Drying ApparatusIn: Anonymous Developments in Heat Transfer, Marco Aurélio Dos Santos Bernardes, InTech.

Pisano, R., Fissore, D., Velardi, S.A., Barresi, A.A., 2010. In-Line Optimization and Control of an Industrial Freeze-Drying Process for Pharmaceuticals. J. Pharm. Sci., 99, 4691-4709. doi: 10.1002/jps.22166.

Pollock, D.D., 1991. Thermocouples: Theory and Properties, 1st Ed., CRC Press, Boca Raton.

Popov, I., Lunev, I., Khamzin, A., Gutina, A., Gusev, Y., Feldman, Y., 2017. The low-temperature dynamic crossover in the dielectric relaxation of ice I-h. PHYSICAL CHEMISTRY CHEMICAL PHYSICS, 19, 28610-28620. doi: 10.1039/c7cp05731h.

Pyne, A., Surana, R., Suryanarayanan, R., 2002. Crystallization of Mannitol below Tg' during Freeze-Drying in Binary and Ternary Aqueous Systems. Pharm. Res., 19, 901-908. doi: 10.1023/A:1016129521485.

Rambhatla, S., Obert, J.P., Luthra, S., Bhugra, C., Pikal, M.J., 2005. Cake Shrinkage During Freeze Drying: A Combined Experimental and Theoretical Study. Pharm. Dev. Technol., 10, 33-40. doi: 10.1081/PDT-35871.

Rambhatla, S., Pikal, M.J., 2003. Heat and mass transfer scale-up issues during freeze-drying, I: Atypical radiation and the edge vial effect. AAPS PharmSciTech, 4, 22-31. doi: 10.1208/pt040214.

Rambhatla, S., Ramot, R., Bhugra, C., Pikal, M.J., 2004a. Heat and mass transfer scale-up issues during freeze drying: II. Control and characterization of the degree of supercooling. AAPS PharmSciTech, 5, 54-62. doi: 10.1208/pt050458.

Rambhatla, S., Ramot, R., Bhugra, C., Pikal, M.J., 2004b. Heat and mass transfer scale-up issues during freeze drying: II. Control and characterization of the degree of supercooling. AAPS PharmSciTech, 5, 54-62. doi: 10.1208/pt050458.

Randolph, T.W., Searles, J.A., 2002. Freezing and annealing phenomena in lyophilization: Effect upon primary drying rate, morphology, and heterogeneity. American Pharmaceutical Review, 5, 46.

Rathore, A.S., 2009. Roadmap for implementation of quality by design (QbD) for biotechnology products. Trends Biotechnol., 27, 546-553. doi: 10.1016/j.tibtech.2009.06.006.

Reubsaet, J.L.E., Beijnen, J.H., Bult, A., van Maanen, R.J., Marchal, J.A.D., Underberg, W.J.M., 1998. Analytical techniques used to study the degradation of proteins and peptides: physical instability. J. Pharm. Biomed. Anal., 17, 979-984. doi: 10.1016/S0731-7085(98)00064-8.

Rey, L.R., 1960. Thermal analysis of eutectics in freezing solutions. Ann. N. Y. Acad. Sci., 85, 510-534. doi: 10.1111/j.1749-6632.1960.tb49979.x.

Rey, L., May, J.C., 2004a. Freeze Drying-Lyophilization of Pharmaceutical and Biological Products, 3rd Ed., Informa Healthcare, London.

Rey, L., May, J.C., 2004b. Freeze Drying-Lyophilization of Pharmaceutical and Biological Products, 3rd Ed., Informa Healthcare, London.

Rey, L., 2010. Freeze-Drying, Lyophilization of Pharmaceutical and Biological Products, 3. ed. Ed., Informa Healthcare, New York.

Roos, Y.H., Finley, J.W., deMan, J.M., 2018. WaterIn: deMan, J.M., Finley, J.W., Hurst, W.J., Lee, C. (Eds.), Principles of Food Chemistry, 4th 2018 Ed., Springer International Publishing AG, Cham, pp. 1-37.

Roth, C., Winter, G., Lee, G., 2001. Continuous measurement of drying rate of crystalline and amorphous systems during freeze-drying using an in situ microbalance technique. J. Pharm. Sci., 90, 1345-1355. doi: 10.1002/jps.1087.

Rowe, T.W.G., Greiff, D., Monroe, J., 1980. , pp. 129-139.

Roy, M.L., Pikal, M.J., 1989. Process-Control in Freeze-Drying - Determination of the End-Point of Sublimation Drying by an Electronic Moisture Sensor. Journal of Parenteral Science and Technology, 43, 60-66.

Rumble, J., 2019. CRC Handbook of Chemistry and Physics, 100th Ed., CRC Press LLC, New York.

Sangshetti, J.N., Deshpande, M., Zaheer, Z., Shinde, D.B., Arote, R., 2017. Quality by design approach: Regulatory need. Arabian Journal of Chemistry, 10, S3412-S3425. doi: 10.1016/j.arabjc.2014.01.025.

Sarciaux, J.E., Hageman, M.J., 1997. Effects of Bovine Somatotropin (rbSt) Concentration at Different Moisture Levels on the Physical Stability of Sucrose in Freeze-Dried rbSt/Sucrose Mixtures. J. Pharm. Sci., 86, 365-371. doi: 10.1021/js960217k.

Schneid, S.C., Gieseler, H., Kessler, W.J., Pikal, M.J., 2009. Non-Invasive Product Temperature Determination during Primary Drying using Tunable Diode Laser Absorption Spectroscopy. J. Pharm. Sci., 98, 3406-3418. doi: 10.1002/jps.21522.

Schneid, S.C., Johnson, R.E., Lewis, M.L., Stärtzel, P., Gieseler, H., 2015. Application of Process Analytical Technology for Monitoring Freeze-Drying of an Amorphous Protein Formulation: Use of Complementary Tools for Real-Time Product Temperature Measurements and Endpoint Detection. J. Pharm. Sci., 104, 1741-1749. doi: 10.1002/jps.24389.

Schneid, S., Gieseler, H., 2008. Evaluation of a New Wireless Temperature Remote Interrogation System (TEMPRIS) to Measure Product Temperature During Freeze Drying. Aaps Pharmscitech, 9, 729-739. doi: 10.1208/s12249-008-9099-8.

Scutella, B., Passot, S., Bourles, E., Fonseca, F., Trelea, I.C., 2017. How Vial Geometry Variability Influences Heat Transfer and Product Temperature During Freeze-Drying. J. Pharm. Sci., 106, 770-778. doi: 10.1016/j.xphs.2016.11.007.

Scutella, B., Plana-Fattori, A., Passot, S., Bourles, E., Fonseca, F., Flick, D., Trelea, I.C., 2017. 3D mathematical modelling to understand atypical heat transfer observed in vial freeze-drying. Appl. Therm. Eng., 126, 226-236. doi: 10.1016/j.applthermaleng.2017.07.096.

Scutella, B., Trelea, I.C., Bourlès, E., Fonseca, F., Passot, S., 2018. Determination of the dried product resistance variability and its influence on the product temperature in pharmaceutical freeze-drying. European Journal of Pharmaceutics and Biopharmaceutics, 128, 379-388. doi: 10.1016/j.ejpb.2018.05.004.

Searles, J.A., Carpenter, J.F., Randolph, T.W., 2001a. Annealing to optimize the primary drying rate, reduce freezing-induced drying rate heterogeneity, and determine T-g ' in pharmaceutical lyophilization. J. Pharm. Sci., 90, 872-887. doi: 10.1002/jps.1040.

Searles, J.A., 2004. Freezing and Annealing Phenomena in LyophilizationIn: Rey, L., May, J.C. (Eds.), Freeze Drying/Lyophilization of Pharmaceutical and Biological Products, 3rd Ed., Vol. 206, Informa Healthcare, London, pp. 52:81.

Searles, J.A., Carpenter, J.F., Randolph, T.W., 2001b. The ice nucleation temperature determines the primary drying rate of lyophilization for samples frozen on a temperature-controlled shelf. J. Pharm. Sci., 90, 860-871. doi: 10.1002/jps.1039.

Shanley, A., 2017. Modernizing Lyophilization: A technology roadmap aims to drive and consolidate improvements in a process that has remained unchanged for more than 70 years. Pharmaceutical Technology Europe, 29, 28.

Smith, G., Arshad, M.S., Polygalov, E., Ermolina, I., 2014a. Factors Affecting the Use of Impedance Spectroscopy in the Characterisation of the Freezing Stage of the Lyophilisation Process: the Impact of Liquid Fill Height in Relation to Electrode Geometry. AAPS PharmSciTech, 15, 261-269. doi: 10.1208/s12249-013-0054-y.

Smith, G., Arshad, M.S., Polygalov, E., Ermolina, I., 2014b. Through-Vial Impedance Spectroscopy of the Mechanisms of Annealing in the Freeze-Drying of Maltodextrin: The Impact of Annealing Hold Time and Temperature on the Primary Drying Rate. J. Pharm. Sci., 103, 1799-1810. doi: 10.1002/jps.23982.

Smith, G., Arshad, M.S., Polygalov, E., Ermolina, I., 2013. An application for impedance spectroscopy in the characterisation of the glass transition during the lyophilization cycle: The example of a 10% w/v maltodextrin solution. European Journal of Pharmaceutics and Biopharmaceutics, 85, 1130-1140. doi: 10.1016/j.ejpb.2013.08.004.

Smith, G., Arshad, M.S., Polygalov, E., Ermolina, I., McCoy, T.R., Matejtschuk, P., 2017. Process Understanding in Freeze-Drying Cycle Development: Applications for Through-Vial Impedance Spectroscopy (TVIS) in Mini-pilot Studies. Journal of Pharmaceutical Innovation, 12, 26-40. doi: 10.1007/s12247-016-9266-5.

Smith, G., Jeeraruangrattana, Y., 2019. Through-Vial Impedance Spectroscopy (TVIS): A New Method for Determining the Ice Nucleation Temperature and the Solidification End PointIn: Fissore, D., Pisano, R., Barresi, A. (Eds.), Freeze Drying of Pharmaceutical Products, CRC Press, pp. N.D.

Smith, G., Jeeraruangrattana, Y., Ermolina, I., 2018. The application of dual-electrode through vial impedance spectroscopy for the determination of ice interface temperatures, primary drying rate and vial heat transfer coefficient in lyophilization process development. European Journal of Pharmaceutics and Biopharmaceutics, 130, 224-235. doi: 10.1016/j.ejpb.2018.05.019.

Smith, G., Polygalov, E., 2019. Through Vial Impedance Spectroscopy (TVIS): A Novel Approach to Process Understanding for Freeze-Drying Cycle DevelopmentIn: Ward, K.R., Matejtschuk, P. (Eds.), Lyophilization of Pharmaceuticals and Biologicals: New Technologies and Approaches, Springer New York, New York, NY, pp. 241-290.

Smith, G., Polygalov, E., Arshad, M.S., Page, T., Taylor, J., Ermolina, I., 2013. An impedance-based process analytical technology for monitoring the lyophilisation process. Int. J. Pharm., 449, 72-83. doi: 10.1016/j.ijpharm.2013.03.060.

Suherman, P.M., Taylor, P.M., Smith, G., 2002. Development of a Remote Electrode System for Monitoring the Water Content of Materials Inside a Glass Vial. Pharm. Res., 19, 337-344. doi: 10.1023/A:1014455304527.

Sutherland, D.T., MacKenzie, A.P., Wise, D.B., 1997. Probe positioning device for a flask freeze drying 6th U.S. Patent 5689895 A.

Sylvester, B., Porfire, A., Van Bockstal, P., Porav, S., Achim, M., Beer, T.D., Tomuţă, I., 2018. Formulation Optimization of Freeze-Dried Long-Circulating Liposomes and In-Line Monitoring of the Freeze-Drying Process Using an NIR Spectroscopy Tool. J. Pharm. Sci., 107, 139-148. doi: 10.1016/j.xphs.2017.05.024.

Tang, X.L., Nail, S.L., Pikal, M.J., 2006. Evaluation of manometric temperature measurement, a process analytical technology tool for freeze-drying: Part I, product temperature measurement. Aaps Pharmscitech, 7, 14.

Tang, X.L., Pikal, M.J., 2004. Design of freeze-drying processes for pharmaceuticals: Practical advice. Pharm. Res., 21, 191-200. doi: PHAM.0000016234.73023.75.

Tang, X.(., Nail, S.L., Pikal, M.J., 2005. Freeze-Drying Process Design by Manometric Temperature Measurement: Design of a Smart Freeze-Dryer. Pharm. Res., 22, 685-700. doi: 10.1007/s11095-005-2501-2.

Tang, X.C., Nail, S.L., Pikal, M.J., 2006a. Evaluation of manometric temperature measurement (MTM), a process analytical technology tool in freeze drying, part III: Heat and mass transfer measurement. AAPS PharmSciTech, 7, E105-E111. doi: 10.1208/pt070497.

Tang, X.C., Nail, S.L., Pikal, M.J., 2006b. Evaluation of manometric temperature measurement, a process analytical technology tool for freeze-drying: Part II measurement of dry-layer resistance. AAPS PharmSciTech, 7, E77-E84. doi: 10.1208/pt070493.

Tchessalov, S., 2017. Application of modelling to lyophilization process design and scale up process validation approaches.

Tempris, 2020. Tempris Lyophilization – Automated Sensor Loading , 2020.

Tenedini, K.J., Jr. Bart, S.G., 2001. Freeze drying apparatus and method employing vapor flow monitoring and/or vacuum pressure control U.S. Patent 622687 B1.

Thompson, T.N., Jr. Ling, W., 2013. Freeze drying method U.S. Patent 8434240 B2.

Trappler, E.H., 2013. Contemporary Approaches to Development and Manufacturing of Lyophilized ParenteralsIn: Kohle, P., Rathore, N., Shah, M. (Eds.), Sterile Product Development : Formulation, Process, Quality and Regulatory Considerations, 2013th Ed., Vol. 6, Springer, New York, NY, pp. 275-213.

Trochim, W.M., Donnelly, J.P., Arora, K., 2014. Research Methods: The Essential Knowledge Base, 2nd Ed., Cengage Learning, GB.

Velardi, S.A., Hammouri, H., Barresi, A.A., 2009. In-line monitoring of the primary drying phase of the freeze-drying process in vial by means of a Kalman filter based observer. Chem. Eng. Res. Design, 87, 1409-1419. doi: 10.1016/j.cherd.2009.03.011.

Velardi, S.A., Barresi, A.A., 2008. Development of simplified models for the freeze-drying process and investigation of the optimal operating conditions. Chem. Eng. Res. Design, 86, 9-22. doi: //dx.doi.org.proxy.library.dmu.ac.uk/10.1016/j.cherd.2007.10.007.

Velardi, S.A., Rasetto, V., Barresi, A.A., 2008. Dynamic Parameters Estimation Method: Advanced Manometric Temperature Measurement Approach for Freeze-Drying Monitoring of Pharmaceutical Solutions. Ind Eng Chem Res, 47, 8445-8457. doi: 10.1021/ie7017433.

Vollrath, I., Pauli, V., Friess, W., Freitag, A., Hawe, A., Winter, G., 2017. Evaluation of Heat Flux Measurement as a New Process Analytical Technology Monitoring Tool in Freeze Drying. J. Pharm. Sci., 106, 1249-1257. doi: 10.1016/j.xphs.2016.12.030.

Walsh, G., 2018. Biopharmaceutical benchmarks 2018. Nat. Biotechnol., 36, 1136-1145. doi: 10.1038/nbt.4305.

Wang, M., 2010. Understandable Electric Circuits, Institution of Engineering and Technology, London.

Ward, K.R., Matejtschuk, P., 2004. The Use of Microscopy, Thermal Analysis, and Impedance Measurements to Establish Critical Formulation Parameters for Freeze-Drying Cycle Development.In: Rey, L.,May, J.C. (Ed.), Freeze Drying-Lyophilization of Pharmaceutical and Biological Products, 3rd Ed., Informa Healthcare, London, pp. 112-135.

Ward, K., Matejtschuk, P., 2019. Characterization of Formulations for Freeze-DryingIn: Ward, K., Matejtschuk, P. (Eds.), Lyophilization of Pharmaceuticals and Biologicals. Methods in Pharmacology and Toxicology, Humana Press, New York, NY, pp. 1-32.

Wiggenhorn, M., Presser, I., Winter, G., 2005. The current state of PAT in freeze-drying. American Pharmaceutical Review, 8, 44.

Willemer, H., 1992. Measurements of temperatures, ice evaporation rates and residual moisture contents in freeze-drying. Dev. Biol. Stand., 74, 123-136.

Yadav, A., Dahiya, M.S., Narwal, P., Hooda, A., Agarwal, A., Khasa, S., 2017. Electrical characterization of lithium bismuth borate glasses containing cobalt/vanadium ions. Solid State Ionics, 312, 21-31. doi: 10.1016/j.ssi.2017.10.006.

Yoshioka, S., Aso, Y., 2005. Glass Transition-Related Changes in Molecular Mobility below Glass Transition Temperature of Freeze-Dried Formulations, as Measured by Dielectric Spectroscopy and Solid State Nuclear Magnetic Resonance. J. Pharm. Sci., 94, 275-287. doi: 10.1002/jps.20244.

Yoshioka, S., Aso, Y., Kojima, S., 1999. The Effect of Excipients on the Molecular Mobility of Lyophilized Formulations, as Measured by Glass Transition Temperature and NMR Relaxation-Based Critical Mobility Temperature. Pharm. Res., 16, 135-140. doi: 10.1023/A:1018891317006.

Zhai, S., Taylor, R., Sanches, R., Slater, N.K.H., 2003. Measurement of lyophilisation primary drying rates by freeze-drying microscopy. Chemical Engineering Science, 58, 2313-2323. doi: 10.1016/S0009-2509(03)00090-3.

Zhai, S., Su, H., Taylor, R., Slater, N.K.H., 2005. Pure ice sublimation within vials in a laboratory lyophiliser; comparison of theory with experiment. Chemical Engineering Science, 60, 1167-1176. doi: 10.1016/j.ces.2004.09.078.

12 Poster Presentations

Multiplexing Through Vial Impedance Spectroscopy (TVIS) with Comparative Pressure Measurement for the Determination of the Primary Drying Endpoint of Immunoglobulin (IgG)

ISL-FD's 9th International Symposium on Lyophilization of Pharmaceuticals, September 2-6, 2019, Ghent, Belgium

Bhaskar Pandya[a], Paul Matejtschuk[b], Yowwares Jeeraruangrattana[a], Geoff Smith[a], Irina Ermolina[a]
[a]Leicester School of Pharmacy, De Montfort University, Leicester, United Kingdom
[b]National Institute of Biological Standards and Control (NIBSC), Potters Bar, United Kingdom

Introduction

- Attaining a long-term stability by freeze-drying can be attractive as it can **eliminate the need for cold chain storage** of biopharmaceutical products (e.g. proteins).
- A precise determination of the point of **complete ice removal** during primary drying has been one of the strategies for avoiding product collapse or eutectic melt [1].
- Common batch techniques include the **comparative pressure measurement**: the Pirani gauge (more sensitive to the water vapour) with a capacitance manometer (CM) (controls the absolute pressure of the chamber). The point at which the Pirani pressure approaches that of CM is taken as the endpoint for the whole batch [2].
- Single vial techniques (e.g. thermocouples, resistance temperature detectors, etc) involve inserting an **invasive probe** into the product to measure the product temperature, which when equals the shelf temperature, is generally taken as the endpoint for the batch; but it is known that **probe containing vials dry faster** than the vials without the invasive probes and front row **edge vials** receive an additional heat contribution via heat **radiation** from the Plexiglass door [3].
- Through Vial Impedance Spectroscopy (**TVIS**) **senses the amount of ice in the vial in real time** by measuring the dielectric properties of the frozen solid by employing a pair of copper electrodes attached externally to a single vial (i.e. **non-product invasive**) [4].
- Previously, the time-line of the imaginary part capacitance at 1 kHz, C"(1kHz), has been used to determine the primary drying endpoint for a simple sucrose solution [4].

Aim and Objectives

The aim of this study is to develop an impedance-based methodology to determine the primary drying endpoint with the following objectives:

- to use the time-line of the C'(100kHz) parameter for determining the primary drying endpoint of ice in a complex protein formulation located at the edge and the core
- to compare the endpoint from TVIS with the endpoint given by the comparative pressure measurement

Materials and Methods

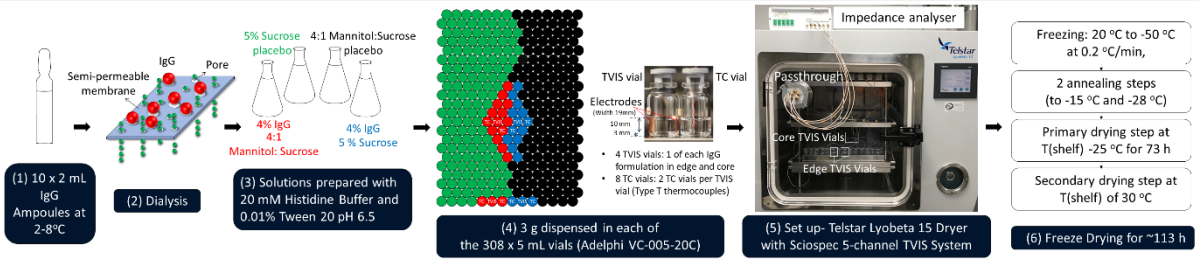

Results and Discussion

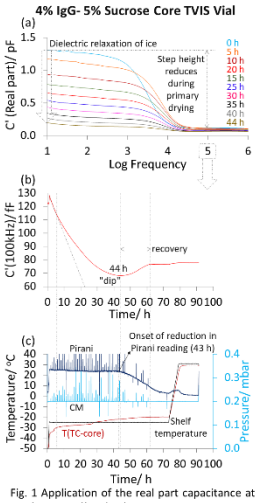

Fig. 1 Application of the real part capacitance at 100 kHz, i.e. C'(100kHz): TVIS is most sensitive to the height of the ice cylinder in intimate contact with the glass wall in the region bounded by the electrodes. When the ice mass retracts from the glass wall, the characteristic "dip" and recovery in C'(100kHz) are subsequently used to track the point of complete ice removal in a single vial.

- The dielectric relaxation of ice was characterized by a step in the real part around 10 kHz (Fig.1a) where,

$$Step\ Height \cong C'(10Hz) - C'(100kHz)$$

- The step height is proportional to the height of the sublimation front which manifests as an ice cylinder when it is in intimate contact with the glass wall bounded by the electrodes.
- For the lgG-sucrose formulation in the core vial, the step height had decreased by 85% by ~44 h, yet the Pirani vapour pressure was still approaching the CM value (Fig.1c).
- The time-line of C'(100kHz) was then used to track sublimation and understand the changes in the shape of the sublimation interface (Fig.1b).
- First 5 h: C'(100kHz) decreased linearly with time; suggests the sublimation front was drying in a horizontal plane.
- 5 to 44 h: the rate of decrease in C'(100kHz) exhibited a non-linear behavior; suggests the shape of the sublimation front had changed over this period.
- At 44 h: a characteristic dip in the time-line was observed; corresponds to the point when the ice mass had retracted from the glass wall.
- After 44 h: C'(100kHz) started to recover as it was still sensitive to the remaining ice mass.
- In Fig.2(b to e), the inflection in time-line of d(C'100kHz)/dt after the completion of the C'(100kHz) recovery was used as an endpoint indicator for all TVIS vials.
- **Endpoint Summary**: Sucrose-lgG edge vial (Fig.2b) dried 11 h earlier than the onset of the reduction in the Pirani vapour pressure (43 h). In addition, the TVIS endpoint for both core TVIS vials (Fig.2d&e) occurred at 62 h and yet the Pirani was still active until 73 h. This may be due to one or both of two factors: (i) other core vials were still drying (most probable) and/or (ii) the Pirani continued to sense water vapour in the dryer even when all the ice had sublimed (least probable).

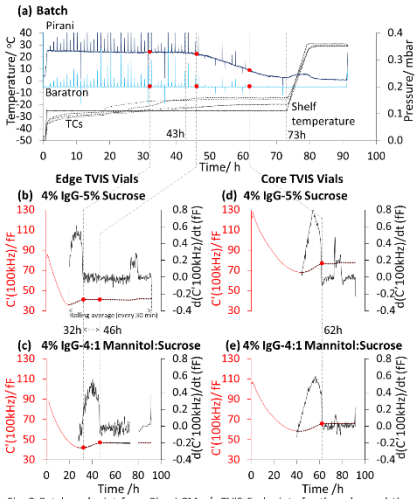

Fig. 2 Batch endpoint from Pirani-CM v/s TVIS Endpoints for the edge and the core TVIS vials containing lgG-Sucrose and lgG-Mannitol rich formulations

TVIS Vial Location	4% lgG with 5% Sucrose	4% lgG with 4:1 Mannitol:Sucrose lgG
Front Edge	32 h	46 h
Core	62 h	62 h

Conclusion

- Core vials may take almost twice as long to dry than edge vials and/or not all core vials dry at the same time.
- TVIS used in conjunction with batch sensors can enhance one's understanding of the hot and cold spots on the shelf.

References

[1] S.M. Patel, T. Doen, M.J. Pikal, Determination of End Point of Primary Drying in Freeze-Drying Process Control, Aaps Pharmscitech 11 (2010) 73-84.
[2] S.L. Nail, W. Johnson, Methodology for in-process determination of residual water in freeze-dried products, Dev. Biol. Stand. 74 (1992) 137.
[3] S. Nail, S. Tchessalov, E. Shalaev, A. Ganguly, E. Renzi, F. Dimarco, L. Wegiel, S. Ferris, W. Kessler, M. Pikal, G. Sacha, A. Alexeenko, T.N. Thompson, C. Reiter, J. Searles, P. Coiteux, Recommended Best Practices for Process Monitoring Instrumentation in Pharmaceutical Freeze Drying—2017, Aaps Pharmscitech 18 (2017) 2379-2393.
[4] G. Smith, E. Polygalov, M.S. Arshad, T. Page, J. Taylor, I. Ermolina, An impedance-based process analytical technology for monitoring the lyophilisation process, Int. J. Pharm. 449 (2013) 72-83.

Acknowledgements

This study was undertaken as part of the Innovate UK AtlasBio Project. Special thanks to Dr Paul Matejtschuk and team at NIBSC.

Application of Through Vial Impedance Spectroscopy for Lyophilization Process Development

Freeze Drying of Pharmaceuticals and Biologicals, September 18 – 21, 2018, Garmisch-Partenkirchen, Germany

Bhaskar Pandya, Geoff Smith, Eugene Polygalov, Irina Ermolina, Leicester School of Pharmacy, De Montfort University, Leicester, United Kingdom

1. INTRODUCTION

Freeze drying process and critical factors

Freeze- drying or lyophilisation is a widely used stabilisation strategy for the downstream processing of several pharmaceutical and biological compounds. A sound understanding of the various heat transfer mechanisms (conduction, convection and radiation) is important for delivering products with the required critical quality attributes. The overall heat contribution from these heat sources is represented by a numerical value termed "vial heat transfer coefficient" (K_v). Vial location is one of the key factors that impacts the value of K_v particularly for the edge vials and the centre/core vials.[1]

Single vial and batch techniques to determine K_v

In practice, K_v is most commonly determined by a gravimetric method and less frequently by the batch techniques such as the Tuneable Diode Laser Absorption Spectroscopy (TDLAS) (Fig 1).

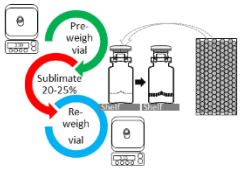

Fig 1A: Illustration of the Gravimetric method for individual vial K_v after 20-25 % ice sublimation

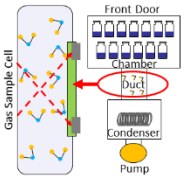

Fig.1B: TDLAS for batch K_v without interruption

The gravimetric method (Fig.1A) involves loading the dryer with pre-weighed vials and weighing them individually after interrupting the primary drying stage following the sublimation of 20-25 % of ice. This approach assumes that the shape of the sublimation interface and the contact of the ice with the walls of the vial won't have changed over this period and therefore the contributions from the various heat transfer mechanisms also won't have changed and therefore drying will have occurred at a constant rate.

In contrast, TDLAS has an advantage over the gravimetric method in that with TDLAS, it is possible to determine K_v without interrupting primary drying. Nevertheless, it doesn't allow one to obtain K_v from individual vials. Further, the application of this technique to model the entire batch relies on a numerical factor that accounts for the edge vial effect.[1] For example, it is assumed that the edge vials dry 50 % faster (i.e. a factor of 1.5) than the core vials.

Through vial impedance spectroscopy (TVIS)

Through vial impedance spectroscopy (TVIS) measures the electrical properties of the glass vial and the contents of the vial. It comprises an electrode system attached on the outside of a standard glass vial. With a dual electrode system, it has been possible to determine K_v over a steady state period for a core vial.[2] The peak imaginary amplitude, C''_{PEAK}, is a direct measure of the ice mass in the vial, and the peak frequency, F_{PEAK}, serves two important roles: (i) it is an indicator of the point when the sublimation interface changes shape and therefore, informs one of a finite time period over which K_v can be determined, (ii) its sensitivity to temperature makes it a reliable parameter for estimating the product temperature during primary drying.

2. AIM

The aim of this work is to demonstrate the application of TVIS for the determination of surrogate drying rate (dC"PEAK/dt) across the shelf.

2. OBJECTIVES

- To calibrate F_{PEAK} from the electrode system with the temperature from a thermocouple in the neighbouring vial during re-heating
- To predict ice temperature, $T(F_{PEAK})$, during primary drying
- To compensate for the temperature dependency of C''_{PEAK} during primary drying
- To define a period of steady state during primary drying
- To assess the impact of vial location on the steady state period and the surrogate drying rate

3. MATERIALS AND METHODS

160 standard 10 mL vials (manufactured by Schott) containing ~3g of double distilled water were used in this work, out of which 5 were modified TVIS measurement vials with copper electrodes (19 by 10 mm), with 4 out of the 5 accompanied by the nearest neighbour vials containing a thermocouple submersed in the liquid at a height corresponding to the midpoint of the liquid bound by the electrodes (Fig. 2A&B). The freeze drying cycle (Fig. 2C) was executed in a Virtis Advantage Plus laboratory freeze dryer equipped with a pass-through for TVIS measurement (Fig. 2D).

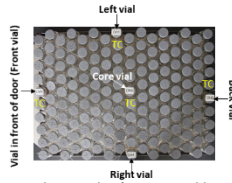

Fig. 2A: Location of measurement vials

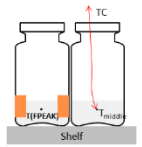

Fig. 2B: Position of thermocouple

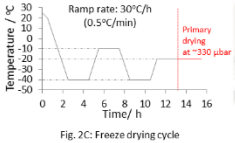

Fig. 2C: Freeze drying cycle

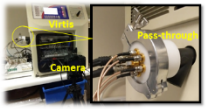

Fig. 2D: Virtis Advantage Plus freeze dryer with a pass-through for TVIS measurement

4. RESULTS AND DISCUSSION

Temperature calibration

The relationships of both F_{PEAK} and C''_{PEAK} with temperature follow a 2nd order polynomial function during re-heating. Fig. 3 demonstrates the temperature dependency for the front TVIS vial.

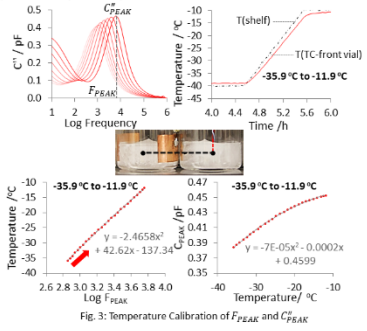

Fig. 3: Temperature Calibration of F_{PEAK} and C''_{PEAK}

Prediction of ice temperature and standardization of C''_{PEAK} in primary drying

The polynomial coefficients from the temperature calibration of F_{PEAK} are used to predict ice temperature, $T(F_{PEAK})$, during primary drying. Fig. 4A shows the ice temperature predicted for the front TVIS vial.

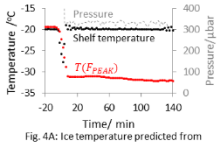

Fig. 4A: Ice temperature predicted from the calibration routine for the front vial

In Fig. 4B, it is clear that C''_{PEAK} is also sensitive to temperature over the first 12 min of primary drying when the shelf temperature and the chamber pressure stabilize. Therefore, C''_{PEAK} requires a standardization factor ($\emptyset$) for temperature compensation:

$$\emptyset(T) = \frac{C''_{PEAK}(T)}{C''_{PEAK}(T_{ref})}$$

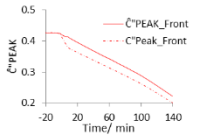

Fig. 4B: Temperature compensation of C''_{PEAK} in primary drying

$C''_{PEAK}(T)$ and $C''_{PEAK}(T_{ref})$ are the peak amplitudes at temperatures (T) and reference temperature (T_{ref}) during the re-heating ramp. In this work, a temperature of -20 °C was used as the reference temperature value

The expression for $\emptyset(T)$ can be re-written in terms of the polynomial coefficients from the temperature calibration of C''_{PEAK}:

$$(T) = \frac{aT^2+bT+c}{aT_{ref}^2+bT_{ref}+c}$$

Values of C''_{PEAK} during primary drying are then standardized to the reference temperature by dividing $C''_{PEAK}(T)$ by $\emptyset(T)$ to give a standardized peak amplitude of $\hat{C}''_{PEAK}$ (Fig. 4B)

$$\hat{C}''_{PEAK} = \frac{C''_{PEAK}(T)}{\emptyset(T)}$$

Determination of the period of steady state during primary drying

It is clear from the photographic images of the front TVIS vial (Fig. 5A) that the shape of the sublimation interface changed over the course of primary drying such that the ice developed a more prominent cone or a dome shaped top surface owing to the additional heat contribution from

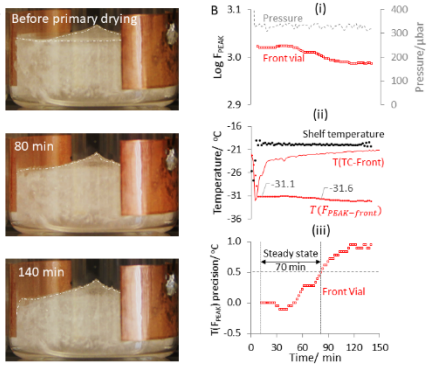

Fig. 5: (A) Images of the sublimation interface in the front vial; (B) Determination of steady state

radiation. It follows that the contact between the ice and the side wall of the glass vial degraded over time. This phenomenon was registered by F_{PEAK} whose time profile suggested the point when the curvature of the sublimation interface started to change (80 min), as in Fig. 5B(i). This becomes clearer when one looks at the trajectory of $T(F_{PEAK})$ which decreases as the ice temperature, sensed by the thermocouple in the neighbouring vial, increases as shown in Fig. 5B(ii).

It is true that as the contact between the ice and the glass wall degrades, the drying rate decreases and the ice temperature increases which is sensed by the thermocouple. However in this case, the thermocouple appeared to sense the gas temperature in the void formed around the tip of the thermocouple's sensing bead.

In order to define the period of steady state (Fig. 5Biii), a pre-defined precision of 0.5 °C for the change in $T(F_{PEAK})$ from -31.1 °C was considered because that corresponded to the first point (12 min) when the shelf temperature and the chamber pressure stabilised. The steady state period lasted for the next 70 min when $T(F_{PEAK})$ was -31.6 °C (82 min) and therefore, agreed with the pre-defined temperature limit.

Assessment of the rate of change in $\hat{C}''_{PEAK}$ during steady state primary drying

It is important to recognize that the methodologies discussed in the previous sections for the front edge vial were also used for studying the other TVIS vials except for the right edge vial which did not accompany a thermocouple in the neighbour vial due to an equipment limitation. The data in Fig. 6 are summarised in Table 1 which clearly demonstrates the heterogeneity of the heat transfer process across the batch.

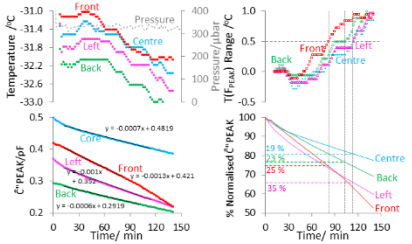

Fig. 6: Heterogeneity in the surrogate drying rate across the shelf

Table 1: Comparison of drying behaviour of TVIS vials over the steady state period

Vial	Steady state period/min	% reduction in $\hat{C}''_{PEAK}$	d($\hat{C}''_{PEAK}$)/dt Factor
Front edge	82	25	1.86
Left edge	114	35	1.43
Back edge	102	23	1.16
Core	114	19	1.00

The use of $T(F_{PEAK})$ to define the steady state period for the vials located in different positions of the shelf is justified when one considers the % reduction in $\hat{C}''_{PEAK}$ which agrees with the gravimetric approach of interrupting primary drying after 20-25 % removal of ice. This reaffirms that over the estimated steady state period, the contributions from the heat sources did not change and therefore drying occurred at a constant rate. Further, the knowledge of the relative differences in the d($\hat{C}''_{PEAK}$)/dt factor across the shelf can be used to allow for a more precise modelling of the freeze-drying process.

5. CONCLUSION

The relative measurements of the surrogate drying rate could provide a more precise definition of the factor that accounts for the edge vial effect.

6. REFERENCES

1. Tchessalov, S. 2017, "Application of modeling to lyophilization process design and scale up: process validation approaches"
2. Smith, G., Jeerarungrattana, Y. & Ermolina, I. 2018, "The application of dual-electrode through vial impedance spectroscopy for the determination of ice interface temperatures, primary drying rate and vial heat transfer coefficient in lyophilization process development", European Journal of Pharmaceutics and Biopharmaceutics, vol. 130, pp. 224-235.

New Impedance Based Methodologies to Determine the Vial Heat Transfer Coefficient and the Endpoint of Primary Drying

Bhaskar Pandya, Geoff Smith*, Eugene Polygalov, Irina Ermolina
Leicester School of Pharmacy, De Montfort University, Leicester LE1 9BH, UK
*E-mail: gsmith02@dmu.ac.uk

APS 8th International PharmSci Conference, September 5-7, 2017; Hatfield, UK

ABSTRACT

Aims: To develop a new methodology to determine the vial heat transfer coefficient (K_V) and the endpoint of primary drying. **Methods:** During a freeze drying experiment, through vial impedance spectroscopy **(TVIS)** was be employed to measure the peak imaginary capacitance, **C''_{PEAK}**, from the imaginary spectra and the high frequency permittivity, **C'(100 kHz)**, from the real spectra. C''_{PEAK} and C'(100 kHz) are considered to be highly sensitive to the amount of ice remaining in the vial. **Results:** Both the normalised time profiles of C''_{PEAK} and C'(100 kHz) followed the same trajectory within the first 15-20 % of ice sublimation and were therefore, used to estimate the sublimation rate and K_V. Whereas, the time profile of C'(100 kHz) alone was used to determine the endpoint of primary drying. A peak in the time profile of C'(100 kHz) towards the end of primary drying occurred around the same time as ice disappeared, as evidenced by time-lapse photography; **Conclusions:** K_V should be calculated only within the first 15-20% of primary drying and C'(100 kHz) can be followed to track the end point.

KEYWORDS: Freeze-drying, PAT, Drying Rate, Endpoint

INTRODUCTION

The freeze-drying cycle comprises (1) freezing to form ice and crystallise out any solutes, (2) primary drying to remove the ice phase by sublimation and (3) secondary drying to remove the remaining unfrozen water which is bound to the remaining matrix of crystalline and amorphous solids, Rey and May (2004). A better fundamental understanding of the coupled heat and mass transfer processes in primary drying requires the characterisation of the vial heat transfer coefficient (K_V). In industry, K_V is determined after the completion of ~30% of ice sublimation from the classic heat/mass balance equation,

$$K_V = dq/dt/ A.\Delta T = (L.dm/dt)/ A.(T_s-T_b)$$

where dq/dt is the rate of heat transfer from the shelf to the bottom of a given vial and is equal to the product of the latent heat of sublimation, L and the drying rate, dm/dt, divided by the product of the vial's cross-sectional area, A and the difference between the product temperature, T_b and the shelf temperature, T_s, Pikal (1984). However, this calculation assumes that the ice layer has been drying in a horizontal plane from the beginning to the time corresponding to 30% of ice sublimation. *The first objective of this work is to present a new methodology based on TVIS that was used to test whether the assumption is true.*

Two parameters, C'(100 kHz) and C''_{PEAK}, of the real and the imaginary capacitance spectra of the TVIS vial, respectively, are considered to be proportional to the amount of ice remaining in the vial, Smith (2016). It is assumed that C''_{PEAK} is proportional to the height of the ice layer that is in contact with the glass wall (Figure 1) whereas C'(100 kHz) measures the bulk of the ice in the vial whether in contact with the vial wall or not. The surface area, A, is assumed to be constant and therefore, it is expected that C''_{PEAK} will decrease at the same rate as C'(100 kHz).

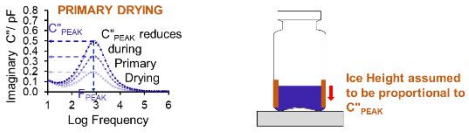

Figure 1: Relationship between C''_{PEAK} and the height of the ice layer

Frequently, the endpoint of primary drying is determined from product thermocouples among several other Process Analytical Technologies (PATs), none of which are free from limitations. *The second objective of this work is to present a new methodology using TVIS to determine the endpoint of primary drying.*

MATERIALS AND METHODS

Double distilled water from "all glass apparatus" was used in this study. The TVIS system comprises a bespoke multichannel high precision impedance analyser which was connected to a TVIS measurement vial, which is a standard 10 mL freeze drying vial (manufactured by Schott) that has been modified with copper electrodes (19 x 10 mm and 10 mm from the base of the vial) attached to the outside of the glass wall (Figure 2).

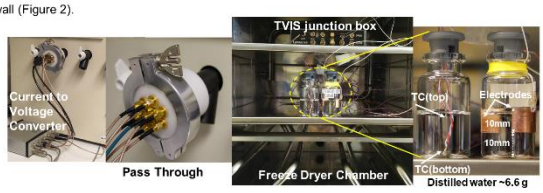

Figure 2: Experimental Set Up

Two Type K thermocouples (TC) were submersed at a range of heights within ~6.6 g of distilled water contained in a clear vial so that the difference in temperature between the top and the bottom could be determined. A TVIS vial was also filled with ~6.6 g of distilled water. Both the vials were then freeze dried in a Virtis Advantage Plus benchtop freeze dryer (Figure 2), by freezing at a shelf temperature of −40 ºC at a ramp of ~36 °C h^{-1}, then temperature cycling to −10 ºC at a ramp of 30°C h^{-1}, (with a hold time of 1 h) and then subjected to primary drying at −15 ºC (40 Pa) until all of the ice disappeared. TVIS capacitance spectra and photographs of the ice sublimation process (using a Canon EOS 550D) were collected every two minutes throughout the freeze-drying process.

RESULTS AND DISCUSSION

- The photographic evidence in Figure 3a shows that at the beginning of the primary drying (0 h) the solid ice block in the TVIS vial was made up of an ice cylinder (black dashed region) in intimate contact with the glass wall and an ice cone on top (dashed red lines).
- The shape of the sublimation interface (the dashed top edge of the ice cylinder) does not change over the first 15-20% of sublimation (i.e. ~0.3-0.5 h). Over this period, C''_{PEAK} was found to be proportional to C'(100 kHz) on the normalised scale (equivalent to 15-18% of ice sublimation) (Figure 3b). During this brief period, the gradient (i.e. drying rate: 2.02 g/h) was determined from the assumption C''_{PEAK} and C'(100 kHz) are both proportional to the amount of ice remaining in the vial.
- Figure 3b shows a divergence of C''_{PEAK} and C'(100 kHz) at 0.5 h owing to the fact that the surface area of the sublimation interface increased from 0.5 h onwards, as confirmed by the photographs.
- The temperature difference between TC_{top} and TC_{base} was ~2ºC over the first 0.2 h of primary drying (Figure 3c) after which TC-top started to increase owing to the fact that the TC-top was no longer in contact with the ice layer (photograph not shown)
- The K_V (~261.3 W m^{-2} K^{-1}) value was determined over the first 0.5 h from the heat/mass balance equation, where L = 2844 Jg^{-1} and dq/dt = 5745 Jh^{-1}, ice temperature was 244.5 K (recorded from TC_{base}), shelf temperature was 258 K and A = 0.00045 m^{-2}. As expected, K_V was 8-10 times higher than the range of values found in the literature (15-25 W m^{-2} K^{-1} at 40 Pa), Brülls (2002) as a consequence of the fact that the current study was undertaken on an isolated vial whereby the radiant heat from the side walls would contribute significantly to the heat transfer co-efficient.

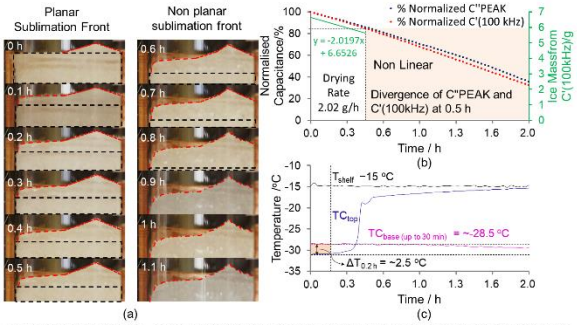

Figure 3: (a) Photographs of the sublimation interface showing a sublimation interface with a constant surface area over the first 0.5 h of of primary drying; (b) Convergence of C''_{PEAK} and C'(100 kHz) parameters over the first 15-20% of sublimation; (c) Difference between the thermocouple temperature close to the top of the ice layer (TC_{top}) and at the base of the vial (TC_{base})

The second objective of this work was to present a new methodology for determining the endpoint of primary drying based on the TVIS parameter C'(100 kHz), which ends in a plateau towards the end of primary drying (Figure 4a). An enlarged version of the plot (Figure 4b) shows a point at which C'(100 kHz) reaches a peak (before decreasing) which corresponds to the point at which the ice disappears as evidenced by time-lapse photography.

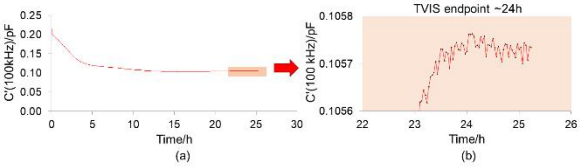

Figure 4: (a) Time profile of C'(100 KHz); (b) and (c) TVIS endpoint agreed with the visual endpoint

CONCLUSIONS

Two conclusions may be made from this work (i) In the case of an isolated vial, K_V should be determined within the first 15-20% of primary drying before the ice interface starts to deviate from a planar drying that would otherwise result in uncertainties in the estimation of the surface area of the ice interface, (ii) The time profile of C'(100 kHz) may be used to detect the endpoint of primary drying.

ACKNOWLEDGEMENTS

A GEA Pharma Systems and Astra Zeneca collaboration and co-funded by Innovate UK.

REFERENCES

Brülls, M., Ramusson, A., 2002. Heat Transfer in Lyophilization. Int J Pharm, 246 (1-2), 1-16.
Pikal, M.J., Roy, M.L., Shah, S., 1984. Mass and Heat Transfer in Vial Freeze-Drying of Pharmaceuticals: Role of the Vial. J Pharm Sci, 73 (9), 1224-1237.
Rey and May (2004) Informa Healthcare. Freeze Drying-Lyophilization of Pharmaceutical and Biological Products (3rd Edt)
Smith G. Through vial impedance spectroscopy. Podium presentation at: SMi Lyophilisation Europe; 2016 Jul 4-5; London, UK.

The Application of Through Vial Impedance Spectroscopy (TVIS) for Optimization Freeze-Drying Process

DE MONTFORT UNIVERSITY LEICESTER
Yowwares Jeerаruangrattana, Bhaskar Pandya, Geoff Smith and Dr Irina Ermolina
Leicester School of Pharmacy, De Montfort University, United Kingdom
International Pharm. Tech. Conference November 4, 2016, Leicester, UK

"Non-invasive, real time lyophilisation process monitoring would increase process understanding and accelerate development of stabilized biopharmaceutical formulations at room temperature."

TVIS Technology

In-line monitoring system for the freeze drying process consisting of:
- Freeze-drying vial with external electrodes
- Pass through for cabling
- External Impedance spectrometer.

TVIS Advantage

1. Non-invasive, real time full cycle lyophilisation monitoring including :
   - Cooling rate, Freezing and Annealing
   - Primary and Secondary Drying end point
2. Optimization of the primary drying process by:
   - Heat Transfer Coefficient (K_V) Determination
   - Dried Product Resistance (R_P) Determination
3. Can be applied in standard freeze dryers
4. Integrated, bench top, single vial, TVIS enabled analytical freeze dryer

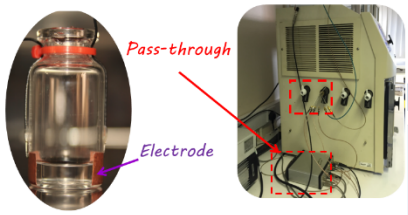

Figure 1. TVIS Technology

TVIS Technology Principle

Process analytical technology based on impedance spectroscopy
- Electrical impedance determines the ability of materials to conduct electricity under an applied voltage .
- Impedance is a function of dielectric and conductive properties and therefore the physical state of vial and its contents.
- Principal parameter effecting measured impedance is resistance/conductivity of sample within the vial.
- Changes in electrical parameters mirror the condition of the sample throughout the lyophilisation process.
- The capacitance spectrum is related to *the resistance/ conductivity and capacitance of the vial contents.*
- Data viewing software (LyoView ™) identifies the peak frequency (F_{PEAK}) and the peak amplitude (C''_{PEAK}) in the imaginary part of the capacitance spectrum
- F_{PEAK} can be used to monitor phase behaviour (ice formation, glass transitions) and product temperature
- C''_{PEAK} can be used to monitor the amount of ice remaining during primary drying, from which the drying rate and the end point may be determined.

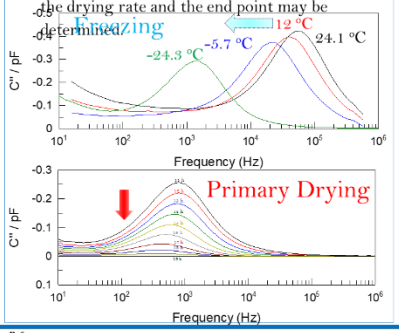

TVIS Applications

Heat Transfer Coefficient (K_V) Determination

- The product temperature($T_{PRODUCT}$) derived by ***TVIS*** is one of the parameters needed for K_V determination
- Sublimation rate or drying rate (dm/dt) is estimated by ***TVIS***

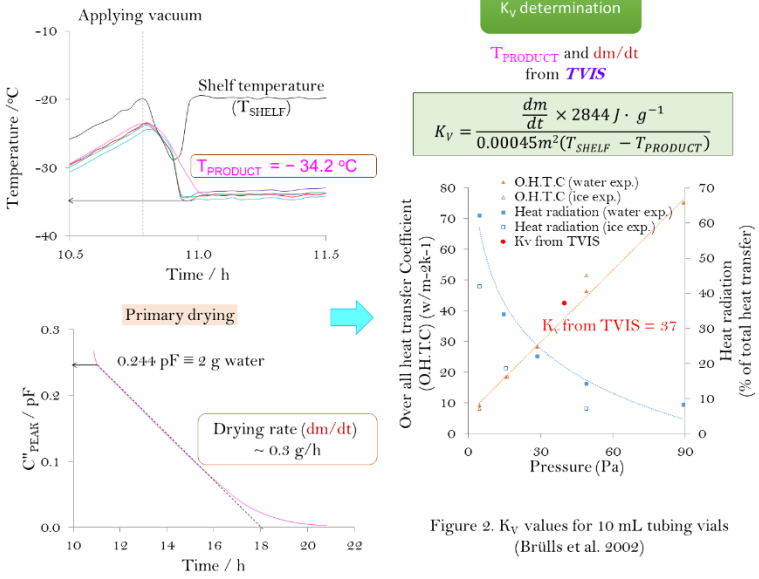

Figure 2. K_V values for 10 mL tubing vials (Brülls et al. 2002)

Dried Product Resistance (R_P) Determination

- C''_{PEAK} from ***TVIS*** is proportional to the amount of ice; therefore it is estimated for drying rate (dm/dt)
- Partial pressure of ice (P_{ICE}) and condenser ($P_{CONDENSER}$) calculated from temperature of ice (T_{ICE}) and condenser ($T_{CONDENSER}$) by using Clausius- Clapeyron derived equation

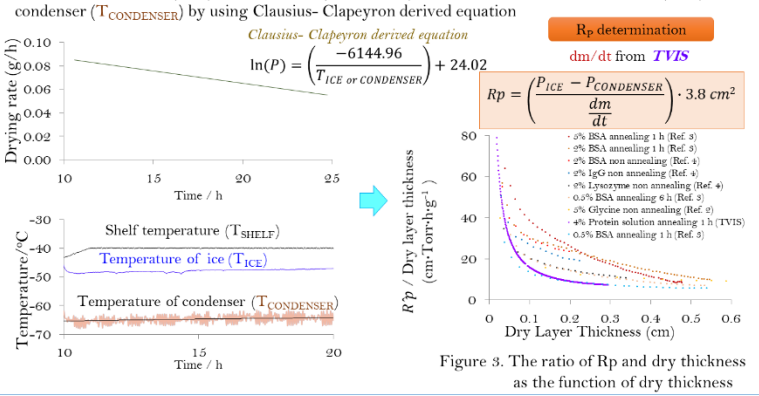

Figure 3. The ratio of Rp and dry thickness as the function of dry thickness

References
1. BRÜLLS, M. and RASMUSON, A. (2002) Heat transfer in vial lyophilization. International Journal of Pharmaceutics, 246 (1–2), pp. 1–16.
2. GIESELER, H., KRAMER, T. and PIKAL, M.J. (2007) Use of manometric temperature measurement (MTM) and SMART™ freeze dryer technology for development of an optimized freeze-drying cycle. Journal of Pharmaceutical Sciences, 96 (12), pp. 3402–3419.
3. JOHNSON, R.E. et al. (2010) Use of manometric temperature measurements (MTM) to characterize the freeze-drying behavior of amorphous protein formulations. Journal of Pharmaceutical Sciences, 99 (6), pp. 2963–2972.
4. LEWIS, L.M. (2010) Characterizing the Freeze-Drying Behavior of Model Protein Formulations. Aaps Pharmscitech, 11 (4), pp. 1690–1696.
5. SMITH, G., POLYAKOV, E. and PAGE, T. (2011) Electrical Monitoring of a Lyophilization Process. GB2450099 (A)
6. TANG, X.C., NAIL, S.L. and PIKAL, M.J. (2005) Freeze-drying process design by manometric temperature measurement: design of a smart freeze-dryer. Pharmaceutical Research, 22 (4), pp. 685–700.

Freeze Drying Monitoring Using LyoDEA® Process Control

Pandya B, Smith G and Ermolina I

Leicester School of Pharmacy, De Montfort University, United Kingdom

The Quality by Design Symposium, March 16, 2016, Leicester, UK

Introduction to Freeze Drying: A Method of Choice

- Freeze-Drying, also known as Lyophilisation, is a means of removing moisture from food, pharmaceuticals, chemicals and biotech products[1].
- In all cases, this method is used to improve the stability of a moisture-sensitive product and/or make the product easier to store or transport[1].
- In the biotechnology industry, freeze-drying is a final processing step to stabilise the protein for long-term storage[1].
- However, freeze drying is an inefficient, expensive and a time consuming process, sometimes requiring several hours from start to finish![2]
- This poster presents a technology called LyoDEA® or Lyophilisation using Dielectric Analysis, that may be used to shorten the duration of the process, thus saving on energy and running costs.

Description of a Freeze-Drying Process

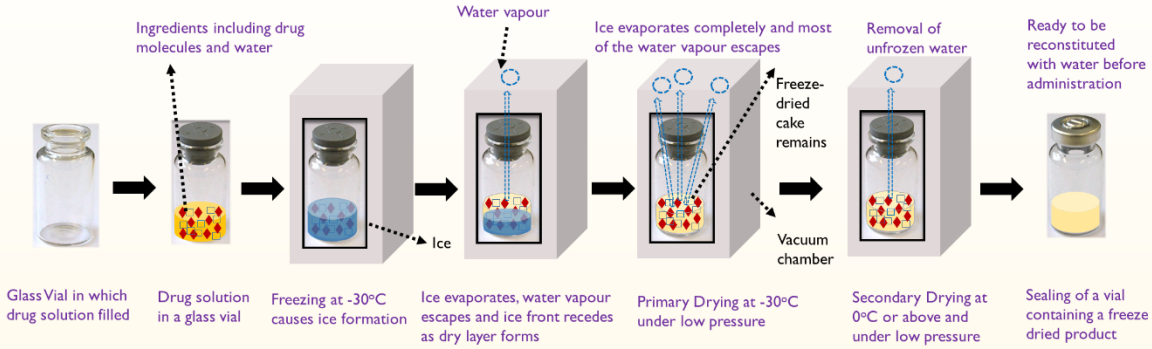

- This is an illustration of how a freeze drying process for a drug solution inside a glass vial occurs inside a vacuum chamber, i.e. one freeze-drying cycle consists of three main steps: Freezing, Primary Drying and Secondary Drying[3].
- Throughout the cycle, the temperature in the vacuum chamber is maintained such that the protein formulation does not get damaged due to excessive heat.
- The drug and ingredient molecules shown here are just for depiction. In reality they are not visible to the naked eye.

Trial-and-Error Approach Methodology: How Long Should a Product be Dried For?

- Today, to determine the duration of drying, the scientist has to adjust the heat input by making minor changes to the temperature of the shelves of a freeze-drier[1].
- But, generally, the scientist finds a shelf temperature close to the "critical/collapse" temperature, i.e. the temperature at which the freeze-dried cake loses its elegance and it does not have sufficient mechanical strength to support its own weight[1].
- Collapse temperature must be avoided at all costs because this would compromise final product quality[3].
- Therefore, the scientist chooses to stay 3°C to 5°C below the collapse temperature as a safety margin[1].
- As a result, the primary drying phase becomes lengthy and less energy efficient.
- It is known that even a 1°C increase in the shelf temperature would reduce the drying time by 13%[1].

Collapsed product | Good quality product

Freeze Drying Will Never be the Same With LyoDEA®

CONTINUOUS MONITORING → CONTROL OF THE PROCESS → SHORTER CYCLE TIMES

- An individual vial monitoring system that predicts the end of the freezing and the primary drying stages[4].
- LyoDEA® will allow the product temperature to be set up as high as possible, but not exceeding the collapse temperature leading to reduction in drying cycle times[4].
- This will have a favourable financial impact on the production of freeze dried products.
- In the other technologies, the temperature sensor makes direct contact with the product inside the vial[4].
- This is not preferred because it can influence the freezing and drying behaviour[4].
- The key difference between LyoDEA® and the other technologies is that LyoDEA® can monitor the process without the use of temperature sensors which make direct contact with the product, known as "Non-Invasive measurement"[4].
- The dielectric analysis is carried out by passing electric current through electrodes located outside the vial: so no product contact![4]

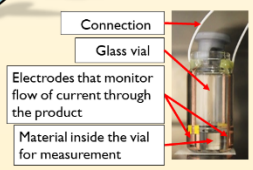

Picture of a vial accompanying the LyoDEA® assembly[4]

So what do we conclude?

Depending on physical state of the product as it is frozen or dried, the frequencies of the current and the peak height change which are detected by the LyoDEA® instrument and this will tell the scientist when to stop drying!

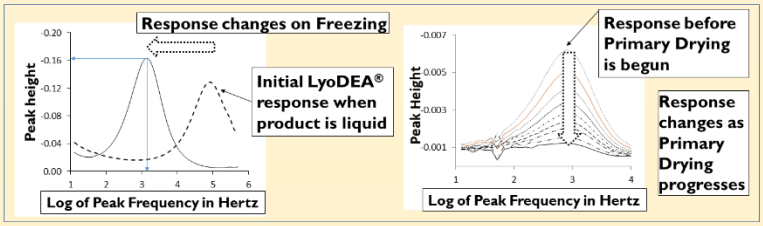

Graphs showing product response before and after freezing and primary drying respectively[4]

References

1. Shon, M., 2013. Optimization of Primary Drying Time Using a Combination of ControLyo™ Nucleation on Demand and SMART™ Freeze Dryer Technology. American Pharmaceutical Review, [Online]. Available: http://www.americanpharmaceuticalreview.com/Featured-Articles/152029-Optimization-of-Primary-Drying-Time-Using-a-Combination-of-ControLyo-Nucleation-on-Demand-and-SMART-Freeze-Dryer-Technology Accessed [18-02-2016].
2. Tang, X., Pikal, M. J., 2004. Design of Freeze Drying Processes for Pharmaceuticals: Practical Advice. *Pharmaceutical Research, 21(2). Pp 191-200.*
3. Chang, B.S., Patro, S.Y., 2004. Freeze-drying Process Development for Protein Pharmaceuticals. In "Lyophilization of Biopharmaceuticals" (Costantino, H.R., Pikal, M.J., eds) American Association of Pharmaceutical Scientists. Pp 113-138.
4. Smith, G., Polygalov, E., Arshad, M.S., Page, T., Taylor, J., Ermolina, E., 2013. An Impedance-Based Process Analytical Technology for Monitoring the Lyophilisation Process. International Journal of Pharmaceutics, 449, pp 72-83.